Electromagnetic instabilities and plasma turbulence driven by the electron-temperature gradient

Toby Adkins
Merton College
University of Oxford

A thesis submitted for the degree of
Doctor of Philosophy in Theoretical Physics

Michaelmas 2022

Electromagnetic instabilities and plasma turbulence driven by the electron-temperature gradient

Toby Adkins

Merton College, University of Oxford

Submitted for the degree of Doctor of Philosophy in Theoretical Physics

Michaelmas 2022

Electromagnetic instabilities and turbulence driven by the electron-temperature gradient are considered in a local slab model of a tokamak-like plasma. Derived in a low-beta asymptotic limit of gyrokinetics, the model describes perturbations at scales both larger and smaller than the electron inertial length d_e, but below the ion Larmor scale ρ_i, capturing both electrostatic and electromagnetic regimes of turbulence. The well-known electrostatic instabilities — slab and curvature-mediated ETG — are recovered, and a new instability is found in the electromagnetic regime, called the Thermo-Alfvénic instability (TAI). It exists in both a slab version (sTAI, destabilising kinetic Alfvén waves) and a curvature-mediated version (cTAI), which is a cousin of the (electron-scale) kinetic ballooning mode (KBM). The cTAI turns out to be dominant at the largest scales covered by the model (greater than d_e but smaller than ρ_i), its physical mechanism hinging on the fast equalisation of the total temperature along perturbed magnetic field lines (in contrast to KBM, which is pressure balanced). A turbulent cascade theory is then constructed, with two energy-injection scales: d_e, where the drivers are slab ETG and sTAI, and a larger (parallel-system-size-dependent) scale, where the driver is cTAI. The latter dominates the turbulent transport if the temperature gradient is greater than a certain critical value, which scales inversely with the electron beta. The resulting heat flux scales more steeply with the temperature gradient than that due to electrostatic ETG turbulence, giving rise to stiffer transport. This can be viewed as a physical argument in favour of near-marginal steady-state in electron-transport-controlled plasmas (e.g., the pedestal) at sufficiently high values of the electron beta. Numerical simulations are then used to demonstrate that electrostatic turbulence driven by the slab ETG does indeed saturate via a critically-balanced, constant-flux cascade of free-energy, which is shown to be the dynamical manifestation of the scale-invariance of electrostatic drift kinetics. Data from simulations shows excellent agreement with the theoretically predicated one- and two-dimensional spectra

of the perturbations. Failure of saturation in electromagnetic turbulence driven by the sTAI is then identified, characterised and discussed. While the model in which these results are derived is simplistic, the new physics that is revealed by it should be of interest to those attempting to model the effect of gradient-driven turbulence in tokamak-relevant configurations, particularly those with high beta and large electron-temperature gradients, in which electromagnetic effects play a significant role.

Acknowledgements

The content of this thesis owes much to the discussions, lively debates and instances of collaboration that I have had with numerous individuals throughout the course of my studies. Though the complete list is too long to include, I would like to single out two instrumental individuals: A. A. Schekochihin, whose acute intellect and wit have gradually sharpened mine over the last eight years; and P. G. Ivanov, whose friendship and belief in my abilities has been vital to many moments of breakthrough and discovery during my research career to date.

More broadly, I would like to thank all of my family (Ara, Martin & Sam) and friends (in particular, Anthony, Adam, Alex, Caleb, David, Eric, Ellie, Ewan, Georgia, Jacob & Marcus) for their constant support throughout my studies. Research is rarely straightforward, and I am so grateful to have a group of people who were happy to share the difficulties with me. In particular, I will be eternally grateful to my wonderful girlfriend Katie, whose constant love and support at every step of this journey has been critical to me making it this far, and which will uncountably prove critical in any future success that I may have.

Lastly, I would like to dedicate this thesis to my late grandfather, the experimental physicist C. J. Adkins. His infinite ability to humour his young grandson's curiosity about the world — whether out on a walk on Midsummer Common in Cambridge, or tinkering over an old oscilloscope in a dusty shed somewhere in Norfolk — almost certainly planted the seed that grew into all that follows.

Contents

List of Figures

Chapter 1

Introduction

An understanding of the heat transport properties of a magnetically confined plasma is crucial to the design of successful tokamak experiments. Since the characteristic correlation length scales associated with the turbulence are small in comparison to the scale of the device, one can usually assume that the turbulence depends only on local equilibrium quantities — such as density, velocity, temperature, electromagnetic fields — and their gradients (though there are cases where the global features of the equilibrium can become important: see, e.g., [2], in the context of the pedestal). Much of the focus of current research is on the turbulence consisting of unstable microscale perturbations. Though there are exceptions (e.g., the trapped-electron mode [3, 4] or the universal instability [5, 6]), the most important of these are often driven either by the ion-temperature gradient (ITG) (see, e.g., [7–9]) or the electron-temperature gradient (ETG) (see, e.g., [10, 11]). These perturbations typically live on ion and electron scales, respectively, although one of the conclusions of this thesis will be to question this expectation with regard to ETG. Strongly driven plasma turbulence — i.e., plasma turbulence with temperature gradients far above the linear-instability thresholds — is believed to saturate by reaching a 'critically balanced' state [12], in which, by analogy with the Kolmogorov theory of hydrodynamic turbulence [13], free energy injected by linear instabilities is nonlinearly transferred (cascaded) to smaller scales, where it is thermalised by collisions. If one can determine the turbulent state of the plasma at saturation, then it is, in principle, possible to determine how the turbulent heat fluxes carried by these perturbations depend on the temperature gradients. Knowing this relationship, one can invert it to find the heating power that needs to be provided to support a particular temperature gradient. In many cases, the heat transport found in this context is described as ‘stiff’ [14]: the heat flux scales steeply with the temperature gradient, so a large increase in heating power does very little to increase the temperature gradient, making achieving temperature gradients far above marginal a difficult task.

Though it has long been understood that ion-scale physics can play a significant role in plasma transport (see references above), there is evidence to suggest that ion-scale instabilities driven by the ion-temperature gradient can be suppressed by strong $\boldsymbol{E} \times \boldsymbol{B}$ shear in steep-gradient regions of a tokamak (e.g., the pedestal), particularly in spherical or low-aspect-ratio configurations (see [15–19], and references therein). This has the effect of reducing the ion contribution to the turbulent heat transport, which instead becomes dominated by the electron channel[1]. This seems to run contrary to the typical ‘gyro-Bohm’ transport estimates, which suggest that the heat flux carried by the electrons will be smaller than that of the ions by a square-root of their mass ratio $\sqrt{m_e/m_i} \ll 1$ — this is based on the (perhaps naive) assumption that the sizes of the turbulent eddies generated on ion and electron scales will be comparable to their Larmor radii ρ_i and ρ_e, respectively. However, it will be one of the important conclusions of this thesis that the relevant scales which determine the electron heat transport are those of the plasma equilibrium, rather than those associated with the small perpendicular scales ρ_e, allowing the electron transport to be dominant despite the potentially small size of their associated turbulent structures. This means that the characterisation of electron-scale instabilities is not only desirable, but indeed necessary for a complete understanding of the heat transport in such systems.

Furthermore, a comprehensive understanding of electromagnetic effects on the microinstability properties of the plasma, and the resultant turbulence, is becoming increasingly important as experimental values of the plasma beta (the ratio of the thermal and magnetic pressures) and, therefore, electromagnetic fluctuations, will be higher in reactor-relevant tokamak scenarios; e.g., ITER is projected to have a plasma beta of up to 2.5% [20, 21], and beta could exceed 15% in a recently proposed STEP equilibrium [22]. Though the investigation of electromagnetic instabilities and turbulence is of general importance within many different types of plasma systems (e.g., astrophysical plasmas, laser plasmas), much of the research in fusion has focused on two particular

---

[1] Note that such a state is consistent with the power-balance constraints required for steady-state tokamak operation as the energy injected into ions can be collisionally transferred into the thermal motion of the electrons.

microinstability classes: micro-tearing modes (MTM) — initially, in simplified models [23–30], later in tokamak geometry [31–36] — and kinetic ballooning modes (KBM) [18, 37–50]. Both of these are intrinsically electromagnetic, requiring the perturbation of the magnetic field's direction and (sometimes) magnitude. Despite significant numerical progress in understanding the behaviour of such modes, however, there is still a certain lack of clarity about the fundamental physical processes that are responsible for them, owing to the complexity of these modes in the general tokamak geometry. Progress in distilling the essential physical ingredients behind electromagnetic destabilisation can be made by means of constructing minimal models.

To this end, in this thesis, we consider electromagnetic instabilities and turbulence driven by the electron-temperature gradient in a local slab model of a tokamak-like plasma, with constant equilibrium gradients, including magnetic drifts but not magnetic shear. The inclusion of the finite gradient and curvature of the magnetic field — in addition to the conventional slab geometry (see, e.g., [51]) — is motivated by recent evidence [52–54] that the modes mediated by these equilibrium quantities can often be the fastest-growing ones in steep-gradient regions of the plasma (e.g., the pedestal), and thus significant in determining its nonlinear saturated state. The governing equations are derived in the low-beta asymptotic limit of gyrokinetics (see, e.g., [55]). The electron plasma beta $\beta_e = 8\pi n_{0e} T_{0e}/B_0^2$ (n_{0e} and T_{0e} are the density and temperature associated with the equilibrium distribution of the electrons and B_0 the equilibrium magnetic field strength) is ordered as $m_e/m_i \ll \beta_e \ll 1$, allowing us to order out compressive magnetic field perturbations while retaining Alfvénic ones. The normalised collisionality $\nu_* = L/\lambda_{ei}$ (λ_{ei} is the electron-ion collisional mean-free path and L some lengthscale associated with the plasma equilibrium) is assumed to be order-unity to capture both collisionless ($\nu_* \to 0$) and collisional ($\nu_* \gg 1$) regimes of turbulence. Our equations also describe perturbations on scales both larger and smaller than the electron inertial scale $d_e = \rho_e/\sqrt{\beta_e}$, at which magnetic flux unfreezes, capturing both electrostatic and electromagnetic regimes of turbulence. Formally, perpendicular wavenumbers are ordered as $\rho_i^{-1} \ll k_\perp \sim d_e^{-1} \ll \rho_e^{-1}$ (sub-ion-Larmor scales).

At appropriately short perpendicular wavelengths (below the d_e scale), we recover the well-known, electrostatic slab ETG (sETG, [56, 57]) and curvature-mediated ETG (cETG, [58]) instabilities. Turning our attention to longer perpendicular wavelengths (above the d_e scale, but still smaller than the ion gyroradius), we demonstrate the existence of the novel Thermo-Alfvénic instability (TAI) that arises in the electromagnetic regime. We show that it exists in both a slab version (sTAI, destabilising kinetic Alfvén waves) and a curvature-mediated version (cTAI), the latter of which is related to the (electron-scale version of) the KBM. In particular, we find that cTAI is the dominant instability on the largest scales covered by the model, with a maximum growth rate that is greater than that of the cETG. This maximum growth rate occurs at a specific, finite parallel wavenumber, unlike cETG, which is two-dimensional. Its physical mechanism hinges on the fast equalisation of the total temperature along perturbed magnetic field lines (in contrast to the KBM, which is approximately pressure balanced; see, e.g., [39, 59]) due to the dominance of either parallel streaming (in the collisionless limit) or thermal conduction (in the collisional one). We also show that the sTAI is stabilised at large parallel wavenumbers by compressional heating, and at large perpendicular wavenumbers by the effects of finite electron inertia (in the collisionless limit) or finite resistivity (in the collisional one). We then map out all of these instabilities in parallel and perpendicular wavenumber space.

Using a critical-balance phenomenology analogous to [12], we then construct a turbulent-cascade theory for the free energy injected by these instabilities. Assuming the cascade to be local, the theory is shown to allow two injection scales: d_e, where the drivers are sETG and sTAI, and a larger scale dependent on the parallel size of the system (the connection length, in the case of a tokamak), where the principal driver is cTAI. We find (within this theoretical approach) that the latter dominates the turbulent transport if the temperature gradient is greater than a certain critical value, which scales inversely with the electron beta. Using constant-flux arguments, we then derive scaling estimates for the turbulent electron heat flux carried by fluctuations at these injection scales, finding that the heat flux due to electromagnetic cTAI turbulence scales more steeply with the temperature gradient than the heat flux due to electrostatic sETG turbulence in this regime, and thus gives rise to stiffer transport. Note that we do not engage with ion physics here, formally assuming that the scale of dominant energy injection for the turbulent cascade lies on sub-Larmor scales.

The electrostatic heat-flux scalings predicted by this turbulent-cascade theory are then shown to arise also as a direct consequence of the scale invariance of drift kinetics in the electrostatic limit — under the assumption that the (local) transport does not depend on the perpendicular size of the system — for which the critically balanced, constant-flux cascade provides a dynamical explanation. This is then confirmed through direct numerical simulations of electrostatic turbulence driven by the (collisional) sETG. These simulations also demonstrate that a constant-flux cascade is compatible with plasma systems where there is not a well-defined scale separation in (perpendicular) wavenumber space between injection (due to equilibrium gradients) and dissipation (due to Landau damping, thermal conduction, finite-Larmor-radius effects, etc.), which is a departure from the usual Kolmogorov picture of hydrodynamic turbulence with a dissipation-free inertial range. Lastly, we perform simulations of electromagnetic turbulence driven by the sTAI, finding that they fail to saturate, a behaviour also observed in more complex electromagnetic gyrokinetic simulations (see, e.g., [60–63] and references therein). Some possible explanations for this behaviour are then examined.

The remainder of this thesis is organised as follows. In Chapter 2, we describe and physically motivate our low-beta model equations, in both the collisionless and collisional limits. Chapter 3 recovers the well-known electrostatic instabilities — sETG and cETG — while Chapter 4 is devoted to the characterisation of the TAI, including a detailed treatment of both sTAI and cTAI. Chapter 5 is a summary of the asymptotic behaviour of these instabilities in wavenumber space, providing a pictorial representation of the linear results of this thesis. In Chapter 6, we construct a cascade theory for the turbulence driven by these instabilities, and derive scaling estimates for the turbulent electron heat fluxes as functions of the electron-temperature gradient, parallel system size and the electron beta. In Chapter 7, we show numerically that electrostatic sETG turbulence saturates via a critically balanced cascade, and relate this to the scale invariance of drift kinetics in the electrostatic limit. Simulations of electromagnetic sTAI turbulence are shown to exhibit a lack of saturation in Chapter 8, and possible explanations are speculated about. Finally, results are summarised and limitations, implications and future directions are briefly discussed in Chapter 9. Given its focus, this thesis shares significant material with [1] in its exploration of the linear instabilities in Chapters 3 and 4. For the sake of brevity, we have not included here any of the associated technical calculations, choosing, instead, to focus on the fundamental physics; a reader looking for further detail can find it in the appendices of [1].

Part I

Linear instabilities: ETG and TAI

Chapter 2

Low-beta equations

We wish to describe dynamics at electron scales (below the ion Larmor scale) of a magnetised plasma, in the presence of electromagnetic perturbations. Our electron species will have an equilibrium temperature gradient, and will be advected by the magnetic drifts associated with a magnetic geometry of constant curvature. Our equations are derived in a low-beta asymptotic limit of gyrokinetics; this allows us to order out compressive magnetic field perturbations while retaining Alfvénic ones. Formally, the electron beta is ordered as $m_e/m_i \ll \beta_e \ll 1$, the normalised collisionality as $\nu_* \sim 1$, and perpendicular wavenumbers as $\rho_i^{-1} \ll k_\perp \sim d_e^{-1} \ll \rho_e^{-1}$ (sub-ion-Larmor scales). In this chapter, we present a summary of these equations and the physical motivation behind them; their detailed derivation can be found in [1].

2.1 Magnetic equilibrium and geometry

The magnetic geometry that we adopt is one of constant magnetic curvature, as this allows us to capture the effect of the magnetic drifts on our plasma while retaining most of the simplicity associated with conventional slab gyrokinetics [51, 64]. We consider a domain positioned in the magnetic field of a current line at a radial distance R from the central axis, and define the $\hat{\boldsymbol{x}}$ and $\hat{\boldsymbol{y}}$ directions as pointing radially outwards and parallel to the central axis, respectively, as shown in Figure 2.1. In the context of the outboard midplane in tokamak geometry, these are analogous to the 'radial' and 'poloidal' coordinates, respectively, terms that we shall adopt in our later discussions. One can think of this geometry as that of a Z-pinch [1, 64–66], meaning that our model will be unable to capture the effects of magnetic shear and the poloidal variation of

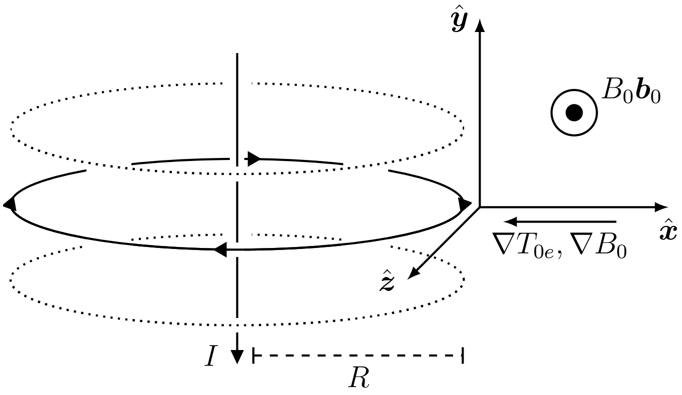

Figure 2.1: Illustration of the constant-curvature geometry, showing the domain positioned at a distance R from the current axis, with the $\hat{\boldsymbol{x}}$ and $\hat{\boldsymbol{y}}$ directions pointing radially outwards and parallel to this axis, respectively. The equilibrium magnetic field is in the $\boldsymbol{b}_0$ direction. Both the equilibrium temperature T_{0e} and equilibrium magnetic field B_0 vary radially, with their scale lengths L_T and L_B, respectively, assumed constant across the domain.

geometric coefficients along the field line (that can, e.g., lead to particle trapping); to include them requires a careful treatment of the toroidal geometry (see, e.g., [67]).

In the geometry considered here, the magnetic field consists of an equilibrium part that is oriented in the $\boldsymbol{b}_0 = \hat{\boldsymbol{z}}$ direction and varies radially, plus a time- and space-dependent fluctuating part:

$$\boldsymbol{B}(\boldsymbol{r}, t) = B_0(x)\boldsymbol{b}_0 + \delta\boldsymbol{B}_\perp(\boldsymbol{r}, t). \tag{2.1}$$

In what follows, we shall express the perpendicular magnetic-field fluctuations in terms of the parallel component of the magnetic vector potential:

$$\delta\boldsymbol{B}_\perp(\boldsymbol{r}, t) = \nabla \times \boldsymbol{A} = -\boldsymbol{b}_0 \times \nabla A_\parallel. \tag{2.2}$$

The component of the magnetic-field fluctuations parallel to the mean field $\delta B_\parallel / B_0$ is negligible in the limit of low beta (this follows from the perpendicular component of Ampère's law, see, e.g., appendix A of [1]). The electric field is related to the magnetic vector potential $\boldsymbol{A}$ and electrostatic potential ϕ by

$$\boldsymbol{E}(\boldsymbol{r}, t) = -\frac{1}{c}\frac{\partial \boldsymbol{A}}{\partial t} - \nabla\phi, \tag{2.3}$$

and is assumed to have no mean part. The equilibrium (mean) magnetic field has the scale length and radius of curvature

$$L_B^{-1} = -\frac{1}{B_0}\frac{\mathrm{d}B_0}{\mathrm{d}x}, \quad R^{-1} = \left|\boldsymbol{b}_0 \cdot \nabla\boldsymbol{b}_0\right|, \tag{2.4}$$

respectively, both of which are assumed to be constant across our domain. For a low-beta plasma, it follows from equilibrium force balance that $R = L_B$, and so we shall henceforth no longer distinguish between them [see (A.72)]. We assume that the background gradient of the temperature T_{0e} associated with the equilibrium distribution of the electrons also varies radially, with scale length

$$L_T^{-1} = -\frac{1}{T_{0e}}\frac{\mathrm{d}T_{0e}}{\mathrm{d}x}, \tag{2.5}$$

which, similarly, is assumed to be constant over the domain. The thermal speed of the electrons is then given by $v_{\mathrm{the}} = \sqrt{2T_{0e}/m_e}$, where m_e is the electron mass. Both the density gradient and the ion temperature gradient are everywhere assumed negligible. The fact that the equilibrium gradients of the electron temperature (2.5) and magnetic field (2.4) are aligned means that, within our simplified geometry, we are only able to capture dynamics in the so-called 'bad-curvature' region of the tokamak (e.g., on the outboard midplane).

2.2 Perturbations from equilibrium

We consider perturbations to the electron distribution function around this local equilibrium, which are assumed to have characteristic frequencies ω and wavenumbers $k_\parallel$ and $k_\perp$ parallel and perpendicular, respectively, to the magnetic field (2.1). Following Appendix A of [1], we adopt the following ordering of frequencies

$$\frac{\omega}{\Omega_e} \sim \beta_e\frac{d_e}{L}, \quad \frac{\omega}{\Omega_i} \sim \frac{d_e}{L}, \tag{2.6}$$

lengthscales:

$$k_\perp\rho_i \gg 1, \quad k_\perp d_e \sim 1, \quad k_\perp\rho_e \sim \sqrt{\beta_e}, \quad k_\parallel L \sim \sqrt{\beta_e}, \quad k_\parallel\lambda_{ei} \sim 1, \quad \frac{k_\parallel}{k_\perp} \sim \sqrt{\beta_e}\frac{d_e}{L}, \tag{2.7}$$

and fluctuation amplitudes:

$$\frac{e\phi}{T_{0e}} \sim \frac{\delta n_e}{n_{0e}} \sim \frac{\delta n_i}{n_{0i}} \sim \frac{\delta T_e}{T_{0e}} \sim \frac{\delta T_i}{T_{0i}} \sim \frac{d_e}{L}, \quad \frac{\delta \boldsymbol{B}_\perp}{B_0} \sim \sqrt{\beta_e}\frac{d_e}{L}, \quad \frac{\delta B_\parallel}{B_0} \sim \beta_e\frac{d_e}{L}, \tag{2.8}$$

in which $\Omega_s = q_s B_0/m_s c$ is the Larmor frequency of species s, q_s its charge, m_s its mass, c is the speed of light, and $L \sim L_B \sim L_T$ is once again some lengthscale associated with the plasma equilibrium. The above ordering of frequencies, lengthscales and amplitudes with respect to the small parameter $d_e/L \sim \rho_i/L$ is the standard gyrokinetic ordering (see, e.g., [55]), to which the ordering in $m_e/m_i \ll \beta_e \ll 1$ is treated as subsidiary. Starting from the gyrokinetic system of equations, one can derive evolution equations for the density (δn_e), parallel velocity ($u_{\parallel e}$), parallel temperature ($\delta T_{\parallel e}$) and perpendicular temperature ($\delta T_{\perp e}$) perturbations of the electrons. These equations are presented in the following sections. As in (2.7), we assume everywhere that the electron Larmor radius ρ_e is small, and so work in the drift-kinetic approximation for the electrons. Furthermore, we will primarily be concerned with dynamics at sub-ion-Larmor scales $k_\perp \sim d_e^{-1} \gg \rho_i^{-1}$, under the approximation of adiabatic ions (see Section 2.2.4). We discuss the consequences of this choice in Section 9.1.1.

2.2.1 Density perturbations

The perturbed electron density satisfies the continuity equation:

$$\frac{\mathrm{d}}{\mathrm{d}t}\frac{\delta n_e}{n_{0e}} + \nabla_\parallel u_{\parallel e} + \frac{\rho_e v_{\mathrm{th}e}}{2L_B}\frac{\partial}{\partial y}\left(\frac{\delta T_{\parallel e}}{T_{0e}} + \frac{\delta T_{\perp e}}{T_{0e}}\right) = 0. \tag{2.9}$$

This says that the density perturbation is subject to three influences: (i) advection by the $\boldsymbol{E}\times\boldsymbol{B}$ motion of the electrons,

$$\frac{\mathrm{d}}{\mathrm{d}t} = \frac{\partial}{\partial t} + \boldsymbol{v}_E\cdot\nabla_\perp, \quad \boldsymbol{v}_E = \frac{\rho_e v_{\mathrm{th}e}}{2}\boldsymbol{b}_0\times\nabla_\perp\varphi, \quad \varphi = \frac{e\phi}{T_{0e}}, \tag{2.10}$$

where $-e$ is the electron charge; (ii) compression or rarefaction due to the perturbed parallel electron flow $u_{\parallel e}\boldsymbol{b}$ along the exact magnetic field, including the perturbation of the magnetic field direction:

$$\nabla_\parallel = \boldsymbol{b}\cdot\nabla = \frac{\partial}{\partial z} + \frac{\delta\boldsymbol{B}_\perp}{B_0}\cdot\nabla_\perp, \quad \frac{\delta\boldsymbol{B}_\perp}{B_0} = -\rho_e\boldsymbol{b}_0\times\nabla_\perp\mathcal{A}, \quad \mathcal{A} = \frac{A_\parallel}{\rho_e B_0}; \tag{2.11}$$

(iii) the magnetic drifts due to the finite curvature and gradient of the magnetic field. The parallel and perpendicular temperature perturbations arise from the velocity dependence of the curvature and ∇B drifts in the gyrokinetic equation [see (A.65)]. The presence of these magnetic drifts is essential for the curvature-mediated instabilities that will be the focus of Section 3.3 and much of Chapter 4.

Note that we have ignored the magnetic-drift terms proportional to $\delta n_e/n_{0e}$ and φ in the continuity equation (2.9), as they will always turn out to be smaller than the magnetic-drift terms proportional to the temperature perturbations in what follows.

This is in a bid to make our equations as simple as possible, while retaining all of the relevant physics. We shall ignore similar terms in our other equations for the perturbations, for the same reason. We would like to emphasise that this limit is not formally an ordering — in the sense that some of the terms that are retained can, in certain meaningful limits, turn out to be as small as those terms that have been neglected — but the latter are negligible always, and so the remaining equations are always no worse off for not having them. Cautious readers may be reassured by the fact that all of the instabilities considered in chapters 3 and 4 are derived in a limit in which this is a valid approximation (see [1]).

2.2.2 Parallel velocity perturbations

The parallel momentum equation associated with the electrons is

$$n_{0e}m_e\frac{\mathrm{d}u_{\parallel e}}{\mathrm{d}t} = -\nabla_{\parallel}p_{\parallel e} - en_eE_{\parallel} - \nu_{ei}m_eu_{\parallel e}. \tag{2.12}$$

The three forces appearing on the right-hand side are, from right to left: (i) the collisional drag against the ions (which are assumed motionless), where ν_{ei} is the electron-ion collision frequency [see (A.3)], (ii) the parallel electric field

$$E_{\parallel} = \boldsymbol{b}\cdot\boldsymbol{E} = -\left(\frac{1}{c}\frac{\partial A_{\parallel}}{\partial t} + \nabla_{\parallel}\phi\right) = -\left(\frac{1}{c}\frac{\mathrm{d}A_{\parallel}}{\mathrm{d}t} + \frac{\partial\phi}{\partial z}\right), \tag{2.13}$$

and (iii) the parallel pressure gradient, which consists of both the parallel gradient of the parallel-pressure perturbation and the projection of the equilibrium temperature gradient onto the perturbed magnetic field:

$$\nabla_{\parallel}p_{\parallel e} = \nabla_{\parallel}\delta p_{\parallel e} + n_{0e}\frac{\delta B_x}{B_0}\frac{\mathrm{d}T_{0e}}{\mathrm{d}x} = n_{0e}T_{0e}\left[\nabla_{\parallel}\left(\frac{\delta n_e}{n_{0e}} + \frac{\delta T_{\parallel e}}{T_{0e}}\right) - \frac{\rho_e}{L_T}\frac{\partial\mathcal{A}}{\partial y}\right]. \tag{2.14}$$

Since an electron flow uncompensated by an ion flow is a current, $u_{\parallel e}$ is related to $A_{\parallel}$ via Ampère's law [see (A.48)]:

$$-en_{0e}u_{\parallel e} = j_{\parallel} = \frac{c}{4\pi}\boldsymbol{b}_0\cdot(\nabla_{\perp}\times\delta\boldsymbol{B}_{\perp}) \quad\Rightarrow\quad u_{\parallel e} = v_{\mathrm{th}e}d_e^2\nabla_{\perp}^2\mathcal{A}. \tag{2.15}$$

The electron inertial scale d_e will be an important quantity throughout this work, as it demarcates the boundary between the electrostatic and electromagnetic regimes in the collisionless limit (see section 2.4). In the collisional limit ($\nu_{ei} \gg \omega$), the frictional term on the right-hand side of (2.12) dominates over the electron inertial term on the left-hand side, meaning that the electron inertia can be neglected.

2.2.3 Temperature perturbations

The parallel temperature $T_{\|e} = T_{0e} + \delta T_{\|e}$ is advected by the local $\boldsymbol{E} \times \boldsymbol{B}$ flow and is locally increased (or decreased) by the compressional heating (or rarefaction cooling) due to $u_{\|e}$, as well as by the (appropriately normalised) perturbed parallel heat flux $\delta q_{\|e}$:

$$\frac{\mathrm{d}T_{\|e}}{\mathrm{d}t} = \frac{\mathrm{d}\delta T_{\|e}}{\mathrm{d}t} + \boldsymbol{v}_E \cdot \nabla_\perp T_{0e} = -\nabla_\| \frac{\delta q_{\|e}}{n_{0e}} - 2T_{0e}\nabla_\| u_{\|e} - \frac{4}{3}\nu_e \left(\delta T_{\|e} - \delta T_{\perp e}\right). \tag{2.16}$$

The factor of 2 in the compressional-heating term (the second on the right-hand side) is due to the fact that we only consider the parallel (1D) motion of the electrons (perpendicular motions are formally small within our ordering, see [1]). The last term on the right-hand side is a consequence of our choice of collision operator[1], and is responsible for collisional temperature isotropisation, with $\nu_e = \nu_{ee} + \nu_{ei}$, and $\nu_{ee} = \nu_{ei}/Z$ the electron-electron collision frequency (Ze is the ion charge).

Similarly, the perpendicular temperature $T_{\perp e} = T_{0e} + \delta T_{\perp e}$ evolves according to

$$\frac{\mathrm{d}T_{\perp e}}{\mathrm{d}t} = \frac{\mathrm{d}\delta T_{\perp e}}{\mathrm{d}t} + \boldsymbol{v}_E \cdot \nabla_\perp T_{0e} = -\nabla_\| \frac{\delta q_{\perp e}}{n_{0e}} - \frac{2}{3}\nu_e \left(\delta T_{\perp e} - \delta T_{\|e}\right), \tag{2.17}$$

where $\delta q_{\perp e}$ is the perturbed perpendicular heat flux. Note the absence of perpendicular compressional heating (perpendicular flows are incompressible). The term expressing the seeding of both parallel and perpendicular temperature perturbations via the advection of the equilibrium temperature profile by the $\boldsymbol{E} \times \boldsymbol{B}$ flow becomes, after a straightforward manipulation, the familiar (electrostatic) linear drive responsible for extracting free energy from the equilibrium temperature gradient:

$$\boldsymbol{v}_E \cdot \nabla_\perp T_{0e} = T_{0e} \frac{\rho_e v_{\mathrm{th}e}}{2L_T} \frac{\partial \varphi}{\partial y}, \tag{2.18}$$

where L_T is defined in (2.5). In order to determine the heat fluxes $\delta q_{\|e}$ and $\delta q_{\perp e}$, kinetic theory is needed, and so we must append to our emerging system of equations the drift-kinetic equation for electrons, of which (2.9), (2.12), (2.16) and (2.17) are four lowest-order moments.

---

[1] Given that our primary concern was not the precise quantitative capture of collisional transport, the derivation of these low-beta equations in [1] used a modified version of the Dougherty operator [68], as it retained the correct conservation properties and captured the effects of friction between electrons and ions without the complexity associated with the full Landau collision operator. Such a choice, however, has little consequence for the dynamics: trivially so in the collisionless limit, while the results of Appendix A make it clear that there are only minor modifications to the collisional equations when derived using the full Landau collision operator.

In the collisional limit, the temperature isotropisation terms in (2.16) and (2.17) are dominant, enforcing $\delta T_{\parallel e} = \delta T_{\perp e} = \delta T_e$ to leading order. In this limit, therefore, we no longer distinguish between parallel and perpendicular temperature perturbations, and obtain an equation for δT_e from the linear combination (1/3)(2.16)+(2/3)(2.17):

$$\frac{\mathrm{d}\delta T_e}{\mathrm{d}t} + \boldsymbol{v}_E \cdot \nabla_\perp T_{0e} = -\frac{2}{3}\nabla_\parallel \frac{\delta q_e}{n_{0e}} - \frac{2}{3} T_{0e} \nabla_\parallel u_{\parallel e}, \tag{2.19}$$

where the (collisional) heat flux $\delta q_e = \delta q_{\parallel e}/2 + \delta q_{\perp e}$ can be expressed in terms of the parallel gradient of the total temperature $T_e = T_{0e} + \delta T_e$ along the exact magnetic field direction:

$$\frac{\delta q_e}{n_{0e} T_{0e}} = -\frac{3}{2}\kappa \nabla_\parallel \log T_e, \quad \kappa = \frac{5 v_{\mathrm{th}e}^2}{18 \nu_e}, \tag{2.20}$$

where κ is the electron thermal diffusivity and

$$\nabla_\parallel \log T_e = \nabla_\parallel \frac{\delta T_e}{T_{0e}} + \frac{\delta B_x}{B_0} \frac{1}{T_{0e}} \frac{\mathrm{d}T_{0e}}{\mathrm{d}x} = \nabla_\parallel \frac{\delta T_e}{T_{0e}} - \frac{\rho_e}{L_T} \frac{\partial \mathcal{A}}{\partial y} \tag{2.21}$$

is the parallel gradient of the *total* electron temperature, which will prove a key quantity in what follows.

2.2.4 Quasineutrality

Finally, as usual, particle density is related to ϕ via quasineutrality, which is the route whereby ions contribute to dynamics. Since, at scales smaller than their Larmor radius $\sim \rho_i$, ions can be viewed as large motionless rings of charge, their density response is Boltzmann:

$$\frac{\delta n_e}{n_{0e}} = \frac{\delta n_i}{n_{0i}} = -\frac{Ze\phi}{T_{0i}} = -\bar{\tau}^{-1}\varphi, \quad \bar{\tau} = \frac{\tau}{Z}, \tag{2.22}$$

where $\tau = T_{0i}/T_{0e}$ is the ratio of the ion to electron equilibrium temperatures. The more general quasineutrality closure is discussed in Section 7.3, but, since we shall focus on scales smaller than this in the majority of our discussions, (2.22) will be sufficient for our purposes.

2.3 Summary of equations

Assembling together all of the above, we end up with the following systems of equations, in the collisionless limit ($\nu_* \to 0$):

$$\frac{\mathrm{d}}{\mathrm{d}t}\frac{\delta n_e}{n_{0e}} + \nabla_\parallel u_{\parallel e} + \frac{\rho_e v_{\mathrm{th}e}}{2L_B}\frac{\partial}{\partial y}\left(\frac{\delta T_{\parallel e}}{T_{0e}} + \frac{\delta T_{\perp e}}{T_{0e}}\right) = 0, \tag{2.23}$$

$$\frac{\mathrm{d}}{\mathrm{d}t}\left(\mathcal{A} - \frac{u_{\parallel e}}{v_{\mathrm{th}e}}\right) = -\frac{v_{\mathrm{th}e}}{2}\left[\frac{\partial \varphi}{\partial z} - \nabla_\parallel\left(\frac{\delta n_e}{n_{0e}} + \frac{\delta T_{\parallel e}}{T_{0e}}\right) + \frac{\rho_e}{L_T}\frac{\partial \mathcal{A}}{\partial y}\right], \tag{2.24}$$

$$\frac{\mathrm{d}}{\mathrm{d}t}\frac{\delta T_{\parallel e}}{T_{0e}} + \nabla_\parallel\left(\frac{\delta q_{\parallel e}}{n_{0e}T_{0e}} + 2u_{\parallel e}\right) + \frac{\rho_e v_{\mathrm{th}e}}{2L_T}\frac{\partial \varphi}{\partial y} = 0, \tag{2.25}$$

$$\frac{\mathrm{d}}{\mathrm{d}t}\frac{\delta T_{\perp e}}{T_{0e}} + \nabla_\parallel\frac{\delta q_{\perp e}}{n_{0e}T_{0e}} + \frac{\rho_e v_{\mathrm{th}e}}{2L_T}\frac{\partial \varphi}{\partial y} = 0, \tag{2.26}$$

or, in the collisional limit ($\nu_* \gg 1$),

$$\frac{\mathrm{d}}{\mathrm{d}t}\frac{\delta n_e}{n_{0e}} + \nabla_\parallel u_{\parallel e} + \frac{\rho_e v_{\mathrm{th}e}}{L_B}\frac{\partial}{\partial y}\frac{\delta T_e}{T_{0e}} = 0, \tag{2.27}$$

$$\frac{\mathrm{d}\mathcal{A}}{\mathrm{d}t} + \frac{v_{\mathrm{th}e}}{2}\frac{\partial \varphi}{\partial z} = \frac{v_{\mathrm{th}e}}{2}\left(\nabla_\parallel\frac{\delta n_e}{n_{0e}} + \nabla_\parallel \log T_e\right) + \nu_{ei}\frac{u_{\parallel e}}{v_{\mathrm{th}e}}, \tag{2.28}$$

$$\frac{\mathrm{d}}{\mathrm{d}t}\frac{\delta T_e}{T_{0e}} - \kappa\nabla_\parallel^2 \log T_e + \frac{2}{3}\nabla_\parallel u_{\parallel e} + \frac{\rho_e v_{\mathrm{th}e}}{2L_T}\frac{\partial \varphi}{\partial y} = 0, \tag{2.29}$$

to which we append the field equations:

$$\frac{\delta n_e}{n_{0e}} = -\bar{\tau}^{-1}\varphi, \quad \frac{u_{\parallel e}}{v_{\mathrm{th}e}} = d_e^2\nabla_\perp^2\mathcal{A}. \tag{2.30}$$

This system is a minimal model for describing low-beta, electromagnetic plasma dynamics — whether collisionless or collisional — driven by a background electron-temperature gradient, and in the presence of magnetic drifts.

2.4 Flux-freezing

These equations describe two broad classes of physical phenomena: electrostatic and electromagnetic, distinguished by whether or not the magnetic field lines are frozen into the electron flow. We shall refer to the perpendicular scale at which the transition between these two regimes occurs as the 'flux-freezing scale'. In the collisionless limit, this scale is given by the balance between the electron inertia and the inductive parallel electric field on the left-hand side of (2.24), viz.,

$$k_\perp d_e \sim 1. \tag{2.31}$$

In the collisional limit, the analogous balance involves, instead of electron inertia, the resistive term — the last on the right-hand side of (2.28). However, in this limit, we shall always deal with perturbations for which the term in (2.28) that contains the projection of the equilibrium temperature gradient onto the perturbed magnetic field [the second part of $\nabla_\parallel \log T_e$ written in (2.21)] is larger than $\partial \mathcal{A}/\partial t$. Therefore, it is with this term that the effect of resistivity will be usefully compared:

$$\omega \lesssim \omega_{*e} \equiv \frac{k_y \rho_e v_{\text{the}}}{2L_T} \sim k_\perp^2 d_e^2 \nu_{ei}, \tag{2.32}$$

where ω_{*e} is the drift frequency associated with the electron-temperature gradient. For modes with $k_y \sim k_\perp$[2], the balance (2.32) can be written as

$$k_\perp d_e \sim \frac{\rho_e}{d_e} \frac{v_{\text{the}}}{L_T \nu_{ei}} = \sqrt{\beta_e} \frac{\lambda_{ei}}{L_T} \equiv \chi^{-1}, \tag{2.33}$$

where $\lambda_{ei} = v_{\text{the}}/\nu_e$ is the electron mean free path. It is the scale at which $k_\perp d_e \chi \sim 1$ that will effectively play the role of the flux-freezing scale in the collisional limit. Note that $\chi^{-1} \ll 1$ (due to the small mean-free-path associated with the collisional limit), meaning that the flux-freezing scale occurs at much longer perpendicular wavelengths than in the collisionless limit.

We shall refer to scales below the flux-freezing scale (2.31) or (2.33) as electrostatic scales (on which electrons are free to flow across field lines without perturbing them), and to scales above the flux-freezing scale as electromagnetic scales (on which the magnetic field is frozen into the electron flow). It is straightforward to show that the electron flow into which the magnetic field lines are frozen on electromagnetic scales (while still remaining below the ion Larmor scale) is given by

$$\boldsymbol{u}_{\text{eff}} = \boldsymbol{v}_E - \frac{\rho_e v_{\text{the}}}{2} \frac{\boldsymbol{b}_0 \times \nabla p_{\parallel e}}{n_{0e} T_{0e}}, \tag{2.34}$$

where $p_{\parallel e} = n_e T_{\parallel e}$, $n_e = n_{0e} + \delta n_e$, and $T_{\parallel e} = T_{0e} + \delta T_{\parallel e}$ are the total parallel pressure, density, and parallel temperature, respectively; in the collisional limit, $\delta T_{\parallel e} \to \delta T_e$, as in section 2.2.3. The flow (2.34) is simply the part of the electron flow velocity perpendicular to the total magnetic field $\boldsymbol{B}$, comprised of the usual $\boldsymbol{E} \times \boldsymbol{B}$ drift velocity $\boldsymbol{v}_E$ [see (2.10)], and a 'diamagnetic' contribution coming from the electron (parallel)

---

[2] Though the balance $k_y \sim k_\perp$ is always well satisfied within our model, in which modes with $k_x \gg k_y$ simply experience strong damping, this will not necessarily be the case in systems with magnetic shear (see Section 9.1.2 for further discussion of this issue).

pressure gradient, manifest in the right-hand side of (2.24) or (2.28). This is distinct from the MHD limit (above the ion Larmor scale), in which the magnetic field is only frozen into $\boldsymbol{v}_E$ due to the dynamics being pressure balanced, a distinction that will prove important in our considerations of electromagnetic instabilities in Chapter 4.

In what follows, all orderings introduced should be considered subsidiary to the orderings that define the collisionless and collisional limits (see appendix A of [1] for more details), and the resultant reduced equations thus to be particular limits of the collisionless [(2.23)-(2.26)] or collisional [(2.27)-(2.29)] equations.

Chapter 3

Electrostatic regime: electron temperature gradient instability

Let us begin our consideration of linear instabilities by examining the more familiar ones that occur at electrostatic scales, before considering what happens at electromagnetic ones.

3.1 Collisionless slab ETG

As explained above, the electrostatic limit corresponds to perpendicular scales $k_\perp d_e \gg 1$. If we strengthen this condition to

$$k_\perp^2 d_e^2 \gg \frac{\omega_{*e}}{\omega} \gtrsim 1, \tag{3.1}$$

then both $\mathcal{A}$ terms in (2.24) can be neglected in comparison with the electron inertia. Furthermore, we would like to consider the slab approximation, in which the magnetic drifts are negligible in comparison with parallel compressions. In terms of wavenumbers, this means that we assume

$$k_\parallel v_{\text{the}} \gg \omega_{de} \left(\frac{L_B}{L_T}\right)^{1/4}, \quad \omega_{de} = \frac{k_y \rho_e v_{\text{the}}}{2L_B}, \tag{3.2}$$

where ω_{de} is the magnetic drift frequency. Though not immediately obvious, it shall turn out that the limit (3.2) allows us to neglect the magnetic drifts in (2.23). Then, the perpendicular temperature perturbation (2.26) becomes decoupled from the remaining equations, leaving us with an electrostatic three-field (δn_e, $u_{\parallel e}$ and $\delta T_{\parallel e}$) system of the kind traditionally used to describe temperature-gradient instabilities in a slab [8]. The slab electron-temperature-gradient (sETG) instability [56, 57] in its most explicit, fluid form is obtained if one further assumes

$$k_\parallel v_{\text{the}} \ll \omega \ll \omega_{*e}. \tag{3.3}$$

Then (2.23)-(2.25) reduce to, approximately,

$$\frac{\mathrm{d}}{\mathrm{d}t}\bar{\tau}^{-1}\varphi = \nabla_\parallel u_{\parallel e}, \quad \frac{\mathrm{d}u_{\parallel e}}{\mathrm{d}t} = -\frac{v_{\text{the}}^2}{2}\nabla_\parallel \frac{\delta T_{\parallel e}}{T_{0e}}, \quad \frac{\mathrm{d}}{\mathrm{d}t}\frac{\delta T_{\parallel e}}{T_{0e}} = -\frac{\rho_e v_{\text{the}}}{2L_T}\frac{\partial \varphi}{\partial y}. \tag{3.4}$$

Linearising and Fourier-transforming, we find the familiar dispersion relation

$$\omega^3 = -\frac{k_\parallel^2 v_{\text{the}}^2 \omega_{*e}\bar{\tau}}{2} \quad \Rightarrow \quad \omega = \operatorname{sgn}(k_y)\left(-1, \frac{1}{2} \pm i\frac{\sqrt{3}}{2}\right)\left(\frac{k_\parallel^2 v_{\text{the}}^2 |\omega_{*e}|\bar{\tau}}{2}\right)^{1/3}. \tag{3.5}$$

The unstable root is the collisionless sETG.

In this limit, the instability works as follows. Suppose that a small perturbation to the parallel electron temperature is created with $k_y \neq 0$ and $k_\parallel \neq 0$, bringing the plasma from regions with higher T_{0e} to those with lower T_{0e} ($\delta T_{\parallel e} > 0$), and vice versa ($\delta T_{\parallel e} < 0$). This temperature perturbation produces alternating hot and cold regions along the (unperturbed) magnetic field. The resulting perturbed temperature gradients drive electron flows from the hot regions to the cold regions [second equation in (3.4)], giving rise to increased electron density in the cold regions [first equation in (3.4)]. By quasineutrality, the electron density perturbation is instantly replicated in the ion density perturbation, and that, via Boltzmann-ion response, creates an electric field that produces a radial $\boldsymbol{E} \times \boldsymbol{B}$ drift that pushes hotter particles further into the colder region, and vice versa [third equation in (3.4)], reinforcing the initial temperature perturbation and thus completing the positive feedback loop required for the instability. This is illustrated in figure 3.1.

The 'fluid' limit (3.3) is physically transparent and easy to handle, primarily because the heat flux (and thus all kinetic effects, such as Landau damping [69]) can, in this limit, be neglected in (2.25). However, the approximation contains the seed of its own destruction: according to (3.5), perturbations with a larger $k_\parallel$ grow faster, and can only be checked by Landau damping when

$$k_\parallel v_{\text{the}} \sim \omega \sim \omega_{*e}. \tag{3.6}$$

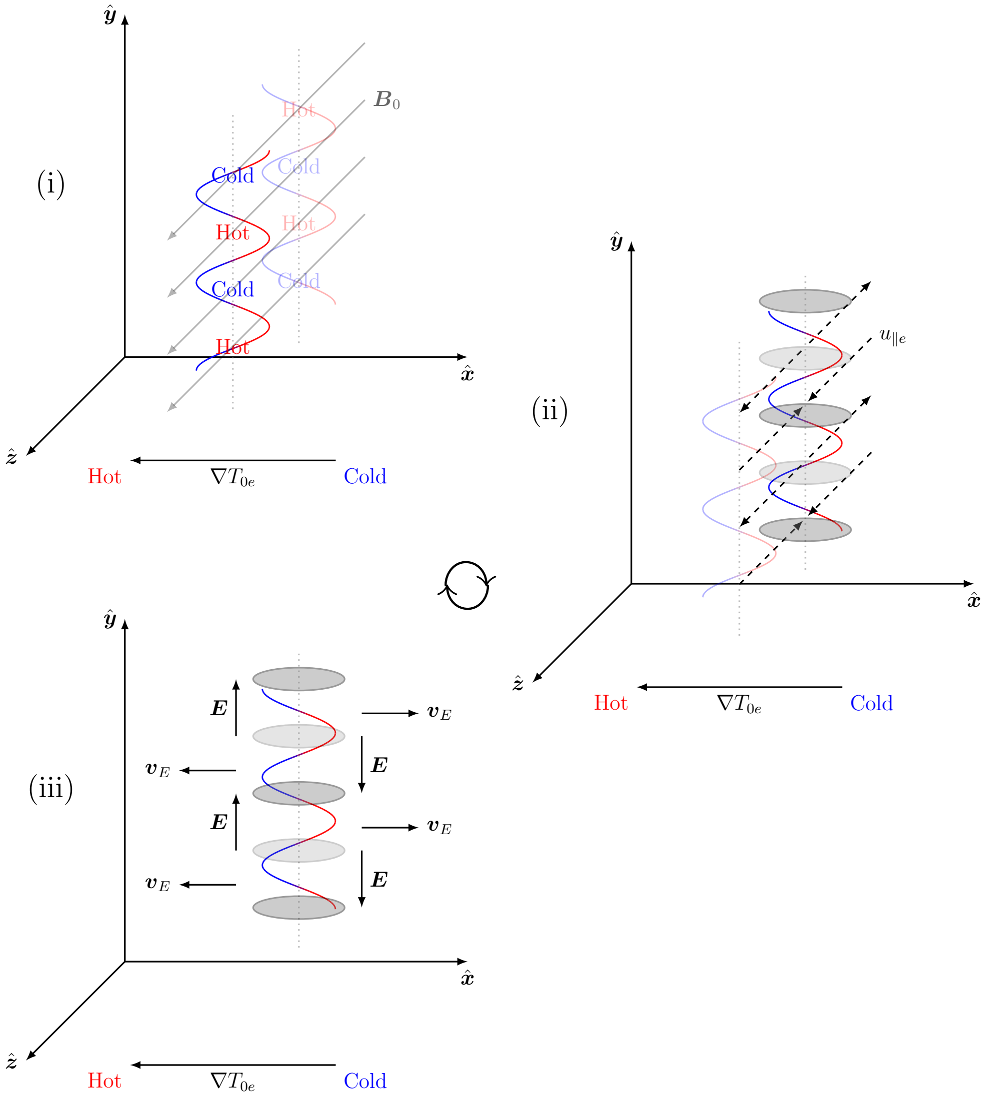

Figure 3.1: A cartoon illustrating the feedback mechanism of the (collisionless) sETG instability. (i) An electron temperature perturbation with $k_y \neq 0$ and $k_\| \neq 0$ (red-and-blue curves) has alternating hot and cold regions along the (unperturbed) magnetic field (grey arrows), and also along $\hat{\boldsymbol{y}}$. (ii) The resulting perturbed temperature gradients drive parallel electron flows $u_{\|e}$ (dashed arrows) from the hot regions into the cold regions, giving rise to increased electron density in the cold regions (over- and under- densities are indicated by the dark- and light-grey ellipses, respectively). (iii) By quasineutrality, the electron-density perturbation gives rise to an exactly equal ion-density perturbation, and that, via Boltzmann-ion response, creates alternating electric fields $\boldsymbol{E}$ in the perpendicular plane (vertical black arrows). This produces an $\boldsymbol{E} \times \boldsymbol{B}$ drift $\boldsymbol{v}_E$ (horizontal black arrows), which pushes hotter particles further into the colder region, and vice versa, reinforcing the initial temperature perturbation and thus completing the positive feedback loop required for the instability. In this cartoon, for the sake of simplicity, we have chosen not to include the phase information between the various perturbations involved; a reader seeking such information will find it in figure 1 of [8] (the equivalent picture for ITG).

Indeed, the collisionless sETG is stabilised by Landau damping above the line in wavenumber space [1]:

$$\mp k_{\parallel} v_{\mathrm{the}} \sqrt{\frac{1+\bar{\tau}}{2}} = \frac{\bar{\tau}\omega_{*e}}{2} \quad \Rightarrow \quad \frac{k_{\parallel} L_T}{\sqrt{\beta_e}} = \pm \frac{\bar{\tau}}{2\sqrt{2(1+\bar{\tau})}} k_y d_e. \tag{3.7}$$

Thus, the fastest-growing collisionless sETG modes are expected to sit in this latter, kinetic regime.

3.2 Collisional slab ETG

An important difference between the collisionless and collisional limits, exemplified by the form of the collisional heat flux (2.20), is the replacement of the parallel streaming rate of electrons $k_{\parallel} v_{\mathrm{the}}$ with the parallel conduction rate $(k_{\parallel} v_{\mathrm{the}})^2/\nu_{ei}$. The collisional analogues of (3.1), (3.2) and (3.3) are thus

$$k_{\perp}^2 d_e^2 \gg \frac{\omega_{*e}}{\nu_{ei}}, \quad \frac{(k_{\parallel} v_{\mathrm{the}})^2}{\nu_{ei}} \gg \omega_{de}, \quad \frac{(k_{\parallel} v_{\mathrm{the}})^2}{\nu_{ei}} \ll \omega \ll \omega_{*e}, \tag{3.8}$$

respectively, for which (2.27), (2.28) and (2.29) reduce to, approximately,

$$\frac{\mathrm{d}}{\mathrm{d}t} \bar{\tau}^{-1} \varphi = \nabla_{\parallel} u_{\parallel e}, \quad \nu_{ei} u_{\parallel e} = -\frac{v_{\mathrm{the}}^2}{2} \nabla_{\parallel} \frac{\delta T_e}{T_{0e}}, \quad \frac{\mathrm{d}}{\mathrm{d}t} \frac{\delta T_e}{T_{0e}} = -\frac{\rho_e v_{\mathrm{the}}}{2L_T} \frac{\partial \varphi}{\partial y}. \tag{3.9}$$

These equations are similar to (3.4), except the parallel temperature gradient is now balanced by the electron-ion frictional force, rather than by electron inertia. The dispersion relation is

$$\omega^2 = i \frac{k_{\parallel}^2 v_{\mathrm{the}}^2 \omega_{*e} \bar{\tau}}{2\nu_{ei}} \quad \Rightarrow \quad \omega = \pm \frac{1 + i\mathrm{sgn}(k_y)}{\sqrt{2}} \left(\frac{k_{\parallel}^2 v_{\mathrm{the}}^2 |\omega_{*e}| \bar{\tau}}{2\nu_{ei}} \right)^{1/2}, \tag{3.10}$$

where the unstable root is the collisional sETG. The physical mechanism of the instability is analogous to that for the collisionless sETG, except the parallel electron flow is now determined instantaneously by the parallel temperature gradient. Similarly to the collisionless sETG, the point of maximum growth of the instability occurs when

$$\frac{(k_{\parallel} v_{\mathrm{the}})^2}{\nu_{ei}} \sim \omega \sim \omega_{*e}, \tag{3.11}$$

which is a balance between dissipation (through conduction, rather than Landau damping) and energy injection due to the background temperature gradient. Similarly to the collisionless case, the collisional sETG is stabilised by thermal conduction above the line [1]:

$$\left(\frac{k_\parallel L_T}{\sqrt{\beta_e}}\right)^4 = \frac{\bar{\tau}^2}{(1+\bar{\tau})a\left(\bar{\tau}+a+5/3\right)^2\left(1+1/Z\right)^2}(k_y d_e \chi)^2, \tag{3.12}$$

where $a = 2\nu_{ei}\kappa/v_{\text{the}}^2 = 5\nu_{ei}/9\nu_e = 5/[9(1+1/Z)]$.

3.3 Curvature-mediated ETG

Both the collisionless and collisional sETG instabilities were derived assuming that the parallel wavelengths were sufficiently short for the compressional terms in (2.23) and (2.27) to be dominant in comparison to the magnetic-drift terms, while still satisfying (3.3) and (3.8). We now consider very long parallel wavelengths for which this is no longer true, ordering our frequencies as

$$k_\parallel v_{\text{the}} \ll \omega_{de} \ll \omega \ll \omega_{*e}, \quad \frac{(k_\parallel v_{\text{the}})^2}{\nu_{ei}} \ll \omega_{de} \ll \omega \ll \omega_{*e} \tag{3.13}$$

in the collisionless and collisional regimes, respectively. This, in fact, amounts to setting $k_\parallel = 0$ everywhere, i.e., we are considering purely two-dimensional modes. In both regimes, our equations reduce to

$$\frac{\mathrm{d}}{\mathrm{d}t}\bar{\tau}^{-1}\varphi = \frac{\rho_e v_{\text{the}}}{L_B}\frac{\partial}{\partial y}\frac{\delta T_{\parallel e}}{T_{0e}}, \quad \frac{\mathrm{d}}{\mathrm{d}t}\frac{\delta T_{\parallel e}}{T_{0e}} = -\frac{\rho_e v_{\text{the}}}{2L_T}\frac{\partial \varphi}{\partial y}, \quad \frac{\delta T_{\parallel e}}{T_{0e}} = \frac{\delta T_{\perp e}}{T_{0e}}. \tag{3.14}$$

The equality between the perpendicular and parallel temperature perturbations arises in the collisionless regime because the dominant balance in both (2.25) and (2.26) is between the time derivative and the ETG injection term, which is also true in the collisional limit and with strengthened isotropisation from collisions. The dispersion relation is

$$\omega^2 = -2\omega_{de}\omega_{*e}\bar{\tau} \quad \Rightarrow \quad \omega = \pm i\left(2\omega_{de}\omega_{*e}\bar{\tau}\right)^{1/2}, \tag{3.15}$$

which is the familiar growth rate of the curvature-mediated ETG (cETG) instability [58]. Physically, this arises due to the fact that the magnitude of the magnetic-drift velocity for a particle is proportional to its kinetic energy, and thus temperature. The presence of some temperature perturbation will cause an electron-density perturbation, as electrons in the hotter regions will drift faster than those in colder regions [first equation in (3.14)]. By quasineutrality, the electron density perturbation gives rise to an

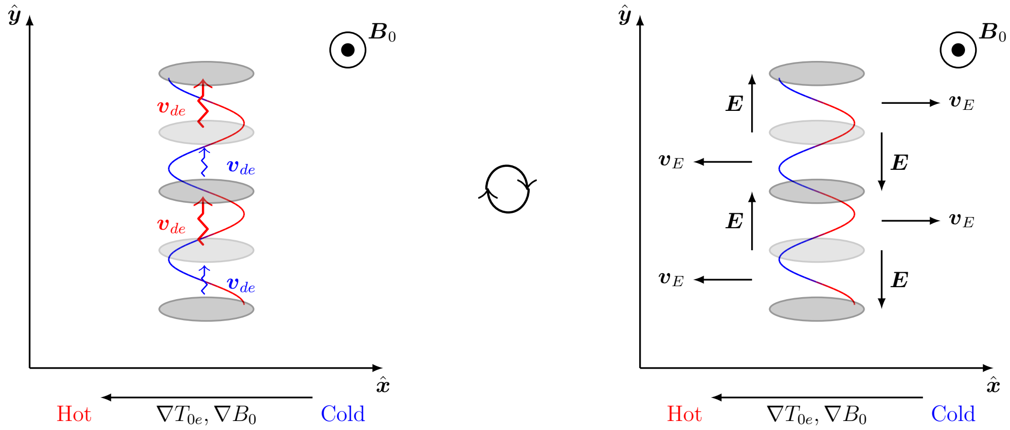

(i) (ii)

Figure 3.2: A cartoon illustrating the feedback mechanism of the (2D) cETG instability. (i) A temperature perturbation with $k_y \neq 0$ (red-and-blue curve) has alternating hot and cold regions along $\hat{\boldsymbol{y}}$. Due to the temperature dependence of the magnetic drifts $\boldsymbol{v}_{de}$, electrons in the hot regions will drift faster than those in the cold regions (red and blue arrows), creating an electron density perturbation (over- and under- densities are indicated by the dark- and light-grey ellipses, respectively). (ii) By quasineutrality, the electron-density perturbation gives rise to an exactly equal ion-density perturbation, and that, via Boltzmann-ion response, creates alternating electric fields $\boldsymbol{E}$ in the perpendicular plane (vertical black arrows). This produces an $\boldsymbol{E} \times \boldsymbol{B}$ drift $\boldsymbol{v}_E$ (horizontal black arrows), which pushes hotter particles further into the colder region, and vice versa, reinforcing the initial temperature perturbation and thus completing the positive feedback loop required for the instability.

exactly equal ion density perturbation, and that, via Boltzmann-ion response, creates an electric field that produces an $\boldsymbol{E} \times \boldsymbol{B}$ drift which pushes hotter particles further into the colder region, and vice versa [second equation in (3.14)], completing the feedback loop required for the instability, as illustrated in figure 3.2. This mechanism is unaffected by collisionality, hence the cETG instability is obtained in both the collisionless and collisional limits.

Given that both the collisionless and collisional sETG instabilities have maximum growth rates $\gamma_{\max} \sim \omega_{*e}$ [see (3.6) and (3.11), respectively], there will always exist a temperature gradient above which the growth rate of the cETG is small in comparison to that of the sETG, viz.,

$$\frac{\gamma_{\max}}{\sqrt{2\omega_{de}\omega_{*e}}} \sim \left(\frac{L_B}{L_T}\right)^{1/2} \gg 1, \tag{3.16}$$

though the exact value of this gradient may be quite large due to differences in numerical prefactors. However, the sETG instabilities only exist at perpendicular scales below the flux-freezing scales (2.31) or (2.33), as they require electrons to be able to flow across field lines without perturbing them. While sETG is stabilised by magnetic tension above the flux-freezing scale, cETG is unaffected by flux freezing as it is an interchange ($k_\parallel = 0$) mode and does not trigger perpendicular magnetic field perturbations $\delta \boldsymbol{B}_\perp$. This means that it will happily survive in the electromagnetic regime.

Chapter 4

Electromagnetic regime: thermo-Alfvénic instability

In the electromagnetic regime [i.e., at perpendicular scales above the flux-freezing scales (2.31) or (2.33)], the magnetic field becomes frozen into the electron flow (2.34), meaning that perpendicular magnetic field perturbations $\delta\boldsymbol{B}_{\perp}$ are created as electrons move across field lines and drag the latter along. This has two important physical consequences that make electrostatic and electromagnetic phenomena distinct: (i) perturbed magnetic fields give rise to currents that, being electron flows, oppose electron density perturbations [this is the sub-ion-scale version of Lorentz tension, manifest in the second term in (2.9)], and (ii) the radial equilibrium temperature gradient now has a component along the exact field line, viz., its projection on to the radial perturbation of the magnetic field. As discussed in Chapter 3, the first effect stabilises the sETG instabilities at the flux-freezing scale. It also gives rise to other electromagnetic phenomena to which we shall return shortly. It is the second effect, however, that will turn out to be crucial in our study of the physics of instabilities in the electromagnetic regime.

Throughout this chapter, we will focus on the collisional limit — equations (2.27), (2.28) and (2.29) — as this will allow us to discuss all of the physics characteristic to the electromagnetic regime without being hampered by the technical detail associated with the full kinetic system. The physical similarly between the instability mechanisms in the collisionless and collisional limits means that we can just signpost the differences between these two limits where appropriate.

Recalling the definition of the parallel derivative (2.11), we consider the parallel gradient of the total temperature (2.21). This gradient can be separated into two terms: the first is the familiar parallel gradient of the temperature perturbation that is present also in the electrostatic regime, and the second is the projection of the equilibrium temperature gradient onto the perturbed magnetic field line that arises *only* in the electromagnetic regime. This is referred to as the magnetic-flutter drive [70, 71]. Like the electrostatic linear drive term (2.18), this term can also be responsible for extracting free energy from the equilibrium temperature gradient.

To aid our discussion, let us derive an evolution equation for $\nabla_\parallel \log T_e$. A useful result is that, for any field ψ,

$$\nabla_\parallel \frac{\mathrm{d}\psi}{\mathrm{d}t} - \frac{\mathrm{d}}{\mathrm{d}t}\nabla_\parallel \psi = -\frac{c}{B_0}\left\{E_\parallel, \psi\right\} = \rho_e \left\{\frac{\mathrm{d}\mathcal{A}}{\mathrm{d}t} + \frac{v_{\text{the}}}{2}\frac{\partial \varphi}{\partial z}, \psi\right\}. \tag{4.1}$$

The first equality follows by writing the nonlinear operators $\mathrm{d}/\mathrm{d}t$ and $\nabla_\parallel$, which we defined in (2.10) and (2.11), respectively, in terms of the Poisson bracket

$$\{f, g\} = \boldsymbol{b}_0 \cdot (\nabla f \times \nabla g) = \frac{\partial f}{\partial x}\frac{\partial g}{\partial y} - \frac{\partial f}{\partial y}\frac{\partial g}{\partial x} \tag{4.2}$$

as follows:

$$\frac{\mathrm{d}}{\mathrm{d}t} = \frac{\partial}{\partial t} + \frac{\rho_e v_{\text{the}}}{2}\{\varphi, \dots\}, \quad \nabla_\parallel = \frac{\partial}{\partial z} - \rho_e \{\mathcal{A}, \dots\}, \tag{4.3}$$

and noticing that the Poisson bracket satisfies the Jacobi identity:

$$\{\mathcal{A}, \{\varphi, \psi\}\} + \{\varphi, \{\psi, \mathcal{A}\}\} + \{\psi, \{\mathcal{A}, \varphi\}\} = 0. \tag{4.4}$$

Therefore, taking $\nabla_\parallel$ of (2.29), we find

$$\begin{aligned}\frac{\mathrm{d}}{\mathrm{d}t}\nabla_\parallel \frac{\delta T_e}{T_{0e}} + \frac{\rho_e v_{\text{the}}}{2L_T}\nabla_\parallel \frac{\partial \varphi}{\partial y} + \rho_e \left\{\frac{\mathrm{d}\mathcal{A}}{\mathrm{d}t} + \frac{v_{\text{the}}}{2}\frac{\partial \varphi}{\partial z}, \frac{\delta T_e}{T_{0e}}\right\}& \\ -\kappa \nabla_\parallel^3 \log T_e + \frac{2}{3}\nabla_\parallel^2 u_{\parallel e} = 0.&\end{aligned} \tag{4.5}$$

Now taking $\partial/\partial y$ of (2.28) we find

$$\frac{\partial}{\partial y}\left(\frac{\mathrm{d}\mathcal{A}}{\mathrm{d}t} + \frac{v_{\text{the}}}{2}\frac{\partial \varphi}{\partial z}\right) = \frac{\mathrm{d}}{\mathrm{d}t}\frac{\partial \mathcal{A}}{\partial y} + \frac{v_{\text{the}}}{2}\nabla_\parallel \frac{\partial \varphi}{\partial y} = \frac{v_{\text{the}}}{2}\frac{\partial}{\partial y}\nabla_\parallel \log p_e + \nu_{ei}\frac{\partial}{\partial y}\frac{u_{\parallel e}}{v_{\text{the}}}, \tag{4.6}$$

where we have recognised the first two terms on the right-hand side for what they are — the parallel gradient of the *total* electron pressure:

$$\nabla_\parallel \log p_e = \nabla_\parallel \frac{\delta n_e}{n_{0e}} + \nabla_\parallel \log T_e. \tag{4.7}$$

Subtracting $(\rho_e/L_T)\cdot$(4.6) from (4.5), we arrive at

$$\frac{\mathrm{d}}{\mathrm{d}t}\nabla_\parallel \log T_e + \rho_e \left\{ \frac{\mathrm{d}\mathcal{A}}{\mathrm{d}t} + \frac{v_{\mathrm{the}}}{2}\frac{\partial \varphi}{\partial z}, \frac{\delta T_e}{T_{0e}} \right\} + \frac{2}{3}\nabla_\parallel^2 u_{\parallel e} + \nu_{ei}\frac{\rho_e}{L_T}\frac{\partial}{\partial y}\frac{u_{\parallel e}}{v_{\mathrm{the}}} = \kappa \nabla_\parallel^3 \log T_e - \frac{\rho_e v_{\mathrm{the}}}{2L_T}\frac{\partial}{\partial y}\nabla_\parallel \log p_e. \tag{4.8}$$

Let us now consider the regime

$$(k_\perp d_e)^2 \nu_{ei} \sim \omega_{de} \ll \omega \ll \omega_{*e} \sim \kappa k_\parallel^2. \tag{4.9}$$

The ordering of the resistive rate and the magnetic drift frequency is such that we can retain perturbations of similar frequencies to the cETG, by analogy to (3.13). However, this time, we assume the parallel wavelength of the perturbations to be short enough, or, equivalently, their frequency to be low enough, for thermal conduction along the field lines to be rapid in comparison to the mode frequency. Then, in the limit (4.9), the left-hand side of (4.8) is negligible in its entirety (being smaller than the right-hand side by at least a factor of ω/ω_{*e}), while the outcome of the competition between the two terms on the right-hand side is controlled by the ratio of the perpendicular drift-wave frequency to the parallel conduction rate:

$$\xi_* = \frac{\omega_{*e}}{\kappa k_\parallel^2}. \tag{4.10}$$

This divides our electromagnetic modes into two physically distinct classes: isothermal ($\xi_* \ll 1$) and isobaric ($\xi_* \gg 1$), the former of which is the focus of the next section, and the latter will be discussed in section 4.4.

4.1 Isothermal curvature-mediated TAI

Previous studies of electromagnetic phenomena driven by an electron-temperature gradient have often assumed the electrons to be isothermal along the perturbed field line [72–75]. In our system, this assumption is valid if the thermal-conduction time dominates over all other timescales, viz., in addition to (4.9),

$$\xi_* \ll 1. \tag{4.11}$$

In the electrostatic regime, without the ability to have perturbations of the magnetic-field direction, adopting such a limit would simply lead to erasure of the temperature perturbation due to Landau damping or thermal conduction, suppressing both the collisionless and collisional sETG, respectively.

The isothermal limit allows the system more leeway in the electromagnetic regime. Given (4.11), the dominant term in (4.8) is the first term on the right-hand side, meaning that, to leading order,

$$\nabla_\parallel \log T_e = \nabla_\parallel \frac{\delta T_e}{T_{0e}} - \frac{\rho_e}{L_T}\frac{\partial \mathcal{A}}{\partial y} = 0, \tag{4.12}$$

i.e., the temperature perturbations, rather than being zero, will always adjust to cancel the variation of the equilibrium temperature along the perturbed field line. At the next order in ξ_*,

$$\kappa \nabla_\parallel^3 \log T_e = \frac{\rho_e v_{\text{the}}}{2L_T}\frac{\partial}{\partial y}\nabla_\parallel \frac{\delta n_e}{n_{0e}} \quad \Rightarrow \quad \frac{|\nabla_\parallel \log T_e|}{|\nabla_\parallel \delta n_e/n_{0e}|} \sim \xi_* \ll 1, \tag{4.13}$$

meaning that we can neglect $\nabla_\parallel \log T_e$ in (2.28). The $\nabla_\parallel u_{\parallel e}$ term in (2.27) is also negligible, as can be confirmed *a posteriori*. Our system (2.27)-(2.29) therefore becomes

$$\frac{\mathrm{d}}{\mathrm{d}t}\frac{\delta n_e}{n_e} = -\frac{\rho_e v_{\text{the}}}{L_B}\frac{\partial}{\partial y}\frac{\delta T_e}{T_{0e}}, \quad \frac{\mathrm{d}\mathcal{A}}{\mathrm{d}t} + \frac{v_{\text{the}}}{2}\frac{\partial \varphi}{\partial z} = \frac{v_{\text{the}}}{2}\nabla_\parallel \frac{\delta n_e}{n_e}, \quad \nabla_\parallel \frac{\delta T_e}{T_{0e}} = \frac{\rho_e}{L_T}\frac{\partial \mathcal{A}}{\partial y}, \tag{4.14}$$

where, by (2.22), $\varphi = -\bar{\tau}\delta n_e/n_e$. The associated dispersion relation is

$$\omega^2 = -2\omega_{de}\omega_{*e}(1+\bar{\tau}) \quad \Rightarrow \quad \omega = \pm i\left[2\omega_{de}\omega_{*e}(1+\bar{\tau})\right]^{1/2}, \tag{4.15}$$

which looks like the familiar cETG growth rate (3.15), but enhanced by an extra order-unity contribution. In fact, this is a physically different and (as far as we know) new[1] instability, which we shall refer to as the curvature-mediated *thermo-Alfvénic instability* (cTAI).

Physically, cTAI proceeds as follows. Suppose that a perturbation $\delta B_x = B_0 \rho_e \partial_y \mathcal{A}$ of the magnetic field is created, with $k_y \neq 0$ and $k_\parallel \neq 0$. According to the second

---

[1] [75] proposed a fluid mechanism for the destabilisation of KAW (see section 4.3.1) via their interaction with the cETG mode (see section 3.3), adopting a purely isothermal limit $\xi_* = 0$ and thus neglecting any finite-heat-flux contributions. Under the ordering (4.9), neglecting equilibrium density gradients and electron finite-Larmor radius contributions, their dispersion relation (23) becomes, in our notation, $\omega^2 = -(2\omega_{de}\omega_{*e} - \omega_{\text{KAW}}^2)(1+\bar{\tau})$. This is the same as (4.18) to lowest order in $\xi_* \ll 1$. Obviously, it does not match the cETG growth rate (3.15) at $k_\parallel = 0$, because the isothermal limit cannot be valid as $k_\parallel \to 0$. Their dispersion relation displays behaviour qualitatively similar to ours in the isobaric limit for $k_\parallel < k_{\parallel c}$ (see section 4.4), in that they capture the stabilising effect of the KAW restoring force at $k_\parallel > 0$, but miss the fact that the peak growth rate (4.15) is achieved at a finite $k_\parallel$ (see section 4.2). Their dispersion relation also does not contain the slab TAI mode (see section 4.3.1) or any isobaric physics (section 4.4).

equation in (4.14), such a perturbation is brought about by a radial displacement of the electron fluid associated with the velocity (2.34), which, recalling the isothermal condition (4.12), can be written as

$$\boldsymbol{u}_{\text{eff}} = \boldsymbol{v}_E - \frac{\rho_e v_{\text{the}}}{2} \boldsymbol{b}_0 \times \nabla \frac{\delta n_e}{n_{0e}} = -\frac{\rho_e v_{\text{the}}}{2} \boldsymbol{b}_0 \times \nabla \left(1 + \bar{\tau}\right) \frac{\delta n_e}{n_{0e}}. \tag{4.16}$$

Due to the presence of the equilibrium temperature gradient, this magnetic-field perturbation will set up an apparent (parallel) variation of the equilibrium temperature along the perturbed field line, as the field line makes excursions into hot and cold regions. However, rapid thermal conduction along the field line instantaneously creates a temperature perturbation that compensates for this temperature variation, in order to enforce isothermality (4.12) [last equation in (4.14)]. This temperature perturbation will cause a parallel density gradient, as electrons in the hotter regions will curvature-drift faster than those in colder regions [first equation in (4.14)]. The resulting parallel pressure gradient must be balanced by a parallel electric field [second equation in (4.14)], whose inductive part leads to an increase in the perturbation of the magnetic field, deforming the field line further into the hot and cold regions, and in doing so completing the feedback loop required for the instability[2]. This is illustrated in figure 4.1.

The physical distinction between cTAI and cETG can be made obvious by the following two observations. First, unlike cETG, cTAI relies vitally on $k_\parallel \neq 0$ and, indeed, on $k_\parallel$ being large enough for the condition (4.11) to be satisfied — even though the growth rate (4.15) ends up being independent of $k_\parallel$. In section 4.2, we shall show that this is the peak growth rate of the instability and that it is achieved at a finite $k_\parallel$ [despite the absence of $k_\parallel$ in (4.15)], while at $k_\parallel = 0$, the cETG growth rate (3.15) is recovered. Secondly, perturbations described by (4.14) can be unstable without the need for them to contain any $\boldsymbol{E} \times \boldsymbol{B}$ flows (i.e., any electrostatic potential φ) — this becomes obvious in the formal limit $\varphi = -\bar{\tau}\delta n_e/n_{0e} \to 0$ as $\bar{\tau} \to 0$ (cold ions). In contrast, the cETG growth rate (3.15) disappears in this limit. This is because cTAI

---

[2] Physically, this feedback loop is perhaps reminiscent of some MHD-like instabilities, such as kinetic ballooning modes (KBMs; see references in Chapter 1). However, as is evident from the second equation in (4.14), the isothermal cTAI does not satisfy the MHD constraint that $E_\parallel = 0$ typical of such modes. Indeed, in the isothermal regime, the magnetic field lines are not frozen into the $\boldsymbol{E} \times \boldsymbol{B}$ flow, as they would be in MHD, but instead into the electron flow velocity (4.16). We therefore consider that the isothermal cTAI can be regarded as a separate instability, rather than a sub-species of KBM — unlike its isobaric counterpart discussed in section 4.4.

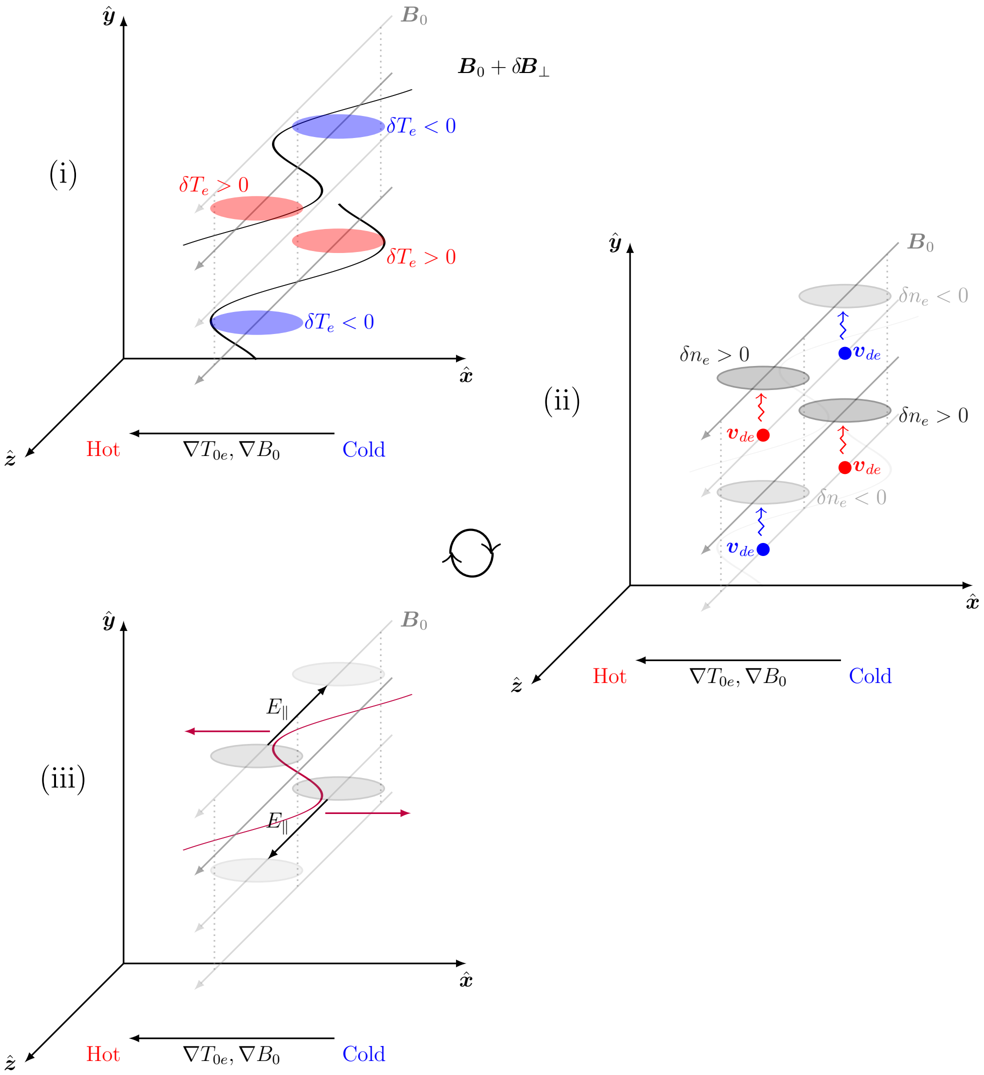

Figure 4.1: A cartoon illustrating the feedback mechanism of the (isothermal) cTAI. (i) A perturbation $\delta B_x = B_0 \rho_e \partial_y \mathcal{A}$ (solid black lines) to the equilibrium magnetic field (grey arrows, darker grey corresponding to the plane of constant y containing δB_x, or the relevant perturbation in subsequent diagrams) is created with $k_y \neq 0$ and $k_\parallel \neq 0$ (we show half a wavelength of the mode along both $\hat{\boldsymbol{y}}$ and $\hat{\boldsymbol{z}}$). Due to the presence of the equilibrium temperature gradient, this will set up a (parallel) variation of the total temperature along the perturbed field line, as the field line makes excursions into hot and cold regions (on the left and right, respectively). However, rapid thermal conduction along the field line instantaneously creates a temperature perturbation that compensates for this temperature variation (red and blue ovals, located in the same planes of constant y as δB_x). (ii) This temperature perturbation will cause a parallel density gradient (over- and under- densities are indicated by the dark and light grey ellipses, respectively, lying in the planes of constant y a quarter of a wavelength above those of δB_x), as electrons in hotter regions will curvature-drift faster than those in colder regions ($\boldsymbol{v}_{de}$, red and blue arrows). (iii) The parallel density gradient must be balanced by a parallel electric field (black arrows, in the same planes of constant y as the density perturbations), whose inductive part leads to an increase in the perturbation of the magnetic field (maroon arrows), deforming the field line further into the hot and cold regions, and in so doing completing the feedback loop for the instability. Note that the maximal rate of change of δB_x occurs where the y-gradient of $E_\parallel$ is at a maximum, as shown.

extracts energy from the background temperature gradient not via $\boldsymbol{E}\times\boldsymbol{B}$ advection of said equilibrium gradient but via thermal conduction of it along the perturbed field lines. In order to complete the instability loop and reinforce the magnetic perturbation δB_x required for this mechanism to work, the system only needs a perturbed density gradient. This is due to the fact that, as we discussed in section 2.3, below the ion Larmor scale, the magnetic field lines are frozen not into the $\boldsymbol{E}\times\boldsymbol{B}$ flow but in the electron flow (2.34), which involves also a 'diamagnetic' contribution from the electron pressure gradient — which, in the isothermal limit, consists just of the perturbed density gradient, as in (4.16). It is because of the presence of this distinct destabilisation mechanism that the cTAI growth rate (4.15) is always strictly greater than the cETG one (3.15). Thus, cTAI is not simply an 'electromagnetic correction' to cETG, but rather the main effect at scales above the flux-freezing scale (2.33) [or (2.31) in the collisionless limit, where, as we shall see shortly, the same instability is present]. This suggests that a purely electrostatic description of these scales is inadequate.

4.2 General TAI dispersion relation

As we have noted above, despite cTAI relying on parallel dynamics, the dispersion relation (4.15) is itself independent of $k_\parallel$. This is because we have thus far only captured the leading-order behaviour in our analysis, and further diligence is required in order to determine the details associated with the parallel dynamics. Let us give this problem the diligence that it is due, and adopt the ordering (4.9) but, for now, $\xi_* \sim 1$. Neglecting both the resistive term in (2.28) and the compressional term in (2.29) — since both are small under (4.9) — and determining $\nabla_\parallel \log T_e$ in (2.28) from the balance of the two terms on the right-hand side of (4.8), viz.,

$$\left(\frac{\rho_e v_{\text{the}}}{2L_T}\frac{\partial}{\partial y} - \kappa\nabla_\parallel^2\right)\nabla_\parallel \log T_e = -\frac{\rho_e v_{\text{the}}}{2L_T}\frac{\partial}{\partial y}\nabla_\parallel \frac{\delta n_e}{n_{0e}}, \tag{4.17}$$

we arrive at the following dispersion relation:

$$\omega^2 = -\left(2\omega_{de}\omega_{*e} - \omega_{\text{KAW}}^2\right)\left(\bar{\tau} + \frac{1}{1+i\xi_*}\right), \tag{4.18}$$

where $\omega_{\text{KAW}} = k_\parallel v_{\text{the}} k_\perp d_e/\sqrt{2}$ is the kinetic-Alfvén-wave (KAW) frequency, the physical origin of which will be discussed in section 4.3.1. The cTAI growth rate is manifest in this expression; adopting the isothermal limit (4.11) and neglecting ω_{KAW}, we re-obtain (4.15) to lowest order in ξ_*.

Though we have thus far focussed on the collisional limit, it turns out that much of what we have done is directly applicable to the collisionless limit if we simply replace the parallel conduction rate with the parallel streaming rate[3], viz., (4.18) remains valid but with

$$\xi_* = \frac{\sqrt{\pi}}{2}\frac{\omega_{*e}}{k_\parallel v_{\mathrm{the}}}. \tag{4.19}$$

The equivalent of the ordering (4.9) in the collisionless regime is

$$\omega_{de} \ll \omega \ll \omega_{*e} \sim k_\parallel v_{\mathrm{the}}, \tag{4.20}$$

and the equations (4.14) are the same; note that in this regime, $\delta T_{\parallel e} = \delta T_{\perp e} = \delta T_e$ because both the parallel and perpendicular temperature are constant along the field line to leading order in ω/ω_{*e}. Furthermore, it is possible to show that (4.8) is also valid in the collisionless limit if one replaces $\delta T_e \to \delta T_{\parallel e}$, $-\kappa \nabla_\parallel \log T_e \to \delta q_{\parallel e}/n_{0e}T_{0e}$, $(2/3)\nabla_\parallel^2 u_{\parallel e} \to 2\nabla_\parallel^2 u_{\parallel e}$, $\nu_{ei}u_{\parallel e} \to \mathrm{d}u_{\parallel e}/\mathrm{d}t$, and the heat flux must now be determined kinetically. The effect is still to enforce isothermality along the field lines, but by means of parallel particle streaming, rather than collisional conduction. This means that cTAI, while being a ‘fluid’ instability, is not an intrinsically collisional one, occurring also in the collisionless, kinetic limit. Its physical picture in the collisionless limit is exactly the same as in the collisional one.

The dispersion relation (4.18) contains most of the interesting features of the TAI physics (see, however, sections 4.3.3 and 4.4.2). The most obvious feature of (4.18) is that both the growth rate and frequency vanish when

$$2\omega_{de}\omega_{*e} = \omega_{\mathrm{KAW}}^2 \quad \Rightarrow \quad \frac{k_{\parallel c}L_T}{\sqrt{\beta_e}} = \left(\frac{L_T}{L_B}\right)^{1/2}\frac{k_y}{k_\perp}. \tag{4.21}$$

This corresponds to the point of transition from the curvature-dominated regime ($k_\parallel < k_{\parallel c}$), on which we will focus in this section, to the KAW-dominated regime ($k_\parallel > k_{\parallel c}$), which will be the subject of section 4.3.1.

---

[3] ξ_* measures the competition between diamagnetic drifts and the rate at which information can propagate along perturbed field lines in the presence of an equilibrium temperature gradient. In the collisional limit, this parallel rate is thermal conduction, as in (4.10), while in the collisionless one it is clearly parallel streaming, as in (4.19). Readers unconvinced by this intuition may consult appendix D of [1] for a rigorous derivation of (4.19), (4.20) and the statements that follow.

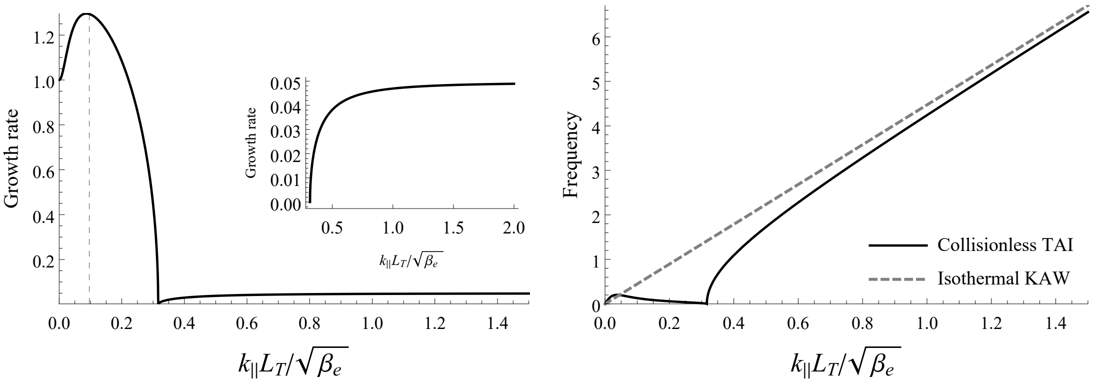

(a) $L_B/L_T = 10$, $k_y d_e = 0.1$ (b) $L_B/L_T = 10$, $k_y d_e = 0.1$

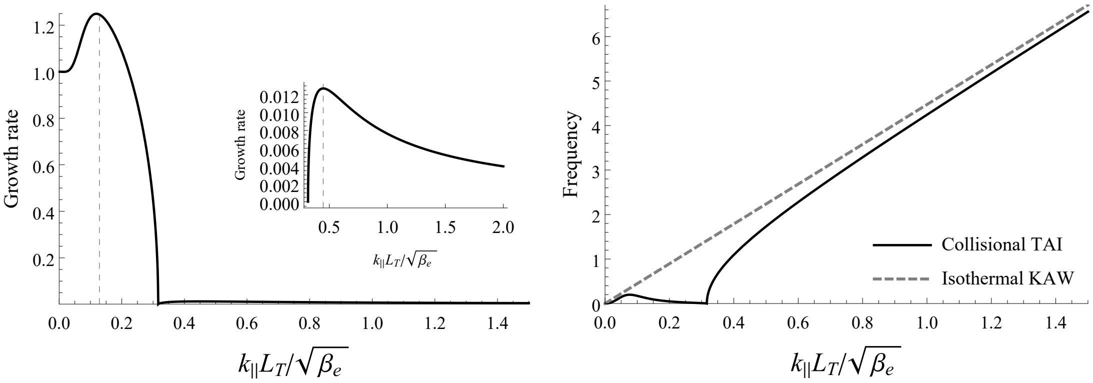

(c) $L_B/L_T = 10$, $k_y d_e \chi = 0.002$ (d) $L_B/L_T = 10$, $k_y d_e \chi = 0.002$

Figure 4.2: (a), (c) The growth-rate and (b), (d) the real frequency of the TAI (4.22) in the isothermal limit (4.11), plotted as functions of $k_\parallel L_T/\sqrt{\beta_e}$ and normalised to the cETG growth rate (3.15) ($\bar{\tau} = 1$). (a) and (b) correspond to the collisionless case, while (c) and (d) to the collisional one. The vertical dashed lines in panels (a) and (c) are for $k_\parallel = k_{\parallel\mathrm{max}}$ given by (4.24). The dashed lines in panels (b) and (d) show the isothermal KAW frequency (4.29). Both the growth rate and the real frequency vanish at the critical parallel wavenumber $k_{\parallel c} L_T/\sqrt{\beta_e} = 0.32$, given by (4.21). The insets in panels (a) and (c) show details of the behaviour of the growth rate for $k_\parallel > k_{\parallel c}$; the vertical dashed line in the inset of panel (c) is the (secondary) maximum at $k_\parallel = \sqrt{2} k_{\parallel c}$ discussed at the end of section 4.3.1. The perpendicular wavenumbers chosen in this figure are all safely below the transition wavenumber (4.26), which is $k_{\perp *} d_e = 0.71$ or $k_{\perp *} d_e \chi = 0.03$ in the collisionless or collisional cases, respectively.

If we extract the real and imaginary parts of (4.18), the (real) frequency $\omega_r = \mathrm{Re}(\omega)$ and the growth rate $\gamma = \mathrm{Im}(\omega)$ of the growing modes can be written as

$$\omega_r^2 = \left|2\omega_{de}\omega_{*e} - \omega_{\mathrm{KAW}}^2\right| \bar{\tau}\, f_-(\xi_*), \quad \gamma^2 = \left|2\omega_{de}\omega_{*e} - \omega_{\mathrm{KAW}}^2\right| \bar{\tau}\, f_+(\xi_*), \tag{4.22}$$

where

$$f_\pm(\xi_*) = \frac{1}{2\bar{\tau}}\left[\sqrt{\left(\bar{\tau} + \frac{1}{1+\xi_*^2}\right)^2 + \frac{\xi_*^2}{(1+\xi_*^2)^2}} \pm \mathrm{sgn}\left(2\omega_{de}\omega_{*e} - \omega_{\mathrm{KAW}}^2\right)\left(\bar{\tau} + \frac{1}{1+\xi_*^2}\right)\right]. \tag{4.23}$$

The growth rate and frequency (4.22) are plotted as functions of $k_\parallel L_T/\sqrt{\beta_e}$ in figure 4.2. For $k_\parallel < k_{\parallel c}$, the growth rate has a maximum for some non-zero $k_\parallel$; it is about to turn out that this maximum corresponds to the cTAI growth rate (4.15), which was derived in the isothermal limit, $\xi_* \ll 1$. Expanding (4.23) in small ξ_* to leading and sub-leading order, and seeking the maximum of the resultant expression with respect to $k_\parallel$, we find that this maximum occurs approximately at

$$\frac{k_{\parallel\mathrm{max}} L_T}{\sqrt{\beta_e}} = \begin{cases} \left[\dfrac{\pi}{64}\dfrac{3+4\bar{\tau}}{(1+\bar{\tau})^2}\dfrac{L_T}{L_B}\right]^{1/4}\left(\dfrac{k_y^2 d_e}{k_\perp}\right)^{1/2}, & \text{collisionless,} \\ \left[\dfrac{81}{50}\dfrac{3+4\bar{\tau}}{(1+\bar{\tau})^2}\dfrac{L_T}{L_B}\right]^{1/6}\left(\dfrac{k_y^2 d_e}{k_\perp}\chi\right)^{1/3}, & \text{collisional,} \end{cases} \tag{4.24}$$

indicated by the vertical dashed lines in panels (a) and (c) of figure 4.2; χ is defined in (2.33). Calculating the growth rate (4.22) at $k_\parallel = k_{\parallel\mathrm{max}}$, one recovers (4.15) up to small corrections, as promised.

This solution, however, is only valid so long as it remains in the isothermal limit (4.11). Evaluating ξ_* at $k_\parallel = k_{\parallel\mathrm{max}}$, we find, defining $\alpha = 1, 2$ in the collisionless and collisional limits, respectively,

$$\xi_*\left(k_{\parallel\mathrm{max}}\right) \sim \frac{k_{\parallel\mathrm{max}}}{k_{\parallel c}} \sim \left(\frac{k_\perp}{k_{\perp *}}\right)^{1/(1+\alpha)} \ll 1 \tag{4.25}$$

provided that $k_\perp \ll k_{\perp *}$, where $k_{\perp *}$ is the perpendicular wavenumber at which $\xi_*\left(k_{\parallel c}\right) \sim 1$, viz.,

$$k_{\perp *} d_e = \begin{cases} \dfrac{4}{\sqrt{\pi}}\left(\dfrac{L_T}{L_B}\right)^{1/2}, & \text{collisionless,} \\ \dfrac{5}{9}\dfrac{L_T}{L_B}\chi^{-1}, & \text{collisional,} \end{cases} \quad \Rightarrow \quad \xi_*(k_{\parallel c}) = \begin{cases} \dfrac{k_\perp}{k_{\perp *}}, & \text{collisionless,} \\ \dfrac{k_\perp^2}{k_{\perp *} k_y}, & \text{collisional.} \end{cases} \tag{4.26}$$

Thus, the isothermal regime is valid at sufficiently long perpendicular wavelengths. At $k_\perp > k_{\perp *}$, a different, isobaric regime takes over, which will be considered in section 4.4.

Lastly, we note that, for $k_\parallel < k_{\parallel c}$, the magnitude of the real frequency is vanishingly small when compared to the growth rate: expanding both the growth rate and the real frequency in (4.22) for $\xi_* \ll 1$, we find

$$\frac{\omega_r^2}{\gamma^2} \approx \frac{\xi_*^2}{4(1+\bar{\tau})^2} \ll 1. \tag{4.27}$$

Thus, cTAI is, like cETG, an (almost) purely growing mode; this is distinct from the case of the sETG, whose frequency and growth rate are comparable at the latter's maximum (see Chapter 3).

4.3 Isothermal KAWs and slab TAI

4.3.1 Isothermal KAWs

If $k_\perp \ll k_\perp^*$, i.e., $\xi_*\left(k_{\parallel c}\right) \ll 1$, then the isothermal approximation (4.12) continues to be satisfied at $k_\parallel > k_{\parallel c}$, but the effects of the magnetic drifts become negligible for $k_\parallel \gg k_{\parallel c}$. In this region, our system (2.27)-(2.29) becomes, approximately,

$$\frac{\mathrm{d}}{\mathrm{d}t}\frac{\delta n_e}{n_{0e}} = -v_{\mathrm{the}}\nabla_\parallel d_e^2 \nabla_\perp^2 \mathcal{A}, \quad \frac{\mathrm{d}\mathcal{A}}{\mathrm{d}t} + \frac{v_{\mathrm{the}}}{2}\frac{\partial \varphi}{\partial z} = \frac{v_{\mathrm{the}}}{2}\nabla_\parallel \frac{\delta n_e}{n_{0e}}, \quad \varphi = -\bar{\tau}\frac{\delta n_e}{n_{0e}}. \tag{4.28}$$

These equations are also valid in the collisionless limit [there is no intrinsically collisional physics in (4.28), as the resistive term in (2.28) is negligible under the ordering (4.9)]. We recognise these as the equations of Electron Reduced Magnetohydrodynamics (ERMHD, see [72] or [76]), which describe the dynamics, linear and nonlinear, of kinetic Alfvén waves (KAWs). Indeed, linearising and Fourier transforming (4.28), we find the dispersion relation

$$\omega^2 = k_\parallel^2 v_{\mathrm{the}}^2 k_\perp^2 d_e^2 \frac{1+\bar{\tau}}{2} = \omega_{\mathrm{KAW}}^2 \left(1+\bar{\tau}\right). \tag{4.29}$$

These are the familiar (isothermal) KAWs that arise in homogeneous systems [51, 72, 73, 76–78]. The physics of these waves is as follows. Suppose that a density perturbation $\delta n_e/n_{0e} = -\bar{\tau}^{-1}\varphi$ with $k_\parallel \neq 0$ is created. This gives rise to a parallel pressure gradient, which manifests itself as a parallel (perturbed) density gradient, as any parallel temperature variation is instantaneously ironed out by rapid parallel streaming or thermal conduction. This parallel pressure gradient must be balanced by the parallel electric field [second equation in (4.28)], whose inductive part, through Ampère's law (2.30), leads to a parallel current. But a parallel current is a parallel electron flow, which leads to compressional rarefaction along the field that opposes the original density perturbation [first equation in (4.28)]. This is also the reason for the reduction of the cTAI growth rate at $k_\parallel > k_{\parallel\max}$ and its vanishing at $k_\parallel = k_{\parallel c}$ [see panels (a) and (c) in figure 4.2]: the parallel compression that provides the restoring force for the KAW perturbations increases as $k_\parallel$ increases, weakening the instability mechanism of the cTAI described in section 4.1.

4.3.2 Isothermal slab TAI

Remarkably, however, it turns out that isothermal KAW, at $k_\parallel > k_{\parallel c}$, are still unstable in the presence of an equilibrium electron temperature gradient: expanding (4.18) or (4.22) for $\xi_* \ll 1$ at $k_\parallel \gg k_{\parallel c}$ (the latter in order to drop the ω_{de} effects), we find

$$\omega_r^2 \approx \omega_{\mathrm{KAW}}^2 (1+\bar{\tau}), \quad \gamma^2 \approx \omega_{\mathrm{KAW}}^2 \frac{\xi_*^2}{4(1+\bar{\tau})}. \tag{4.30}$$

By analogy with sETG, we shall henceforth refer to this KAW-dominated TAI as the 'slab' TAI (sTAI); it was our original motivation for calling the instability 'thermo-Alfvénic'[4].

The precise mechanism by which the isothermal sTAI operates is somewhat subtler than cTAI, relying on the fact that the isothermal condition (4.12) that led to (4.29) is, in fact, only approximately satisfied. Indeed, $\nabla_\parallel \log T_e$ is determined, in the collisional limit, at next order in ξ_* by (4.13) which, linearising and Fourier transforming, can be written as

$$\left(\nabla_\parallel \log T_e\right)_{\boldsymbol{k}} = -i\xi_* \left(\nabla_\parallel \frac{\delta n_e}{n_{0e}}\right)_{\boldsymbol{k}}. \tag{4.31}$$

This means that a small but finite parallel gradient of temperature effectively introduces a correction to the parallel density gradient in (4.28) that is $\pi/2$ out of phase with the contribution that enables the isothermal KAWs. This gives rise to the instability (4.30) in both the collisional limit, and, it turns out, the collisionless one, where (4.31) also

---

[4] The sTAI instability appears to be a close relative of the 'electron magnetothermal instability' (eMTI) discovered by [79] in their treatment of stratified plasma atmospheres, and analysed by them in the high-beta limit appropriate to the astrophysical applications on which they were focused.

holds but with ξ_* given by (4.19). Restoring finite parallel temperature gradients in (4.28), we have

$$\frac{\mathrm{d}}{\mathrm{d}t}\frac{\delta n_e}{n_{0e}} = -v_{\mathrm{the}}\nabla_\parallel d_e^2 \nabla_\perp^2 \mathcal{A}, \qquad \frac{\mathrm{d}\mathcal{A}}{\mathrm{d}t} + \frac{v_{\mathrm{the}}}{2}\frac{\partial \varphi}{\partial z} = \frac{v_{\mathrm{the}}}{2}\nabla_\parallel \frac{\delta n_e}{n_{0e}} + \frac{v_{\mathrm{the}}}{2}\nabla_\parallel \log T_e, \tag{4.32}$$

with dispersion relation

$$\omega^2 = \omega_{\mathrm{KAW}}^2(1+\bar{\tau} - i\xi_*) \quad \Rightarrow \quad \omega \approx \pm\omega_{\mathrm{KAW}}\left(\sqrt{1+\bar{\tau}} - \frac{i\xi_*}{2\sqrt{1+\bar{\tau}}} + \dots\right), \tag{4.33}$$

whose real and imaginary parts are exactly the frequency and growth rate (4.30).

If we restore the magnetic-drift terms in the density equation, we find, in the collisionless limit, that the sTAI growth rate increases from zero at $k_\parallel = k_{\parallel c}$ to a finite, $k_\parallel$-independent limit (4.30) at $k_\parallel \gg k_{\parallel c}$, viz.,

$$\gamma \to \frac{1}{4}\sqrt{\frac{\pi}{2(1+\bar{\tau})}}k_\perp d_e \omega_{*e} = \sqrt{\frac{\omega_{de}\omega_{*e}}{2(1+\bar{\tau})}}\frac{k_\perp}{k_{\perp *}}, \tag{4.34}$$

where $k_{\perp *}$ is given by (4.26) [see figure 4.2(a), inset]. As we shall see shortly in section 4.3.3, this value only persists up to a certain $k_\parallel$ where sTAI is stabilised by compressional heating, which was neglected in (4.18). In the collisional limit, $\gamma \to 0$ as $k_\parallel \to \infty$ (also, in fact, shown to go to $\gamma < 0$ in section 4.3.3). The growth rate has a maximum at $k_\parallel = \sqrt{2}k_{\parallel c}$, which is shown by the vertical dashed line in the inset of figure 4.2(c). The growth rate at this maximum is [1]

$$\gamma = \frac{k_\perp^2 d_e^2 v_{\mathrm{the}}^2}{8\sqrt{2(1+\bar{\tau})}\kappa}\sqrt{\frac{\omega_{*e}}{\omega_{de}}} = \frac{1}{2}\sqrt{\frac{\omega_{de}\omega_{*e}}{2(1+\bar{\tau})}}\frac{k_\perp^2}{k_{\perp *}k_y}. \tag{4.35}$$

Both the maximum growth rates (4.34) and (4.35) are manifestly much smaller than the maximum growth rate of cTAI (4.15) as long as $k_\perp \ll k_{\perp *}$, i.e., as long as the isothermal approximation, in which all of these results have been derived in the first place, is valid.

Thus, at long perpendicular wavelengths ($k_\perp \ll k_{\perp *}$), the dominant instability is cTAI, reaching its maximum growth rate (4.15) at the parallel wavenumber (4.24).

4.3.3 Stabilisation of isothermal slab TAI

The sTAI growth rates do not, in fact, stay positive to infinite parallel wavenumbers. The instability is eventually quenched by the compressional-heating term in the temperature equation [(2.25) or (2.29) in the collisionless and collisional limits, respectively] that begins to compete with the TAI drive.

To show this, let us consider the collisional limit and, instead of (4.9), the ordering

$$(k_\perp d_e)^2 \nu_{ei} \ll \omega \sim \omega_{*e} \ll \kappa k_\parallel^2. \tag{4.36}$$

In this limit, the system is still isothermal to leading order in $\xi_* \ll 1$, but now we must also retain the compressional heating term in (4.8) to determine $\nabla_\parallel \log T_e$ at next order: instead of (4.13), we have, therefore,

$$\kappa \nabla_\parallel^3 \log T_e = \frac{\rho_e v_{\rm the}}{2L_T} \frac{\partial}{\partial y} \nabla_\parallel \frac{\delta n_e}{n_{0e}} + \frac{2}{3} \nabla_\parallel^2 u_{\parallel e}. \tag{4.37}$$

Furthermore, it turns out that we must also retain the resistive term in (2.28) at this order as it will end up making a contribution of the same order as the second term in (4.37). Thus, the second equation in (4.32) is replaced by

$$\frac{\mathrm{d}\mathcal{A}}{\mathrm{d}t} + \frac{v_{\rm the}}{2} \frac{\partial \varphi}{\partial z} = \frac{v_{\rm the}}{2} \nabla_\parallel \frac{\delta n_e}{n_{0e}} + \frac{v_{\rm the}}{2} \nabla_\parallel \log T_e + \nu_{ei} \frac{u_{\parallel e}}{v_{\rm the}}, \tag{4.38}$$

Combining (4.37) and (4.38) with the density equation, still the same as in (4.32), we obtain the following dispersion relation

$$\omega^2 - \omega_{\rm KAW}^2 (1 + \bar{\tau} - i\xi_*) = -i \left(\frac{2}{3} + a \right) \frac{\omega}{\kappa k_\parallel^2} \omega_{\rm KAW}^2, \tag{4.39}$$

where a is defined as below (3.12). This is the same as (4.33) apart from the right-hand side, previously neglected. At the stability boundary, the frequency ω must be purely real, and both the real and imaginary parts of (4.39) must vanish individually, giving

$$\omega^2 = \omega_{\rm KAW}^2 (1 + \bar{\tau}), \quad \omega = -\frac{\omega_{*e}}{a + 2/3} \quad \Rightarrow \quad \mp \omega_{\rm KAW} \sqrt{1 + \bar{\tau}} = \frac{\omega_{*e}}{a + 2/3}. \tag{4.40}$$

For $k_y \sim k_\perp$, (4.40) are lines of constant $k_\parallel$ in wavenumber space, limiting the isothermal sTAI at large parallel wavenumbers:

$$\frac{k_\parallel L_T}{\sqrt{\beta_e}} = \pm \frac{1}{(a + 2/3)\sqrt{2(1 + \bar{\tau})}} \frac{k_y}{k_\perp}. \tag{4.41}$$

This stabilisation of the isothermal sTAI was not captured in the TAI dispersion relation (4.18) because the ordering (4.9) did not formally allow frequencies comparable to the drift wave frequency, required by (4.40).

In the collisionless limit, we also find that the sTAI is stabilised above a line of constant $k_\parallel$ [1]

$$\pm \omega_{\rm KAW} \sqrt{1 + \bar{\tau}} = \frac{\omega_{*e}}{2} \quad \Rightarrow \quad \frac{k_\parallel L_T}{\sqrt{\beta_e}} = \pm \frac{1}{2\sqrt{2(1 + \bar{\tau})}} \frac{k_y}{k_\perp}, \tag{4.42}$$

due again to the competition between the compressional heating in the equation for the parallel temperature (2.25) and the TAI drive. Appendix D of [1] details a collisionless calculation analogous to that performed above in the collisional limit, but the latter is sufficient here for illustrating the physics underlying the stabilisation mechanism. In both cases, the stabilisation of sTAI does not appear in figure 4.2 (and, later, in figure 4.3) because the orderings (4.9) or (4.20) that lead to the TAI dispersion relation (4.18) do not formally allow this stabilisation; instead, readers will find it in the insets of figures 5.3(c) and 5.4(c) in the collisionless and collisional limits, respectively, where solutions of a more precise dispersion relation are shown.

Though useful for delineating the precise regions of instability in the $(k_\perp, k_\parallel)$ space, this stabilisation of the isothermal sTAI is of secondary importance because it is cTAI that is the dominant instability at long perpendicular wavelengths ($k_\perp \ll k_{\perp *}$), which was the main conclusion of section 4.3.2.

4.4 Isobaric limit

Let us now consider what happens in the opposite limit of short perpendicular wavelengths, $k_\perp \gg k_\perp^*$, corresponding to thermal conduction (or its collisionless analogue, parallel streaming) being weak in comparison with the ω_{*e} driving, viz.,

$$\xi_* \gg 1. \tag{4.43}$$

Assuming this in addition to (4.9) or (4.20), we find that the dominant term in (4.8) is the second term on the right-hand side, meaning that, to leading order,

$$\nabla_\parallel \log p_e = \nabla_\parallel \log T_e + \nabla_\parallel \frac{\delta n_e}{n_{0e}} = 0. \tag{4.44}$$

This is the isobaric limit, in which the total *pressure* is constant along the perturbed field lines, rather than just the total temperature. That is, the temperature perturbation has to adjust to cancel not just the variation of the equilibrium temperature along the perturbed field line, as was the case in the isothermal limit, but now also the variation of the perturbed density. At next order in ξ_*, from (4.8), we have

$$\frac{\rho_e v_{\text{the}}}{2L_T} \frac{\partial}{\partial y} \nabla_\parallel \log p_e = -\kappa \nabla_\parallel^3 \frac{\delta n_e}{n_{0e}} \quad \Rightarrow \quad \frac{|\nabla_\parallel \log p_e|}{|\nabla_\parallel \delta n_e / n_{0e}|} \sim \frac{1}{\xi_*} \ll 1, \tag{4.45}$$

so we can now neglect the entire right-hand side of (2.28), reducing the latter equation to $E_\parallel = 0$. For $k_\parallel \ll k_{\parallel c}$, i.e. neglecting the KAW restoring force, our system (2.27)-(2.29) therefore becomes

$$\frac{\mathrm{d}}{\mathrm{d}t}\frac{\delta n_e}{n_{0e}} = -\frac{\rho_e v_{\mathrm{the}}}{L_B}\frac{\partial}{\partial y}\frac{\delta T_e}{T_{0e}}, \quad \frac{\mathrm{d}\mathcal{A}}{\mathrm{d}t} + \frac{v_{\mathrm{the}}}{2}\frac{\partial \varphi}{\partial z} = 0, \quad \nabla_\parallel \frac{\delta T_e}{T_{0e}} = \frac{\rho_e}{L_T}\frac{\partial \mathcal{A}}{\partial y} - \nabla_\parallel \frac{\delta n_e}{n_{0e}}, \tag{4.46}$$

where $\varphi = -\bar{\tau}\delta n_e/n_e$. As with the isothermal cTAI, these equations remain valid in the collisionless limit, because $\delta T_{\parallel e} = \delta T_{\perp e} = \delta T_e$ to leading order in ω/ω_{*e}.

In (4.46), the temperature perturbation is determined from the third equation, which is simply the isobaric condition (4.44). However, given the ordering (4.9), the correction to δT_e due to the density perturbation is small, viz., $\delta n_e/n_{0e} \sim (\omega_{de}/\omega)\delta T_e/T_{0e}$, which follows from the first equation in (4.46). That is, to leading order, there is no difference between the isothermal and isobaric conditions when it comes to determining the temperature perturbation. Hence, the associated dispersion relation is

$$\omega^2 = -2\omega_{de}\omega_{*e}\bar{\tau} \quad \Rightarrow \quad \omega = \pm i \left(2\omega_{de}\omega_{*e}\bar{\tau}\right)^{1/2}. \tag{4.47}$$

Analysing — and plotting, in figure 4.3 — the dispersion relation (4.22) in the isobaric regime, both collisional and collisionless, we find that the maximum of the growth rate in the region $k_\parallel < k_{\parallel c}$ occurs at $k_\parallel = 0$, i.e., it is, in fact, the 2D cETG mode that has the fastest growth. At finite $k_\parallel$, it is weakened by the presence of the restoring force associated with KAWs, reaching $\gamma = 0$ at $k_\parallel = k_{\parallel c}$ — this is evident in panels (a) and (c) of figure 4.3.

The dispersion relation (4.47) is identical to the cETG dispersion relation (3.15). This is because the second equation in (4.46) is simply $E_\parallel = 0$, implying that the magnetic field is now frozen into the $\boldsymbol{E} \times \boldsymbol{B}$ flow, as are the temperature perturbations [see (2.34), wherein the second term vanishes in the isobaric limit]. This is distinct to the case of the isothermal cTAI introduced in section 4.1, where the magnetic field was frozen into a *different* velocity field than the temperature perturbations, viz., the mean electron flow (4.16). As a result, unlike in the isothermal case, there is no enhancement of the cETG growth rate by the TAI mechanism in the isobaric regime: (4.47) can simply be regarded as an extension of the familiar cETG into the electromagnetic regime. However, physically, the isobaric cTAI is not an interchange mode, since it involves $k_\parallel \neq 0$. Its mechanism is similar to its isothermal cousin (figure 4.1), except the balance along the perturbed field is of pressure rather than temperature. It may

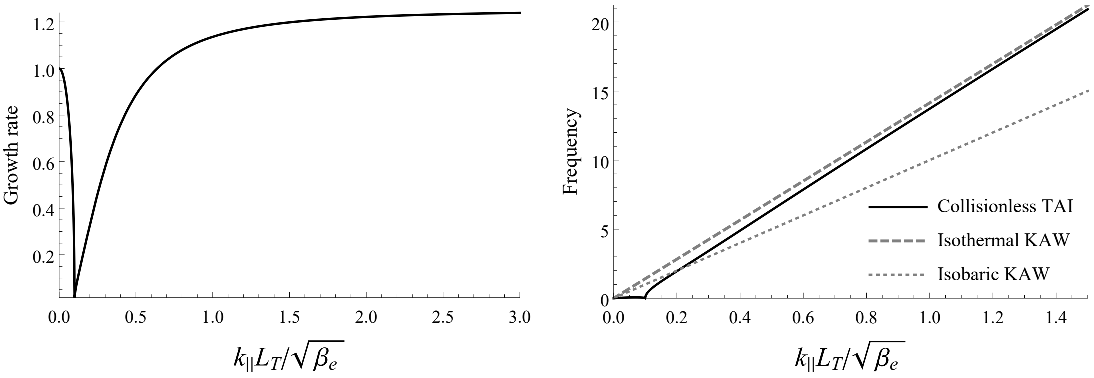

(a) $L_B/L_T = 100$, $k_y d_e = 0.8$ (b) $L_B/L_T = 100$, $k_y d_e = 0.8$

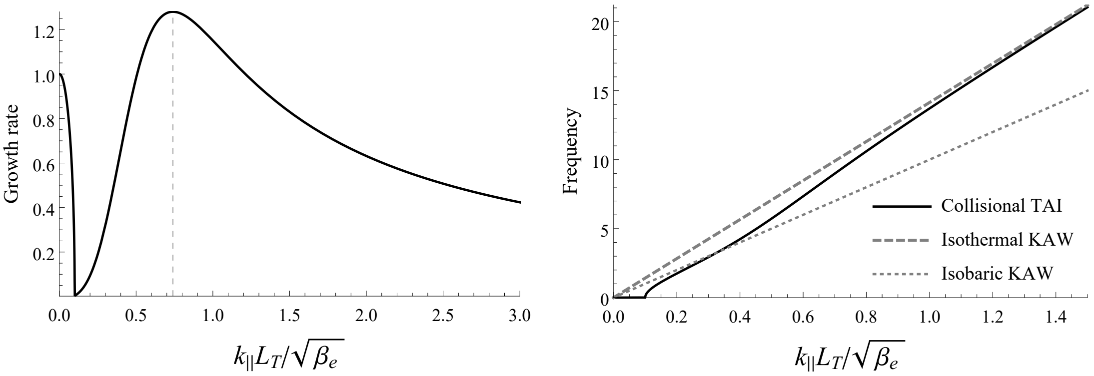

(c) $L_B/L_T = 100$, $k_y d_e \chi = 0.1$ (d) $L_B/L_T = 100$, $k_y d_e \chi = 0.1$

Figure 4.3: (a), (c) The growth-rate and (b), (d) the real frequency of the TAI (4.22) in the isobaric limit (4.43), plotted as functions of $k_{\|}L_T/\sqrt{\beta_e}$ and normalised to the cETG growth rate (3.15) ($\bar{\tau} = 1$). (a) and (b) correspond to the collisionless case, while (c) and (d) the collisional one. The vertical dashed line in (c) is for $k_{\|\max}$ given by (4.54). The dashed and dotted lines in panels (b) and (d) are the isothermal (4.29) and isobaric (4.49) KAW frequencies, respectively. Both the growth rate and the real frequency vanish at the critical parallel wavenumber $k_{\|c}L_T/\sqrt{\beta_e} = 0.1$, given by (4.21). The perpendicular wavenumbers chosen in this figure are all safely above the transition wavenumber (4.26), which is $k_{\perp *}d_e = 0.23$ or $k_{\perp *}d_e\chi = 0.003$ in the collisionless or collisional cases, respectively. The parallel wavenumber corresponding to the transition between the isobaric and isothermal regimes at a fixed k_y (viz., for $\xi_* \sim 1$) is given by $k_{\|}L_B/\sqrt{\beta_e} = 0.35$ or 0.36 in the collisionless and collisional cases, respectively. We chose a very large value of L_B/L_T to show the asymptotic regimes clearly.

therefore be appropriate to regard it as an electron-scale extension of MHD-like modes, such as the kinetic ballooning mode (KBM) — indeed, the condition $E_\parallel = 0$, which is a direct consequence of pressure balance (4.44), is often invoked as a signature of such modes [39, 59].

4.4.1 Isobaric slab TAI

For $k_\parallel \gg k_{\parallel c}$, and still assuming (4.43), our system (2.27)-(2.29) becomes, approximately,

$$\frac{\mathrm{d}}{\mathrm{d}t}\frac{\delta n_e}{n_{0e}} = -v_{\mathrm{the}}\nabla_\parallel d_e^2 \nabla_\perp^2 \mathcal{A}, \qquad \frac{\mathrm{d}\mathcal{A}}{\mathrm{d}t} + \frac{v_{\mathrm{the}}}{2}\frac{\partial \varphi}{\partial z} = 0, \qquad \varphi = -\bar{\tau}\frac{\delta n_e}{n_{0e}}. \tag{4.48}$$

As with the isothermal KAW, these equations are also valid in the collisionless limit. They are similar to (4.28), except that the parallel electric field is now zero because the parallel gradient of the perturbed pressure vanishes. This new system describes the dynamics of *isobaric* KAWs — so called because they obey (4.44). Their dispersion relation is

$$\omega^2 = k_\parallel^2 v_{\mathrm{the}}^2 k_\perp^2 d_e^2 \frac{\bar{\tau}}{2} = \omega_{\mathrm{KAW}}^2 \bar{\tau}. \tag{4.49}$$

These isobaric KAW, which arise in strongly driven systems (large ω_{*e}), work in a similar fashion to their isothermal cousins described at the beginning of section 4.3.1, except the inductive part of the parallel electric field now creates a magnetic perturbation and, therefore, a parallel current, from the electrostatic part of the parallel electric field, rather than from a combination of the latter and the parallel pressure gradient.

Like the isothermal KAW, the isobaric KAW are unstable to sTAI: expanding (4.18) or (4.22) for $\xi_* \gg 1$ at $k_\parallel \gg k_{\parallel c}$, we find

$$\omega_r^2 = \omega_{\mathrm{KAW}}^2 \bar{\tau}, \qquad \gamma^2 = \omega_{\mathrm{KAW}}^2 \frac{1}{4\bar{\tau}\xi_*^2}, \tag{4.50}$$

which is (4.49) once again but with a small, but finite, growth rate. In a similar fashion to the isothermal sTAI described in section 4.3.1, the instability arises due to the fact that the isobaric condition (4.44) that led to (4.48) is, in fact, only approximately satisfied. In the collisional limit, $\nabla_\parallel \log p_e$ is determined at next order in ξ_*^{-1} by (4.45), which, linearising and Fourier transforming, can be written as

$$\left(\nabla_\parallel \log p_e\right)_{\boldsymbol{k}} = \frac{1}{i\xi_*}\left(\nabla_\parallel \frac{\delta n_e}{n_{0e}}\right)_{\boldsymbol{k}}. \tag{4.51}$$

This means that there will be a term in the second equation in (4.48) that is $\pi/2$ out of phase with the electrostatic contribution to the parallel electric field that enables the isobaric KAW. The result is the instability (4.50), which exists also in the collisionless limit, but with ξ_* given by (4.19). Indeed, restoring finite pressure gradients in (4.48), we have

$$\frac{\mathrm{d}}{\mathrm{d}t}\frac{\delta n_e}{n_{0e}} = -v_{\mathrm{th}e}\nabla_\| d_e^2 \nabla_\perp^2 \mathcal{A}, \quad \frac{\mathrm{d}\mathcal{A}}{\mathrm{d}t} + \frac{v_{\mathrm{th}e}}{2}\frac{\partial \varphi}{\partial z} = \frac{v_{\mathrm{th}e}}{2}\nabla_\| \log p_e, \tag{4.52}$$

leading to the dispersion relation

$$\omega^2 = \omega_{\mathrm{KAW}}^2\left(\bar{\tau} + \frac{1}{i\xi_*}\right) \quad \Rightarrow \quad \omega \approx \pm\omega_{\mathrm{KAW}}\left(\sqrt{\bar{\tau}} - \frac{i}{2\sqrt{\bar{\tau}}\xi_*} + \dots\right), \tag{4.53}$$

whose real and imaginary parts are exactly the frequency and growth rate (4.50).

As $k_\|$ is increased, the isobaric limit (4.43) must eventually break down and be replaced by the isothermal limit (4.11). This means that there will be a transition between isobaric and isothermal KAW, and the associated limits of sTAI, occurring, clearly, at $\xi_* \sim 1$. In the collisionless limit, the growth rate once again asymptotes to a constant value as $k_\| \to \infty$ ($\xi_* \to 0$) — this is just the isothermal limit (4.34) except now, since $k_\perp \gg k_{\perp *}$, this growth rate is large in comparison with the cETG growth rate achieved at $k_\| = 0$ [see figure 4.3(a), noting the normalisation]. Note that $\gamma \sim \omega_{\mathrm{KAW}}$ near the transition $\xi_* \sim 1$ (i.e., at $k_\| \sim \omega_{*e}/v_{\mathrm{th}e}$), but $\gamma \ll \omega_{\mathrm{KAW}}$ as $k_\| \to \infty$. In the collisional limit, there is peak growth at $\xi_* \sim 1$, or

$$k_{\|\max} \sim \sqrt{\frac{\omega_{*e}}{\kappa}} \sim \frac{1}{v_{\mathrm{th}e}}\sqrt{\omega_{*e}\nu_e}. \tag{4.54}$$

Determining the precise prefactor, which depends only on $\bar{\tau}$ and is, thus, order unity, is only possible numerically, but is, at any rate, inessential. The growth rate at this wavenumber is

$$\gamma \sim \omega_{\mathrm{KAW}} \sim k_\perp d_e \sqrt{\omega_{*e}\nu_e}. \tag{4.55}$$

Again, this growth rate is large in comparison with the cETG peak growth rate at $k_\| = 0$:

$$\frac{\gamma}{\sqrt{2\omega_{de}\omega_{*e}}} \sim k_\perp d_e \sqrt{\frac{\nu_e}{\omega_{de}}} \sim \left(\frac{k_\perp}{k_{\perp *}}\right)^{1/2} \gg 1. \tag{4.56}$$

Figure 4.3 illustrates all of this behaviour. We remind the reader that at large $k_\parallel$ (i.e., in the deep isothermal regime), the instability is quenched by compressional heating in both collisional and collisionless limits (see section 4.3.3).

Thus, the isobaric ($k_\perp \gg k_{\perp *}$) regime of the TAI is quite different from the isothermal one: the dominant instability is again electromagnetic, rather than electrostatic, but it is the slab TAI — an instability of KAWs reaching peak growth at the parallel wavenumber where the relevant parallel timescale — either the parallel-streaming or thermal-conduction rate in the collisionless or collisional regimes, respectively — is comparable to ω_{*e}. It must be appreciated, of course, that this behaviour only occurs in a relatively narrow interval of perpendicular wavelengths satisfying $k_{\perp *} \ll k_\perp \ll d_e^{-1}$ (or $\ll d_e^{-1}\chi^{-1}$ in the collisional regime). For $k_\perp d_e \gtrsim 1$ (or χ^{-1} in the collisional regime), it is replaced by the electrostatic instabilities described in section 3.

4.4.2 Stabilisation of isobaric slab TAI

As was the case with the isothermal sTAI, the isobaric sTAI is also stabilised within a certain region of wavenumber space, this time due to the effects of finite resistivity, or finite electron inertia, in the parallel momentum equation — (2.24) or (2.28) in the collisionless and collisional limits, respectively.

To work out this stabilisation, we once again consider the collisional limit and, instead of (4.9), the ordering

$$(k_\perp d_e)^2 \nu_{ei} \sim \omega \sim \kappa k_\parallel^2 \ll \omega_{*e}. \tag{4.57}$$

A direct consequence of this ordering is that one has to retain the resistive term in the leading-order parallel momentum equation, viz., the second equation in (4.52), coming from (2.28), is replaced with

$$\frac{\mathrm{d}\mathcal{A}}{\mathrm{d}t} + \frac{v_{\mathrm{the}}}{2}\frac{\partial \varphi}{\partial z} = \frac{v_{\mathrm{the}}}{2}\nabla_\parallel \log p_e + \nu_{ei}\frac{u_{\parallel e}}{v_{\mathrm{the}}}. \tag{4.58}$$

This means that, instead of the system being isobaric to leading order in $\xi_* \gg 1$, the parallel pressure gradient now balances the electron-ion frictional force:

$$\nabla_\parallel \log p_e + \frac{2\nu_{ei} u_{\parallel e}}{v_{\mathrm{the}}^2} = 0. \tag{4.59}$$

This is obvious from (4.8) in the limit (4.57). To next order, we must now retain both the time derivative of $\nabla_\parallel \log T_e$ and the compressional heating term in (4.8):

$$\frac{\rho_e v_{\mathrm{th}e}}{2L_T}\frac{\partial}{\partial y}\left(\nabla_\parallel \log p_e + \frac{2\nu_{ei}u_{\parallel e}}{v_{\mathrm{th}e}^2}\right) = \left(\frac{\mathrm{d}}{\mathrm{d}t} - \kappa\nabla_\parallel^2\right)\left(\nabla_\parallel \frac{\delta n_e}{n_{0e}} + \frac{2\nu_{ei}u_{\parallel e}}{v_{\mathrm{th}e}^2}\right) - \frac{2}{3}\nabla_\parallel^2 u_{\parallel e}. \tag{4.60}$$

Combining (4.58), (4.60) and the density equation from (4.52), we find the dispersion relation

$$\omega^2 - \omega_{\mathrm{KAW}}^2\left(\bar{\tau} + \frac{1}{i\xi_*}\right) = -\frac{1}{i\xi_*}\frac{(k_\perp d_e)^2\nu_{ei}}{\kappa k_\parallel^2}\omega^2 - \frac{1}{\xi_*}\left(\frac{5}{3} + a\right)\frac{\omega}{\kappa k_\parallel^2}\omega_{\mathrm{KAW}}^2, \tag{4.61}$$

where a is the same numerical constant as in (4.39). This is the same as (4.53), apart from the right-hand side, previously neglected. The second term on the right-hand side simply leads to a small, in $\xi_* \ll 1$, modification of the (real) frequency, and so can be neglected.

As usual, at the stability boundary, the frequency ω must be purely real, and both the real and imaginary parts of (4.61) must vanish individually, giving

$$\omega^2 = \omega_{\mathrm{KAW}}^2\bar{\tau}, \quad \frac{(k_\perp d_e)^2\nu_{ei}}{\kappa k_\parallel^2}\omega^2 = \omega_{\mathrm{KAW}}^2 \quad \Rightarrow \quad \frac{(k_\perp d_e)^2\nu_{ei}}{\kappa k_\parallel^2} = \frac{1}{\bar{\tau}}. \tag{4.62}$$

This is a line $k_\parallel \propto k_\perp$ in wavenumber space; moving from small to large parallel wavenumbers, there is a sliver of stability around this line, above which (viz., towards higher $k_\parallel$) the isobaric sTAI grows again to its peak at $\xi_* \sim 1$: see Figure 5.4(a). As with the case of the isothermal sTAI, this stabilisation was not captured by the general TAI dispersion relation (4.18) because the ordering (4.9) did not formally allow frequencies comparable to both the heat-conduction and the resistive-dissipation rates, required by (4.62).

In the collisionless limit, we find that the isobaric sTAI is stabilised at the flux-freezing scale (2.31) [1]

$$k_\perp d_e = \frac{1}{\sqrt{\bar{\tau}}}. \tag{4.63}$$

This is not via a mechanism analogous to the collisional case, as there are no resistive effects in the collisionless limit, but is instead due to the effect of finite electron inertia appearing in the parallel-momentum equation (2.24) (see appendix D.7.3 of [1] for further details).

The stabilisation of the isobaric sTAI is somewhat more relevant than the stabilisation of the isothermal sTAI (section 4.3.3), owing to the fact that the isobaric sTAI is the dominant instability for $k_{\perp *} \ll k_\perp \ll d_e^{-1}$ (or $\ll d_e^{-1}\chi^{-1}$ in the collisional regime). However, we shall discover in section 6.3.1 that the isobaric sTAI contributes only an order-unity amount to the turbulent energy injection — rather than introducing significant qualitative differences — and so the (linear) stabilisation thereof appears to be of little consequence in the nonlinear context.

Chapter 5

Summary of linear instabilities

In chapters 3 and 4, we introduced the linear instabilities supported by our low-beta system of equations in the electrostatic and electromagnetic regimes, respectively. In both the collisionless and collisional limits, we found that there were four main instabilities: slab ETG [sETG, (3.5) or (3.10)], curvature-mediated ETG [cETG, (3.15)], slab TAI [sTAI, (4.34) or (4.55)] and curvature-mediated TAI [cTAI, (4.15)]. Before moving on to our discussions of the turbulence supported by these modes, it will be useful to take stock of what we have learned by surveying the locations of each of these instabilities in wavenumber space. Throughout the discussions that follow, we will assume $k_y \sim k_\perp$, and so consider $(k_\perp, k_\parallel)$ to be the relevant wavenumber-space coordinates. We shall also assume $\bar{\tau} \sim 1$, implying that both species have roughly comparable temperatures and, more crucially, that $\bar{\tau}$ has no dependence on perpendicular wavenumbers (as it could do, for example, on scales comparable to the ion Larmor radius; see Section 7.3, or appendix A of [1]).

5.1 Collisionless limit

Let us first focus on the collisionless limit. At electrostatic scales $k_\perp \gtrsim d_e^{-1}$ [i.e., below the flux-freezing scale (2.31)], we have both the sETG and cETG instabilities. The transition between these two instabilities occurs when their growth rates are comparable, viz.,

$$(k_\parallel^2 v_{\text{the}}^2 \omega_{*e})^{1/3} \sim (\omega_{de}\omega_{*e})^{1/2} \quad \Rightarrow \quad \frac{k_\parallel L_T}{\sqrt{\beta_e}} \sim \left(\frac{L_T}{L_B}\right)^{3/4} k_y d_e. \tag{5.1}$$

The sETG instability begins to be quenched by Landau damping when its growth rate becomes comparable to the parallel streaming rate [cf. (3.7)]:

$$(k_\parallel^2 v_{\mathrm{the}}^2 \omega_{*e})^{1/3} \sim k_\parallel v_{\mathrm{the}} \quad \Rightarrow \quad \frac{k_\parallel L_T}{\sqrt{\beta_e}} \sim k_y d_e. \tag{5.2}$$

Note that this is the same line as that corresponding to the maximum of the sETG growth rate, viz., $k_\parallel v_{\mathrm{the}} \sim \omega_{*e}$. However, it must be stressed that this is only true asymptotically, as is evident from Figure 5.3(a),(d). Furthermore, careful analysis of the collisionless dispersion relation reveals that the sETG instability is also effectively stabilised — with only exponentially small growth rates remaining — around the flux-freezing scale [1, 80]. This 'fluid' stabilisation occurs when its growth rate becomes comparable to the KAW frequency:

$$(k_\parallel^2 v_{\mathrm{the}}^2 \omega_{*e})^{1/3} \sim \omega_{\mathrm{KAW}} \quad \Rightarrow \quad \frac{k_\parallel L_T}{\sqrt{\beta_e}} \sim (k_\perp d_e)^{-2}. \tag{5.3}$$

For $k_{\perp *} \lesssim k_\perp \lesssim d_e^{-1}$, the dominant instability is the isobaric sTAI, which is separated from the cETG instability by $k_\parallel = k_{\parallel c}$. The cETG instability in this perpendicular-wavenumber range, and for $k_\parallel \lesssim k_{\parallel c}$, can also be thought about as either the isobaric version of cTAI or the electron version of KBM (see section 4.4). The isobaric sTAI instability at $k_\parallel \gtrsim k_{\parallel c}$ is stabilised around the flux-freezing scale $k_\perp d_e \sim 1$ [see (4.63)]. The area bounded by the lines $k_\perp d_e \sim 1$, $k_\parallel = k_{\parallel c}$ and (5.3) thus contains only exponentially small growth rates that would be quenched by the effects of finite dissipation in any real physical system.

For $k_\perp \lesssim k_{\perp *}$, the cETG (or isobaric cTAI) instability is superseded by the isothermal cTAI, which is now the dominant instability, and is separated from sTAI along the horizontal line $k_\parallel = k_{\parallel c}$. The sTAI growth rate is cut off at large parallel wavenumbers due to the effect of parallel compression [see (4.42)], viz., when

$$\omega_{\mathrm{KAW}} \sim \omega_{*e} \quad \Rightarrow \quad \frac{k_\parallel L_T}{\sqrt{\beta_e}} \sim 1. \tag{5.4}$$

This is all illustrated in figure 5.1, where the solid line shows the location of the peak growth rate at each k_y — following, at $k_\perp \lesssim k_{\perp *}$, the peak growth of the isothermal cTAI (4.24), and at $k_\perp \geqslant k_{\perp *}$, the boundary $\xi_* \sim 1$ between the isothermal and isobaric regimes. The increase of the growth rate with k_y is unchecked in the drift-kinetic approximation that we have adopted, and requires the damping effects associated with

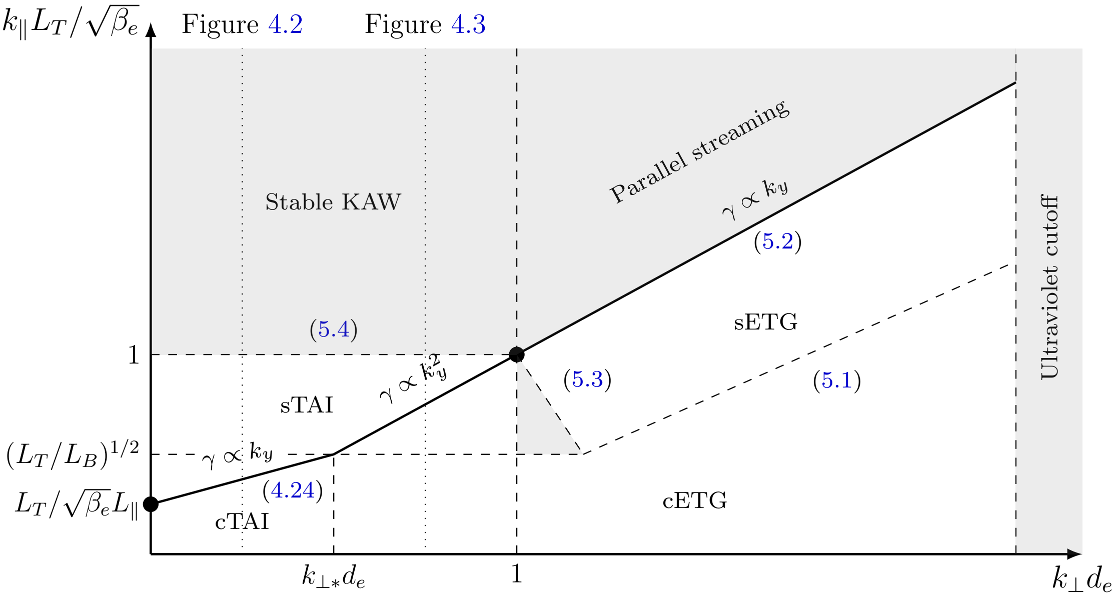

Figure 5.1: Collisionless modes in the $(k_\perp, k_\parallel)$ plane, where the axes are plotted on logarithmic scales. The dotted lines are the asymptotic boundaries between the various modes, with the shaded regions indicating stability; these are plotted more quantitatively in figure 5.3(a). At electrostatic scales (i.e., those below the flux-freezing scale, $k_\perp d_e > 1$), the curvature-mediated ETG [cETG, (3.15)] transitions into the slab ETG [sETG, (3.5)] along the boundary (5.1), while the sETG is damped by parallel streaming above (5.2). 'Fluid' stabilisation of the sETG occurs along (5.3). At electromagnetic scales (i.e., those above the flux-freezing scale, $k_\perp d_e < 1$), slab TAI [sTAI, (4.50)] is stabilised along $k_\perp d_e \sim 1$, meaning that the region enclosed by the lines $k_\perp d_e \sim 1$, $k_\parallel = k_{\parallel c}$, and (5.3) contains only exponentially small growth rates, and can thus effectively be considered stable [note that $k_{\parallel c} L_T/\sqrt{\beta_e} = (L_T/L_B)^{1/2}$, see (4.21)]. The cETG transitions into the curvature-mediated TAI [cTAI, (4.15)] along $k_\perp = k_{\perp *}$, with $k_{\perp *}$ defined in (4.26). cTAI is separated from sTAI by the horizontal line $k_\parallel = k_{\parallel c}$, while sTAI is stabilised by compressional heating at the horizontal line given by (5.4), transitioning into purely oscillatory (isothermal) KAWs (4.29). Electron finite-Larmor-radius (FLR) effects eventually provide an ultraviolet cutoff at large perpendicular wavenumbers $k_\perp d_e$, though this is outside the range of validity of our drift-kinetic approximation. Note that the transition to ion-scale physics at small perpendicular wavenumbers $k_\perp \rho_i \lesssim 1$ lies outside our adiabatic-ion approximation. The solid black line indicates the location of the maximum growth rate at each fixed $k_\perp$, while the solid dots are the (possible) locations of the energy-containing scale(s) (see Chapter 6). The dotted vertical lines indicate the location in $k_\perp$ of figures 4.2 and 4.3, which show the isothermal and isobaric regimes, respectively.

the finite Larmor radius (FLR) of the electrons to be taken into account; this will introduce some ultraviolet cutoff in perpendicular wavenumbers. At the largest scales, we must eventually encounter ion dynamics, but the effects that this may have are outside the scope of this thesis. All of these modes are, of course, limited by the finite parallel system size $L_{\parallel}$, meaning that the smallest accessible parallel wavenumber is $k_{\parallel} \sim L_{\parallel}^{-1}$.

5.2 Collisional limit

The picture is qualitatively similar in the collisional limit, except the transition between the electrostatic and electromagnetic regimes is modified, as discussed in section 2.3. At electrostatic scales $k_{\perp} \gtrsim d_e^{-1}\chi^{-1}$ [i.e., those below the flux-freezing scale (2.33)], we once again have both the (collisional) sETG and cETG instabilities, whose growth rates become comparable when

$$\left(\frac{k_{\parallel}^2 v_{\text{the}}^2 \omega_{*e}}{\nu_{ei}}\right)^{1/2} \sim (\omega_{de}\omega_{*e})^{1/2} \quad \Rightarrow \quad \frac{k_{\parallel} L_T}{\sqrt{\beta_e}} \sim \left(\frac{L_T}{L_B}\right)^{1/2} (k_y d_e \chi)^{1/2}. \tag{5.5}$$

The sETG instability is now quenched by thermal conduction at [cf. (3.12)]

$$\left(\frac{k_{\parallel}^2 v_{\text{the}}^2 \omega_{*e}}{\nu_{ei}}\right)^{1/2} \sim \kappa k_{\parallel}^2 \quad \Rightarrow \quad \frac{k_{\parallel} L_T}{\sqrt{\beta_e}} \sim (k_y d_e \chi)^{1/2}. \tag{5.6}$$

Note that this is the same line as that corresponding to the maximum of the collisional-sETG growth rate, viz., $(k_{\parallel} v_{\text{the}})^2/\nu_{ei} \sim \omega_{*e}$. As in the collisionless case, this is, of course, only true asymptotically: see figure 5.4(a),(d).

For $k_{\perp *} \lesssim k_{\perp} \lesssim d_e^{-1}\chi^{-1}$, the dominant instability is once again the isobaric sTAI, separated from cETG by $k_{\parallel} = k_{\parallel c}$. As in the collisionless limit, the cETG instability in this perpendicular-wavenumber range, and for $k_{\parallel} \lesssim k_{\parallel c}$, can also be thought of as either the isobaric version of cTAI or the electron version of KBM (see section 4.4). The isobaric sTAI instability is stabilised due to the effects of finite resistivity along the line [cf. (4.62)]

$$\kappa k_{\parallel}^2 \sim (k_{\perp} d_e)^2 \nu_{ei} \quad \Rightarrow \quad \frac{k_{\parallel} L_T}{\sqrt{\beta_e}} \sim k_{\perp} d_e \chi. \tag{5.7}$$

For $k_{\perp} \lesssim k_{\perp *}$, the cETG (or isobaric cTAI) instability is superseded by the isothermal cTAI, which is once again the dominant instability, and is separated from the

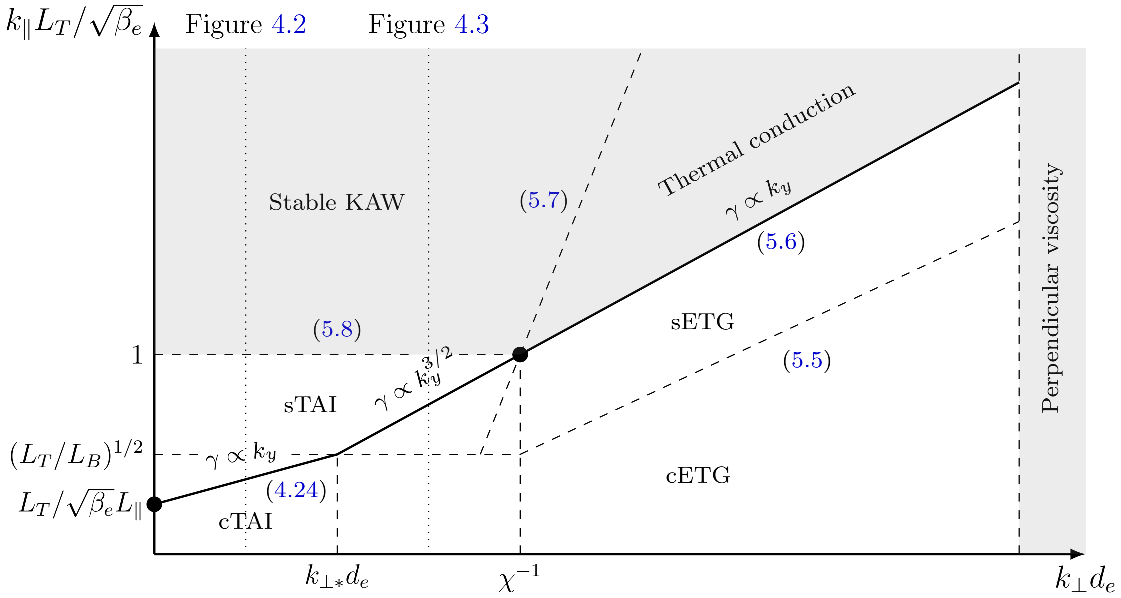

Figure 5.2: Collisional modes in the $(k_\perp, k_\parallel)$ plane, where the axes are plotted on logarithmic scales. The dotted lines are the asymptotic boundaries between the various modes, with the shaded regions indicating stability; these are plotted more quantitatively in figure 5.4(a). At electrostatic scales (i.e., those below the flux-freezing scale, $k_\perp d_e \chi > 1$), the curvature-mediated ETG [cETG, (3.15)] transitions into the (collisional) slab ETG [sETG, (3.10)] along the boundary (5.5). sETG is damped by parallel heat conduction above (5.6). At electromagnetic scales (i.e., those above the flux-freezing scale, $k_\perp d_e \chi < 1$), the slab TAI [sTAI, (4.50)] is stabilised by the effects of finite resistivity along (5.7), while cETG transitions into the curvature-mediated TAI [cTAI, (4.15)] at $k_\perp = k_{\perp *}$, with $k_{\perp *}$ defined in (4.26). cTAI is separated from sTAI by the horizontal line $k_\parallel = k_{\parallel c}$ [note that $k_{\parallel c} L_T/\sqrt{\beta_e} = (L_T/L_B)^{1/2}$, see (4.21)], while the sTAI is stabilised by compressional heating at the horizontal line given by (5.8), transitioning into purely oscillatory (isothermal) KAWs (4.29). Perpendicular electron viscosity will eventually provide an ultraviolet cutoff for these modes at large perpendicular wavenumbers $k_\perp d_e$, though this is outside the range of validity of our drift-kinetic approximation. As in figure 5.1, the ion-scale range $k_\perp \rho_i \lesssim 1$ is left outside our considerations. The solid black line indicates the location of maximum growth at each fixed $k_\perp$, while the solid dots are (possible) locations of the energy containing scale(s) (see Chapter 6). The dotted vertical lines indicate the location in $k_\perp$ of figures 4.2 and 4.3, which show the isothermal and isobaric regimes, respectively.

isothermal sTAI by $k_\parallel = k_{\parallel c}$. As in the collisionless case, the isothermal sTAI is cut off at large parallel wavenumbers due to the effects of parallel compression [see (4.40)], viz.,

$$\omega_{\mathrm{KAW}} \sim \omega_{*e} \quad \Rightarrow \quad \frac{k_\parallel L_T}{\sqrt{\beta_e}} \sim 1. \tag{5.8}$$

This is all illustrated in figure 5.2, where the solid line again shows the location of the fastest growth for each k_y. As in the collisionless case, modes are stabilised at large perpendicular numbers, this time by perpendicular electron viscosity, and limited by the parallel system size for small parallel wavenumbers. However, they are now also limited at large parallel wavenumbers by the mean free path λ_{ei}, at which the collisional approximation breaks down, to be replaced by the collisionless one. This means that the maximum parallel wavenumber allowed in this collisional limit is $k_\parallel \sim \lambda_{ei}^{-1}$.

All of the boundaries between modes derived in this chapter are, of course, only asymptotic illustrations, and do not quantitatively reproduce, for example, the exact stability boundaries in wavenumber space (which are derived in appendices D and E of [1]). However, given that the arguments of the following chapter rely on scaling estimates, rather than quantitative relationships between parameters, the illustrations of the layout of wavenumber space provided by figures 5.1 and 5.2 will be sufficient for our purposes. For the sake of completeness, we have also included plots of the growth-rates in the collisionless and collisional limits that were generated by numerically solving the complete dispersion relations in each of these limits, given by (D23) and (E15) in [1], respectively. These are shown in figures 5.3 and 5.4, respectively, and are valid at all wavenumbers shown for the chosen parameters. In particular, we would like to draw the reader's attention to the similarity between figures 5.3(a) or 5.4(a) and figures 5.1 or 5.2, in that the former reproduce all of the key features of the latter that were predicted using the naïve estimates of this chapter.

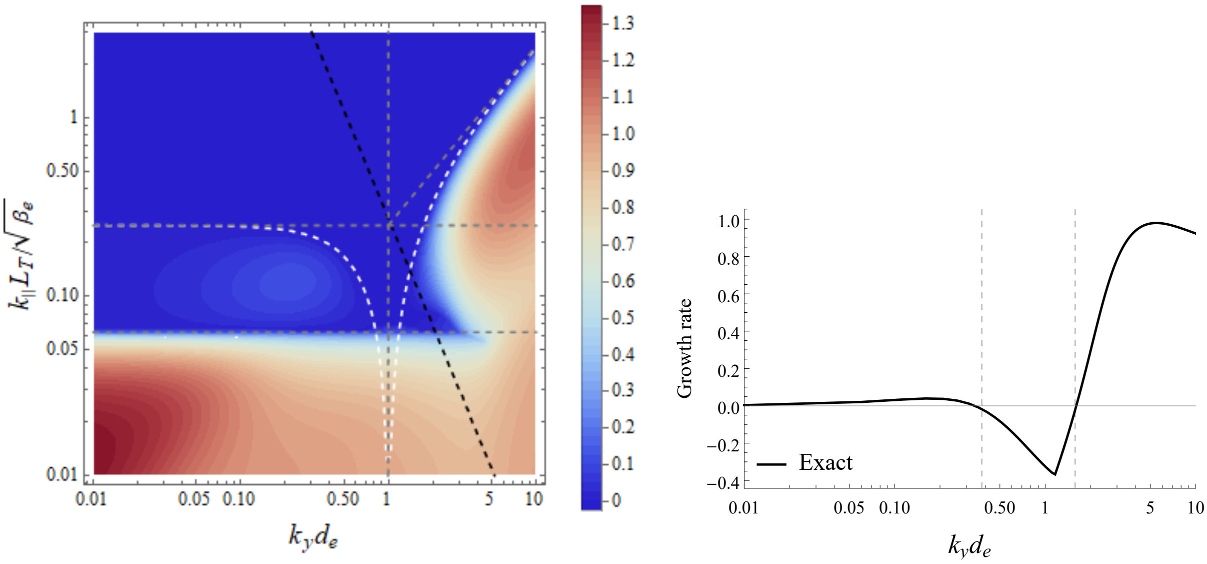

(a) $L_B/L_T = 250$, $k_x d_e = 0$

(b) $k_\parallel L_T/\sqrt{\beta_e} = 0.2$

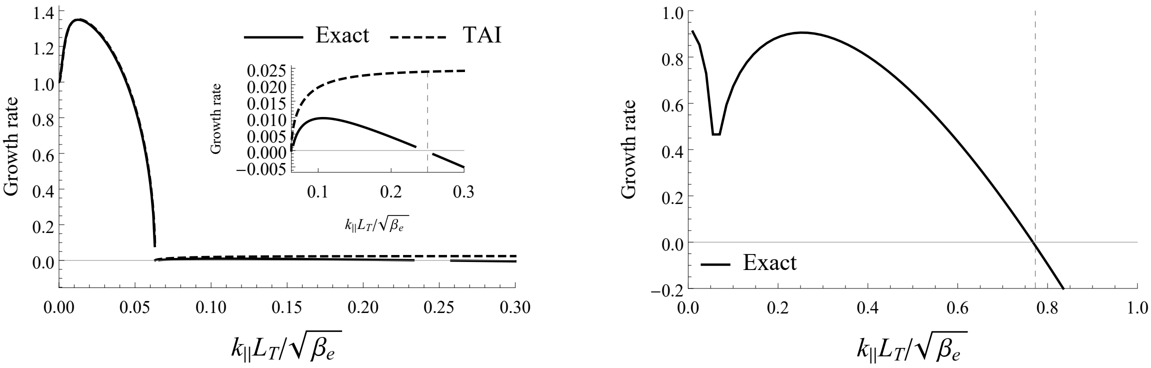

(c) $k_y d_e = 0.01$

(d) $k_y d_e = 3.5$

Figure 5.3: The growth rates of the collisionless instabilities normalised to the cETG growth rate (3.15), and with $\bar{\tau} = 1$. We chose a large value of L_B/L_T in order to show the asymptotic regimes clearly. Panel (a) is a contour plot of the positive growth rates ($\gamma > 0$) in the $(k_y, k_\parallel)$ plane. The white dashed line is the exact stability boundary derived in [1], while the upper and lower horizontal lines are, respectively, (4.42) (corresponding to the stabilisation of the isothermal sTAI at large parallel wavenumbers) and $k_\parallel = k_{\parallel c}$, as defined in (4.21). The vertical grey dashed line is (4.63), around which the isobaric sTAI is stabilised; the slanted grey dashed line on the right is the sETG stability boundary (3.7); the slanted black dashed line is the 'fluid' sETG stability boundary (5.3). Panel (b) is a cut of the growth rate along $k_\parallel L_T/\sqrt{\beta_e} = 0.2$ (plotted against a logarithmic scale), in which the vertical grey dashed lines correspond to the two branches of the exact stability boundary, between which the growth rate is negative. Panels (c) and (d) are cuts of the growth rate for $k_y d_e = 0.1$ and $k_y d_e = 3.5$, respectively. The inset in panel (c) shows the growth rate for $k_\parallel > k_{\parallel c}$; the vertical grey dashed line is (4.42), while the same line in panel (d) is (3.7). The dashed curve in panel (c) is the growth rate predicted by the approximate TAI dispersion relation (4.18). The small discontinuity in the growth rate to the left of $k_\parallel = k_{\parallel c}$ in panel (c) is due to the difficulty of resolving such a rapid change in the growth rate over a small range of $k_\parallel$ on a finite grid. We draw the reader's attention to the enhancement of the cETG growth rate by the cTAI mechanism that can be seen from the red contours in the bottom left-hand corner of panel (a).

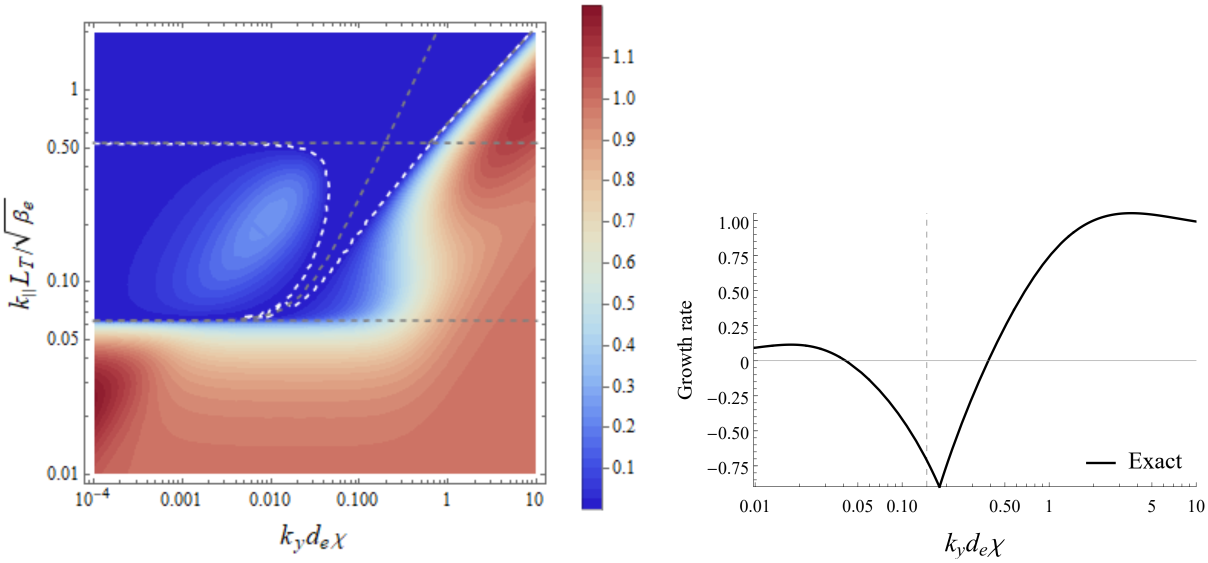

(a) $L_B/L_T = 250$, $k_x d_e \chi = 0$

(b) $k_{\|}L_T/\sqrt{\beta_e} = 0.4$

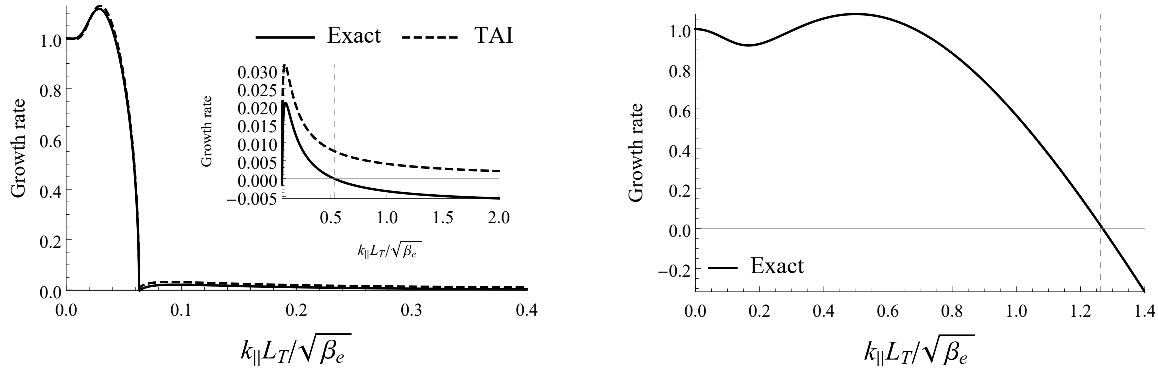

(c) $k_y d_e \chi = 0.0002$

(d) $k_y d_e \chi = 3.5$

Figure 5.4: The growth rates of the collisional instabilities normalised to the cETG growth rate (3.15), and with $\bar{\tau} = 1$. We chose a large value of L_B/L_T in order to show the asymptotic regimes clearly. Panel (a) is a contour plot of the positive growth rates ($\gamma > 0$) in the $(k_y, k_{\|})$ plane. The white dashed line is the exact stability boundary derived in [1], while the upper and lower horizontal lines are, respectively, (4.41) (corresponding to the stabilisation of the isothermal sTAI at large parallel wavenumbers) and $k_{\|} = k_{\|c}$, as defined in (4.21). The slanted grey dashed line on the left is (4.62), around which the isobaric sTAI is briefly stabilised; the slanted grey dashed line on the right is the electrostatic stability boundary (3.12). Panel (b) is a cut of the growth rate along $k_{\|}L_T/\sqrt{\beta_e} = 0.4$ (plotted against a logarithmic scale), in which the vertical grey dashed line is (4.62). Panels (c) and (d) are cuts of the growth rate for $k_y d_e \chi = 0.001$ and $k_y d_e \chi = 3.5$, respectively. The inset in panel (c) shows the growth rate for $k_{\|} > k_{\|c}$; the vertical grey dashed line is (4.42), while the same line in panel (d) is (3.12). The dashed curve in panel (c) is the growth rate predicted by the approximate TAI dispersion relation (4.18). We draw the reader's attention to the enhancement of the cETG growth rate by the cTAI mechanism that can be seen from the red contours in the bottom left-hand corner of panel (a).

Part II

Turbulence and transport

Chapter 6

Free-energy cascades

The last two chapters were devoted to fully characterising the electrostatic ("ETG-like") and electromagnetic ("TAI-like") instabilities that exist on sub-ion-Larmor scales within our system of low-beta equations. In this chapter, we present an *a priori* turbulent-cascade theory for the free energy injected by these instabilities, which will then be numerically tested in chapters 7 and 8.

6.1 Free energy

Magnetised plasma systems containing small perturbations around a Maxwellian equilibrium nonlinearly conserve free energy, which is a quadratic norm of the magnetic perturbations and the perturbations of the distribution functions of both ions and electrons away from the Maxwellian. In the system that we are considering, the (normalised) free energy takes the form [1]

$$\frac{W}{n_{0e}T_{0e}} = \int \frac{\mathrm{d}^3\boldsymbol{r}}{V} \left(\frac{\varphi \bar{\tau}^{-1}\varphi}{2} + |d_e \boldsymbol{\nabla}_\perp \mathcal{A}|^2 + \frac{1}{2}\frac{\delta n_e^2}{n_{0e}^2} + \frac{u_{\parallel e}^2}{v_{\mathrm{th}e}^2} + \frac{1}{4}\frac{\delta T_{\parallel e}^2}{T_{0e}^2} + \frac{1}{2}\frac{\delta T_{\perp e}^2}{T_{0e}^2} + \dots \right). \tag{6.1}$$

The '. . . ' stand for the squares of further moments of the perturbed distribution function (such as the parallel and perpendicular heat fluxes $\delta q_{\parallel e}, \delta q_{\perp e}$, etc.). In the collisional limit, these further moments of the perturbed distribution function are negligible, and (6.1) becomes

$$\frac{W}{n_{0e}T_{0e}} = \int \frac{\mathrm{d}^3\boldsymbol{r}}{V} \left(\frac{\varphi \bar{\tau}^{-1}\varphi}{2} + |d_e \boldsymbol{\nabla}_\perp \mathcal{A}|^2 + \frac{1}{2}\frac{\delta n_e^2}{n_{0e}^2} + \frac{3}{4}\frac{\delta T_e^2}{T_{0e}^2} \right). \tag{6.2}$$

The free energy is a nonlinear invariant, i.e., it is conserved by nonlinear interactions [55], but can be injected into the system by equilibrium gradients, and is dissipated by collisions; even when these are small, they are always eventually accessed via phase-mixing of the distribution function towards small velocity scales and nonlinear interactions towards small spatial scales.

In view of this, the time-evolution of the free energy (6.1) can be written as [1]

$$\frac{1}{n_{0e}T_{0e}}\frac{\mathrm{d}W}{\mathrm{d}t} = \varepsilon - D, \tag{6.3}$$

where D stands for the collisional dissipation, and ε is the injection rate due, in our system, to the electron-temperature gradient:

$$\varepsilon = \frac{1}{L_T}\int\frac{\mathrm{d}^3\boldsymbol{r}}{V}\begin{cases}\left(\frac{1}{2}\frac{\delta T_{\parallel e}}{T_{0e}} + \frac{\delta T_{\perp e}}{T_{0e}}\right)v_{Ex} + \frac{\frac{1}{2}\delta q_{\parallel e} + \delta q_{\perp e}}{n_{0e}T_{0e}}\frac{\delta B_x}{B_0}, & \text{collisionless,}\\ \frac{3}{2}\frac{\delta T_e}{T_{0e}}v_{Ex} + \frac{\delta q_e}{n_{0e}T_{0e}}\frac{\delta B_x}{B_0}, & \text{collisional,}\end{cases} \tag{6.4}$$

where

$$v_{Ex} = -\frac{\rho_e v_{\mathrm{th}e}}{2}\frac{\partial\varphi}{\partial y}, \quad \frac{\delta B_x}{B_0} = \rho_e\frac{\partial\mathcal{A}}{\partial y}, \quad \frac{\delta q_e}{n_{0e}T_{0e}} = -\frac{3}{2}\kappa\nabla_\parallel\log T_e. \tag{6.5}$$

The expression multiplying $1/L_T$ is the 'turbulent' heat flux due to the energy transport by the $\boldsymbol{E}\times\boldsymbol{B}$ flows and to the heat fluxes along the perturbed field lines. The first term in (6.4) is the energy injection by ETG (Chapter 3), and the second is by TAI (Chapter 4). Evidently, the latter is only present in the electromagnetic regime, when perturbations of the magnetic-field direction are allowed. In the absence of dissipation ($D = 0$), (6.3) expresses overall entropy conservation for the plasma: the entropy of the fluctuations on the left-hand side is balanced by the entropy generated by the turbulent transport of equilibrium quantities on the right-hand side.

Free energy is normally the quantity whose cascade from large (injection) to small (dissipation) scales determines the properties of a plasma's turbulent state (see [72, 81], and references therein). Temperature-gradient-driven turbulence is no exception [12], and so we devote the remainder of this chapter to working out at what scales and to what saturated amplitudes the ETG-TAI injection (6.4) will drive turbulent fluctuations. Note that we will henceforth assume that all of the nonlinear dynamics is local, in that we will ignore any possible cross-scale interactions between turbulence driven by the ETG and TAI.

6.2 Electrostatic turbulence

6.2.1 Collisionless slab ETG turbulence

Following [12], we shall conjecture that our fully developed electrostatic turbulence always organises itself into a state wherein there is a local cascade of the free energy (6.1) that carries the injected power ε from the outer scale, through some putative 'inertial range', to the dissipation scale. The outer scale is something that we will have to determine, while the dissipation scale will be near $k_\perp \rho_e \sim 1$, and so outside the range of validity of our drift-kinetic approximation.

The perpendicular nonlinearity in our equations is the advection of fluctuations by the fluctuating $\boldsymbol{E} \times \boldsymbol{B}$ flows. Therefore, we take the nonlinear turnover time associated with such a cascade to be the nonlinear $\boldsymbol{E} \times \boldsymbol{B}$ advection rate:

$$t_{\mathrm{nl}}^{-1} \sim k_\perp v_E \sim \rho_e v_{\mathrm{the}} k_\perp^2 \bar{\varphi} \sim \Omega_e (k_\perp \rho_e)^2 \bar{\varphi}. \tag{6.6}$$

Here and in what follows, $\bar{\varphi}$ refers to the characteristic amplitude of the electrostatic potential at the scale $k_\perp^{-1}$, rather than to the Fourier transform of the field. More formally, we shall take $\bar{\varphi}$ to be defined by

$$\bar{\varphi}^2 = \int_{k_\perp}^{\infty} \mathrm{d}k'_\perp \, E_\perp^{\varphi}(k'_\perp), \quad E_\perp^{\varphi}(k_\perp) \equiv 2\pi k_\perp \int_{-\infty}^{\infty} \mathrm{d}k_\parallel \left\langle |\varphi_{\boldsymbol{k}}|^2 \right\rangle, \tag{6.7}$$

where $E_\perp^{\varphi}(k_\perp)$ is the 1D perpendicular energy spectrum, $\varphi_{\boldsymbol{k}}$ the spatial Fourier transform of the potential, and the angle brackets denote an ensemble average. Perturbations of other quantities, such as the velocity, parallel temperature, magnetic field, etc., will similarly be taken to refer to their characteristic amplitude at a given perpendicular scale.

Assuming that any possible anisotropy in the perpendicular plane can be neglected[1], a Kolmogorov-style constant-flux argument leads to the scaling of the amplitudes in the inertial range:

$$\frac{\bar{\tau}^{-1} \bar{\varphi}^2}{t_{\mathrm{nl}}} \sim \varepsilon = \mathrm{const} \quad \Rightarrow \quad \bar{\varphi} \sim \left(\frac{\varepsilon}{\Omega_e} \right)^{1/3} (k_\perp \rho_e)^{-2/3}. \tag{6.8}$$

---

[1] The existence of such a state is not always guaranteed: e.g., [82] found that the saturated state of electrostatic ETG turbulence existed in a zonally-dominated state, which evidently violates this assumption. In fact, the zonal state is much closer to being 2D isotropic than a streamer-dominated state; [12] explicitly invoked zonal flows to enforce isotropy. We shall find in Section 7.2.1, however, that the assumption of isotropy in the inertial range is indeed well-satisfied.

The scaling (6.8) translates into the following 1D spectrum:

$$E_\perp^\varphi(k_\perp) \sim \frac{\bar{\varphi}^2}{k_\perp} \propto k_\perp^{-7/3}, \tag{6.9}$$

the same as was obtained, using a similar argument, and confirmed numerically, by [12] for electrostatic, gyrokinetic ITG turbulence. In making this argument, we have assumed that the free-energy density at a given scale $k_\perp^{-1}$ can be adequately represented by the first term in the integrand of (6.1), i.e., that all the other fields whose squares contribute to the free energy are either small or comparable to φ, but never dominant in comparison with it. Whether this is true will depend on the nature of the turbulent fluctuations supported by the system in any given part of the $(k_\perp, k_\parallel)$ space through which the cascade might be taking free energy on its journey towards dissipation. Let us specialise to the region of the wavenumber space (marked 'sETG' in figure 5.1) where the fluctuations are collisionless, electrostatic drift waves described by (3.4). From the first two equations of (3.4),[2]

$$\bar{\tau}^{-1}\bar{\varphi} \sim \frac{k_\parallel v_{\text{the}}}{\omega}\frac{\bar{u}_{\parallel e}}{v_{\text{the}}} \sim \left(\frac{k_\parallel v_{\text{the}}}{\omega}\right)^2 \frac{\delta \bar{T}_{\parallel e}}{T_{0e}}, \tag{6.10}$$

where evidently we ought to estimate $\omega \sim t_{\text{nl}}^{-1}$. Then, all three fluctuating fields do indeed have the same size and the same scaling if we posit

$$t_{\text{nl}}^{-1} \sim k_\parallel v_{\text{the}}. \tag{6.11}$$

This is a statement of *critical balance*, whereby the characteristic time associated with propagation along the field lines is assumed comparable to the nonlinear advection rate t_{nl}^{-1} at each perpendicular scale $k_\perp^{-1}$ — [12] justified this by the standard causality argument borrowed from MHD turbulence [83–86]: two points along the field line can only remain correlated with one another if information can propagate between them faster than they are decorrelated by the nonlinearity. We have taken the rate of information propagation along the field lines to be $k_\parallel v_{\text{the}}$; it is not immediately obvious that this should work given that $k_\parallel v_{\text{the}}$ is the rate of phase mixing (which, in the linear theory, is expected to give rise to Landau damping) rather than of wave propagation,

---

[2] The linear part of the third equation in (3.4) tells us that $\delta \bar{T}_{\parallel e}/T_{0e} \sim (\omega_{*e}/\omega)\bar{\varphi}$ but, as we are about to discover, this is only true at the outer scale, while in the inertial range, the ETG injection term is subdominant.

and why Landau damping is ineffective in the nonlinear state [87, 88]. We shall revisit the role of dissipation in critically-balanced turbulence in Section 7.2.4.

Combining (6.6), (6.8) and (6.11), we find

$$k_\parallel v_{\rm the} \sim t_{\rm nl}^{-1} \sim \Omega_e \left(\frac{\varepsilon}{\Omega_e}\right)^{1/3} (k_\perp \rho_e)^{4/3}. \tag{6.12}$$

By comparison, for the most unstable sETG modes, (3.6) gives us

$$k_\parallel v_{\rm the} \sim \omega_{*e} \sim k_y \rho_e \frac{v_{\rm the}}{L_T}. \tag{6.13}$$

These modes grow at a rate $\omega_{*e} \propto k_y$. This means that the nonlinear interactions must overwhelm the linear instability in the inertial range.[3] The outer scale, i.e., the scale that limits the inertial range on the infrared side and at which the free energy is effectively injected, is then the scale at which the nonlinear cascade rate and the rate of maximum growth of the instability are comparable: balancing (6.12) and (6.13), we get

$$\Omega_e (k_\perp^o \rho_e)^2 \bar{\varphi}^o \sim k_\parallel^o v_{\rm the} \sim \omega_{*e}^o \quad \Rightarrow \quad \bar{\varphi}^o \sim (k_\perp^o L_T)^{-1}, \quad k_y^o \rho_e \sim k_\parallel^o L_T, \tag{6.14}$$

where the superscript 'o' refers to quantities at the outer scale.

Now, in order to determine $k_\perp^o$, we need a further constraint. [12] found it by conjecturing that $k_\parallel^o$ in (6.14) would be set by the parallel system size $L_\parallel$ (the connection length $\sim \pi q L_B$, in the case of tokamaks). This was the only reasonable choice because there was no lower cutoff in $k_\perp$ of the (electrostatic) ITG-unstable modes. This is not, however, the case in our model of the sETG instability, which is stabilised at the flux-freezing scale (2.31), i.e., at $k_\perp d_e \sim 1$. It appears to be a general rule, confirmed by numerical simulations [89], that the outer scale is, in fact, determined by the smallest possible $k_y \rho_e$ or the smallest possible $k_\parallel L_T$, whichever is larger. Putting this within the visual context of figure 5.1, the outer scale is set either by $k_\parallel^o \sim L_\parallel^{-1}$ or by $k_\perp^o \sim d_e^{-1}$, whichever is encountered first when moving along the solid black line from the

---

[3] Here is another way to see this. Imagine that the sETG instability dominates energy injection at each scale and that the energy thus injected is removed to the next smaller scale by the nonlinearity, at a rate $t_{\rm nl}^{-1}$. Such a scheme would be consistent if the energy flux injected at each scale by the instability were larger than the flux arriving to this scale from larger scales. Let us see if this is possible. Balancing the nonlinear energy-removal rate (6.12) with the injection rate ω_{*e}, we learn that $\bar{\varphi} \sim (k_\perp L_T)^{-1}$ (corresponding to a 1D spectrum $\propto k_\perp^{-3}$). The injected energy flux is then $\varepsilon \sim \omega_{*e} \bar{\varphi}^2 \sim \Omega_e (\rho_e/L_T)^3 (k_\perp \rho_e)^{-1}$. So it declines at smaller scales, and is easily overwhelmed by the nonlinear transfer from larger scales.

ultraviolet cutoff towards larger scales. The former possibility, $k_\parallel^o \sim L_\parallel^{-1}$, is realised when $L_\parallel \ll L_T/\sqrt{\beta_e}$, and the latter, $k_\perp^o \sim d_e^{-1}$, otherwise. Thus,

$$k_\perp^o d_e \sim \frac{k_\parallel^o L_T}{\sqrt{\beta_e}} \sim \begin{cases} \dfrac{L_T}{L_\parallel\sqrt{\beta_e}}, & \dfrac{L_\parallel\sqrt{\beta_e}}{L_T} \ll 1, \\ 1. & \dfrac{L_\parallel\sqrt{\beta_e}}{L_T} \gtrsim 1. \end{cases} \tag{6.15}$$

Let us now estimate the energy flux that is injected by sETG at the outer scale (6.15): considering the first term in the expression for the energy flux (6.4) (the second, involving finite perturbations to the magnetic field, is negligible in the electrostatic regime) and ignoring any possibility of a non-order-unity contribution from phase factors, we have

$$\varepsilon \sim \omega_{*e}^o \bar{\varphi}^o \frac{\delta \bar{T}_{\parallel e}^o}{T_{0e}} \sim \frac{v_{\mathrm{th}e}\rho_e^2}{L_T^3\sqrt{\beta_e}}(k_\perp^o d_e)^{-1}, \tag{6.16}$$

where we have used $\delta \bar{T}_{\parallel e}^o/T_{0e} \sim \bar{\varphi}^o$ and (6.14). This quantity is directly related to the turbulent heat flux: combining (6.16) with (6.15), we get

$$Q^{\mathrm{sETG}} \sim n_{0e}T_{0e}\varepsilon L_T \sim Q_{\mathrm{gB}} \begin{cases} \dfrac{L_\parallel}{L_T}, & \dfrac{L_\parallel\sqrt{\beta_e}}{L_T} \ll 1, \\ \dfrac{1}{\sqrt{\beta_e}}, & \dfrac{L_\parallel\sqrt{\beta_e}}{L_T} \gtrsim 1, \end{cases} \tag{6.17}$$

where the 'gyro-Bohm' flux is $Q_{\mathrm{gB}} = n_{0e}T_{0e}v_{\mathrm{th}e}\left(\rho_e/L_T\right)^2$. Note that the temperature-gradient scaling in (6.17) is only valid for sufficiently large $L_\parallel/L_T$ as our analysis ignores any finite critical temperature gradients associated with the sETG instability. The first expression in (6.17) is the same scaling as that obtained by [12], but this time for electrostatic turbulence driven by an electron temperature gradient[4]. In the formal limit of $\beta_e \to 0$, this is the only possible outcome because the second inequality in (6.17) can never be satisfied. At finite β_e, however, in the sense in which it is allowed by our ordering and for sufficiently large temperature gradients, we obtain a different, less steep scaling of the turbulent heat flux, given by the second expression in (6.17).

Whether the scaling (6.17) is relevant in our system depends on the dominant energy injection therein being from the electrostatic sETG drive at $k_\perp d_e \gtrsim 1$. That is,

---

[4] [90] found such a scaling of the heat flux with L_B/L_T in their investigations of nonlinear pedestal turbulence driven by ETG modes [see their equation (1), and the following discussion] suggesting, perhaps, that this scaling may hold in more realistic — and complex — plasma systems than that considered here.

in fact, far from guaranteed if $L_\parallel > L_T/\sqrt{\beta_e}$, i.e., if sufficiently small $k_\parallel$ are allowed for the electromagnetic instabilities to matter — and so for the outer scale to be located at even larger scales along the thick black line in figure 5.1. Another reason why we must consider the electromagnetic part of the wavenumber space is to do with the cETG instability. At $k_\perp d_e \gtrsim 1$, its growth rate is always small in comparison with the with sETG [for the large L_B/L_T that we are considering here, see (3.16)], but it is a 2D mode, so it is not stabilised at $k_\perp d_e \sim 1$ (it does not bend magnetic fields) and there is no reason to assume that it cannot provide the dominant energy injection at some large scale $k_\perp d_e \ll 1$. There, it competes with TAI (Chapter 4), so we shall have to examine the TAI turbulence alongside the cETG one, as in Section 6.3.

6.2.2 Collisional slab ETG turbulence

For collisional sETG turbulence, the argument proceeds similarly to section 6.2.1. Instead of (6.10), we now have, in view of (3.9),

$$\bar{\tau}^{-1}\bar{\varphi} \sim \frac{k_\parallel v_{\text{the}}}{\omega}\frac{\bar{u}_{\parallel e}}{v_{\text{the}}} \sim \frac{(k_\parallel v_{\text{the}})^2}{\omega\nu_{ei}}\frac{\delta\bar{T}_e}{T_{0e}} \sim \frac{\delta\bar{T}_e}{T_{0e}}, \tag{6.18}$$

where we assume that all frequencies, including the nonlinear rate (6.6), are now comparable to the rate of parallel thermal conduction [instead of the parallel streaming rate; see (3.11)]:

$$t_{\text{nl}}^{-1} \sim \omega \sim \frac{(k_\parallel v_{\text{the}})^2}{\nu_{ei}}. \tag{6.19}$$

This condition now replaces (6.11) as the 'critical-balance' conjecture, whereby the parallel scale of the perturbations is determined in terms of their perpendicular scale. Note that, since now $\bar{u}_{\parallel e}/v_{\text{the}} \ll \bar{\varphi}$, it is still reasonable to estimate the free-energy density by $\sim \bar{\tau}^{-1}\bar{\varphi}^2$.

At the outer scale, using (3.11) and (6.19), we find, analogously to (6.14),

$$\Omega_e(k_\perp^o\rho_e)^2\bar{\varphi}^o \sim \frac{(k_\parallel^o v_{\text{the}})^2}{\nu_{ei}} \sim \omega_{*e} \quad \Rightarrow \quad \bar{\varphi}^o \sim (k_\perp^o L_T)^{-1}, \quad k_y^o\rho_e \sim (k_\parallel^o)^2 L_T\lambda_{ei}. \tag{6.20}$$

Note that the relationship between the parallel and perpendicular outer scales can be recast as

$$\frac{k_\parallel^o L_T}{\sqrt{\beta_e}} \sim \left(k_y^o d_e\chi\right)^{1/2}, \quad \chi \equiv \frac{L_T}{\lambda_{ei}\sqrt{\beta_e}} \tag{6.21}$$

where χ is defined as in (2.33).

By analogous logic to the collisionless sETG case, the outer scale can be set either by the parallel system size or by the flux-freezing scale (2.33), $k_\perp d_e \chi \sim 1$, depending on which is encountered first by the thick black line in figure 5.2 when descending towards larger scales. The result is

$$k_\perp^o d_e \chi \sim \begin{cases} \left(\dfrac{L_T}{L_\parallel \sqrt{\beta_e}} \right)^2, & \dfrac{L_\parallel \sqrt{\beta_e}}{L_T} \ll 1, \\ 1, & \dfrac{L_\parallel \sqrt{\beta_e}}{L_T} \gtrsim 1. \end{cases} \tag{6.22}$$

In view of (6.20), the energy flux is again given by (6.16), which, with the substitution of (6.22), becomes

$$\varepsilon \sim \frac{v_{\text{th}e} \rho_e^2}{L_T^3 \sqrt{\beta_e}} \chi \begin{cases} \left(\dfrac{L_\parallel \sqrt{\beta_e}}{L_T} \right)^2, & \dfrac{L_\parallel \sqrt{\beta_e}}{L_T} \ll 1, \\ 1, & \dfrac{L_\parallel \sqrt{\beta_e}}{L_T} \gtrsim 1. \end{cases} \tag{6.23}$$

Therefore, finally, the turbulent heat flux is

$$Q_\nu^{\text{sETG}} \sim Q_{\text{gB}} \begin{cases} \dfrac{\chi}{\sqrt{\beta_e}} \left(\dfrac{L_\parallel \sqrt{\beta_e}}{L_T} \right)^2, & \dfrac{L_\parallel \sqrt{\beta_e}}{L_T} \ll 1, \\ \dfrac{\chi}{\sqrt{\beta_e}}, & \dfrac{L_\parallel \sqrt{\beta_e}}{L_T} \gtrsim 1. \end{cases} \tag{6.24}$$

These are the collisional analogues of the scalings (6.17), and are both proportional to the electron collision frequency ($\propto \lambda_{ei}^{-1}$). Such a scaling of turbulent heat flux with collisionality was identified by [82] from their simulations of electrostatic ETG turbulence, though their argument relied on consideration of the dynamics of zonal flows within their electron-scale system, and so the comparison is superficial.

6.3 Electromagnetic turbulence

6.3.1 KAW-dominated, slab TAI turbulence

On the large-scale side of the flux-freezing scales (2.31) and (2.33), for $k_{\perp *} \lesssim k_\perp \lesssim d_e^{-1}$ (or $d_e^{-1}\chi^{-1}$ in the collisional limit), the dominant instability is the isobaric sTAI (see section 4.4), an instability of kinetic Alfvén waves. KAW turbulence has been studied quite extensively, both numerically [91–99] and observationally [100–102], in the context of the ‘kinetic-range’ free-energy cascade in the solar wind [72, 76, 78]. The theory of this cascade proceeds along the same lines as the theory of any critically balanced cascade in a wave-supporting anisotropic medium [86] and leads again to a $k_\perp^{-7/3}$ energy spectrum [72, 91] or, with some modifications, to a $k_\perp^{-8/3}$ one [94, 95], which appears to be closer to what is observed.

Ignoring the latter nuance, it is easy to see that the re-emergence of the $k_\perp^{-7/3}$ spectrum is unsurprising, as the arguments of section 6.2 that led to (6.8) and (6.9) are unchanged for KAWs. What is changed, however, is the linear propagation rate that must be used in the critical-balance conjecture: the parallel scale $k_\parallel^{-1}$ of a perturbation is now the distance that an (isobaric) KAW can travel in one nonlinear time, so, from (4.49), we have, instead of (6.11) or (6.19),

$$\omega_{\mathrm{KAW}} \sim k_\parallel v_{\mathrm{th}e} k_\perp d_e \sim t_{\mathrm{nl}}^{-1}, \tag{6.25}$$

where t_{nl} is still given by (6.6)[5]. Note that here, and in what follows, $k_\parallel$ is now taken with respect to the total magnetic-field direction $\boldsymbol{b} = \boldsymbol{b}_0 + \delta\boldsymbol{B}_\perp/B_0$, rather than simply with respect to the equilibrium magnetic-field direction $\boldsymbol{b}_0$.

This is the standard argument of KAW-turbulence theory (see references above), which, however, was developed for situations in which energy arrived to sub-Larmor scales from larger scales (i.e., from $k_\perp\rho_i < 1$) and cascaded down to smaller scales — as indeed it typically does in space-physical and astrophysical contexts. In contrast, here we are dealing with an energy source in the form of an ETG-driven instability, the isobaric sTAI, which operates most vigorously at the smallest electromagnetic scales. Indeed, as we saw at the end of section 4.4.1, for a given $k_\perp d_e$, the sTAI growth rate peaks at $\xi_* \sim 1$, and is of the order of the KAW frequency ω_{KAW} at that scale. This gives

$$\gamma \sim \omega_{\mathrm{KAW}} \sim \begin{cases} \omega_{*e} k_\perp d_e \sim \dfrac{v_{\mathrm{th}e}}{L_T\sqrt{\beta_e}}(k_\perp\rho_e)^2, & \text{collisionless,} \\ \sqrt{\omega_{*e}\nu_e}\, k_\perp d_e \sim \dfrac{v_{\mathrm{th}e}}{\sqrt{L_T\lambda_{ei}\beta_e}}\,(k_\perp\rho_e)^{3/2}, & \text{collisional,} \end{cases} \tag{6.26}$$

---

[5] This t_{nl} is the nonlinear time associated with the fluctuating $\boldsymbol{E}\times\boldsymbol{B}$ flows, coming from the convective time derivative (2.10). In the electromagnetic regime, there is, in addition to this, the nonlinearity associated with the parallel gradients being taken along perturbed magnetic field lines, including finite $\delta\boldsymbol{B}_\perp$, as in (2.11). However, it is straightforward to show [by, e.g., estimating the sizes of the nonlinear terms appearing in (4.14), (4.32) or (4.52)] that the $\boldsymbol{E}\times\boldsymbol{B}$ nonlinearity is either comparable to, or larger than, the $\delta\boldsymbol{B}_\perp$ nonlinearity in all of the regimes of interest, meaning that we may continue to use (6.6) as our estimate for the nonlinear time.

where we used $k_\parallel \sim \omega_{*e}/v_{\rm the}$ and $k_\parallel \sim (\omega_{*e}/\kappa)^{1/2} \sim (\omega_{*e}\nu_e)^{1/2}/v_{\rm the}$ for the collisionless and collisional estimates, respectively. Comparing (6.26) with (6.12), we see that, in both cases, the instability growth rate increases faster with $k_\perp$ than the nonlinear cascade rate $t_{\rm nl}^{-1} \propto k_\perp^{4/3}$. It is intuitively obvious that these two rates reach parity at the flux-freezing scale, $k_\perp d_e \sim 1$ or $k_\perp d_e \chi \sim 1$, in the collisionless and collisional limits, respectively. This can be formally confirmed by a calculation analogous to the one in section 6.2. Thus, the dominant injection occurs at the small-scale end of the putative 'inertial range'. In the absence of any inverse cascade, there is nothing to push the energy towards larger scales. This means that the balances (6.8), (6.12) and (6.25) are not, in fact, realised for KAW turbulence driven by the isobaric sTAI.

In order to predict the power injected by sTAI, and the associated contribution to the turbulent heat flux, we resurrect the argument that, for sETG, we tossed aside in footnote 3. We conjecture that the sTAI instability dominates the energy injection at each scale, and the energy thus injected is removed to the next smaller scale by the nonlinearity, at a rate $t_{\rm nl}^{-1}$; we shall confirm a posteriori that this is a consistent scheme. The resulting balance gives us, using (6.6) and (6.26),

$$t_{\rm nl}^{-1} \sim \Omega_e (k_\perp \rho_e)^2 \bar{\varphi} \sim \gamma \quad \Rightarrow \quad \bar{\varphi} \sim \begin{cases} \dfrac{d_e}{L_T}, & \text{collisionless,} \\ \dfrac{d_e}{\sqrt{L_T \lambda_{ei}}} (k_\perp \rho_e)^{-1/2}, & \text{collisional,} \end{cases} \tag{6.27}$$

and $\delta \bar{B}_\perp / B_0 \sim k_\perp \rho_e \bar{\mathcal{A}} \sim (\rho_e/d_e)\bar{\varphi}$ [where we have used $k_\perp d_e \bar{\mathcal{A}} \sim \bar{\varphi}$, which follows from the first equation in (4.49) with $\omega \sim \omega_{\rm KAW}$]. The corresponding energy spectra (6.7) are $\propto k_\perp^{-1}$ and $\propto k_\perp^{-2}$ in the collisionless and collisional regimes, respectively. The injected power is

$$\gamma \bar{\varphi}^2 \sim \frac{v_{\rm the} \rho_e^2}{L_T^3 \sqrt{\beta_e}} \begin{cases} (k_\perp d_e)^2, & \text{collisionless,} \\ (k_\perp d_e)^{1/2} \chi^{3/2}, & \text{collisional,} \end{cases} \tag{6.28}$$

where χ is defined in (2.33) or (6.21). This means that, at each scale, the energy that arrives from larger scales can be ignored in comparison with the energy injected locally by sTAI — unlike for the sETG cascade, this scale-by-scale injection scheme is consistent for 'sTAI turbulence'.

It is clear from (6.28) that the injected power is dominated by the flux-freezing scale (2.31) or (2.33), where it reaches parity with the power injected by sETG, (6.16) or (6.23), and where also the sTAI approximation breaks down and sETG takes over. Thus, the turbulent heat flux due to the sTAI turbulence is given by the same expression as that for the sETG turbulence at sufficiently large temperature gradients — the second expressions in (6.17) and (6.24). The only effect of sTAI is to equip the sETG turbulence spectrum (6.9) with an electromagnetic tail at long wavelengths — scaling as $k_\perp^{-1}$ and $k_\perp^{-2}$ in the collisionless and collisional cases, respectively — but without changing by more than an order-unity amount its ability to transport energy[6].

6.3.2 Curvature-mediated-TAI turbulence

At $k_\perp \lesssim k_{\perp *}$, the isothermal cTAI replaces the isobaric sTAI as the dominant instability. Since the nonlinear cascading is still done by the $\boldsymbol{E} \times \boldsymbol{B}$ flows, the nonlinear time is still given by (6.6). However, how to work out the 'inertial-range' scalings for this cascade is not obvious: since the real frequency is vanishingly small in comparison to the growth rate at the cTAI maximum [see (4.27)], there is no obvious analogue of the 'critical balance' conjectures (6.11) or (6.25); indeed, it is not even a given that the cascade will be local in wavenumber space. We shall not be deterred by this uncertainty, as we can, in fact, still calculate the injected free-energy flux (6.4) by considering solely the fluctuations at the injection scale; we shall then propose a way of determining what that scale is, and hence calculate the turbulent heat flux.

First, let us assume that the dominant free-energy injection will occur at the wavenumbers (4.24), where the cTAI growth rate is largest, and given by (4.15):

$$\gamma \sim \frac{k_y^o \rho_e v_{\mathrm{th}e}}{\sqrt{L_B L_T}}. \tag{6.29}$$

This is consistent with our prior assumption [see, e.g., (6.14)] that the scale of dominant free-energy injection is determined by the balance between the nonlinear cascade rate and the rate of the maximum growth of the instability. Unlike for the electrostatic modes, the second, 'electromagnetic' term in (6.4) — involving energy transport due

---

[6] This conclusion is based on the (asymptotic) assumption that both sTAI and sETG inject energy around the same outer scale $k_\parallel^o L_T/\sqrt{\beta_e} \sim 1$, $k_\perp^o d_e \sim 1$ (or $\sim \chi^{-1}$ in the collisional limit). However, a more quantitative analysis of the stability properties of the collisionless and collisional systems shows that sTAI is stabilised slightly towards the large-scale side of this assumed outer scale, while sETG is stabilised slightly towards the small-scale side of it (see Section 4.4.2 and Figure 5.3(a) or Figure 5.4). Thus, in principle, it is possible to assess the comparative roles of these two instabilities in a quantitative way (e.g., numerically).

to heat flux along perturbed field lines — must contribute to the energy injection by cTAI. Let us estimate its size at the outer scale. The third equation in (4.14) gives us

$$\frac{\delta\bar{B}_x^o}{B_0} \sim k_y^o \rho_e \bar{\mathcal{A}} \sim k_\parallel^o L_T \frac{\delta\bar{T}_e^o}{T_{0e}}. \tag{6.30}$$

Recalling (2.20), we estimate the size of the perturbed heat flux in the collisional limit from (4.31):

$$\frac{\delta\bar{q}_e^o}{n_{0e}T_{0e}} \sim \kappa\nabla_\parallel \log\bar{T}_e^o \sim \kappa\xi_*^o k_\parallel^o \frac{\delta\bar{n}_e^o}{n_{0e}} \sim \frac{\omega_{*e}^o}{k_\parallel^o}\bar{\varphi}^o. \tag{6.31}$$

Analogously, in the collisionless limit, we find that (see appendix D of [1])

$$\frac{\delta\bar{q}_{\parallel e}^o}{n_{0e}T_{0e}} \sim \frac{\delta\bar{q}_{\perp e}^o}{n_{0e}T_{0e}} \sim \xi_*^o \frac{\delta\bar{n}_e^o}{n_{0e}} \sim \frac{\omega_{*e}^o}{k_\parallel^o}\bar{\varphi}^o. \tag{6.32}$$

Thus, in both limits, the electromagnetic contribution to the free-energy injection can be written, at the outer scale, as

$$\varepsilon \sim \frac{1}{L_T}\frac{\delta\bar{q}_e^o}{n_{0e}T_{0e}}\frac{\delta\bar{B}_x^o}{B_0} \sim \omega_{*e}^o\bar{\varphi}^o\frac{\delta\bar{T}_e^o}{T_{0e}}, \tag{6.33}$$

meaning that it is comparable to the first term in (6.4), the electrostatic contribution due to energy transport by the $\boldsymbol{E}\times\boldsymbol{B}$ flow.

The potential at the outer scale can once again be estimated from the balance of the nonlinear time (6.6) with the growth rate (6.29):

$$\rho_e v_{\text{the}}(k_\perp^o)^2\bar{\varphi} \sim \gamma \quad \Rightarrow \quad \bar{\varphi}^o \sim \frac{1}{k_\perp^o\sqrt{L_B L_T}}, \tag{6.34}$$

while the temperature perturbations can be related to φ^o via the first equation in (4.14):

$$\frac{\delta\bar{T}_e^o}{T_{0e}} \sim \frac{\gamma}{\omega_{de}^o}\frac{\delta\bar{n}_e^o}{n_{0e}} \sim \left(\frac{L_B}{L_T}\right)^{1/2}\bar{\varphi}^o \sim (k_\perp^o L_T)^{-1}. \tag{6.35}$$

Therefore, the injected energy flux (6.33) is

$$\varepsilon \sim \frac{v_{\text{the}}\rho_e^2}{L_T^3\sqrt{\beta_e}}\left(\frac{L_T}{L_B}\right)^{1/2}(k_\perp^o d_e)^{-1}. \tag{6.36}$$

We must now determine $k_\perp^o$. We conjecture that, like in sETG turbulence, the nonlinear interaction rate in cTAI turbulence will increase faster with $k_\perp$ than the growth rate (6.29), $\gamma \propto k_y$. This would certainly be the case if the cascade were local, wherein the Kolmogorov-style argument leading to (6.8) applied (in which case $t_{\rm nl}^{-1} \propto k_\perp^{4/3}$ again). Then $k_\perp^o$ will be the smallest that it can be. Since it is related to $k_\parallel^o$ via (4.24) [corresponding to the maximum growth rate (6.29)] viz.,

$$\frac{k_\parallel^o L_T}{\sqrt{\beta_e}} \sim \begin{cases} \left(\dfrac{L_T}{L_B}\right)^{1/4} (k_\perp^o d_e)^{1/2}, & \text{collisionless,} \\ \left(\dfrac{L_T}{L_B}\right)^{1/6} (k_\perp^o d_e \chi)^{1/3}, & \text{collisional,} \end{cases} \tag{6.37}$$

we can treat this expression as the analogue of the last expression in (6.14) or (6.20). As we did in our treatment of sETG turbulence in sections 6.2.1 and 6.2.2, we now posit that the parallel outer scale of cTAI turbulence will be set by the system's parallel size, $k_\parallel^o \sim L_\parallel^{-1}$. Then, from (6.37),

$$k_\perp^o d_e \sim \begin{cases} \dfrac{L_T^{3/2} L_B^{1/2}}{\beta_e L_\parallel^2}, & \text{collisionless,} \\ \dfrac{L_T^{3/2} L_B^{1/2} \lambda_{ei}}{\beta_e L_\parallel^3}, & \text{collisional.} \end{cases} \tag{6.38}$$

This, of course, assumes that there is no dynamics at larger scales that can set the perpendicular outer-scale. We discuss the constraints set by this assumption in section 9.1.1.

Using (6.38) in (6.36), we can estimate the heat flux due to cTAI turbulence:

$$Q^{\rm cTAI} \sim n_{0e} T_{0e} \varepsilon L_T \sim Q_{\rm gB} \begin{cases} \dfrac{1}{\sqrt{\beta_e}} \dfrac{L_T}{L_B} \left(\dfrac{L_\parallel \sqrt{\beta_e}}{L_T}\right)^2, & \text{collisionless,} \\ \dfrac{\chi}{\sqrt{\beta_e}} \dfrac{L_T}{L_B} \left(\dfrac{L_\parallel \sqrt{\beta_e}}{L_T}\right)^3, & \text{collisional.} \end{cases} \tag{6.39}$$

In order for this construction to be valid, $L_\parallel$ must be large enough for $k_\parallel^o \sim L_\parallel^{-1} \lesssim k_{\parallel c}$, the latter given by (4.21) — otherwise the system cannot access the cTAI regime in the first place. The condition for this is

$$\frac{k_\parallel^o L_T}{\sqrt{\beta_e}} \lesssim \left(\frac{L_T}{L_B}\right)^{1/2} \quad \Leftrightarrow \quad \frac{L_\parallel \sqrt{\beta_e}}{L_T} \gtrsim \left(\frac{L_B}{L_T}\right)^{1/2}. \tag{6.40}$$

Thus, cTAI turbulence is relevant for temperature gradients that are even larger than those needed to access the sETG and sTAI regimes described by (6.17) and (6.24). By comparing the heat fluxes (6.39) with the second expressions in (6.17) and (6.24), it is not hard to ascertain that the cTAI fluxes are larger than the sETG-sTAI ones as long as (6.40) is satisfied.

6.4 Summary of turbulent regimes

In sections 6.2 and 6.3, we found scaling estimates for the turbulent heat fluxes arising from sETG, sTAI and cTAI in both the collisionless and collisional limits. Which of these scalings is realised is determined by the size of the electron temperature gradient L_T for given values of $L_\parallel$, L_B and β_e. There are three distinct regimes.

For

$$k_\perp^o d_e \sim \frac{L_T}{L_\parallel \sqrt{\beta_e}} \gg 1 \quad \Leftrightarrow \quad \frac{L_\parallel \sqrt{\beta_e}}{L_T} \ll 1, \tag{6.41}$$

the system contains only electrostatic (perpendicular) scales, and the heat flux will simply be that arising from sETG turbulence, given by the first expressions in (6.17) and (6.24) in the collisionless and collisional limits, respectively. For

$$k_{\parallel c} \lesssim \frac{1}{L_\parallel} \lesssim \frac{\sqrt{\beta_e}}{L_T} \quad \Leftrightarrow \quad 1 \lesssim \frac{L_\parallel \sqrt{\beta_e}}{L_T} \lesssim \left(\frac{L_B}{L_T}\right)^{1/2}, \tag{6.42}$$

the system can access electromagnetic (perpendicular) scales, with the (isobaric) sTAI and stable KAW being added to the collection of possible modes. However, we showed in section 6.3.1 that the only effect of the sTAI was to equip the sETG turbulent spectrum with an electromagnetic tail at longer wavelengths, with at most an order-unity enhancement of the turbulent heat flux. This heat flux is still the same as that arising from the sETG turbulence, but with the outer scaled fixed at the flux-freezing scale — it is given by the second expressions in (6.17) and (6.24). Finally, for

$$\frac{1}{L_\parallel} \lesssim k_{\parallel c} \quad \Leftrightarrow \quad \frac{L_\parallel \sqrt{\beta_e}}{L_T} \gtrsim \left(\frac{L_B}{L_T}\right)^{1/2}, \tag{6.43}$$

the system has a large enough parallel size to activate cTAI. The resultant turbulent heat flux, given by (6.39), dominates over that due to the sETG and sTAI. We note that this last condition (6.43) can also be written in terms of the normalised temperature gradient L_B/L_T as follows:

$$\frac{L_B}{L_T} \gtrsim \frac{1}{\beta_e} \left(\frac{L_B}{L_\parallel}\right)^2. \tag{6.44}$$

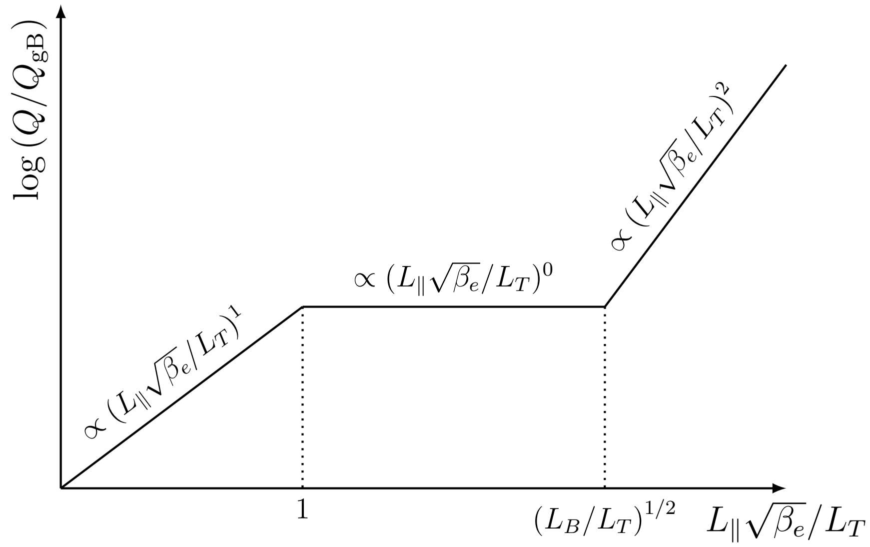

(a) Collisionless limit (6.45)

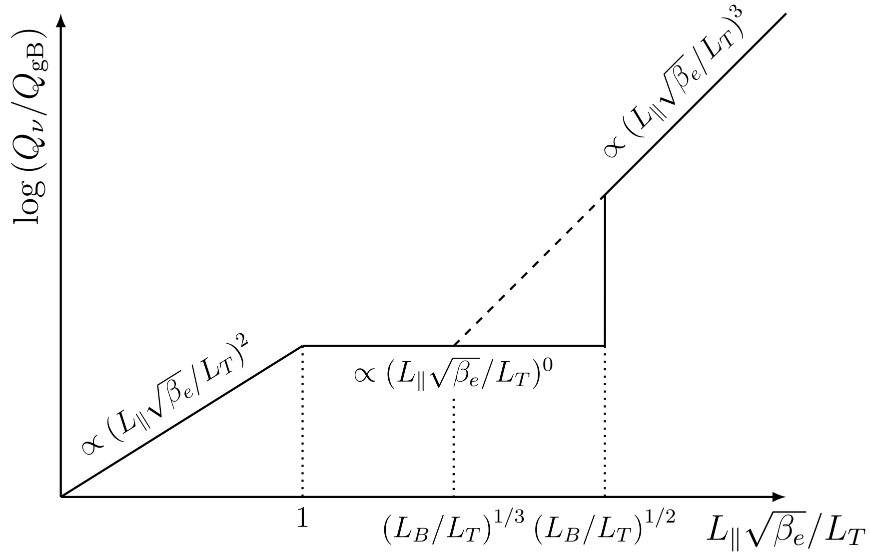

(b) Collisional limit (6.46)

Figure 6.1: The scaling of the turbulent heat-flux with $L_\parallel\sqrt{\beta_e}/L_T$ in the (a) collisionless and (b) collisional limits. As the temperature gradient is increased, the electron transport initially becomes less stiff, as flux freezing pins down the ETG injection scale, after which it stiffens again as cTAI takes over.

To summarise, we can write the turbulent heat flux in the collisionless limit as

$$Q \sim Q_{\mathrm{gB}} \frac{1}{\sqrt{\beta_e}} \begin{cases} \dfrac{L_\parallel \sqrt{\beta_e}}{L_T}, & \dfrac{L_\parallel \sqrt{\beta_e}}{L_T} \ll 1, \\ 1, & 1 \lesssim \dfrac{L_\parallel \sqrt{\beta_e}}{L_T} \lesssim \left(\dfrac{L_B}{L_T}\right)^{1/2}, \\ \dfrac{L_T}{L_B} \left(\dfrac{L_\parallel \sqrt{\beta_e}}{L_T}\right)^2, & \dfrac{L_\parallel \sqrt{\beta_e}}{L_T} \gtrsim \left(\dfrac{L_B}{L_T}\right)^{1/2}, \end{cases} \tag{6.45}$$

or, in the collisional limit, as

$$Q_\nu \sim Q_{\mathrm{gB}} \frac{\chi}{\sqrt{\beta_e}} \begin{cases} \left(\dfrac{L_\parallel \sqrt{\beta_e}}{L_T}\right)^2, & \dfrac{L_\parallel \sqrt{\beta_e}}{L_T} \ll 1, \\ 1, & 1 \lesssim \dfrac{L_\parallel \sqrt{\beta_e}}{L_T} \lesssim \left(\dfrac{L_B}{L_T}\right)^{1/2}, \\ \dfrac{L_T}{L_B} \left(\dfrac{L_\parallel \sqrt{\beta_e}}{L_T}\right)^3, & \dfrac{L_\parallel \sqrt{\beta_e}}{L_T} \gtrsim \left(\dfrac{L_B}{L_T}\right)^{1/2}. \end{cases} \tag{6.46}$$

Notably, this implies that the effect of increasing β_e [or increasing $L_\parallel/L_T \sim \pi q(L_B/L_T)$, as in a tokamak edge], is first to make the electron heat transport less stiff, as flux freezing pins down the ETG injection scale, and then to stiffen it back again, as cTAI takes over. This is sketched in figure 6.1. A striking (and perhaps disturbing) feature of these results is the discontinuity in the collisional turbulent heat flux around the transition between the sTAI- and cTAI-dominated regimes, described by the last two expressions in (6.46). Comparing these, it is easy to see that the latter is larger than the former for

$$\frac{L_\parallel \sqrt{\beta_e}}{L_T} \gtrsim \left(\frac{L_B}{L_T}\right)^{1/3}. \tag{6.47}$$

This condition is obviously met before the parallel system size is large enough in order to activate the cTAI, meaning that the sTAI regime must persist — despite it supporting a notionally lower flux than that predicted by the cTAI scaling — until the inequality in (6.43) is satisfied, at which point the cTAI takes over, leading to the discontinuity. Whether this and the other simple 'twiddle-algebra' considerations that led to (6.45) and (6.46) survive the encounter with quantitative reality is the subject of the following chapters 7 and 8.

Chapter 7

Critical balance in electrostatic ETG turbulence

The majority of kinetic plasma turbulence theory has been developed for situations in which energy is assumed to arrive into the system from larger scales (e.g., from $k_\perp \rho_i < 1$), from where it cascades down towards smaller ones (see [72] and references therein) — this is typically the case in space-physical and astrophysical contexts, where the energy is often injected by large-scale MHD processes. The conclusions of the previous chapter were predicated on the assumption that such a turbulent cascade also exists in systems for which the energy does not simply arrive from large scales to be processed, but is instead injected by microscale instabilities that are found at every perpendicular scale throughout the putative inertial range. In our case, these are the ETG and TAI, which source microscale perturbations by extracting free energy from the equilibrium electron temperature gradient. It is not obvious *a priori*, however, that gradient-driven systems of this type will organise themselves to support such a cascade, with a well-defined (and well-separated) outer scale, inertial range and dissipation scale. Though there is some evidence to suggest that this does occur in the context of gyrokinetic ITG turbulence [12], there have been few other demonstrations of the existence of such cascades within the context of gradient-driven turbulence, despite their potentially central role in determining the saturated turbulent state (see, e.g., [103–105]). In this chapter, we employ numerical simulations to demonstrate in a detailed way, and, we think, beyond reasonable doubt, the validity of the theory of ETG turbulence outlined in Section 6.2. In Section 7.1, we begin by showing that the predicted scaling of the heat flux with parallel system size follows directly from the scale invariance of drift kinetics in the electrostatic limit. This scaling is then validated numerically in Section 7.1.5. The underlying physical dynamics behind this scaling are then elucidated in Section 7.2, demonstrating that electrostatic sETG turbulence indeed saturates via a critically balanced cascade of energy to small scales.

7.1 Drift-kinetic scale invariance

In Chapter 6, we used constant-flux arguments to derive scalings for turbulent heat fluxes resulting from critically balanced electrostatic slab-ETG turbulence — these were given by the first expression in (6.45) and (6.46), which we summarise here as

$$Q \sim Q_{\mathrm{gB}} \begin{cases} \dfrac{L_\parallel}{L_T}, & \text{collisionless,} \\[2ex] \dfrac{L_T}{\lambda_{ei}} \left(\dfrac{L_\parallel}{L_T} \right)^2, & \text{collisional,} \end{cases} \tag{7.1}$$

where once again $Q_{\mathrm{gB}} = n_{0e} T_{0e} v_{\mathrm{th}e} \left(\rho_e / L_T \right)^2$. (7.1) predicts a particular scaling of the heat flux with the parallel system size $L_\parallel$; in this context, $L_\parallel$ can be thought of either as a measure of a quantity analogous to the connection length $\pi q R$ in tokamak geometry (where q is the safety factor and R the major radius) or a proxy for the temperature-gradient scale length. It turns out, however, that we did not actually need to invoke the arguments of Chapter 6 in order to arrive at these scalings: they are in fact a consequence of the scale invariance of drift kinetics in the electrostatic limit (although explaining how the system "implements" this scale invariance will require a return to the physics of critical balance).

7.1.1 Electrostatic scale invariance

To show this, we take as our starting point the gyrokinetic equation (A.20). In the drift-kinetic limit $k_\perp \rho_s \ll 1$, all gyroaverages in (A.20) turn into unity operators, and, making use of the definition of the gyrokinetic potential (A.21), we find:

$$\begin{aligned} &\frac{\partial}{\partial t} \left[h_s - \frac{q_s}{T_{0s}} \left(\phi - \frac{v_\parallel A_\parallel}{c} + \frac{T_{0s}}{q_s} \frac{v_\perp^2}{v_{\mathrm{th}s}^2} \frac{\delta B_\parallel}{B_0} \right) f_{0s} \right] + \left(v_\parallel \boldsymbol{b}_0 + \boldsymbol{v}_{ds} \right) \cdot \nabla h_s \\ &+ \frac{c}{B_0} \boldsymbol{b}_0 \cdot \left[\nabla \left(\phi - \frac{v_\parallel A_\parallel}{c} + \frac{T_{0s}}{q_s} \frac{v_\perp^2}{v_{\mathrm{th}s}^2} \frac{\delta B_\parallel}{B_0} \right) \times \nabla \left(h_s + f_{0s} \right) \right] = \sum_{s'} C_{ss'}^{(\ell)}[h_s], \end{aligned} \tag{7.2}$$

where h_s is the non-Boltzmann part of the fluctuating distribution function of species s, now a function of the particle position $\boldsymbol{r}$, to lowest order in $k_\perp \rho_s \ll 1$. In (7.2), $\boldsymbol{v}_{ds}$

is the sum of the curvature and ∇B drift velocities [see (7.10)] and $C_{ss'}^{(\ell)}$ is the linearised Landau collision operator [see (A.22)]. Decomposing h_s into parts that are even and odd in the parallel velocity $v_\parallel$, viz.,

$$h_s^{\mathrm{even}}(\boldsymbol{r}, v_\parallel, v_\perp, t) = \frac{1}{2}\left[h_s(\boldsymbol{r}, v_\parallel, v_\perp, t) + h_s(\boldsymbol{r}, -v_\parallel, v_\perp, t)\right], \tag{7.3}$$

$$h_s^{\mathrm{odd}}(\boldsymbol{r}, v_\parallel, v_\perp, t) = \frac{1}{2}\left[h_s(\boldsymbol{r}, v_\parallel, v_\perp, t) - h_s(\boldsymbol{r}, -v_\parallel, v_\perp, t)\right], \tag{7.4}$$

it follows straightforwardly from (7.2) that h_s^{even} and h_s^{odd} satisfy, respectively,

$$\begin{aligned} &\frac{\partial}{\partial t}\left[h_s^{\mathrm{even}} - \frac{q_s}{T_{0s}}\left(\phi + \frac{T_{0s}}{q_s}\frac{v_\perp^2}{v_{\mathrm{th}s}^2}\frac{\delta B_\parallel}{B_0}\right)f_{0s}\right] + v_\parallel \boldsymbol{b}_0\cdot\nabla h_s^{\mathrm{odd}} + \boldsymbol{v}_{ds}\cdot\nabla h_s^{\mathrm{even}} \\ &+ \frac{c}{B_0}\boldsymbol{b}_0\cdot\left[\nabla\left(\phi + \frac{T_{0s}}{q_s}\frac{v_\perp^2}{v_{\mathrm{th}s}^2}\frac{\delta B_\parallel}{B_0}\right)\times\nabla h_s^{\mathrm{even}}\right] + \frac{c}{B_0}\boldsymbol{b}_0\cdot\left[\nabla\left(-\frac{v_\parallel A_\parallel}{c}\right)\times\nabla h_s^{\mathrm{odd}}\right] \\ &+ \frac{c}{B_0}\boldsymbol{b}_0\cdot\left[\nabla\left(\phi + \frac{T_{0s}}{q_s}\frac{v_\perp^2}{v_{\mathrm{th}s}^2}\frac{\delta B_\parallel}{B_0}\right)\times\nabla f_{0s}\right] = \sum_{s'} C_{ss'}^{(\ell)}\left[h_s^{\mathrm{even}}\right], \end{aligned} \tag{7.5}$$

and

$$\begin{aligned} &\frac{\partial}{\partial t}\left[h_s^{\mathrm{odd}} - \frac{q_s}{T_{0s}}\left(-\frac{v_\parallel A_\parallel}{c}\right)f_{0s}\right] + v_\parallel \boldsymbol{b}_0\cdot\nabla h_s^{\mathrm{even}} + \boldsymbol{v}_{ds}\cdot\nabla h_s^{\mathrm{odd}} \\ &+ \frac{c}{B_0}\boldsymbol{b}_0\cdot\left[\nabla\left(\phi + \frac{T_{0s}}{q_s}\frac{v_\perp^2}{v_{\mathrm{th}s}^2}\frac{\delta B_\parallel}{B_0}\right)\times\nabla h_s^{\mathrm{odd}}\right] + \frac{c}{B_0}\boldsymbol{b}_0\cdot\left[\nabla\left(-\frac{v_\parallel A_\parallel}{c}\right)\times\nabla h_s^{\mathrm{even}}\right] \\ &+ \frac{c}{B_0}\boldsymbol{b}_0\cdot\left[\nabla\left(-\frac{v_\parallel A_\parallel}{c}\right)\times\nabla f_{0s}\right] = \sum_{s'} C_{ss'}^{(\ell)}\left[h_s^{\mathrm{odd}}\right], \end{aligned} \tag{7.6}$$

where we have used the isotropy of the linearised Landau collision operator (A.22) to simplify the right-hand side. Similarly, the field equations (A.23)-(A.25) become

$$0 = \sum_s q_s\left[-\frac{q_s\phi}{T_{0s}}n_{0s} + \int \mathrm{d}^3\boldsymbol{v}\, h_s^{\mathrm{even}}\right], \tag{7.7}$$

$$\nabla_\perp^2 A_\parallel = -\frac{4\pi}{c}\sum_s q_s \int \mathrm{d}^3\boldsymbol{v}\, v_\parallel h_s^{\mathrm{odd}}, \tag{7.8}$$

$$\nabla_\perp^2 \delta B_\parallel = -\frac{4\pi}{c}\boldsymbol{b}_0\cdot\left[\nabla_\perp\times\sum_s q_s\int \mathrm{d}^3\boldsymbol{v}\,\boldsymbol{v}_\perp h_s^{\mathrm{even}}\right]. \tag{7.9}$$

Note that in (7.5) and (7.6), we have assumed that the (radial) gradient of the equilibrium distribution function ∇f_{0s} is an even function of $v_\parallel$ — this is only the case in systems without any equilibrium flows, as we have been assuming throughout this thesis.

We now wish to consider transformations of the system of equations (7.5)-(7.9) that can be made whilst preserving the size of perpendicular equilibrium gradients, viz., at a fixed L_{T_s}, L_n, L_B, etc. It is relatively obvious from considering, e.g., the magnetic-drift velocity

$$\boldsymbol{v}_{ds} = \frac{\boldsymbol{b}_0}{\Omega_s} \times \left(v_\parallel^2 \boldsymbol{b}_0 \cdot \boldsymbol{\nabla} \boldsymbol{b}_0 + \frac{1}{2} v_\perp^2 \boldsymbol{\nabla} \log B_0 \right), \tag{7.10}$$

that any rescaling of the velocity variables $v_\parallel$ and $v_\perp$ — at fixed equilibrium magnetic-field strength — would require a compensatory rescaling of R and L_B [as defined in (2.4)] in order to preserve the magnitude and direction of $\boldsymbol{v}_{ds}$. Therefore, we will henceforth restrict ourselves to transformations involving only the spatial and time coordinates. In a similar vein to [106], we consider the following one-parameter transformation:

$$\tilde{h}_s^{\text{even}} = \lambda^{a_e}\, h_s^{\text{even}}(x/\lambda^{a_\perp}, y/\lambda^{a_\perp}, z/\lambda^{a_\parallel}, t/\lambda^{a_t}), \tag{7.11}$$

$$\tilde{\phi} = \lambda^{a_e}\, \phi(x/\lambda^{a_\perp}, y/\lambda^{a_\perp}, z/\lambda^{a_\parallel}, t/\lambda^{a_t}), \tag{7.12}$$

$$\delta\tilde{B}_\parallel = \lambda^{a_e}\, \delta B_\parallel(x/\lambda^{a_\perp}, y/\lambda^{a_\perp}, z/\lambda^{a_\parallel}, t/\lambda^{a_t}), \tag{7.13}$$

$$\tilde{h}_s^{\text{odd}} = \lambda^{a_o}\, h_s^{\text{odd}}(x/\lambda^{a_\perp}, y/\lambda^{a_\perp}, z/\lambda^{a_\parallel}, t/\lambda^{a_t}), \tag{7.14}$$

$$\tilde{A}_\parallel = \lambda^{a_o + 2a_\perp} A_\parallel(x/\lambda^{a_\perp}, y/\lambda^{a_\perp}, z/\lambda^{a_\parallel}, t/\lambda^{a_t}), \tag{7.15}$$

where x, y and z are the radial, binormal and parallel coordinates, respectively, the tildes indicate the transformed distribution functions and fields, and the a_i's are some real constants parametrising the transformation. These can be fixed by demanding that the transformation leaves (7.5) and (7.6) invariant, as we shall do shortly.

The rescaling (7.11)-(7.15) is the most general one-parameter transformation of drift-kinetics that can be made while allowing (although not requiring) the spatial isotropy of structures in the perpendicular plane. The field equations of quasineutrality (7.7) and perpendicular Ampère's law (7.9) imply that the amplitudes of the 'even' fields must be rescaled in the same way, as in (7.11)-(7.13), while the rescaling of the amplitudes of the 'odd' fields is similarly constrained by parallel Ampère's law (7.8), as in (7.14) and (7.15). The spatial and time coordinates can then be rescaled independently, with the caveat that the radial and binormal coordinates should be rescaled in the same way in order not to rule out perpendicular isotropy.

Let us now specialise to the electrostatic limit, in which we neglect all contributions of $A_\parallel$ and $\delta B_\parallel$ to (7.5) and (7.6). Then it is possible to show, and confirm by inspection, that the resultant electrostatic drift-kinetic system is invariant under the transformation

$$\tilde{h}_s^{\mathrm{even}} = \lambda^2\, h_s^{\mathrm{even}}(x/\lambda^2, y/\lambda^2, z/\lambda^{2/\alpha}, t/\lambda^2), \tag{7.16}$$

$$\tilde{\phi} = \lambda^2\, \phi(x/\lambda^2, y/\lambda^2, z/\lambda^{2/\alpha}, t/\lambda^2), \tag{7.17}$$

$$\tilde{h}_s^{\mathrm{odd}} = \lambda^{2/\alpha}\, h_s^{\mathrm{odd}}(x/\lambda^2, y/\lambda^2, z/\lambda^{2/\alpha}, t/\lambda^2), \tag{7.18}$$

where we have chosen $a_e = 2$ without loss of generality, and $\alpha = 1, 2$ in the collisionless and collisional limits[1], respectively, as in Chapter 4. Mathematically, the existence of this transformation is a consequence of the scale invariance of electrostatic drift kinetics. In the absence of finite-Larmor-radius effects associated with ρ_s — manifest in the gyroaverages and the resultant Bessel functions appearing in the gyrokinetic equation (A.20) — there is no intrinsic perpendicular scale within the system, with nothing to distinguish any perpendicular scale from any other.

7.1.2 Consequences for transport

We now consider the consequences of the transformation (7.16)-(7.18) for turbulent transport. The rate of free-energy injection in electrostatic drift kinetics is given by (see, e.g., [55])

$$\varepsilon = \sum_s \varepsilon_s, \tag{7.19}$$

---

[1] In the collisionless limit, the collision operator can be neglected in its entirety, from which it is easy to show that $a_e = a_o = a_\perp = a_\parallel = a_t$ is the only choice of a_i's that leaves the equations invariant. The collisional limit is somewhat more subtle. As we have done throughout the remainder of this thesis, we consider the case where the rate of thermal conduction is comparable to the frequency of the perturbations, viz., $\omega \sim (k_\parallel v_{\mathrm{the}})^2/\nu_{ss'} \ll \nu_{ss'}$ ($\nu_{ss'}$ is the characteristic collision frequency between species s and s'), and order $\omega h_s^{\mathrm{even}} \sim k_\parallel v_{\mathrm{th}s} h_s^{\mathrm{odd}}$. In the resultant collisional expansion, the collision operator will be forced to vanish at leading order (see Appendix A.4.1), and can only survive at higher order due to the presence of finite-Larmor-radius effects (see Appendix A.4.3), which have been neglected within the drift-kinetic approximation. At first order, one obtains, from (7.6), a balance between the parallel streaming of h_s^{even} and the collision operator acting on h_s^{odd} (see Appendix A.4.2). At second order, one evolves h_s^{even} via (7.5) with the collision operator neglected (see Appendix A.4.3). One can then show that $a_e = 2a_o = a_\perp = 2a_\parallel = a_t$ is the only choice of parameters that leaves the drift-kinetic equations invariant. The nature of such an expansion means that any constraints on the a_i's inferred from (7.11)-(7.15) will only be valid to second order within the collisional expansion, and not to any higher orders. However, given that the solvability conditions (A.34) and (A.47) guarantee that a closed system can be obtained solely from these two orders, we do not consider this particularly problematic.

with

$$\varepsilon_s = -\int \frac{\mathrm{d}^3\boldsymbol{r}}{V} \int \mathrm{d}^3\boldsymbol{v}\, h_s^{\mathrm{even}} \frac{c}{B_0} \boldsymbol{b}_0 \cdot (\nabla\phi \times \nabla \log f_{0s})\,. \tag{7.20}$$

Then, using (7.16)-(7.18), we find that this injection rate transforms as

$$\tilde{\varepsilon}_s = \lambda^2 \varepsilon_s \quad \Rightarrow \quad \tilde{Q}_s = \lambda^2 Q_s, \tag{7.21}$$

where the right-hand expression follows from the fact that the heat flux is related to the rate of energy injection by $Q_s \sim n_{0s} T_{0s} \varepsilon_s L_{T_s}$.

Suppose that our original solutions for h_s^{even} and ϕ were periodic in x, y and z with domain sizes L_x, L_y and $L_\parallel$, respectively. Then the transformed solutions $\tilde{h}_s^{\mathrm{even}}$ and $\tilde{\phi}$ are still periodic in x, y and z, except with domain sizes $\lambda^2 L_x$, $\lambda^2 L_y$ and $\lambda^{2/\alpha} L_\parallel$, implying that

$$\tilde{Q}_s(\lambda^2 L_x, \lambda^2 L_y, \lambda^{2/\alpha} L_\parallel) = \lambda^2 Q_s(L_x, L_y, L_\parallel). \tag{7.22}$$

The heat flux will, of course, depend on other system parameters, e.g., equilibrium gradients and collisionality. These, however, will remain unchanged under the transformation, and so we did not write them explicitly in (7.22). Now, in a strongly magnetised (gyrokinetic) plasma, structures generated by the turbulent fluctuations are ordered comparable to the scales of the equilibrium in the parallel direction ($k_\parallel^{-1} \sim L_\parallel$), but must remain microscopic in the perpendicular direction ($k_\perp^{-1} \sim \rho_s$). This means that, as the perpendicular domain size (i.e., $L_\perp \sim L_x \sim L_y \sim \rho_s$) is increased, there must come a point at which the turbulence, and its resultant heat flux, become independent of the perpendicular domain size; if this were not the case, then the heat flux would diverge as $L_\perp/\rho_s \to \infty$, implying that drift kinetics is not a valid local model of the plasma. We thus assume that the heat flux is independent of the perpendicular domain size, viz., independent of L_x and L_y. Then, given that λ can be chosen arbitrarily, (7.22) directly implies that

$$Q_s \propto L_\parallel^\alpha, \tag{7.23}$$

where once again $\alpha = 1, 2$ in the collisionless and collisional limits, respectively. Remarkably, (7.23) reproduces the dependence on $L_\parallel$ of the heat fluxes (7.1), as well as that predicted by [12] in the context of ITG-driven gyrokinetic turbulence (if one takes

$L_\parallel$ to be the connection length). Given the assumption that the heat flux is independent of perpendicular domain size, (7.23) follows directly from the scale invariance of electrostatic drift kinetics manifest in the transformation (7.16)-(7.18). This means that the electrostatic heat-flux scalings predicted by the arguments of Chapter 6 are in some sense *inevitable* (subject to the assumptions stated above), and, as we proceed to show numerically in Section 7.1.3, are indeed satisfied.

Let us discuss the significance of the fact that the heat flux scales with the parallel system size. As we conjectured in Section 6.2, and will confirm numerically in Section 7.1.5, the outer scale for electrostatic sETG driven turbulence is set by the parallel system size $k_\parallel^o L_\parallel \sim 1$. Such a choice goes back to the work by [12], who, similarly, conjectured, and numerically verified, that the outer scale of electrostatic, gyrokinetic ITG turbulence in tokamak geometry was set by the connection length $L_\parallel \sim qR$. While in their case, like ours, this was the only scale that could be reasonably viewed as the characteristic system size (the spatial inhomogeneity of the magnetic equilibrium), there was also another, arguably more physically intuitive, reason available for its role in determining the large-scale cutoff for the ITG turbulence: one could assume that any turbulent structures correlated on parallel scales longer than the connection length would be damped in the stable ("good-curvature") region on the inboard side of the tokamak. Thus, one could believe that the operative reason for the significance of $L_\parallel \sim qR$ was the presence of large-scale dissipation, rather than, as we have now concluded, the breaking of scale invariance by inhomogeneity (or, in our case, the finiteness of a periodic box). Indeed, in the present context, $L_\parallel$ corresponds to the longest scale associated with any parallel inhomogeneities that break scale invariance, but is manifestly not related to any form of dissipation triggered by the presence of such inhomogeneities. A practical implication of this conclusion for more realistic systems appears to be that any long-scale parallel inhomogeneity should be sufficient to break scale invariance, without the need for an energy sink — this could matter for the analysis of turbulence in, e.g., edge plasmas [53, 54] or in stellarators [107], where magnetic fields have parallel structure on scales shorter than the connection length.

All of these considerations, however, were predicated on the assumption that $k_\perp \rho_s \ll 1$, as the existence of the transformation (7.16)-(7.18) relies on the scale invariance of the drift-kinetic limit. Restoring finite-Larmor-radius (FLR) effects by reverting to the (electrostatic) gyrokinetic equation will evidently break this property, as the scales

$k_\perp \sim \rho_s^{-1}$ will now appear explicitly in the equations through the Bessel functions. Though there are, of course, exceptions [53, 54], the general effect of these Bessel functions is to provide a cutoff for instabilities at large perpendicular wavenumbers. In terms of the "instability landscapes" depicted in figures 5.1 and 5.2, this typically restricts the region of instability on the ultraviolet side, providing a sink of energy (dissipation) beyond the wavenumbers where the sETG growth rate peaks. The constant-flux arguments of Chapter 6 assumed that there was sufficient separation between the outer scale and these dissipation regions in order to allow an inertial range to develop at the intermediate scales. Should such a separation exist, the system will effectively be drift-kinetic in the inertial range and, crucially, at the outer scale, where the results of this section will continue to apply, despite the system being fully gyrokinetic. In other words, even if drift-kinetic scale invariance is broken at small scales, the assumption behind (7.23) is that the transport is set by the outer scale, which is in the drift-kinetic limit, and the relevant breaking of scale-invariance is done by $L_\parallel$ (as we argued earlier, it cannot be $L_\perp$, lest the local gyrokinetic ordering be broken). The dynamical argument of Chapter 6 — based on the competition between the nonlinear time and the growth rate of the instability setting the outer scale for the turbulence on scales well-separated from any dissipation regions — is then the physical mechanism whereby this scale invariance is realised. This was the case in [12], who confirmed the scaling (7.23) using fully gyrokinetic, Cyclone-Base-Case [108] `GS2` simulations. Note that the scale separation required for such a state is far from guaranteed: non-zero magnetic shear, for example, can create long-wavelength modes with binormal wavenumbers $k_y \rho_i \sim 1$ but narrow radial structures near mode-rational surfaces on the scale $k_x \rho_e \sim 1$ [67, 109]. Whether the results of this section are robust to the effects of significant magnetic shear and other equilibrium shaping that can amplify the importance of FLR — and thus undermine the possible separation between FLR effects and a putative outer scale — is a subject for future work. Similarly, it is worth noting that including ion-scale physics within our model (by allowing for a finite mass-ratio m_e/m_i) is another possible route by which scale invariance could be broken, though we consider this to be outside the scope of this current work. For now, we shall focus on verifying (7.23) and explaining why the physical assumptions that underlie it are indeed correct within the context of the model of ETG-driven turbulence that we have been considering throughout this thesis.

7.1.3 Electrostatic equations

There is recent evidence [64, 66] to suggest that collisional, fluid models are capable of providing remarkable insight about the dynamics of more general physical systems, while retaining the advantage of being (comparatively) simple to handle both numerically and analytically. In light of this, here, and throughout the remainder of this chapter, we will focus on the collisional limit — all of the characteristic instabilities that we have considered have both collisionless and collisional counterparts, meaning that the collisional limit can serve as a qualitative proxy for our more general ETG system.

To proceed, we must specialise the collisional system of equations (2.27)-(2.29) to the electrostatic limit $k_\perp d_e \chi \gg 1$. On these scales, the resistive term on the right-hand side of (2.28) is larger than all other terms containing $\mathcal{A}$ by a factor of β_e [see (A.96)] — the latter of which can consequently be neglected — while all of the nonlinearities contained in the parallel derivatives (2.11) are also small in β_e [see (A.97)]. This implies that (2.28) becomes an explicit expression for the perturbed parallel electron velocity, viz.,

$$u_{\parallel e} = -\frac{v_{\text{the}}^2}{2\nu_{ei}} \frac{\partial}{\partial z} \left(\frac{\delta n_e}{n_{0e}} - \varphi + \frac{\delta T_e}{T_{0e}} \right). \tag{7.24}$$

$\mathcal{A}$ thus ceases to be a dynamic field: it is instantaneously determined from the parallel gradient of the pressure, as was indeed the case for the collisional sETG (see Section 3.2). Substituting (7.24) into (2.27) and (2.29), recalling the definition of the conductivity (2.20), and making use of the quasineutrality condition (2.22) to express the density perturbations $\delta n_e / n_{0e}$ in terms of φ, we find

$$\frac{\mathrm{d}}{\mathrm{d}t} \bar{\tau}^{-1} \varphi - \left(1 + \frac{1}{\bar{\tau}} \right) \frac{c_{\varphi\varphi} v_{\text{the}}^2}{2\nu_{ei}} \frac{\partial^2 \varphi}{\partial z^2} + \frac{c_{\varphi T} v_{\text{the}}^2}{2\nu_{ei}} \frac{\partial^2}{\partial z^2} \frac{\delta T_e}{T_{0e}} = 0, \tag{7.25}$$

$$\frac{\mathrm{d}}{\mathrm{d}t} \frac{\delta T_e}{T_{0e}} + \frac{2}{3} \left(1 + \frac{1}{\bar{\tau}} \right) \frac{c_{T\varphi} v_{\text{the}}^2}{2\nu_{ei}} \frac{\partial^2 \varphi}{\partial z^2} - \frac{2}{3} \frac{c_{TT} v_{\text{the}}^2}{2\nu_{ei}} \frac{\partial^2}{\partial z^2} \frac{\delta T_e}{T_{0e}} = -\frac{\rho_e v_{\text{the}}}{2L_T} \frac{\partial \varphi}{\partial y}, \tag{7.26}$$

where

$$c_{\varphi\varphi} = 1, \quad c_{\varphi T} = c_{T\varphi} = 1, \quad c_{TT} = 1 + \frac{5}{9(1+1/Z)} \tag{7.27}$$

are coefficients determined by the inversion of the collision operator (see [1]); the equality between $c_{\varphi T}$ and $c_{T\varphi}$ is a manifestation of Onsager symmetry [110]. In (7.25) and

(7.26), we have ignored any instances of magnetic-field gradients; this corresponds to the limit of a very steep electron temperature gradient, in which one expects the sETG to be the dominant source of energy injection, as was assumed in Section 6.2; the effect of restoring finite magnetic-field gradients is discussed in Section 7.3.

Together, (7.25) and (7.26) form a closed, two-field system describing the evolution of the potential φ and temperature $\delta T_e/T_{0e}$ perturbations in the presence of an electron temperature gradient. Unsurprisingly, given that they were derived as an asymptotic subsidiary limit of drift kinetics, these equations are invariant under the transformation (7.16)-(7.18), viz., the rescaled fields

$$\tilde{\varphi} = \lambda^2\, \varphi(x/\lambda^2, y/\lambda^2, z/\lambda, t/\lambda^2), \quad \delta\tilde{T}_e = \lambda^2\, \delta T_e(x/\lambda^2, y/\lambda^2, z/\lambda, t/\lambda^2), \tag{7.28}$$

are also solutions to (7.25) and (7.26). This is a consequence of the fact that we are considering scales $k_\perp d_e \chi \gg 1$, on which the flux-freezing scale (2.33) is no longer an important, or indeed relevant, perpendicular spatial scale. In fact, as we show in Appendix A.5.3, (7.25) and (7.26) are valid within wavenumber range [cf. (A.95)]

$$\sqrt{\beta_e} \ll k_\parallel L_T \ll 1, \quad (d_e\chi)^{-1} = \beta_e \rho_e^{-1}\frac{\lambda_{ei}}{L_T} \ll k_\perp \ll \rho_e^{-1}\frac{\lambda_{ei}}{L_T}, \tag{7.29}$$

i.e., at perpendicular scales much smaller than the flux-freezing scale, but much larger than those on which one encounters the effects of electron thermal diffusion due to the finite Larmor motion of the electrons; formally, these scales are at the intersection of two asymptotic limits, as we discuss in Appendix A.5.3. In other words, (7.25) and (7.26) describe physics on scales

$$k_\parallel L_T \sim \sqrt{\sigma}, \quad k_\perp \rho_\perp \sim 1, \quad \rho_\perp = \frac{\beta_e}{\sigma} d_e \chi = \frac{\rho_e}{\sigma}\frac{L_T}{\lambda_{ei}}, \tag{7.30}$$

where σ is some arbitrary constant satisfying $\beta_e \ll \sigma \ll 1$ — the fact that it should be arbitrary follows from the fact that there is no special scale within the wavenumber ranges (7.29). Our normalisation of perpendicular and parallel wavenumbers within (7.25) and (7.26) will thus also be arbitrary, up to the definition of σ.

Given that we are going to focus explicitly on collisionally driven instabilities, due diligence suggests that we should work with a set of equations that capture the collisional limit as accurately as possible, so as to ensure that if any of the resultant nonlinear dynamics depends on, e.g., specific details of the collision operator, then it is properly described. In this sense, (2.27)-(2.29), along with (7.25) and (7.26), are somewhat suspect, given that they were derived using a simplified collision operator that was appropriate for the Hermite-Laguerre expansion considered in [1]. However, we show in Appendix A that (7.25) and (7.26) remain valid even when derived with the correct linearised Landau collision operator [see (A.22)], with the only difference being the replacement of the collisional coefficients (7.27) with

$$c_{\varphi\varphi} = c_1, \quad c_{\varphi T} = c_{T\varphi} = c_1 + c_2, \quad c_{TT} = c_3 + c_1 \left(1 + \frac{c_2}{c_1}\right)^2, \tag{7.31}$$

where c_1, c_2 and c_3 are the (positive) ion-charge-dependent coefficients determined from the linearised Landau collision operator [see Appendix A.4.2 and, in particular, (A.50)]. This puts the status of (7.25) and (7.26) as the correct collisional, electrostatic sETG-driven system beyond reproach (although it will not, in any event, make much difference). Note that for $Z = 1$, $c_1 \approx 1.94$, $c_2 \approx 1.39$, and $c_3 \approx 3.16$, in agreement with [111].

7.1.4 Numerical implementation

In what follows, these equations are solved numerically in a triply periodic box of size L_x, L_y and $L_\parallel$ using a pseudo-spectral algorithm. Numerical integration is done in Fourier space (n_x, n_y and $n_\parallel$ are the number of Fourier harmonics in the respective directions) with the nonlinear term calculated in real space using the 2/3 rule for dealiasing [112]. We integrate the linear terms implicitly in time using the Crank-Nicolson method, while nonlinear terms are integrated explicitly using the Adams-Bashforth three-step method. This integration scheme is similar to the one implemented in the popular gyrokinetic code `GS2` [10, 113].

Perpendicular hyperviscosity is introduced in order to provide an ultraviolet (large-wavenumber) cutoff for the instabilities, achieved by the replacement of the convective time derivative on the left-hand side of (7.25) and (7.26) with

$$\frac{\mathrm{d}}{\mathrm{d}t} + (-1)^{n_\nu} \nu_\perp \left(\rho_\perp \nabla_\perp\right)^{2n_\nu}, \tag{7.32}$$

where $\nu_\perp$ is the "hyper-collision" frequency and $n_\nu \geqslant 2$. With this change, our equations now depend on only the following dimensionless parameters: the perpendicular and parallel box sizes $L_x/\rho_\perp$, $L_y/\rho_\perp$ and $L_\parallel\sqrt{\sigma}/L_T$, the hyper-collision frequency $2(\rho_\perp/\rho_e)^2\nu_\perp/\nu_{ei}$, and the power of the hyperviscous diffusion operator n_ν. Convergence

	$L_x/\rho_\perp$	$L_y/\rho_\perp$	$L_\parallel\sqrt{\sigma}/L_T$	n_x	n_y	$n_\parallel$	$2(\rho_\perp/\rho_e)^2\nu_\perp/\nu_{ei}$	n_ν
Baseline	40	40	20	191	191	31	0.00050	2
High resolution	40	40	20	383	383	63	0.00015	2

Table 7.1: The parameters used in the baseline and high-resolution simulations. Both simulations had $\tau = Z = 1$.

scans in n_x, n_y, and perpendicular box size $L_x = L_y = L_\perp$ were carried out on a baseline simulation (see table 7.1) to ensure that the chosen resolution adequately resolved the dynamics, and to verify that $L_\perp$ was made large enough so that it did not significantly affect the simulation results, as was required for the arguments of Section 7.1.2.

We have found that our results do not depend on the specific details of the hyperviscosity, viz., $\nu_\perp$ and n_ν. It can be viewed as a numerical tool that allows us to capture the dynamics of the system within a finite simulation domain and resolution, and is not intended to model a specific physical process. Readers uneasy with this may take the view that (7.32) represents the physical sink of energy that exists at higher perpendicular wavenumbers. The fact that our results end up being independent of hyperviscosity is, however, significant. The addition of (7.32) breaks the scale invariance associated with the transformation (7.28), similar to the way in which FLR effects formally break drift-kinetic scale invariance in the context of gyrokinetics. One could thus question the inevitability of the scaling of the heat flux (7.23) within our system of equations. Furthermore, the fact that the growth rate of the sETG will peak at a perpendicular scale entirely determined by the hyperviscosity — since (7.25) and (7.26) contain no intrinsic perpendicular wavenumber cutoff — may be a cause for concern, as the most unstable perpendicular scale is often thought to play a central role in determining turbulent transport. Both of these concerns can be dispelled by the realisation that neither the scale-invariance (Section 7.1.2) nor constant-flux (Section 6.2) arguments for the scaling of the turbulent heat flux rested on details about the state of the system at small perpendicular scales; in both cases, it was the *outer scale* that was central in determining the transport. The fact that we find that our results are indeed independent of hyperviscosity is in fact a non-trivial validation of our theory.

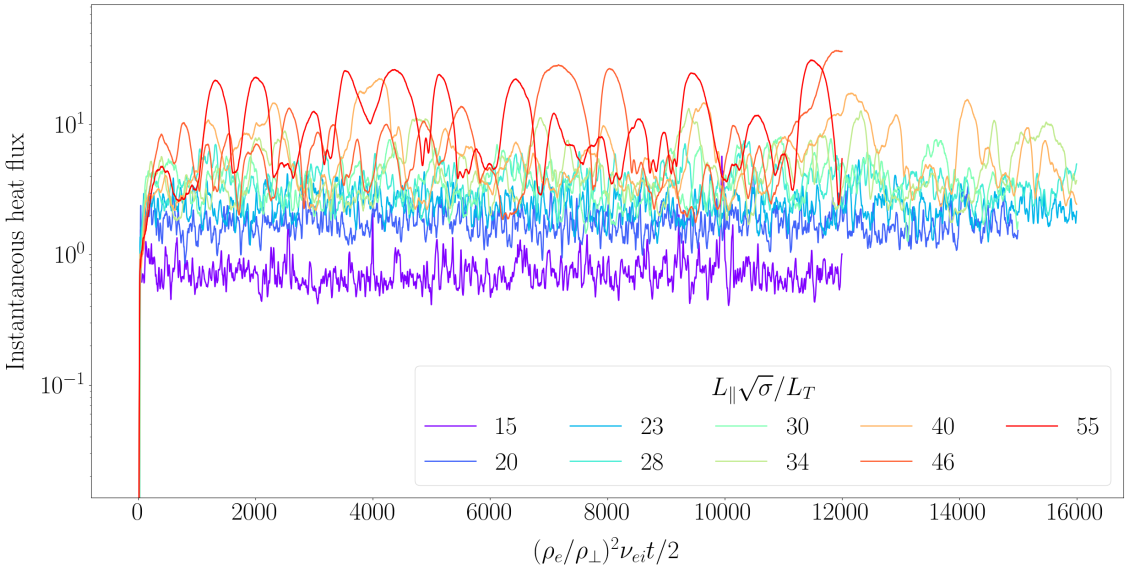

Figure 7.1: Timetraces of the instantaneous heat flux from simulations in which $L_\parallel\sqrt{\sigma}/L_T$ was varied from 15 to 55, plotted against a logarithmic scale. One observes higher-amplitude, longer-timescale oscillations in the heat flux for simulations with larger $L_\parallel\sqrt{\sigma}/L_T$.

7.1.5 Scan in $L_\parallel/L_T$

In order to test the dependence of the turbulent heat flux on $L_\parallel$ predicted by both the scale-invariance and constant-flux arguments, we performed a series of simulations in which $L_\parallel\sqrt{\sigma}/L_T$ was varied between 15 and 55 at fixed parallel resolution (viz., fixed ratio of $L_\parallel\sqrt{\sigma}/L_T$ to $n_\parallel$), while keeping all other parameters the same as in the baseline simulation (see table 7.1). Each simulation was run to long times to ensure that saturation had been reached; for the scan based on the baseline simulation, this varied between 12000 and 16000 $(\rho_e/\rho_\perp)^2\nu_{ei}t/2$, depending on the value of $L_\parallel\sqrt{\sigma}/L_T$. This is because the (perpendicular) outer scale for the simulations with larger $L_\parallel\sqrt{\sigma}/L_T$ lies closer to the perpendicular box scale, leading to larger-amplitude, longer-timescale oscillations in the observed heat flux (see Figure 7.1) and, consequently, a longer required simulation time to ensure that the system has reached a statistical steady state.

In Figure 7.2, we plot the time average of the (normalised) turbulent heat flux due to the fluctuating $\boldsymbol{E}\times\boldsymbol{B}$ flows — viz., the first expression multiplying $1/L_T$ in the collisional version of (6.4) [see also (7.37)] — normalised to $(\rho_\perp/\rho_e)Q_{\mathrm{gB}}$, with $Q_{\mathrm{gB}} = n_{0e}T_{0e}v_{\mathrm{th}e}(\rho_e/L_T)^2$, as previously. It is clear that the simulation data agrees extremely well with the theoretical scaling (7.1). Similarly, Figure 7.3 shows that the

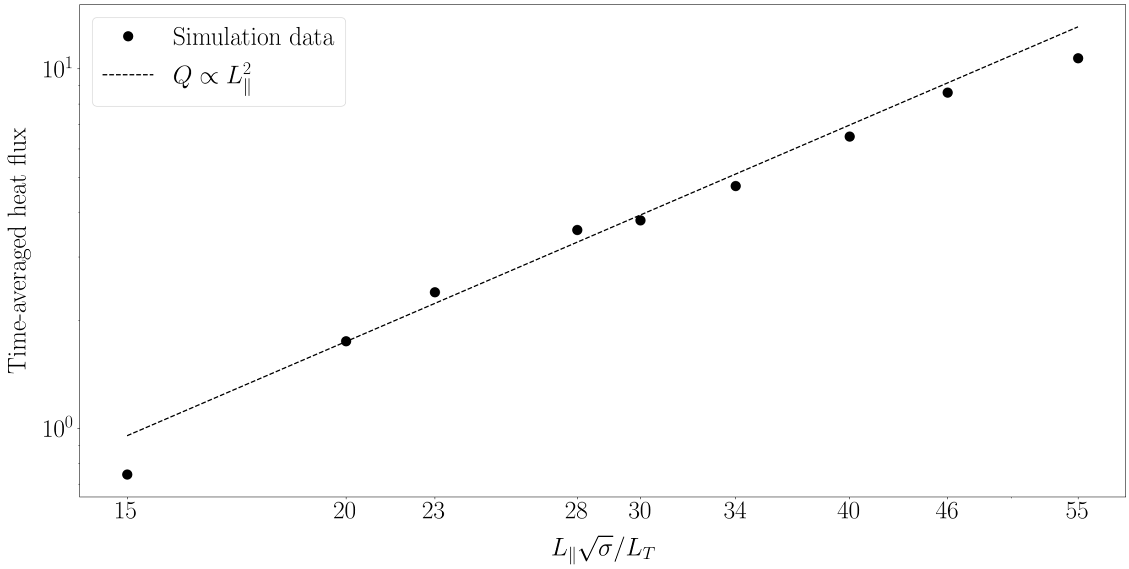

Figure 7.2: The scaling of the turbulent heat flux with $L_\parallel/L_T$, plotted against logarithmic axes. The black points are the simulation data, while the theoretical prediction [see (7.1) or (7.23)] is shown by the dashed black line. A logarithmic fit to the data gives a slope of 1.98.

scaling of both the perpendicular outer scale $k_\perp^o$ with $L_\parallel/L_T$ and the amplitude of the electrostatic potential with the perpendicular outer scale agree well with the respective theoretical predictions (6.22) and (6.14). In these measurements, the (perpendicular) outer scale was determined as corresponding to the wavenumber where the maximum of the 1D perpendicular spectrum of the free-energy injection [cf. (6.4)]

$$\varepsilon_{\boldsymbol{k}}(k_\perp) = 2\pi k_\perp \int_{-\infty}^{\infty} \mathrm{d}k_\parallel \, \frac{3}{2} \mathrm{Re} \left\langle i\omega_{*e}\varphi_{\boldsymbol{k}}^* \frac{\delta T_{e\boldsymbol{k}}}{T_{0e}} \right\rangle \tag{7.33}$$

is achieved [the asterisk denotes complex conjugation and the brackets an ensemble average, as in (6.7)]. When analysing the output of simulations, we consider ensemble averages to be equal to time averages over a period following saturation and the establishment of a statistical steady state [e.g., after $(\rho_e/\rho_\perp)^2\nu_{ei}t/2 \sim 2000$ in Figure 7.1]. The outer scale is most often defined to be the integral scale of the 1D perpendicular energy spectrum (6.7), viz.,

$$k_\perp^o \equiv \frac{\displaystyle\int_0^\infty \mathrm{d}k_\perp \, k_\perp E_\perp^\varphi(k_\perp)}{\displaystyle\int_0^\infty \mathrm{d}k_\perp \, E_\perp^\varphi(k_\perp)}. \tag{7.34}$$

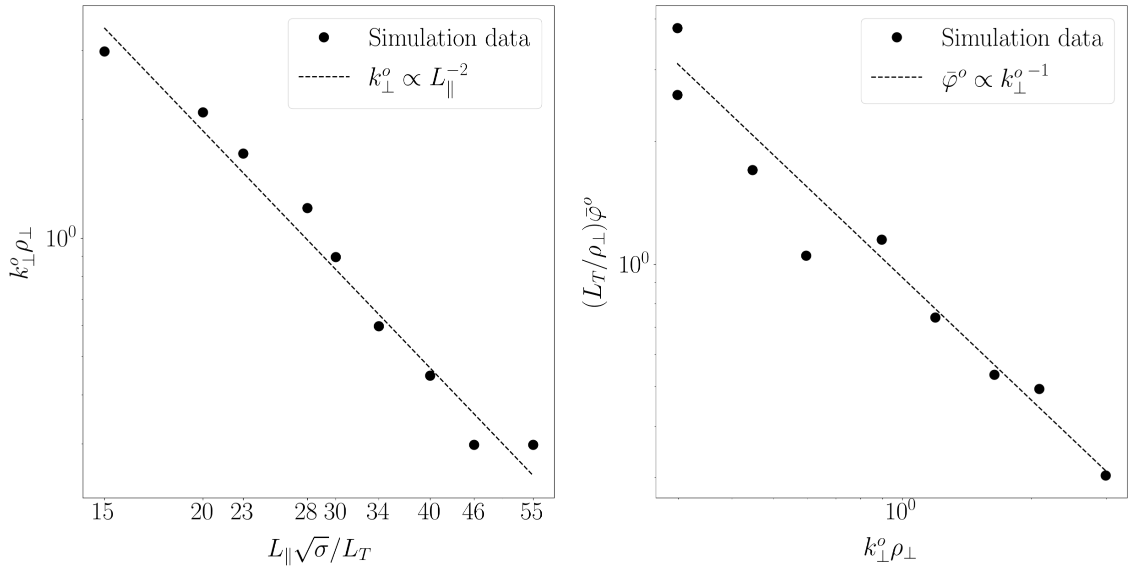

(a)

(b)

Figure 7.3: (a) The scaling of the perpendicular outer scale $k_\perp^o \rho_\perp$ [defined as the peak wavenumber of (7.33)] with $L_\parallel/L_T$; (b) The scaling of the amplitude of the electrostatic potential $\bar{\varphi}^o$ with the perpendicular outer scale [defined as the amplitude of φ at $k_\perp = k_\perp^o$]. The black points are the simulation data, while the theoretical prediction the black dashed line [see (6.20)]. A logarithmic fit to the data gives a slope of -1.99 and -0.95 in (a) and (b), respectively.

However, given that, physically, we are interested in the outer scale as the scale at which the free energy is effectively injected, the choice to maximise (7.33) seems a straightforward one in systems where energy is injected by local instabilities like the sETG. Furthermore, finding the outer scale by maximising (7.33) gave better agreement with the theoretical prediction than adopting (7.34), suggesting that, perhaps, the former is a better measure of the outer scale for such systems.

The remarkable agreement seen in figures 7.2 and 7.3, however, should not be a cause of complacency: the fact that the system conforms to the predicted scalings with parallel system size is not sufficient evidence to conclude that energy transfer towards small scales occurs via the constant-flux, critically balanced cascade of energy that was proposed in Section 6.2. Indeed, one must be especially diligent to determine the exact nonlinear mechanism giving rise to such macroscopic ‘observables’. To complete our picture, and explain these observations, we thus need to consider the dynamics in the inertial range. This is the subject of the following section.

7.2 Inertial-range dynamics

As we discussed in Section 6.1, our system conserves the quadratic norm of the perturbations of the electron distribution function away from equilibrium, i.e., the free-energy (6.2), which we write here explicitly in terms of our two fields φ and $\delta T_e/T_{0e}$ as

$$\frac{W}{n_{0e}T_{0e}} = \int \frac{\mathrm{d}^3\boldsymbol{r}}{V}\left[\frac{1}{2\bar{\tau}}\left(1+\frac{1}{\bar{\tau}}\right)\varphi^2 + \frac{3}{4}\frac{\delta T_e^2}{T_{0e}^2}\right]. \tag{7.35}$$

In going from (6.2) to (7.35), we have once again made use of quasineutrality (7.70) to express $\delta n_e/n_{0e}$ in terms of φ, and ignored the term involving $\mathcal{A}$, as the energy associated with perturbations to the magnetic field direction is negligible in this electrostatic limit. (7.35) is the invariant that is cascaded by our turbulence, being injected by the ETG and dissipated by the effects of collisions. It is straightforward to show that the resultant free-energy budget is

$$\frac{1}{n_{0e}T_{0e}}\frac{\mathrm{d}W}{\mathrm{d}t} = \varepsilon - D_\parallel - D_\perp, \tag{7.36}$$

where

$$\varepsilon = \frac{1}{L_T}\int \frac{\mathrm{d}^3\boldsymbol{r}}{V}\,\frac{3}{2}\frac{\delta T_e}{T_{0e}}v_{Ex}, \quad v_{Ex} = -\frac{\rho_e v_{\mathrm{th}e}}{2}\frac{\partial\varphi}{\partial y}, \tag{7.37}$$

is the energy injection from the equilibrium temperature gradient, and

$$D_\parallel = \frac{v_{\mathrm{th}e}^2}{2\nu_{ei}}\int\frac{\mathrm{d}^3\boldsymbol{r}}{V}\left\{c_{\varphi\varphi}\left[\left(1+\frac{1}{\bar{\tau}}\right)\frac{\partial\varphi}{\partial z} - \frac{c_{\varphi T}}{c_{\varphi\varphi}}\frac{\partial}{\partial z}\frac{\delta T_e}{T_{0e}}\right]^2 + \left(c_{TT} - \frac{c_{\varphi T}^2}{c_{\varphi\varphi}}\right)\left(\frac{\partial}{\partial z}\frac{\delta T_e}{T_{0e}}\right)^2\right\}, \tag{7.38}$$

$$D_\perp = \nu_\perp\int\frac{\mathrm{d}^3\boldsymbol{r}}{V}\left[\left(\rho_\perp^{n_\nu}\nabla_\perp^{n_\nu}\varphi\right)^2 + \frac{3}{2}\left(\rho_\perp^{n_\nu}\nabla_\perp^{n_\nu}\frac{\delta T_e}{T_{0e}}\right)^2\right], \tag{7.39}$$

are the dissipation due to (parallel) thermal conduction and (perpendicular) hyperviscosity, respectively. Note that the prefactor of the last term in (7.38) is equal to c_3 [see (7.31)], and thus positive. The remainder of this section is devoted to characterising fully the dynamics between the outer scale, that dominates the energy injection ε, and the dissipation (inner) scale, that dominates $D_\perp$. We will find that the dissipative nature of the parallel dynamics, and the resultant presence of $D_\parallel$ in the free-energy budget, places a significant constraint on the behaviour of the system in the inertial range.

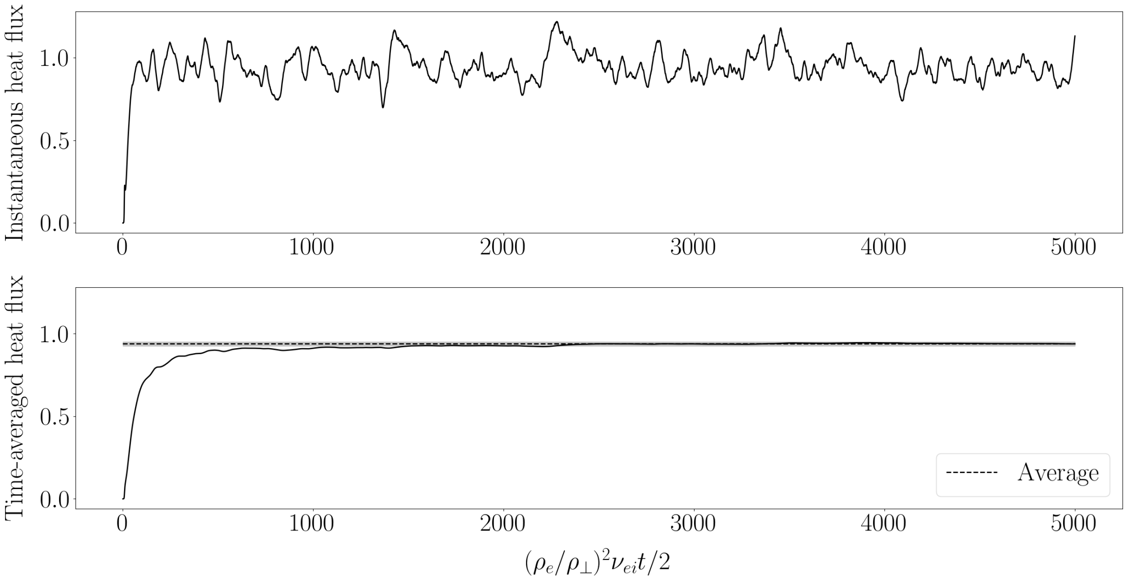

Figure 7.4: Turbulent heat flux in the high-resolution simulation (see table 7.1). The upper and lower panels show, respectively, the instantaneous and (rolling) time-averaged heat fluxes in solid black. The dashed horizontal line in the lower panel is the average value — as calculated over the entire time interval — while the transparent grey region around this value shows the error bar associated with the mean, calculated by means of a moving window average. The time-averaged heat flux converges to within the final error bar by $(\rho_e/\rho_\perp)^2\nu_{ei}t/2 \sim 2000$.

To ensure that we had sufficient numerical resolution for these investigations, we conducted a 'high-resolution' simulation (see table 7.1), on which we shall now focus. Due to the computational demands introduced by the higher resolution, the simulation was run only up to 5000 $(\rho_e/\rho_\perp)^2\nu_{ei}t/2$; this was sufficient to ensure that the heat flux had converged to some average value (see Figure 7.4).

7.2.1 Perpendicular isotropy

Throughout Chapter 6, we assumed $k_x \sim k_y \sim k_\perp$ because there was no *a priori* reason to suspect that the turbulence would preference anisotropic structures. This assumption of perpendicular isotropy is not obviously true and must be tested. Indeed, the maximum sETG growth rate (3.5) or (3.10) is at $k_x = 0$, and so the outer-scale energy injection is predominantly into so-called 'streamers': highly anisotropic ($k_x \ll k_y$) structures that can be identified in real space from the alternating structure of horizontal bands along the poloidal direction. In the context of ITG-driven turbulence,

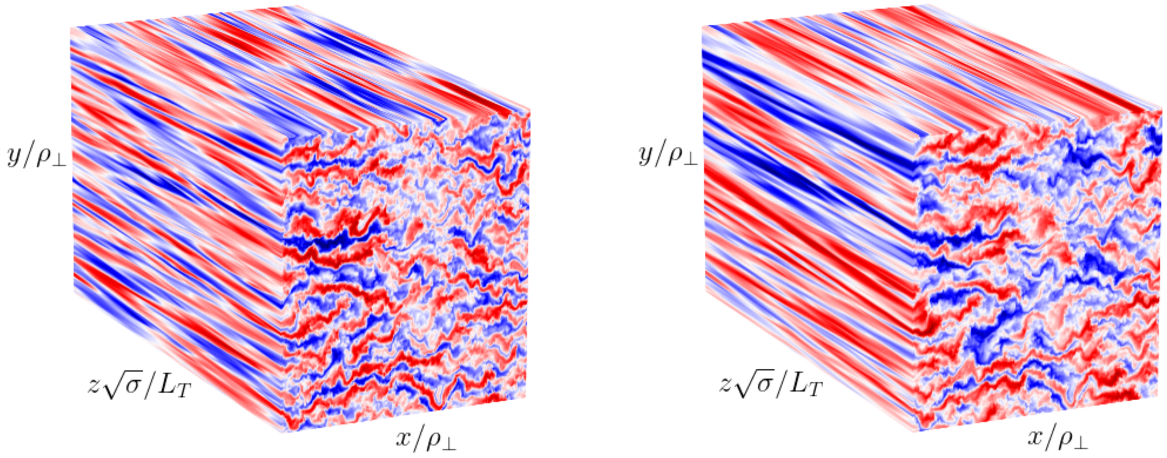

(a) $(L_T/\rho_\perp)\varphi$ (b) $(L_T/\rho_\perp)\delta T_e/T_{0e}$

Figure 7.5: Real-space snapshots of the (a) electrostatic potential and (b) temperature perturbations from the high-resolution simulation at $(\rho_e/\rho_\perp)^2\nu_{ei}t/2 = 3000$ (see table 7.1). The coordinate axes are as shown, while the red and blue colours correspond to regions of positive and negative fluctuation amplitude. The turbulence does not appear to be isotropic on the large scales that are visible in these plots (streamers are manifest), but it will turn out that it is isotropic in the inertial-range (see Section 7.2.1).

it has often been assumed that these streamers are broken apart by zonal flows (see [8, 12] and references therein), restoring isotropy at the outer scale, and from which isotropy in the inertial range is then assumed to follow. In ETG-driven turbulence, however, the role of zonal flows is less obvious, and the existence of an isotropic state far from guaranteed — the real-space snapshots of Figure 7.5 suggest that the system is in fact dominated by streamer-like structures on the largest scales, and there is minimal zonal-flow activity. We shall discuss the role of zonal flows further in Section 7.3.

To assess how isotropic the saturated state is, we plot the two-dimensional spectra

$$E^\varphi(k_x, k_y) = \int_{-\infty}^{\infty} \mathrm{d}k_\parallel \left\langle |\varphi_{\boldsymbol{k}}|^2 \right\rangle, \tag{7.40}$$

$$E^\varphi(k_\perp, \theta) = k_\perp \int_{-\infty}^{\infty} \mathrm{d}k_\parallel \left\langle |\varphi_{\boldsymbol{k}}|^2 \right\rangle, \tag{7.41}$$

in panels (a) and (b) of Figure 7.6, respectively. Here and in what follows, $\theta = \tan^{-1}(k_y/k_x)$ is the polar angle in the perpendicular wavenumber plane. In both representations, we find that the spectrum is approximately isotropic with respect to the perpendicular wavenumbers: at scales sufficiently smaller than the outer scale (viz., in the inertial range) contours of constant E^φ are either circles, in the case of (7.40), or

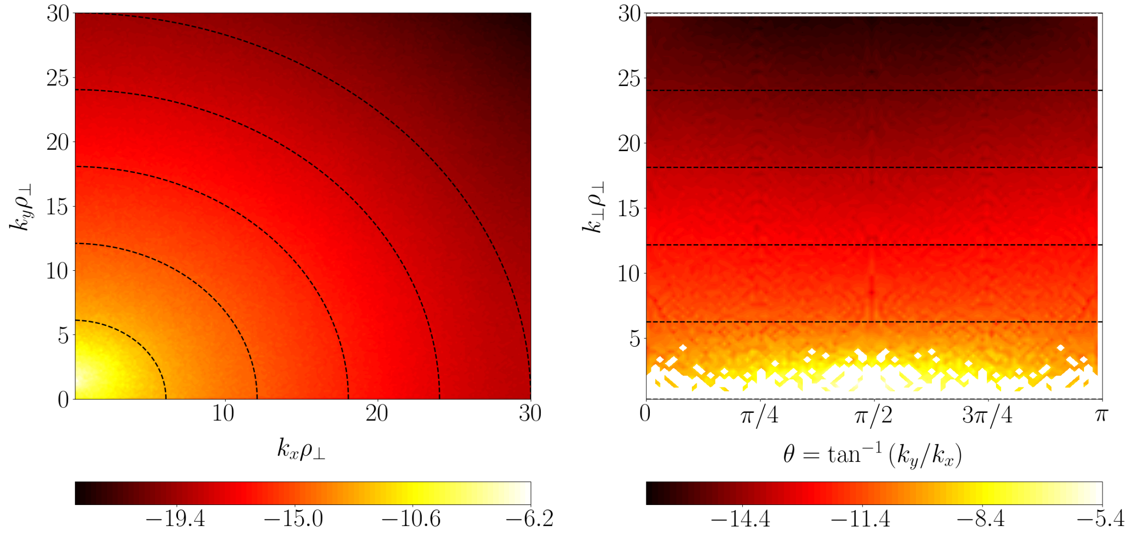

(a) $\log E^{\varphi}(k_x, k_y)$ (b) $\log E^{\varphi}(k_\perp, \theta)$

Figure 7.6: Contour plots of the two-dimensional spectra of the electrostatic potential perturbations: (a) in Cartesian coordinates, with the radial and poloidal wavenumbers plotted on the horizontal and vertical axes, respectively. Contours of constant $E^{\varphi}(k_x, k_y)$ (7.40) (black dashed lines) are approximately circular far away from the origin, where injection is localised; (b) in plane-polar coordinates, with $\theta = \tan^{-1}(k_y/k_x)$ and $k_\perp\rho_\perp$ plotted on the horizontal and vertical axes, respectively. Contours of constant $E^{\varphi}(k_\perp, \theta)$ (7.41) (black dashed lines) are approximately horizontal far away from $k_\perp\rho_\perp \lesssim 1$, where injection is localised.

horizontal lines, in the case of (7.41). The corresponding spectra for the temperature perturbations, defined analogously to (7.40) and (7.41), display a similar isotropy, as in Figure 7.7. The system thus appears to be isotropic in the inertial range, despite the fact that the largest scales are anisotropic due to the existence of streamers and the lack of vigorous zonal flows to break them apart.

7.2.2 Revisiting critical balance

An important observation about our equations (7.25) and (7.26) that we have not yet made is that, given the definition of the convective time derivative $\mathrm{d}/\mathrm{d}t$ (2.10), the nonlinearity in the φ equation (7.25) vanishes identically. This means that $\delta T_e/T_{0e}$ is, in fact, the only field that is advected nonlinearly on the nonlinear turnover time t_{nl}^{-1} (6.12), with φ being ‘sourced’ by the temperature perturbations through the last term on the right-hand side of (7.25). However, the scaling of the potential with perpendicular wavenumbers (6.8) was derived assuming that the free-energy density

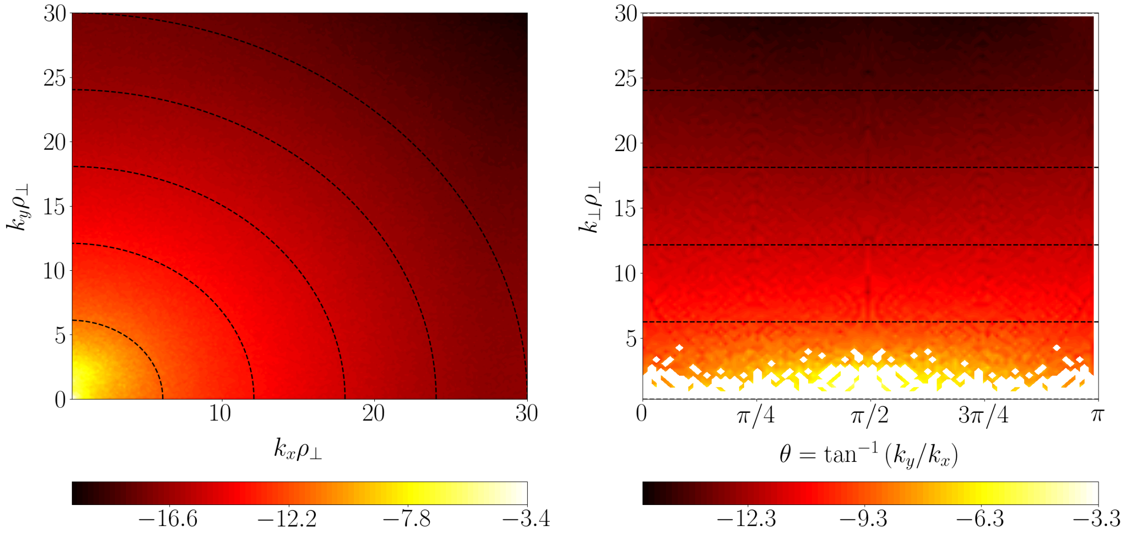

(a) $\log E^T(k_x, k_y)$ (b) $\log E^T(k_\perp, \theta)$

Figure 7.7: The same as Figure 7.6, except for the two-dimensional spectra of the temperature perturbations. Once again, contours of constant (a) $E^T(k_x, k_y)$ or (b) $E^T(k_\perp, \theta)$ (black dashed lines) are either, respectively, circles or approximately horizontal lines away from where injection is localised.

being advected at a given scale $k_\perp^{-1}$ was dominated by the contribution to (7.35) arising from the electrostatic potential — it is not obvious that this should still hold in a case where φ itself is not being advected nonlinearly. Let us assume instead that the free-energy density is dominated by the contribution arising from the temperature perturbation, viz., instead of (6.8), we have

$$t_{\rm nl}^{-1}\frac{\delta\bar{T}_e^2}{T_{0e}^2} \sim \varepsilon = \text{constant} \quad \Rightarrow \quad \bar{\varphi}\frac{\delta\bar{T}_e^2}{T_{0e}^2} \sim \frac{\varepsilon}{\Omega_e}(k_\perp\rho_e)^{-2}. \tag{7.42}$$

To estimate the size of the electrostatic potential, we balance its time derivative with the last term in (7.25), yielding

$$\bar{\varphi} \sim \frac{\omega_\parallel}{\omega}\frac{\delta\bar{T}_e}{T_{0e}}, \quad \omega_\parallel \equiv \frac{\left(k_\parallel v_{\rm the}\right)^2}{\nu_{ei}}, \tag{7.43}$$

which, unlike in (6.18), we expect to hold at each scale, since φ is sourced linearly by $\delta T_e/T_{0e}$ at each scale. (7.43) implies that the potential and temperature perturbations will be comparable at both the outer-scale (6.20) and throughout the inertial range if one adopts the critical balance conjecture as (6.19), viz.

$$t_{\rm nl}^{-1} \sim \omega \sim \omega_\parallel. \tag{7.44}$$

Combining (7.42) and (7.44), one re-obtains the previous scaling of inertial-range amplitudes and of the nonlinear time

$$\bar{\varphi} \sim \frac{\delta \bar{T}_e}{T_{0e}} \sim \left(\frac{\varepsilon}{\Omega_e}\right)^{1/3} (k_\perp \rho_e)^{-2/3}, \quad t_{\rm nl}^{-1} \sim \Omega_e \left(\frac{\varepsilon}{\Omega_e}\right)^{1/3} (k_\perp \rho_e)^{4/3}, \tag{7.45}$$

as well as the resultant 1D perpendicular energy spectra:

$$E_\perp^\varphi(k_\perp) \sim E_\perp^T(k_\perp) \sim \frac{\bar{\varphi}^2}{k_\perp} \propto k_\perp^{-7/3}, \tag{7.46}$$

where $E_\perp^T$ is defined analogously to $E_\perp^\varphi$ [see (6.7)]. Then, using the second expression in (7.45), (7.44) translates into the following proportionality relationship between parallel and perpendicular scales in the inertial range:

$$k_\parallel \propto k_\perp^{2/3}. \tag{7.47}$$

Defining the 1D parallel energy spectrum

$$E_\parallel^\varphi(k_\parallel) \equiv 2\pi \int_0^\infty \mathrm{d}k_\perp k_\perp \left\langle |\varphi_{\boldsymbol{k}}|^2 \right\rangle, \tag{7.48}$$

where the angle brackets once again denote the ensemble average, and the corresponding temperature spectrum defined analogously, the combination of (7.47) and the scaling of the electrostatic potential (6.8) imply the following inertial-range scaling:

$$\bar{\varphi} \propto k_\parallel^{-1} \quad \Rightarrow \quad E_\parallel^\varphi(k_\parallel) \sim E_\parallel^T(k_\parallel) \sim \frac{\bar{\varphi}^2}{k_\parallel} \propto k_\parallel^{-3}. \tag{7.49}$$

The 1D spectra (7.46) and (7.49) are plotted in Figure 7.8. Both follow quite well the predicted scaling below the outer scale, at least up until the point at which the spectrum begins to steepen due to the effects of dissipation: namely, either hyperviscosity or parallel thermal conduction. To understand the relative roles of these sources of dissipation within the turbulence, however, we need to consider 2D spectra, as in the following section.

7.2.3 Two-dimensional spectra

To test our understanding of the inertial range more vigorously, it is interesting to consider the 2D spectra:

$$E_{\rm 2D}^\varphi(k_\parallel, k_\perp) = 2\pi k_\perp \left\langle |\varphi_{\boldsymbol{k}}|^2 \right\rangle, \tag{7.50}$$

$$E_{\rm 2D}^T(k_\parallel, k_\perp) = 2\pi k_\perp \left\langle |\delta T_{e\boldsymbol{k}}/T_{0e}|^2 \right\rangle. \tag{7.51}$$

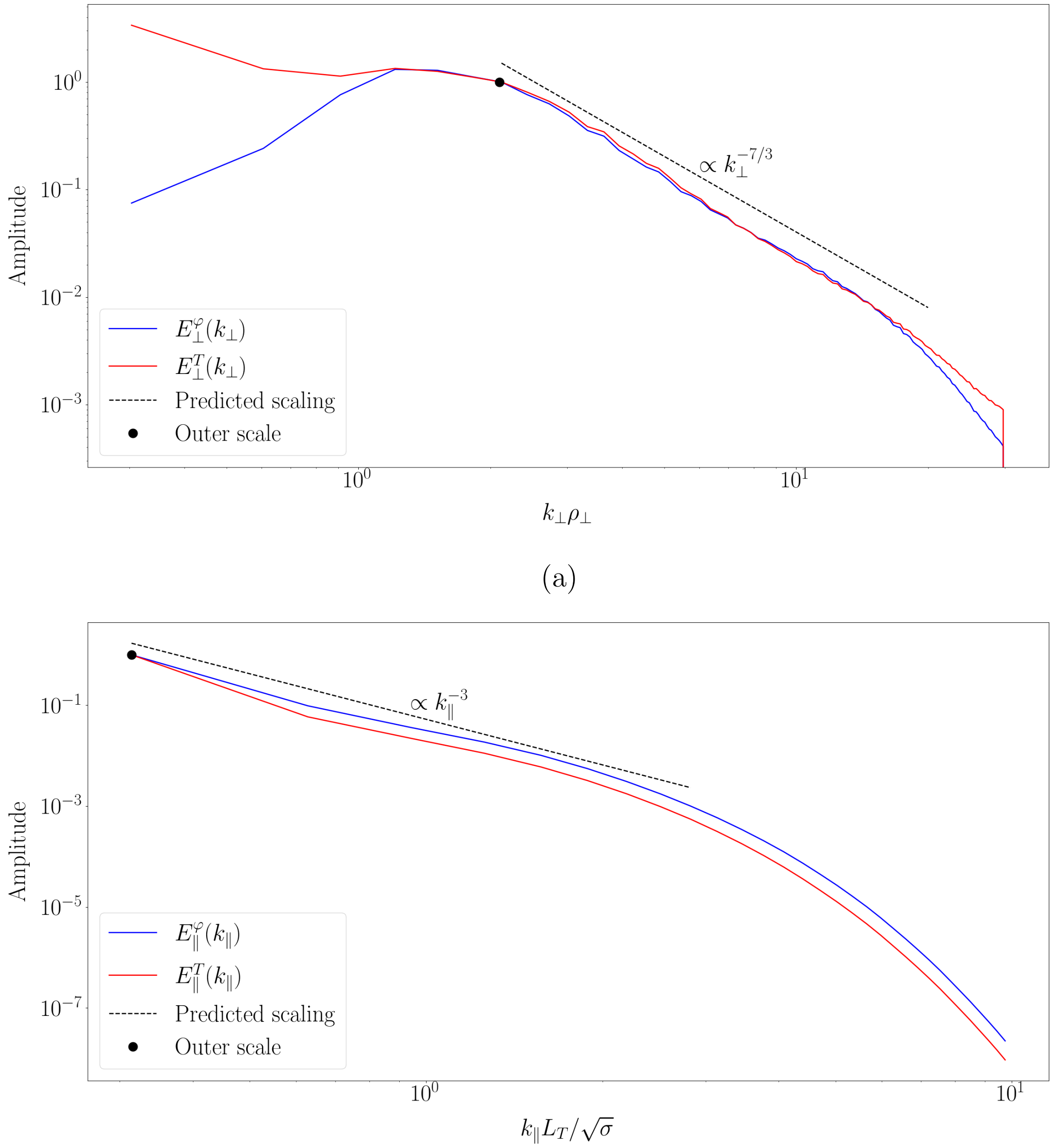

(a)

(b)

Figure 7.8: The 1D (a) perpendicular (6.7) and (b) parallel (7.48) energy spectra, normalised to their value at the outer scale. The spectra of the electrostatic potential are plotted in blue, those of the temperature perturbations are in red. The predicted inertial-range scalings (7.46) and (7.49) are shown by the dashed black lines. The location of the outer scale is indicated by the black dot. In (a), this is calculated from the maximum of (7.33), while in (b), it is calculated from the maximum of the 1D parallel spectrum of the energy injection, defined analogously to (7.33).

Unlike in the previous section, we can no longer assume that $E^{\varphi}_{\parallel,\perp} \sim E^{T}_{\parallel,\perp}$; this was only true as we were previously considering "integrated" 1D spectra dominated by the wavenumbers where the critical-balance conjecture (7.44) was assumed satisfied, and the two fields thus exhibiting the same scaling $\bar{\varphi} \sim \delta\bar{T}_e/T_{0e}$ [cf. (7.43) for $\omega \sim \omega_{\parallel}$]. With this in mind, we will first consider the spectrum of the temperature perturbations, from which the spectrum of the potential perturbations can then be inferred.

We consider two wavenumber regions, above and below the "critical-balance line" (7.47):

$$E^{T}_{\mathrm{2D}}(k_{\parallel}, k_{\perp}) \sim \begin{cases} k_{\parallel}^{-a} k_{\perp}^{b}, & k_{\parallel} \gtrsim k_{\perp}^{2/3}, \\ k_{\perp}^{-c} k_{\parallel}^{d}, & k_{\parallel} \lesssim k_{\perp}^{2/3}, \end{cases} \tag{7.52}$$

where a, b, c, and d are positive constants to be determined. Here, and in what follows, whenever our expressions appear to be dimensionally incorrect, this is because we have chosen to normalise our wavenumbers to the outer scale $k_{\parallel}L_{\parallel} \to k_{\parallel}$, $k_{\perp}/k_{\perp}^{o} \to k_{\perp}$ so as to reduce notational clutter.

Evidently, the scalings in the two regions in (7.52) must match along the boundary $k_{\parallel} \sim k_{\perp}^{2/3}$, giving

$$a + d = \frac{3}{2}\left(b + c\right). \tag{7.53}$$

Then, if $a > 1$, $k_{\parallel} \sim k_{\perp}^{2/3}$ will be the energy-containing parallel wavenumber at a given $k_{\perp}$. The 1D perpendicular spectrum is, therefore,

$$E^{T}_{\perp}(k_{\perp}) = \int \mathrm{d}k_{\parallel}\, E^{T}_{\mathrm{2D}}(k_{\parallel}, k_{\perp}) \sim \int_{0}^{k_{\perp}^{2/3}} \mathrm{d}k_{\parallel}\, k_{\perp}^{-c} k_{\parallel}^{d} \sim k_{\perp}^{-c+\frac{2}{3}(1+d)}. \tag{7.54}$$

This must match the scaling (7.46) of the 1D perpendicular spectrum derived from the constant-flux conjecture, implying that

$$c = \frac{2}{3}(1+d) + \frac{7}{3}. \tag{7.55}$$

The final two constraints follow from imposing boundary conditions as $k_{\parallel}, k_{\perp} \to 0$ at constant $k_{\perp}, k_{\parallel}$. The scaling of the spectrum as $k_{\perp} \to 0$ (in the region $k_{\parallel} \gtrsim k_{\perp}^{2/3}$) can be determined purely kinematically: the low-$k_{\perp}$ asymptotic behaviour of a homogenous isotropic system must be $k_{\perp}^{3}$, implying that

$$b = 3. \tag{7.56}$$

This is a fairly standard result[2] (see, e.g., [87]). The scaling as $k_\parallel \to 0$ (in the region $k_\parallel \lesssim k_\perp^{2/3}$) follows from causality. Indeed, in Section 6.2, we argued that the critical balance (7.44) is a causality condition: two points along a field line can only remain correlated with one another if information can propagate between them faster than they are decorrelated by the nonlinearity, viz., fluctuations become decorrelated for $\omega_\parallel \lesssim t_{\rm nl}^{-1}$. This latter condition is exactly $k_\parallel \lesssim k_\perp^{2/3}$, meaning that the parallel spectrum of the perturbations in this region must be the spectrum of white noise, implying

$$d = 0. \tag{7.57}$$

Combining (7.53)-(7.57), we find

$$a = 9, \quad c = 3, \tag{7.58}$$

which gives us the following scalings of the 2D spectrum of the temperature perturbations[3]:

$$E_{\rm 2D}^T(k_\parallel, k_\perp) \sim \begin{cases} k_\parallel^{-9} k_\perp^3, & k_\parallel \gtrsim k_\perp^{2/3}, \\ k_\perp^{-3} k_\parallel^0, & k_\parallel \lesssim k_\perp^{2/3}. \end{cases} \tag{7.59}$$

Turning now to the 2D spectrum of the potential perturbations, analogously to (7.52), the conditions (7.53) and (7.55) are unmodified — the spectrum must still be continuous along $k_\parallel \sim k_\perp^{2/3}$, and match the scaling of the 1D perpendicular spectrum that follows from the constant-flux conjecture, which is the same for both the potential and temperature perturbations. Similarly, the scaling of the spectrum as $k_\perp \to 0$ (in the

---

[2] Though not one that is universally true. For example, [114] (see also appendix C of [115]) showed that a $k_\perp^1$ scaling could emerge through a balance between turbulent diffusion and the nonlinear 'source' that would otherwise give rise to the $k_\perp^3$ scaling. Let us estimate the rate of turbulent diffusion in our system. The dominant contributions to the turbulent diffusion coefficient D will be those on the energy-containing scales $k_\parallel \sim k_\perp^{2/3}$, so $D \sim v_E^2 t_{\rm nl} \sim \tilde{\omega}_\parallel / \tilde{k}_\perp^2$, where have used the critical-balance condition (7.44), and the tildes denote quantities evaluated along $k_\parallel \sim k_\perp^{2/3}$ (at small perpendicular scales relative to those that we are considering). The rate of turbulent diffusion will thus be $k_\perp^2 D \sim \tilde{\omega}_\parallel (k_\perp/\tilde{k}_\perp)^2 \ll \omega_\parallel$, since we are in the region $k_\parallel \gtrsim k_\perp^{2/3}$ where $\omega_\parallel \gg \tilde{\omega}_\parallel$ and $k_\perp \ll \tilde{k}_\perp$. The effects of turbulent diffusion are thus negligible, and so we are justified in adopting the $k_\perp^3$ scaling. Note that the survival of the $k_\perp^3$ scaling is a noteworthy feature of our system, where the $k_\parallel \gtrsim k_\perp^{2/3}$ dynamics are dominated by parallel dissipation due to thermal conductivity, rather than by waves (as in [115]). We shall discuss further consequences of this distinction in Section 7.2.4.

[3] [87] obtained, through identical methods, a similar result in their considerations of long-wavelength electrostatic turbulence. Specifically, they found that $a = 5$ and $c = 11/3$ — this was a consequence of the fact that they considered collisionless turbulence, for which the critical-balance condition is $k_\parallel \sim k_\perp^{4/3}$ [see (6.12)].

region $k_\parallel \gtrsim k_\perp^{2/3}$) will once again be $k_\perp^3$ by the same kinematic argument, implying that $b = 3$. However, the causality argument that led to the white-noise scaling at $k_\parallel \lesssim k_\perp^{2/3}$ now no longer holds, because φ cannot be directly decorrelated by the nonlinearity. Instead, it inherits its scaling from $\delta T_e/T_{0e}$ via the balance (7.43), viz.,

$$E_{\rm 2D}^{\varphi} \sim \frac{\omega_\parallel^2}{\omega^2} E_{\rm 2D}^{T} \sim \frac{k_\parallel^4 k_\perp^{-3}}{\omega^2}, \tag{7.60}$$

where we have used $\omega_\parallel \propto k_\parallel^2$ and the second expression in (7.59). Now, in the region $k_\parallel \lesssim k_\perp^{2/3}$, we expect thermal conductivity in the temperature equation to be subdominant to the nonlinear rate, and so estimating $\omega \sim t_{\rm nl}^{-1} \propto k_\perp^{4/3}$ in (7.60), we find that

$$d = 4. \tag{7.61}$$

Combining (7.53), (7.55) and (7.61), it follows that

$$a = 9, \quad c = \frac{17}{3}, \tag{7.62}$$

which gives us the following scalings of the 2D spectrum of the potential fluctuations:

$$E_{\rm 2D}^{\varphi}(k_\parallel, k_\perp) \sim \begin{cases} k_\parallel^{-9} k_\perp^3, & k_\parallel \gtrsim k_\perp^{2/3}, \\ k_\perp^{-17/3} k_\parallel^4, & k_\parallel \lesssim k_\perp^{2/3}. \end{cases} \tag{7.63}$$

Note that the perpendicular wavenumber scaling in (7.63) for $k_\parallel \lesssim k_\perp^{2/3}$ is consistent with the assumption that the frequency is comparable to the nonlinear rate [cf. (7.60) for $\omega \sim t_{\rm nl}^{-1}$].

Cuts of the 2D spectra (7.50) and (7.51) at constant $k_\perp$ and $k_\parallel$ are shown in figures 7.10 and 7.9, respectively, showing good agreement with the scalings predicted by (7.59) and (7.63). The full 2D spectrum of the temperature perturbations is plotted in Figure 7.11.

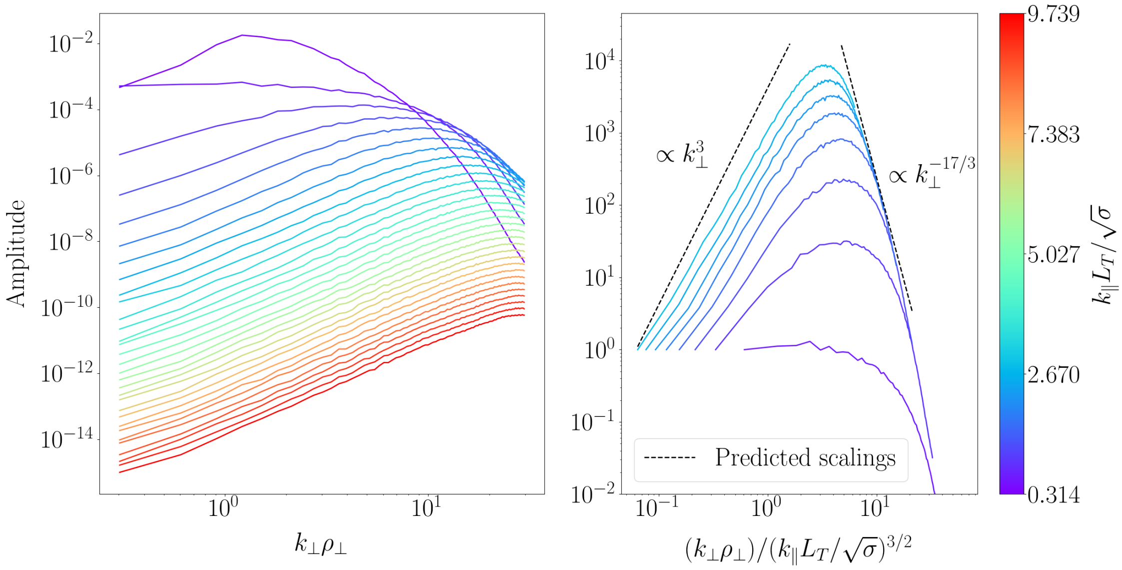

(a) $E_{\mathrm{2D}}^{\varphi}(k_\parallel = \mathrm{constant}, k_\perp)$

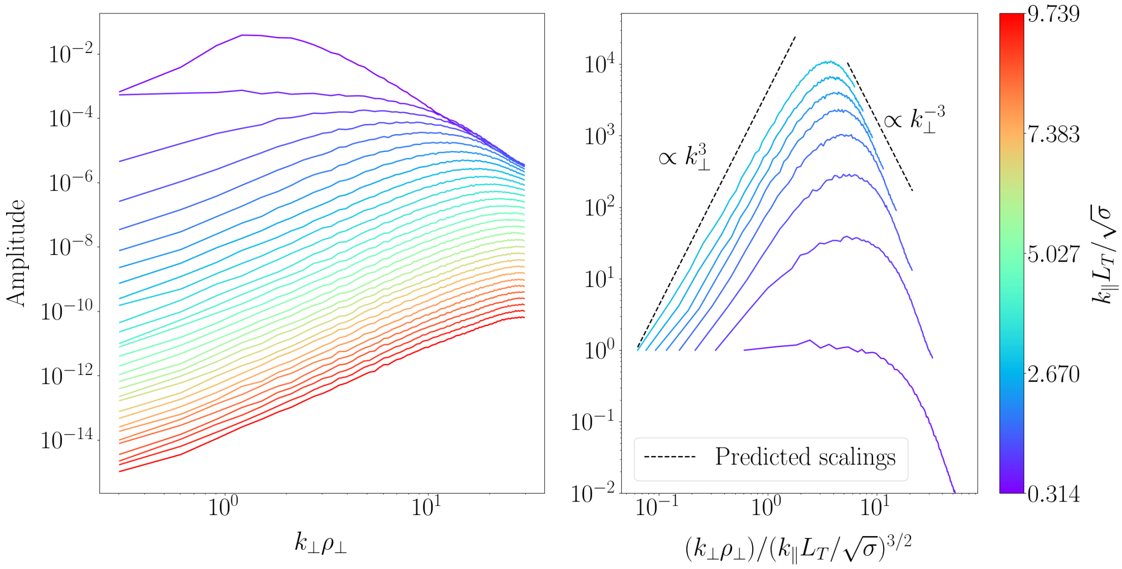

(b) $E_{\mathrm{2D}}^{T}(k_\parallel = \mathrm{constant}, k_\perp)$

Figure 7.9: Cuts of the 2D spectra of the (a) electrostatic potential and (b) temperature perturbations at constant $k_\parallel$. The colours indicate the value of $k_\parallel L_T/\sqrt{\sigma}$ for a given cut. The left-hand panels show the entire spectrum plotted as a function of $k_\perp \rho_\perp$. The right-hand panels show selected cuts for $k_\parallel L_T/\sqrt{\sigma}$ within the inertial range, with the horizontal axis rescaled according to the critical-balance relation (7.47). The black dashed lines show the predicted scalings (7.63) and (7.59) in panels (a) and (b), respectively. The spectra show reasonable agreement with the scalings at both small and large (perpendicular) scales, despite the effects of hyperviscosity being present on the smallest scales.

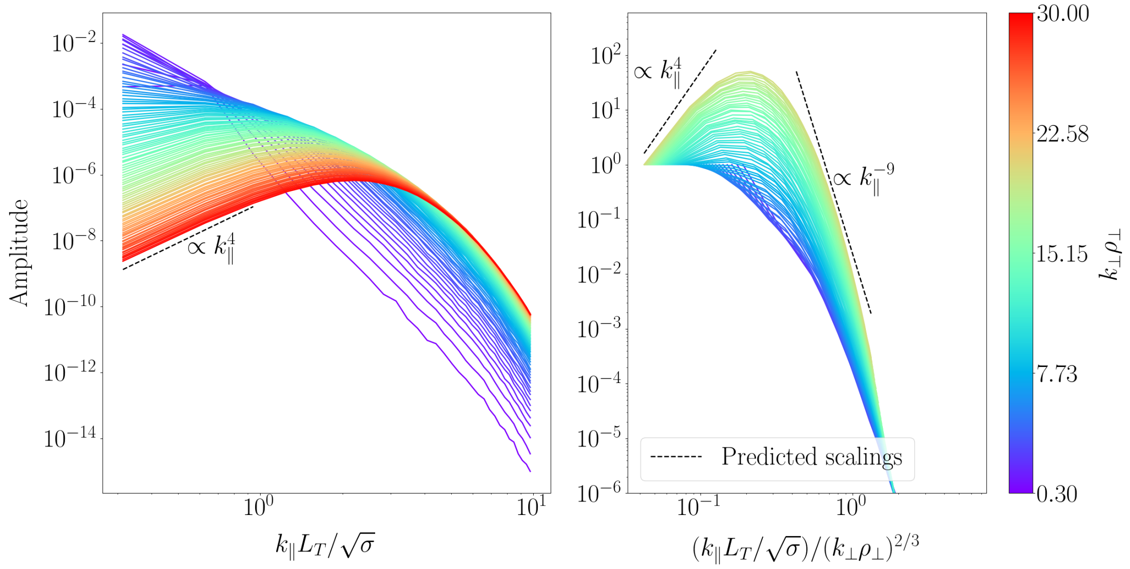

(a) $E_{2\mathrm{D}}^{\varphi}(k_\parallel, k_\perp = \text{constant})$

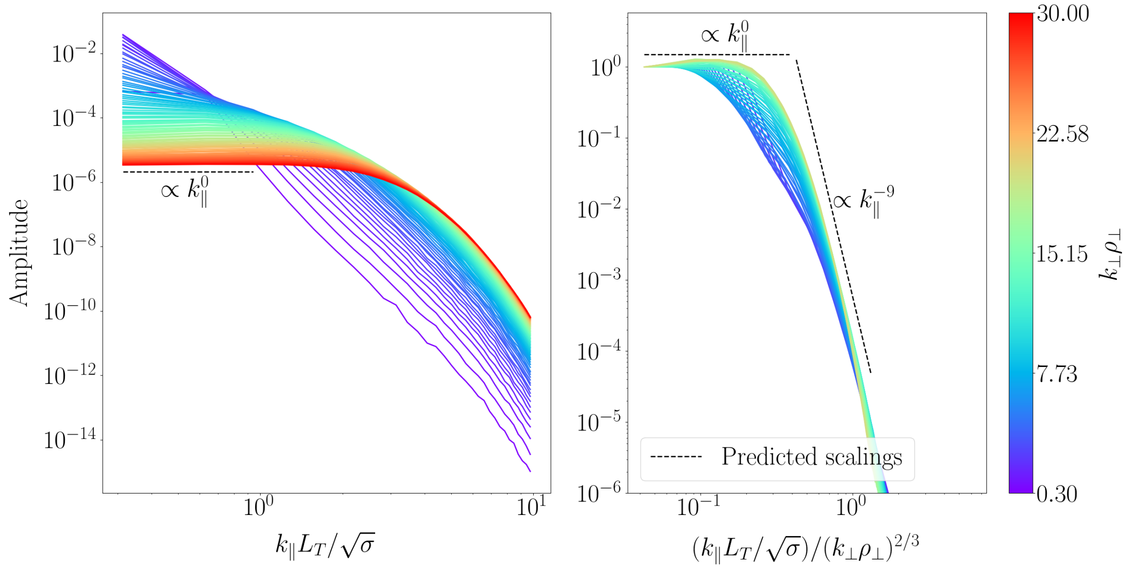

(b) $E_{2\mathrm{D}}^{T}(k_\parallel, k_\perp = \text{constant})$

Figure 7.10: Cuts of the 2D spectra of the (a) electrostatic potential and (b) temperature perturbations at constant $k_\perp$. The colours indicate the value of $k_\perp\rho_\perp$ for a given cut. The left-hand panel shows the entire spectrum plotted as a function of $k_\parallel L_T$. The right-hand panel shows cuts of the spectrum for $k_\perp\rho_\perp$ within the inertial range, with the horizontal axis rescaled according to the critical-balance relation (7.47). The black dashed lines show the predicted scalings (7.63) and (7.59) in panels (a) and (b), respectively. There is very good agreement with the predicted scalings, especially for those at $k_\parallel \lesssim k_\perp^{2/3}$, which extend well-beyond the inertial range to higher $k_\perp\rho_\perp$, as can be seen from the left-hand panel — this is not surprising because the causality argument is not sensitive to the precise details of the decorrelation physics.

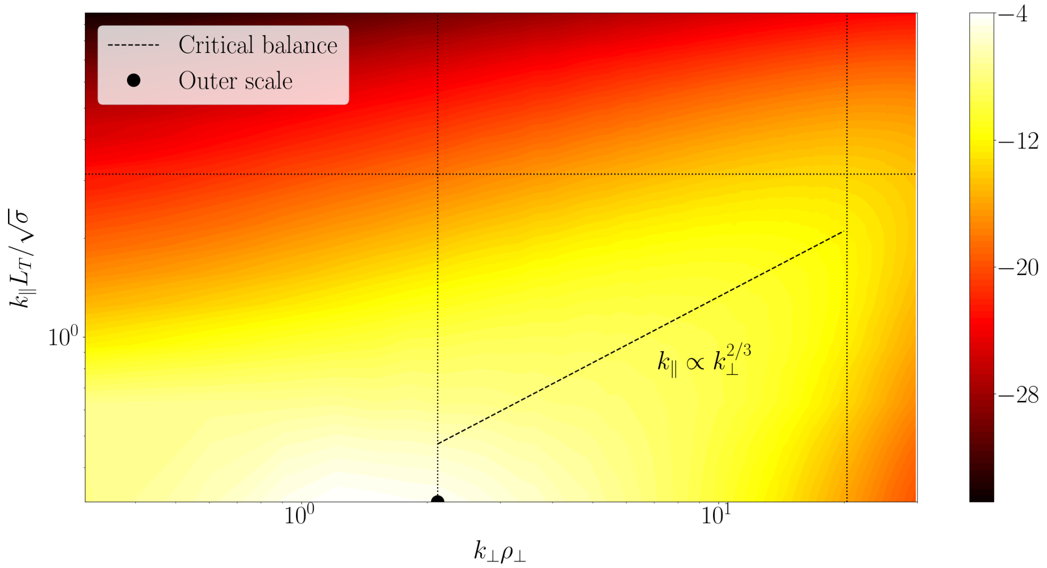

Figure 7.11: A contour plot of the logarithm of the 2D spectrum (7.51) of the temperature perturbations in the $(k_\parallel, k_\perp)$ plane. The line of critical balance is shown as the dashed black line, while the outer scale is shown by the black dot. The horizontal dotted line shows the upper bound on the parallel-wavenumber cuts plotted in the right-hand panels of Figure 7.9. Similarly, the vertical dotted lines show the lower and upper bound on the perpendicular wavenumber cuts plotted in the right-hand panels of Figure 7.10.

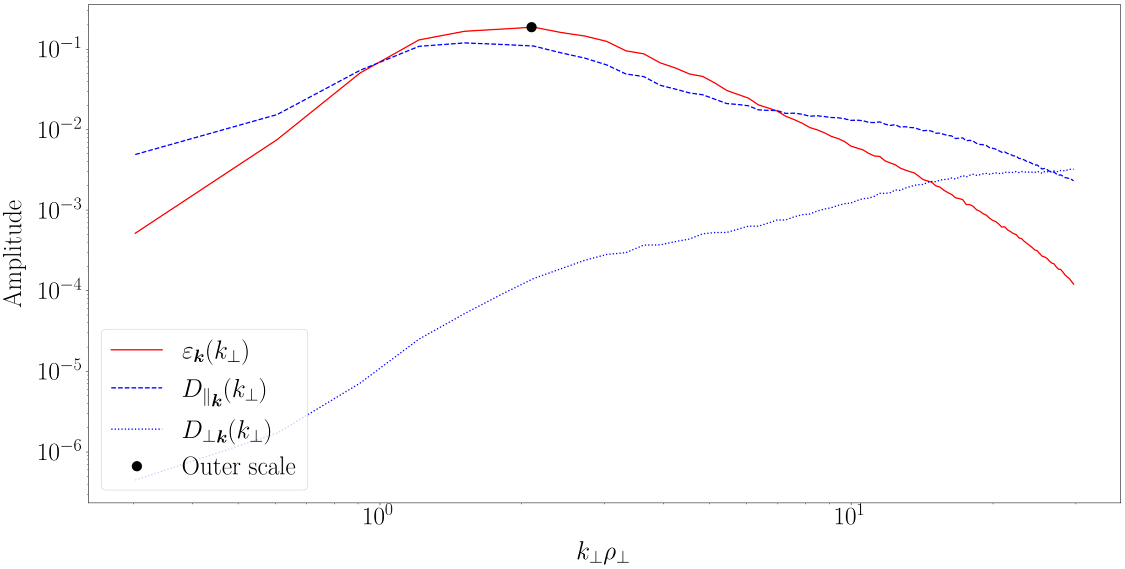

Figure 7.12: 1D perpendicular spectra of the energy injection (7.33) (solid red), parallel dissipation (7.64) (dashed blue) and perpendicular dissipation (7.65) (dotted blue). The location of the outer scale is shown by the black dot. It is clear that the rate of parallel dissipation is significant throughout almost all of the wavenumber range, while perpendicular dissipation takes over at the very smallest scales.

7.2.4 Dissipation in critically-balanced turbulence

Throughout this chapter, we have been assuming that there exists a separation of scales between the outer scale and the dissipative scales, with energy being carried from the former to the latter via a constant-flux cascade. However, a perceptive reader may have noticed that this assumption is not obviously satisfied: the existence of the collisional sETG depends intrinsically on the presence of thermal conduction (see Section 3.2), which is a (primarily) dissipative effect. Plotting, in Figure 7.12, the perpendicular wavenumber spectrum of the injection (7.33) alongside that of the parallel and perpendicular dissipation, defined as [cf. (7.38) and (7.39)]

$$D_{\parallel\boldsymbol{k}}(k_\perp) = 2\pi k_\perp \int_{-\infty}^{\infty} \mathrm{d}k_\parallel \left\langle \omega_\parallel \left[c_{\varphi\varphi} \left| \left(1+\frac{1}{\bar{\tau}}\right)\varphi_{\boldsymbol{k}} - \frac{c_{\varphi T}}{c_{\varphi\varphi}} \frac{\delta T_{e\boldsymbol{k}}}{T_{0e}} \right|^2 + \left(c_{TT} - \frac{c_{\varphi T}^2}{c_{\varphi\varphi}} \right) \left| \frac{\delta T_{e\boldsymbol{k}}}{T_{0e}} \right|^2 \right] \right\rangle, \tag{7.64}$$

$$D_{\perp\boldsymbol{k}}(k_\perp) = 2\pi k_\perp \int_{-\infty}^{\infty} \mathrm{d}k_\parallel \left\langle (k_\perp \rho_\perp)^{2n_\nu} \nu_\perp \left(|\varphi_{\boldsymbol{k}}|^2 + \frac{3}{2} \left| \frac{\delta T_{e\boldsymbol{k}}}{T_{0e}} \right|^2 \right) \right\rangle, \tag{7.65}$$

we see that the parallel dissipation is significant, and comparable to the energy injection, throughout almost the entire wavenumber range. How, then, is the presence of this dissipation throughout the majority of the (perpendicular) wavenumber space consistent with the idea that the turbulence proceeds via a constant-flux cascade? The answer lies in the very steep parallel wavenumber scaling of the 2D spectra (7.59) and (7.63) in the region $k_\parallel \gtrsim k_\perp^{2/3}$. In terms of timescales, this wavenumber constraint corresponds to $\omega_\parallel \gtrsim t_{\mathrm{nl}}^{-1}$, and thus to a region of dominant thermal conduction that attempts to erase parallel structure created by the turbulence. In fact, this region is so efficient at erasing parallel structure that it is an ineffective dissipation region for free energy: the free energy cannot be nonlinearly transferred into this region in an efficient way, and instead cascades towards higher perpendicular wavenumbers along the critical balance line, eventually encountering the effects of perpendicular dissipation, introduced, in this case, through hyperviscosity. Thus, in effect, the parallel conduction region becomes a ‘barrier’ that constrains the cascade of energy in wavenumber space to remain below the critical balance line $k_\parallel \sim k_\perp^{2/3}$. It thus appears that the system organises itself in such a way as to maintain a constant-flux cascade to small scales, despite the presence of dominant (parallel) dissipation.

The causality argument behind the critical-balance conjecture must therefore be modified as follows. Since there is no mechanism to preserve the parallel coherence of structures created by perpendicular mechanisms (via injection due to the ETG, or nonlinear cascade), one expects them to break up in the parallel direction to as fine scales as the system will allow. The limiting factor for this parallel refinement is that if structures reach parallel scales such that $k_\parallel \gtrsim k_\perp^{2/3}$, they are immediately wiped out by heat conduction. This process is so efficient that there is little nonlinear coupling into such small parallel scales: parallel dissipation acts not as a sink for the cascade, but as a "wall" along which the cascade is constrained to take place.

One could dismiss this observation as being a peculiarity of the collisional model that we have chosen to consider, given that the dissipative nature of collisional sETG instability (3.10) is hard-wired by assumption. However, this picture is not entirely different from what is observed in more generic systems of plasma turbulence: e.g., [116] observed an overlap of the spatial scales of energy injection and dissipation in electrostatic, ion-scale toroidal gyrokinetic simulations, as did [96] in the context of Alfvénic turbulence. Indeed, the same behaviour could also be relevant in the context of kinetic ETG-driven turbulence. The growth rate of the collisionless sETG (3.5) is limited by the parallel streaming rate $k_\parallel v_{\mathrm{the}}$, which is also the rate of Landau damping; viewed within the context of the current discussion, this suggests, perhaps, that Landau damping could play a dissipative role similar to that of the thermal conduction in determining the way in which the system organises itself in order to support a constant-flux cascade of energy to small scales. Then, the rates of either parallel streaming or thermal conduction appearing in the critical balances (6.11) and (6.19), respectively, can also be interpreted as being there because they are the rates of parallel dissipation, rather than parallel information propagation, limiting any further refinement of the parallel scale of the turbulent structures.

Taken together, the numerical evidence from the scan in $L_\parallel/L_T$ (Section 7.1.5) and consideration of the 1D and 2D energy spectra (sections 7.2.2 and Section 7.2.3, respectively) seems to us to be quite conclusive: collisional, electrostatic, sETG-driven turbulence saturates via a critically balanced, constant-flux nonlinear cascade of free energy to small perpendicular scales, with thermal conductivity limiting the cascade of free energy in parallel wavenumbers, clamping it to the line of critical balance $k_\parallel \propto k_\perp^{2/3}$. This is, in fact, one of only two existent numerical demonstrations of the existence of such a state within gradient-driven turbulence of this kind — the other being [12], in the context of ITG turbulence. The fact that turbulence in gradient-driven systems appears to behave similarly to those in which energy is injected by explicitly large-scale processes is encouraging from the perspective of theory, as it suggests that existing insights into, and experience of, the latter can be applied to the former, significantly less well studied case.

7.3 Finite magnetic-field gradients

As discussed in Section 7.1.3, we have been working in the limit of a very steep electron temperature gradient, in comparison to which the magnetic-field gradient could be neglected everywhere that it appeared in our equations. Formally, this corresponds to the limit of $L_B/L_T \to \infty$. Let us now consider the effect of including magnetic-field gradients within our electrostatic ETG system; restoring the magnetic-drift terms in (7.25) and (7.26) gives [see (A.98) and (A.99), respectively]:

$$\frac{\mathrm{d}}{\mathrm{d}t}\bar{\tau}^{-1}\varphi - \left(1+\frac{1}{\bar{\tau}}\right)\frac{c_{\varphi\varphi}v_{\mathrm{th}e}^2}{2\nu_{ei}}\frac{\partial^2\varphi}{\partial z^2} + \frac{c_{\varphi T}v_{\mathrm{th}e}^2}{2\nu_{ei}}\frac{\partial^2}{\partial z^2}\frac{\delta T_e}{T_{0e}} + \frac{\rho_e v_{\mathrm{th}e}}{L_B}\frac{\partial}{\partial y}\left[\left(1+\frac{1}{\bar{\tau}}\right)\varphi - \frac{\delta T_e}{T_{0e}}\right] = 0, \tag{7.66}$$

$$\frac{\mathrm{d}}{\mathrm{d}t}\frac{\delta T_e}{T_{0e}} + \frac{2}{3}\left(1+\frac{1}{\bar{\tau}}\right)\frac{c_{T\varphi}v_{\mathrm{th}e}^2}{2\nu_{ei}}\frac{\partial^2\varphi}{\partial z^2} - \frac{2}{3}\frac{c_{TT}v_{\mathrm{th}e}^2}{2\nu_{ei}}\frac{\partial^2}{\partial z^2}\frac{\delta T_e}{T_{0e}} - \frac{2}{3}\frac{\rho_e v_{\mathrm{th}e}}{L_B}\frac{\partial}{\partial y}\left[\left(1+\frac{1}{\bar{\tau}}\right)\varphi - \frac{7}{2}\frac{\delta T_e}{T_{0e}}\right] = -\frac{\rho_e v_{\mathrm{th}e}}{2L_T}\frac{\partial\varphi}{\partial y}. \tag{7.67}$$

Evidently, the presence of these terms introduces another instability into the system, the cETG (3.15), which could modify its turbulent transport properties. In particular, the turbulence theory of Section 6.2.2 assumed that the sETG was the dominant source of energy injection; this is only the case at sufficiently large L_B/L_T [see (3.16)], meaning that we would expect departures from the behaviour observed in the previous sections to be most significant for L_B/L_T of order unity.

A series of simulations were conducted in which L_B/L_T was varied, with all other parameters being kept the same as in the baseline simulation (see table 7.1); the heat flux from these simulations is plotted in Figure 7.13. It is readily apparent that the introduction of finite magnetic-field gradient led to a failure of saturation for all simulations where L_B/L_T was above the linear critical gradient for the sETG instability:

$$\frac{L_B}{L_T} > \frac{1}{2}\left(\bar{\tau} + \frac{40}{9}\frac{1}{\bar{\tau}^2}\right), \tag{7.68}$$

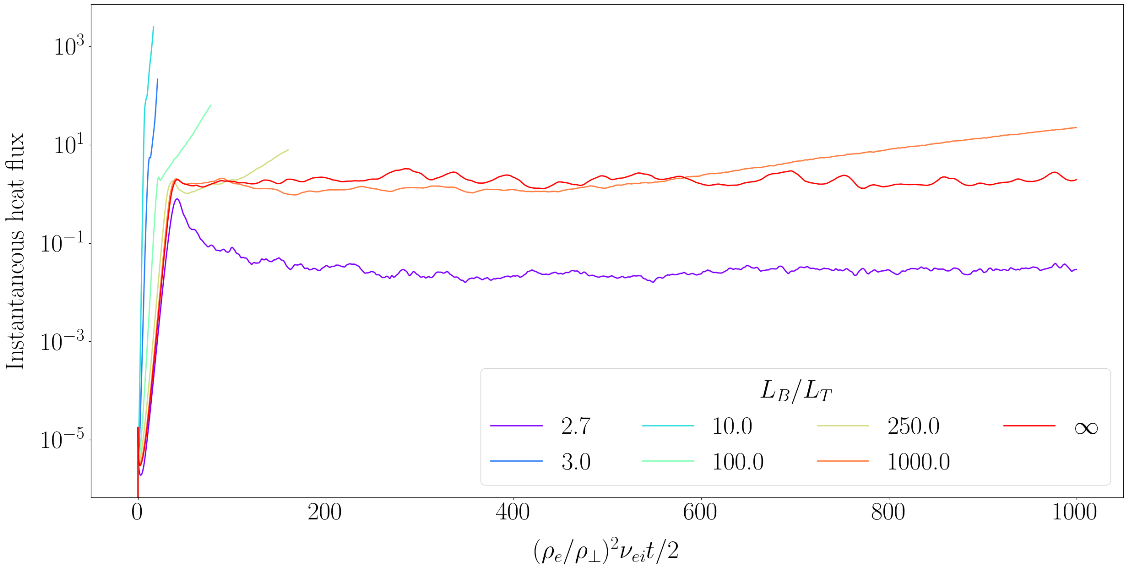

Figure 7.13: Timetraces of the instantaneous heat flux from simulations with finite L_B/L_T, with the limit of $L_B/L_T \to \infty$ shown for comparison. All parameters are the same as the baseline simulation (see table 7.1). The heat flux grows without bound in all simulations with (finite) L_B/L_T above the linear critical gradient (7.68) (≈ 2.72 for $\bar{\tau} = 1$), with the rate of divergence decreasing as L_B/L_T is increased. These simulations were stopped after shorter times due to computational demands. Note that we are potentially dealing with a case of non-interchangeability of limits, in that the long-time behaviour from a simulation in which $L_B/L_T \to \infty$ is not the same as that from one in which L_B/L_T is taken to infinity at long times; in the former case, the heat flux converges, while in the latter, it does not.

a threshold that can straightforwardly be derived from (7.66) and (7.67). This lack of saturation appears to be robust to changes in box size, box aspect ratio, and resolution in all of the coordinate directions.

This effect was first encountered in fluid simulations of ITG-driven turbulence by [117], who observed that saturation could be restored by adopting the modified adiabatic electron response (see, e.g., [74]) that one encounters on ion scales:

$$\frac{\delta n_i}{n_{0i}} = \frac{\delta n_e}{n_{0e}} = \frac{e(\phi - \overline{\phi})}{T_{0e}} \equiv \frac{e\phi'}{T_{0e}}, \tag{7.69}$$

where $\overline{\phi}$ and ϕ' denote the zonal and non-zonal components of the electrostatic potential. Indeed, (7.69) has been found to be crucial for capturing essential zonal flow physics [64, 66, 118]. Physically, this can be explained by the fact that (7.69) reserves a special status for zonal flows, in that it allows there to be non-trivial nonlinear interactions between the $\overline{\phi}$ and ϕ' through, e.g., the electrostatic $\boldsymbol{E} \times \boldsymbol{B}$ nonlinearity contained in the convective derivative (2.10).

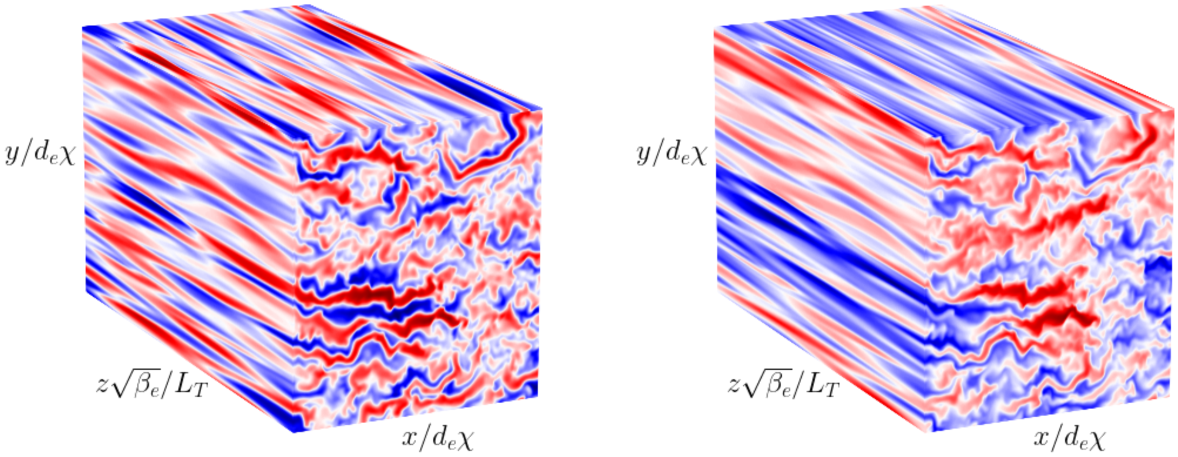

(a) $(L_T/\rho_\perp)\varphi$

(b) $(L_T/\rho_\perp)\delta T_e/T_{0e}$

Figure 7.14: Real-space snapshots of the (a) electrostatic potential and (b) temperature perturbations from the simulation with $L_B/L_T = 1000$ from Figure 7.13, taken at $(\rho_e/\rho_\perp)^2\nu_{ei}t/2 = 200$. The coordinate axes are as shown, while the red and blue colours correspond to regions of positive and negative fluctuation amplitude. At these early times, the turbulence appears similar to that of saturated sETG turbulence for $L_B/L_T \to \infty$ (cf. Figure 7.5), despite the eventual lack of saturation.

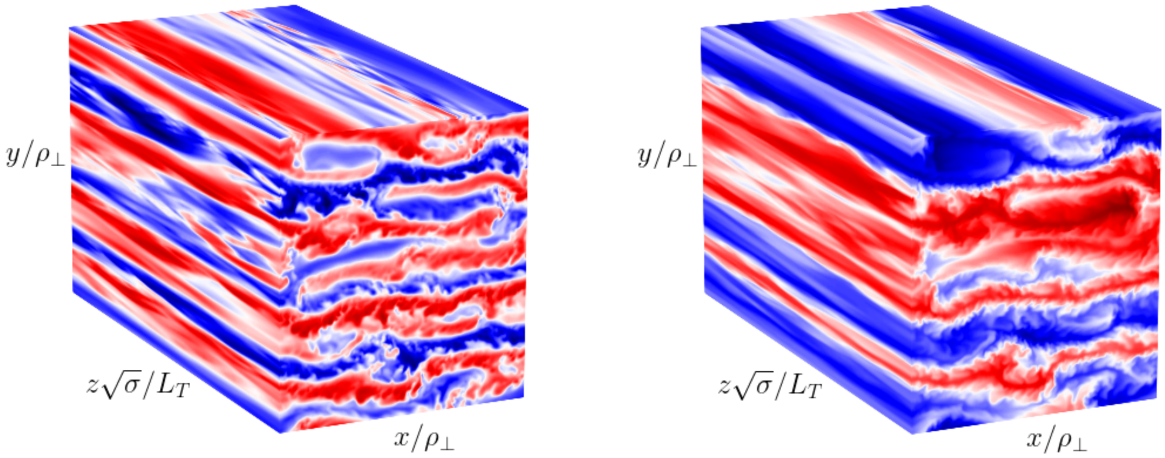

(a) $(L_T/\rho_\perp)\varphi$

(b) $(L_T/\rho_\perp)\delta T_e/T_{0e}$

Figure 7.15: The same as Figure 7.14, except taken at $(\rho_e/\rho_\perp)^2\nu_{ei}t/2 = 1000$. The indefinite growth of the heat flux is associated with the formation of large-scale, approximately two-dimensional streamer structures that appear to be robust to all types of nonlinear shearing.

However, as we discussed in Section 7.2.2, the adiabatic ion response (2.22) causes the nonlinearity in the continuity equation (7.66) to vanish identically. Crucially, this means that (7.66) lacks any nonlinearity capable of generating two-dimensional secondary instabilities that are often responsible for the generation of zonal flows and destruction of streamers generated by curvature-driven instabilities [64, 119–121]. Indeed, the lack of saturation in the case of our ETG simulations appears to be due to the inability of the system to break apart streamers once they have been established by the cETG; the existence of such streamers causes the heat flux to diverge as they 'short circuit' the heat transport across the radial domain. Even if the simulation initially appears to saturate after the linear phase, it will eventually form large-scale streamers that appear to be robust to all types of nonlinear shearing, as seen clearly in the real-space snapshots of cETG turbulence shown in figures 7.14 and 7.15.

This suggests, perhaps, that the adiabatic ion response (2.22) is insufficient to saturate ETG-scale turbulence in the presence of finite magnetic-field gradients, and one may have to resort to other closures for the ions. One such closure including scales comparable to the ion-Larmor radius was introduced in [1], given by

$$\frac{\delta n_e}{n_{0e}} = -\bar{\tau}^{-1}\varphi + \frac{1}{n_{0i}} \int \mathrm{d}^3\boldsymbol{v} \, \langle g_i \rangle_{\boldsymbol{r}} \, , \tag{7.70}$$

where $\bar{\tau}^{-1}$ is now an operator defined as follows:

$$-\bar{\tau}^{-1}\varphi = -\frac{Z}{\tau}(1-\hat{\Gamma}_0)\varphi \approx \begin{cases} \dfrac{Z}{2\tau}\rho_i^2\nabla_\perp^2\varphi, & k_\perp\rho_i \ll 1, \\ -\dfrac{Z}{\tau}\varphi, & k_\perp\rho_i \gg 1, \end{cases} \tag{7.71}$$

and the operator $\hat{\Gamma}_0$ can be expressed, in Fourier space, in terms of the modified Bessel function of the first kind: $\Gamma_0 = I_0(\alpha_i)e^{-\alpha_i}$, where $\alpha_i = (k_\perp\rho_i)^2/2$. The presence of the non-adiabatic ion distribution function g_i in (7.70), however, means that one would have also to include a self-consistent treatment of ions in order to make use of this closure. Should this, or other similar closures, allow for saturation, this would then imply that one must always appeal, at least in part, to ion-scale physics for saturation of electrostatic cETG-driven turbulence. The extent to which such considerations are relevant, however, depends on whether or not the system being considered contains any electromagnetic physics, and thus on the value of the (electron) plasma beta β_e. Indeed, for $\beta_e \gtrsim m_e/m_i$, the flux-freezing scale d_e (or $d_e\chi$, in the collisional limit) is encountered before (i.e., is smaller than) the ion Larmor radius ρ_i when moving towards larger perpendicular scales (to the left in figures 5.1 and 5.2). Provided that the wavenumber interval between d_e and ρ_i is sufficiently wide to allow for the presence of either sTAI or cTAI, the mechanisms of saturation in such a system could be vastly different than in the electrostatic regime; this is the subject of the following section.

Lastly, a perceptive reader may have noticed that the validity of scale-invariance results of Section 7.1 did not depend on any stipulations about the perpendicular equilibrium gradients of the system, apart from the requirement that their size must preserved under any transformation considered. This means that the transformation of electrostatic drift kinetics (7.16)-(7.18), and the resultant scaling of the heat flux (7.23), are also valid in the case of finite magnetic field gradients; indeed, it is straightforward to show that (7.66) and (7.67) are also invariant under the transformation (7.28). How, then, is the lack of saturation in simulations with finite magnetic field gradients compatible with this result? The answer to this question lies in the fact that in writing (7.22), we implicitly assumed the heat flux to be independent of time, i.e., that it has been able to reach a statistical steady state. If this is not the case, (7.22) has to be replaced with

$$\tilde{Q}_s(\lambda^2 L_x, \lambda^2 L_y, \lambda^{2/\alpha} L_\parallel, t/\lambda^2) = \lambda^2 Q_s(L_x, L_y, L_\parallel, t), \tag{7.72}$$

which, even under the assumption that the heat flux is independent of perpendicular box size, does not lead to the scaling (7.23). Thus, there is no contradiction with scale invariance. If we had been able to find a case of cETG turbulence that saturated, we would have expected the scaling (7.23) for the corresponding heat flux (although not necessarily the same detailed inertial-range structure as for the sETG turbulence that we studied above), but in any event, no such saturated cases presented themselves. Perhaps interestingly, the case of $L_B/L_T = 1000$, which had a long period of seemingly saturated behaviour before its heat flux began to diverge, did have a heat flux during that period with the same magnitude as the sETG one ($L_B/L_T \to \infty$), and indeed all the other cases went nonlinear around that same magnitude of the heat flux as well (see Figure 7.13).

Chapter 8

Electromagnetic TAI-driven turbulence

One aspect of turbulent transport that has baffled tokamak modellers in recent years is the failure to find a saturated state in local, nonlinear electromagnetic simulations. In many cases, the turbulent heat flux in these simulations grows without bound, with energy principally being injected on large scales, and no statistical steady state is ever established. Though there are some proposed explanations for this behaviour (see, e.g., [60–63] and references therein), its physical cause remains largely unclear. This chapter is devoted to the consideration of this issue in the context of the low-beta system with which we have been working throughout this thesis. In particular, we find that nonlinear simulations of purely sTAI-driven turbulence display a failure of saturation, similarly to the aforementioned gyrokinetic simulations. The nature of this "blow-up" (a term that we shall adopt henceforth) is characterised in Section 8.1, while Section 8.2 outlines some of the possible mechanisms responsible. Lastly, in Section 8.3, we revisit the broader subject of drift-kinetic scale invariance and how it may apply, or otherwise, in the electromagnetic regime. In many ways, the material presented in this chapter is incomplete: we do not yet have a satisfyingly conclusive narrative about the saturation (or lack thereof) of electromagnetic turbulence in the same way that there was in Chapter 7 for the electrostatic sETG regime. Our results demonstrate, however, that electromagnetic tokamak turbulence is not very well understood — even within the context of our dramatically simplified model — and so remains an exciting and attractive area of active and future research.

8.1 Non-saturation of sTAI turbulence

Let us consider the simplest possible case of electromagnetically driven turbulence available within our reduced model: that driven by the sTAI, in the absence of any equilibrium magnetic-field gradients. Though this is somewhat restrictive, it will allow us to focus on the fundamental physics behind electromagnetic destabilisation without the further complications that arise to due to the presence of magnetic drifts, viz., we will not have to consider turbulence simultaneously driven by both the sTAI and cTAI. Note also that in restricting ourselves to sTAI-driven turbulence, we will be considering a case of saturation failure that is electromagnetic in an essential way, and is manifestly different from the one involving magnetic drifts considered in Section 7.3.

Such a system is described by (2.27)-(2.29), with the magnetic drifts neglected in the density equation. However, to be consistent with the pedagogy of Section 7.1.3, we will adopt an equivalent set of equations derived using the correct linearised Landau collision operator [see (A.89)-(A.91)]:

$$\frac{\mathrm{d}}{\mathrm{d}t}\bar{\tau}^{-1}\varphi - v_{\mathrm{the}}\nabla_\parallel d_e^2\nabla_\perp^2\mathcal{A} = 0, \tag{8.1}$$

$$\frac{\mathrm{d}\mathcal{A}}{\mathrm{d}t} + \frac{v_{\mathrm{the}}}{2}\frac{\partial\varphi}{\partial z} = -\frac{v_{\mathrm{the}}}{2}\nabla_\parallel\bar{\tau}^{-1}\varphi + \left(1+\frac{c_2}{c_1}\right)\frac{v_{\mathrm{the}}}{2}\left(\nabla_\parallel\frac{\delta T_e}{T_{0e}} - \frac{\rho_e}{L_T}\frac{\partial\mathcal{A}}{\partial y}\right) + \frac{\nu_{ei}}{c_1}d_e^2\nabla_\perp^2\mathcal{A}, \tag{8.2}$$

$$\frac{\mathrm{d}}{\mathrm{d}t}\frac{\delta T_e}{T_{0e}} - \kappa\nabla_\parallel\left(\nabla_\parallel\frac{\delta T_e}{T_{0e}} - \frac{\rho_e}{L_T}\frac{\partial\mathcal{A}}{\partial y}\right) + \frac{2}{3}\left(1+\frac{c_2}{c_1}\right)v_{\mathrm{the}}\nabla_\parallel d_e\nabla_\perp^2\mathcal{A} = -\frac{\rho_e v_{\mathrm{the}}}{2L_T}\frac{\partial\varphi}{\partial y}, \tag{8.3}$$

where the field equations (2.30) have been used to express the density and parallel velocity perturbations in terms of the electrostatic and parallel magnetic vector potentials, respectively. The ion-charge-dependent coefficients c_1, c_2, and c_3 are the same as those in (7.31), while $\kappa = c_3 v_{\mathrm{the}}^2/3\nu_{ei}$ is now the electron thermal conductivity. Rescaling the collisionality and thermal conductivity as $\nu_{ei}/c_1 \to \nu_{ei}$, $c_1\kappa \to \kappa$, it is straightforward to see that (8.1)-(8.3) are identical to (2.27)-(2.29) apart from the presence of the additive c_2/c_1 factors in (8.2) and (8.3); the physical origin of these 'thermal forces' is discussed in Appendix A.5.2. This noted, a concerned reader may rest assured that (8.1)-(8.3) reproduce all of the linear instabilities considered in chapters 3 and 4 up to order-unity modifications to constant coefficients — our results are robust with respect to the exact choice of collision operator.

	$L_x/d_e\chi$	$L_y/d_e\chi$	$L_\parallel\sqrt{\beta_e}/L_T$	n_x	n_y	$n_\parallel$	$2\chi^2\nu_\perp/\nu_{ei}$	n_ν
sTAI simulation	800	800	80	191	191	31	1.0	2

Table 8.1: Table showing the parameters used in the simulation representative of the lack of saturation in electromagnetic sTAI turbulence. The simulation has $\tau = Z = 1$.

This three-field system (8.1)-(8.3) was simulated using the same numerical method as that described in Section 7.1.4. Hyperviscosity of the form [cf. (7.32)]

$$\frac{\mathrm{d}}{\mathrm{d}t} + (-1)^{n_\nu}\nu_\perp\left(d_e\chi\nabla_\perp\right)^{2n_\nu}, \tag{8.4}$$

was once again used in order to provide an ultraviolet wavenumber cutoff for the instabilities and, in particular, to allow us to restrict our consideration to the electromagnetic scales $k_\perp d_e\chi \ll 1$ on which the sTAI resides. With (8.4) appended, our system of equations (8.1)-(8.3) depends on the following dimensionless parameters: the perpendicular and parallel box sizes $L_x/d_e\chi$, $L_y/d_e\chi$, and $L_\parallel\sqrt{\beta_e}/L_T$, the hyper-collision frequency $2\chi^2\nu_\perp/\nu_{ei}$, and the power of the hyperviscous diffusion operator n_ν.

So far, none of the simulations of (8.1)-(8.3) that we attempted have been able to reach saturation, despite exploring a relatively large amount of the available parameter space, viz., the observed blow-up seems to be robust to changes in parallel and perpendicular box sizes, their aspect ratio, resolution in all of the coordinate directions, and hyperviscosity. The fact that we observe such a blow up is, in a sense, unsurprising, given that simulations of electromagnetic, gradient-driven turbulence are notoriously difficult to saturate. We are reasonably confident that this blow-up is not due to an accumulation of numerical errors within the code: its pseudo-spectral nature makes it robust against many of the numerical instabilities associated with calculating derivatives via finite-difference methods, and we have verified that the code nonlinearly conserves the free energy (6.2) at all times down to a level of precision consistent with the timestep being used. Furthermore, its relative simplicity has allowed us to check the implementation exhaustively to ensure that it is working as intended by, e.g., benchmarking the linear part of the solver against analytical expressions or stress-testing the kernels used to compute each of the nonlinear terms individually. The following discussion will thus be predicated on the assumption that the blow-up is physical — related to the mechanisms of saturation of electromagnetic turbulence in of our reduced model — rather than due to some purely numerical issue.

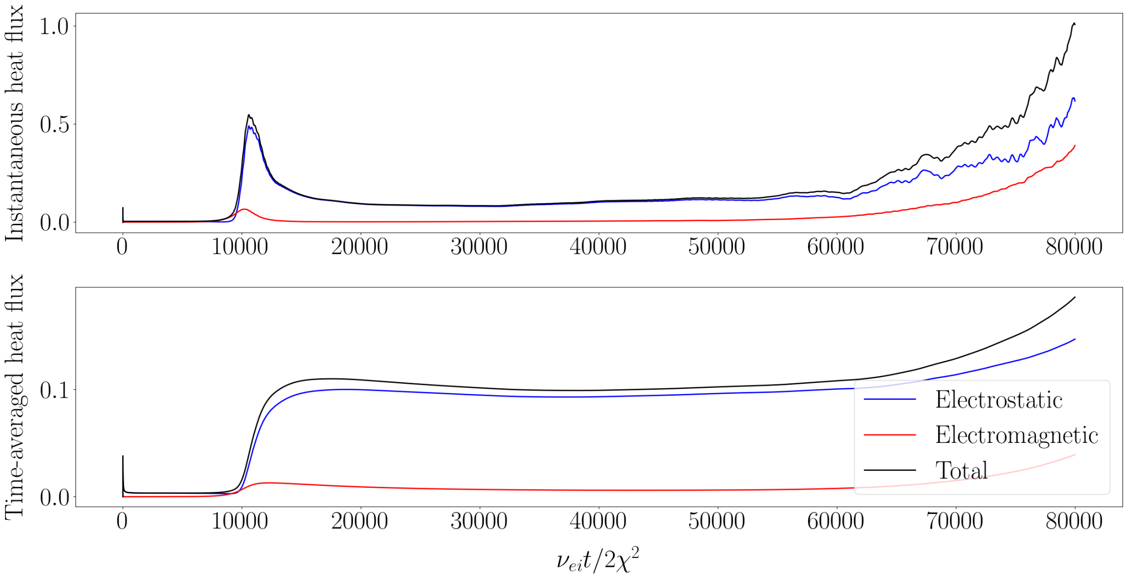

Figure 8.1: Turbulent heat flux in the simulation with parameters given in table 8.1. The upper and lower panels show, respectively, the instantaneous and (rolling) time-averaged heat fluxes. The electrostatic and electromagnetic contributions to the heat flux are shown in blue and red, respectively, while the total heat flux is shown in black. After initial linear growth, apparent saturation is observed around $\nu_{ei}t/2\chi^2 \sim 10000$, but the system has not in fact reached a steady state — due to the secular growth of a particular large-scale mode — with the heat flux beginning to grow significantly at later times.

To examine the nature of this electromagnetic blow-up, we consider a representative simulation, whose parameters can be found in table 8.1. The magnitude of the hyperviscosity was chosen so as to ensure that there were no wavenumbers unstable to the (electrostatic) sETG instability, meaning that all energy injection must be due to the sTAI. In Figure 8.1, we plot the time evolution of the (normalised) turbulent heat flux, which is composed of two parts: (i) the electrostatic contribution due to the fluctuating $\boldsymbol{E} \times \boldsymbol{B}$ flow, given by the first expression multiplying $1/L_T$ in the collisional version of (6.4); and (ii) the electromagnetic contribution due to heat flow along perturbed magnetic field lines (magnetic flutter), given by the second. As expected, the simulation undergoes a period of linear growth due to the sTAI (the electromagnetic heat flux is dominant during the initial part of the linear phase) until around $\nu_{ei}t/2\chi^2 \sim 10000$, after which it appears to reach nonlinear saturation, settling into an apparent steady state by $\nu_{ei}t/2\chi^2 \sim 20000$. However, as the simulation continues to run, we see that both the electrostatic and electromagnetic contributions to the heat flux begin to grow at $\nu_{ei}t/2\chi^2 \sim 50000$, seemingly without bound. This growth is not arrested if one allows the simulation to run to even longer times. However, we have not been able to run to *significantly* longer times due to the associated computational demands; we cannot disregard the possibility that saturation at large amplitudes could indeed still occur, but we think it unlikely given the nature of the blow-up.

In Figure 8.2, we plot the time evolution of individual poloidal wavenumbers $k_y d_e \chi$ from the simulation. The smaller scales are initially damped by the effects of hyperviscosity, while larger scales, where hyperviscosity is negligible, grow slowly. These, however, are not the most unstable wavenumbers, since the sTAI peaks at smaller scales $k_\perp d_e \chi \sim 1$ (see the discussion at the end of Section 4.4.1); the growth of these most unstable wavenumbers eventually triggers the linear phase, after which most of the modes are damped by some nonlinear 'saturation' process. Figures 8.3 and 8.4 show real-space snapshots of the simulation during and after the linear phase, respectively. The presence of the sTAI is evident in the former: the instability is clearly three-dimensional, as seen from the parallel structure manifest in all of the fields, and is Alfvénic in nature, since the electrostatic and magnetic vector potential perturbations are approximately in phase [we expect that $\mathcal{A} \sim k_\perp d_e \varphi$ for a KAW-like perturbation; see, e.g., (4.32)]. This represents the first numerical confirmation of the fact that the sTAI instability exists and is able to drive turbulence which, the question of the blow-up aside, is a non-trivial result in itself. From Figure 8.4, it is clear that the magnetic vector potential is already dominated by larger scales than the other two fields following the nonlinear 'saturation', corroborating the spectral evidence from Figure 8.2(b).

As time progresses, we eventually see the emergence of a large-scale mode that seems to grow without bound, mirroring the growth of the heat flux seen on the far right of Figure 8.1. As can be seen in Figure 8.5, this mode is dominated by the second harmonics in both the parallel and poloidal directions, viz., it corresponds to the wavenumbers $k_y d_e \chi = 0.0157$ ($n_y = 2$) and $k_\parallel L_T/\sqrt{\beta_e} = 0.157$ ($n_\parallel = 2$). This is particularly obvious from the real-space snapshots of the magnetic vector potential perturbations, which are almost entirely composed of these larger scales [cf. with Figure 8.2(b) at late times]; the electrostatic potential and temperature perturbations consist of some smaller-scale, mostly two-dimensional structure superimposed on this large-scale background. It is clear from Figure 8.2 that this mode exhibits secular growth throughout the simulation at a rate comparable to its rate of linear growth, eventually breaking the apparent steady-state established around $\nu_{ei} t/2\chi^2 \sim 20000$

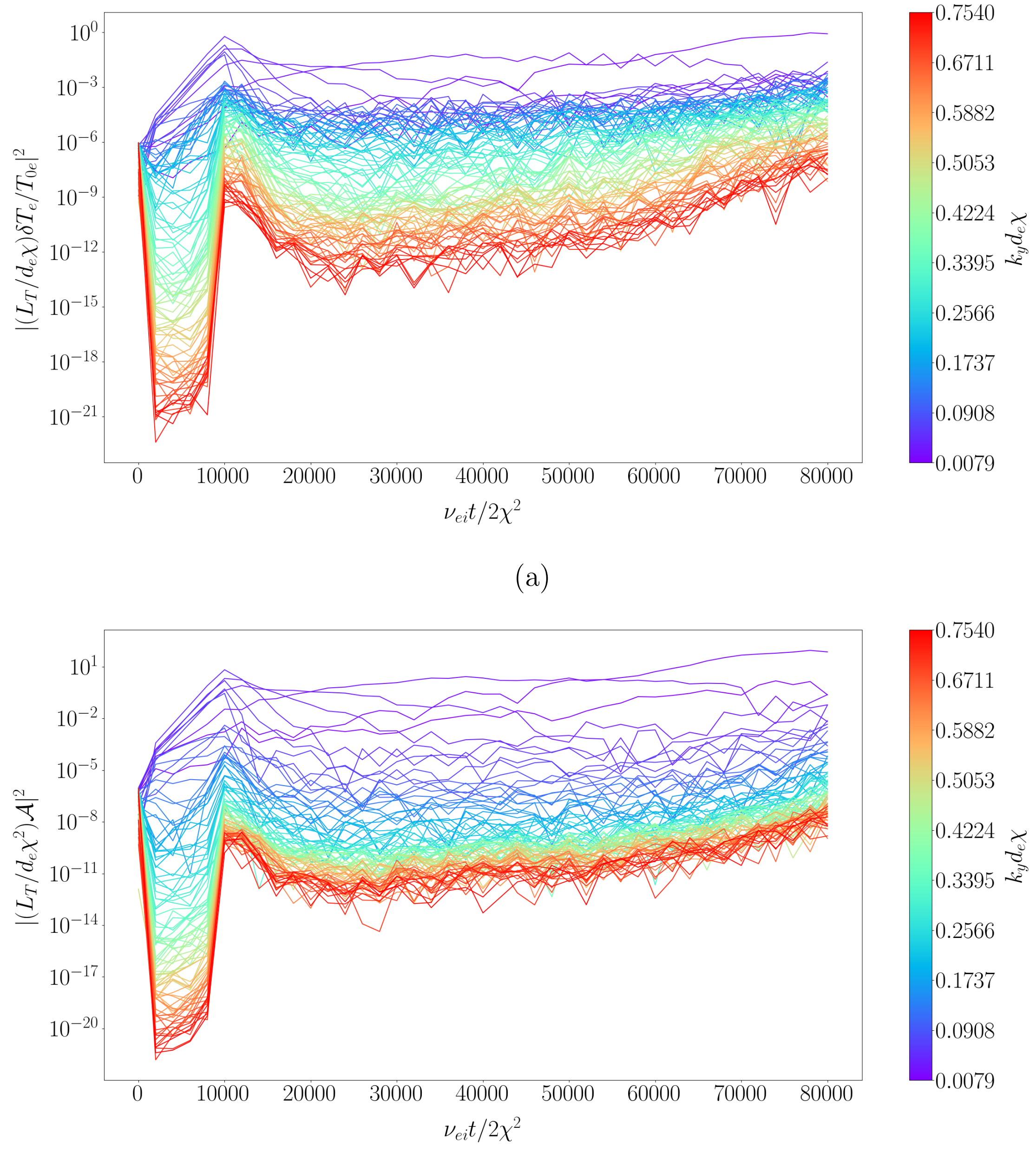

(a)

(b)

Figure 8.2: The time-evolution of individual poloidal wavenumbers $k_y d_e \chi$ of the (a) temperature and (b) parallel magnetic vector potential perturbations in the simulation described in table 8.1, and for $k_x d_e \chi = 0$ and $k_\parallel L_T/\sqrt{\beta_e} = 0.157$. The electrostatic potential and temperature perturbations display qualitatively similar behaviour, and so we have not included the former here. The dominant (growing) wavenumber at late times in both panels is $k_y d_e \chi = 0.0157$, corresponding to the second poloidal harmonic (i.e., $n_y = 2$). Throughout its evolution, the parallel magnetic vector potential is dominated by large-scale modes; the amplitudes of all but the first decade of wavenumbers are negligible by comparison [note the scale of the colour bar].

(see Figure 8.1). The dominance of this mode at late times has been observed in all simulations, regardless of changes in perpendicular and parallel box sizes, as well as their aspect ratio. Once it has been established, amplitudes appear to grow indefinitely, and the system never reaches a steady state.

8.2 Speculations on non-saturation

It is not currently clear as to why these simulations of electromagnetic sTAI-driven turbulence are unable to saturate. It is not obvious, for example, why the system wants to form a large-scale mode in the first place, given that the energy injection occurs at smaller scales and that the offending mode emerges out of a state of apparent saturation that manages to persist for a long time. In the remainder of this section, we examine a number of possible explanations for this lack of saturation; this material is entirely speculative in nature.

8.2.1 Lack of zonal dynamics

As we discussed in Section 7.3, the adiabatic ion response (2.22) causes the nonlinearity in the continuity equation (8.1) to vanish identically. Crucially, this means that (8.1) lacks any nonlinearity capable of generating zonal flows via a secondary instability associated with the Reynolds stress — viz., from interactions between the density and potential perturbations — which might have caused shearing of the problematic large-scale modes. Indeed, examining the zonal and non-zonal components of the perturbations in the simulation described in table 8.1, it is clear that the zonal components are at least an order of magnitude smaller than the non-zonal ones at all times throughout the simulation (see Figure 8.6). It is thus possible that the lack of saturation in these electromagnetic simulations is a consequence of the fact that electron-scale simulations are generically difficult to saturate in cases where they form large-scale structures, as the sub-dominant nature of zonal flows means that they are not easily eroded once established. This assertion can be tested directly in our system of equations (8.1)-(8.3). In the absence of magnetic-field gradients, the contribution from the non-adiabatic ion distribution function g_i to the quasineutrality closure (7.70) vanishes, meaning that we can adopt (7.70) without having to include a self-consistent

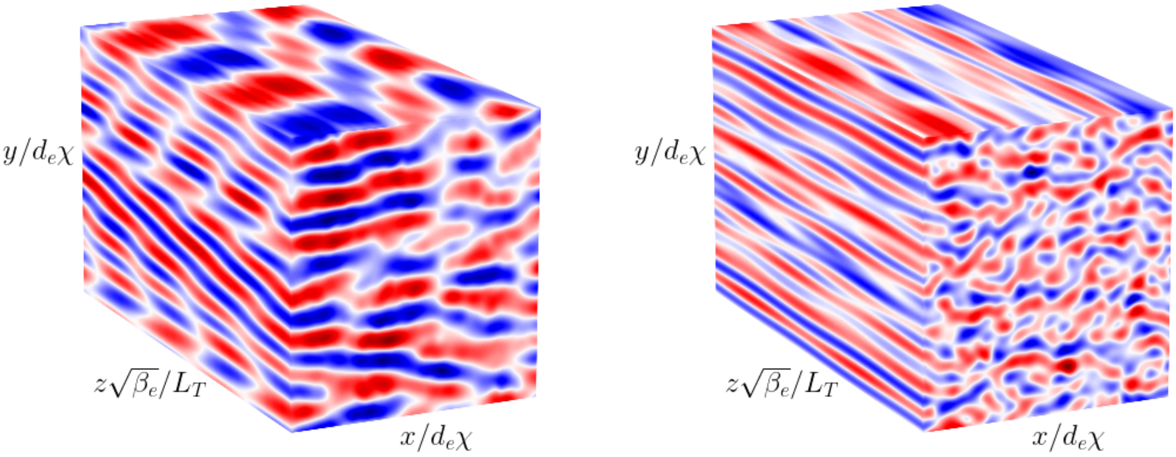

(a) $(L_T/d_e\chi)\varphi$

(b) $(L_T/d_e\chi)\delta T_e/T_{0e}$

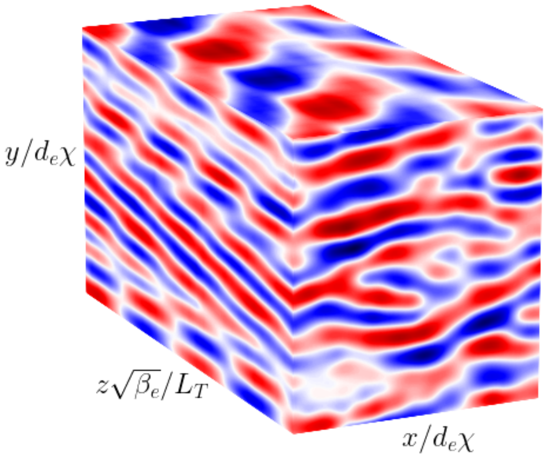

(c) $(L_T/d_e\chi^2)\mathcal{A}$

Figure 8.3: Real-space snapshots of the (a) electrostatic potential, (b) temperature, and (c) parallel magnetic vector potential perturbations from the simulation described in table 8.1, taken at $\nu_{ei}t/2\chi^2 = 8000$ during the linear phase. The coordinate axes are as shown, while the red and blue colours correspond to regions of positive and negative fluctuation amplitude. The three-dimensional nature of the sTAI can be seen in the parallel structure manifest in all of the fields, as can the Alfvénic character of the instability in the fact that the electrostatic and magnetic vector potential perturbations are approximately in phase [we expect that $\mathcal{A} \sim k_\perp d_e \varphi$ for a KAW-like perturbation; see, e.g., (4.32)].

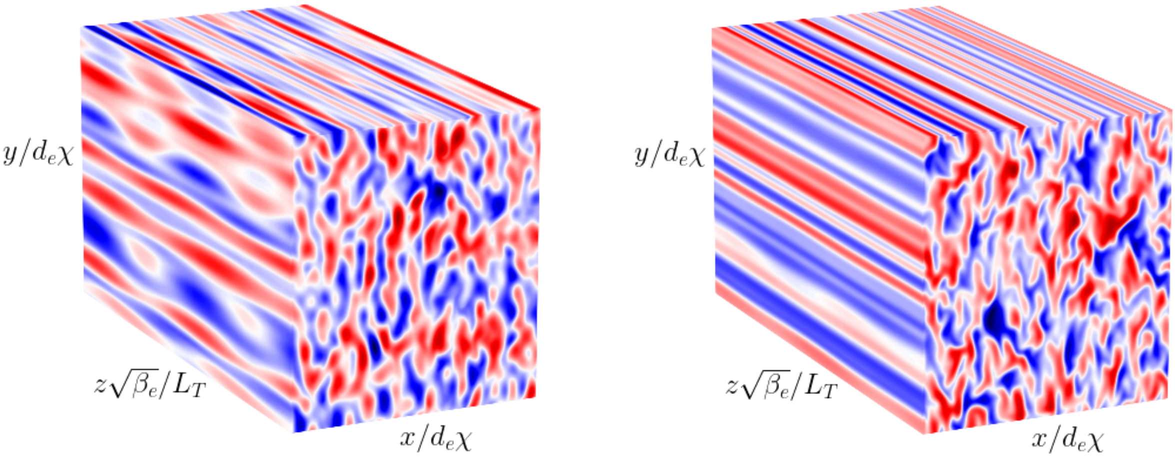

(a) $(L_T/d_e\chi)\varphi$ (b) $(L_T/d_e\chi)\delta T_e/T_{0e}$

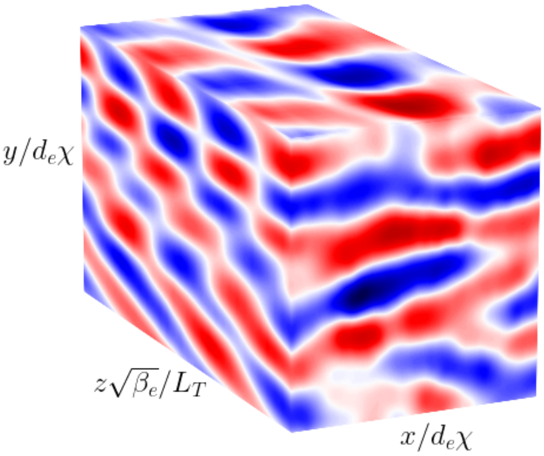

(c) $(L_T/d_e\chi^2)\mathcal{A}$

Figure 8.4: The same as Figure 8.3, except taken at $\nu_{ei}t/2\chi^2 = 20000$ following the linear phase. The structure of the potential and temperature perturbations is relatively isotropic in the perpendicular plane, while the latter appears to be almost two-dimensional. The magnetic vector potential is now at significantly larger scales than the other two fields, displaying a streamer-like structure, albeit one with a non-zero $k_\parallel$.

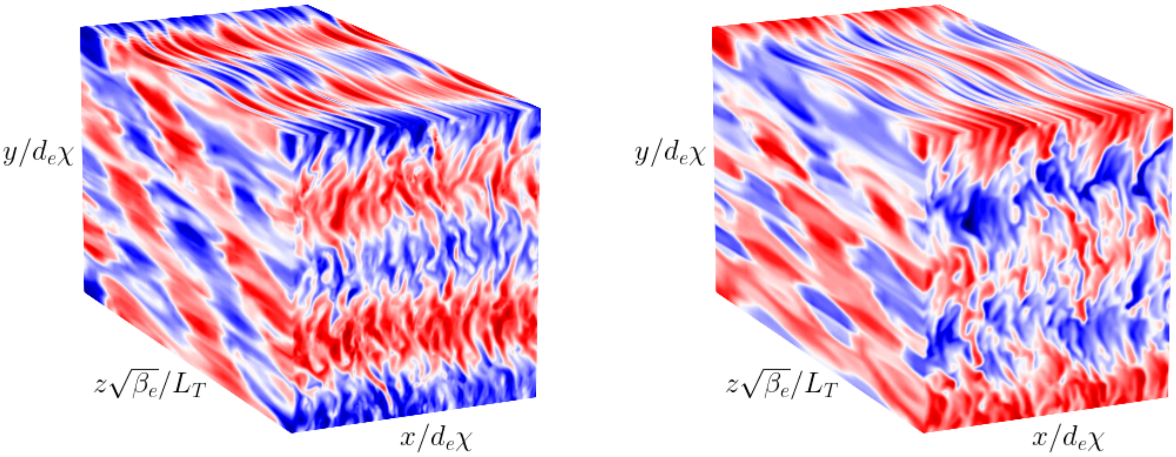

(a) $(L_T/d_e\chi)\varphi$

(b) $(L_T/d_e\chi)\delta T_e/T_{0e}$

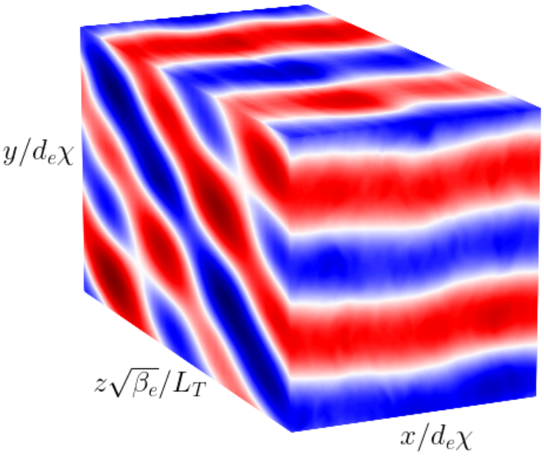

(c) $(L_T/d_e\chi^2)\mathcal{A}$

Figure 8.5: The same as Figure 8.3, except taken at $\nu_{ei}t/2\chi^2 = 80000$, when the heat flux is growing without bound. The lack of saturation is associated with a now fully-developed streamer-like structure (with non-zero parallel and poloidal variation) in the parallel magnetic vector potential. This structure appears to be impervious to all mechanisms of nonlinear shearing.

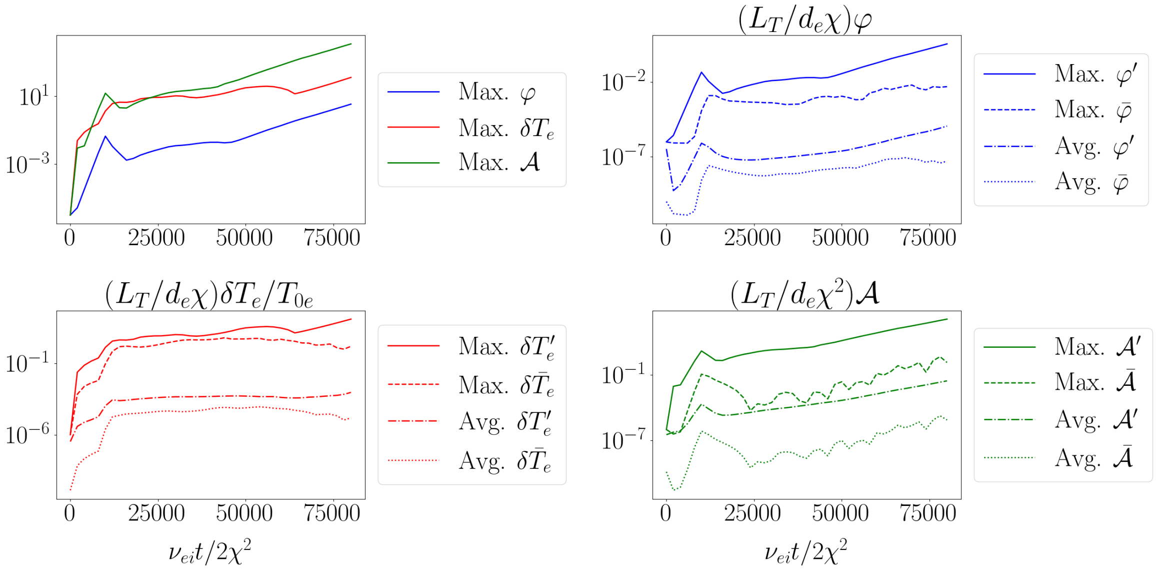

Figure 8.6: The time-evolution of the zonal and nonzonal components of the perturbations in the simulation described in table 8.1. The top left panel shows the maximum amplitude of each of the fields. In the remaining panels, the zonal and non-zonal components are, in the usual way, indicated by the overbar and prime; e.g., $\bar{\varphi}$ and φ' are the zonal and non-zonal components of the electrostatic potential, respectively, as in (7.69).

treatment of the ions. This restores the nonlinearity in the continuity equation (8.1), viz.,

$$\frac{\mathrm{d}}{\mathrm{d}t}\bar{\tau}^{-1}\varphi = \frac{\partial}{\partial t}\bar{\tau}^{-1}\varphi + \frac{\rho_e v_{\mathrm{th}e}}{2}\left\{\varphi, \bar{\tau}^{-1}\varphi\right\}, \tag{8.5}$$

where $\bar{\tau}$ is now an operator, given by (7.71). The Reynolds stress is manifest in the nonlinearity in (8.5): considering scales $k_\perp \rho_i \ll 1$, it becomes, via (7.71),

$$\lim_{k_\perp \rho_i \ll 1} \left\{\varphi, \bar{\tau}^{-1}\varphi\right\} = -\left\{\varphi, \rho_s^2 \nabla_\perp^2 \varphi\right\}, \tag{8.6}$$

where $\rho_s = \sqrt{Z/2\tau}\rho_i$ is the ion sound radius. [64] showed that the Reynolds stress plays a key role in enabling saturation in ITG-driven turbulence, in that it is responsible for the turbulent generation (and restoration) of zonal flows activity that results in the shearing of large-scale eddies generated by the curvature-mediated ITG instability. It would be interesting to see whether the Reynolds stress is capable of playing a similar role within our electromagnetic simulations by, e.g., generating sufficiently large zonal flows to be able to break apart the growing mode(s) responsible for the blow-up. This is a subject for future work.

8.2.2 Reynolds and Maxwell stresses

Closely related to the above considerations is the question of the relative roles of Reynolds and Maxwell stresses in determining the saturated state of the turbulence. The finite perturbations of the magnetic-field direction encountered in the electromagnetic regime give rise to the nonlinearity within the parallel derivative [see (2.11)], which in the continuity equation (8.1) manifests itself as

$$v_{\text{the}} \nabla_{\parallel} d_e^2 \nabla_{\perp}^2 \mathcal{A} = v_{\text{the}} \frac{\partial}{\partial z} d_e^2 \nabla_{\perp}^2 \mathcal{A} - \rho_e v_{\text{the}} \left\{ \mathcal{A}, d_e^2 \nabla_{\perp}^2 \mathcal{A} \right\}. \tag{8.7}$$

The nonlinearity in (8.7) is the Maxwell stress, which, within (8.1), has the opposite sign to that of the Reynolds stress, if the latter is not zero, as in (8.6). This implies that the generation of zonal flows, or otherwise, within our model of electromagnetic turbulence will involve a competition between the Reynolds and Maxwell stresses, with the former perhaps promoting their formation like in ITG turbulence [64], and the latter resisting it. As discussed in the previous section, the simulations that we have thus far conducted have assumed adiabatic ions, for which the Reynolds stress vanished, and in which no saturation is observed. If the above reasoning is sound, this may be due to the Maxwell stress winning a fight to which its opponent is a no-show.

Re-introducing the Reynolds stress through the adoption of the quasineutrality closure (7.70), as in (8.5), would allow us to determine the outcome of the competition between these stresses. In particular, it would give rise to another length scale to which the flux-freezing scale (2.33) can be meaningfully compared, viz., the ion Larmor radius ρ_i. The ratio of the latter to the former, given by

$$\frac{\rho_i}{d_e \chi} \sim \sqrt{\frac{m_i}{m_e}} \beta_e \frac{\lambda_{ei}}{L_T}, \tag{8.8}$$

effectively controls the size of the Reynolds stress within our electromagnetic system; this was infinite in the adiabatic-ion approximation, viz., when considering wavenumbers $k_{\perp} d_e \chi \sim 1$ but $k_{\perp} \rho_i \gg 1$. It is then possible, for example, that there will exist a value of (8.8) below which the Reynolds stress becomes large enough to generate zonal flows, despite the presence of the Maxwell stress attempting to prevent this, and thus allowing the system to saturate. Given the dependence of (8.8) on the electron beta, this would imply the existence of a 'critical' value of β_e below which the system is able to saturate, which could have profound implications for the saturation of electromagnetic gyrokinetic turbulence within more general systems. Such a prediction could be directly tested in gyrokinetic simulations by varying the parameters appearing in (8.8), such as the mass-ratio.

8.2.3 Invariants and inverse cascades

In addition to the free energy (6.2), the electromagnetic system of equations (8.1)-(8.3) has a second (nonlinear) invariant, the (electron-scale version of) cross-helicity:

$$H = \int \frac{\mathrm{d}^3\boldsymbol{r}}{V} \frac{\delta n_e}{n_{0e}} \mathcal{A} = -\int \frac{\mathrm{d}^3\boldsymbol{r}}{V} \left(\bar{\tau}^{-1}\varphi\right) \mathcal{A}. \tag{8.9}$$

This is a particular case from a class of 2D invariants of gyrokinetics, which are conserved by 3D systems in certain limits (see appendix F of [72], or appendix A of [77]). The time evolution of H follows straightforwardly from (8.1) and (8.2):

$$\frac{\mathrm{d}H}{\mathrm{d}t} = \varepsilon_H - D_H \tag{8.10}$$

where the helicity injection rate is

$$\varepsilon_H = -\left(1+\frac{c_2}{c_1}\right) \int \frac{\mathrm{d}^3\boldsymbol{r}}{V} \frac{v_{\mathrm{the}}}{2} \left(\bar{\tau}^{-1}\varphi\right) \left(\nabla_\parallel \frac{\delta T_e}{T_{0e}} - \frac{\rho_e}{L_T}\frac{\partial \mathcal{A}}{\partial y}\right), \tag{8.11}$$

and D_H is the rate of helicity dissipation due to a combination of resistivity and hyperviscosity; its exact form is irrelevant for the purposes of the current discussion. Should there exist scales at which $\varepsilon_H \neq 0$ and others where neither ε_H nor D_H are important, the existence of this additional invariant could lead to inverse cascades and saturation failures (see, e.g., [122] or [123]).

Note, however, that gyrokinetics in up-down symmetric equilibria has a parity symmetry [124, 125]:

$$(x, y, z, v_\parallel, h_s, \varphi, \mathcal{A}, \delta B_\parallel) \to (-x, y, -z, -v_\parallel, -h_s, -\varphi, \mathcal{A}, -\delta B_\parallel), \tag{8.12}$$

where the odd parity of the gyrokinetic distribution function h_s implies also odd parity for any of its moments that are even in $v_\parallel$, viz., $\delta n_e/n_{0e}$, $\delta T_e/T_{0e}$, etc. Our equations (8.1)-(8.3), being derived in an asymptotic limit of gyrokinetics, retain this symmetry, which is manifest on inspection. The helicity injection rate (8.12) is odd under the parity transformation (8.12), $\varepsilon_H \to -\varepsilon_H$, and should thus vanish within our turbulent system; the same is true about the helicity (8.9) itself, rendering its consideration seemingly irrelevant.

However, [126] showed that the decay of non-helical plasma turbulence — in which an MHD analogue of (8.9) (the magnetic helicity) vanishes by construction — is constrained by the existence of another (non-zero) integral invariant (the 'Hosking integral', analogous to the Loitsyansky and Saffman integrals of hydrodynamic turbulence) that expresses the conservation of the random helicity "patches" contained in sufficiently large volumes. Considerations of this kind have also been shown to carry over, in a certain sense, to the case of forced turbulence [114], suggesting that, perhaps, they could also apply in gradient-driven systems such as ours. For (8.1)-(8.3), the analogue of the Hosking integral would be

$$I_H(\boldsymbol{r}) = \int \frac{\mathrm{d}^3\boldsymbol{r'}}{V} \left\langle \bar{H}(\boldsymbol{r})\bar{H}(\boldsymbol{r}+\boldsymbol{r'})\right\rangle, \tag{8.13}$$

where $\bar{H} = (\delta n_e/n_{0e})\mathcal{A}$ is the helicity density, and the brackets denote an ensemble average. It is possible that, despite the helicity (8.9) formally vanishing due to the parity symmetry (8.12), the conservation of random magnetic helicity — that can be spontaneously generated patchwise, but vanishes over the entire volume of the system — according to (8.13) could be constraining the electromagnetic, sTAI-driven turbulence in such a way as to prevent its saturation by promoting an inverse cascade of energy to large scales. Whether this is indeed true is for future investigations to determine, but the possible conservation of integrals such as (8.13) presents an interesting avenue of investigation into the present issue of non-saturation.

8.3 Scale invariance in the electromagnetic regime

Before concluding our discussions of electromagnetic turbulence, it is perhaps appropriate to revisit the drift-kinetic scale invariance that we considered in Section 7.1. The transformation (7.16)-(7.18) only holds in the electrostatic regime, in which the terms involving $A_\parallel$ and $\delta B_\parallel$ in (7.5) and (7.6) can be neglected; these must be restored in the electromagnetic regime. Given that the parallel (compressive) magnetic-field perturbation always appears alongside ϕ in the combination

$$\phi + \frac{T_{0s}}{q_s}\frac{v_\perp^2}{v_{\mathrm{th}s}^2}\frac{\delta B_\parallel}{B_0}, \tag{8.14}$$

and with which it shared an identical transformation [see (7.12) and (7.13)], its inclusion does not, in fact, modify the electrostatic arguments of sections 7.1.1 and 7.1.2.

It is the presence of perpendicular magnetic-field perturbations, however, that proves problematic: the terms involving $A_\parallel$ in (7.5) and (7.6) cannot be made simultaneously invariant alongside the other terms under a transformation of the type (7.11)-(7.15) — these terms generate more constraint equations than there are free parameters (the a_i's), rendering the only solution the trivial one, viz., all $a_i = 0$. Physically, this is because the inclusion of non-zero $A_\parallel$ introduces the important perpendicular scale with which we have principally been concerned in this thesis: the flux-freezing scale d_e (or $d_e\chi$, in the collisional limit), implicit in the Laplacian on the left-hand side of (7.8). This demands a fixed relationship between the rescaling of the amplitudes of h_s^{odd} and $A_\parallel$ that depends on $a_\perp$ [see (7.14) and (7.15)][1]; it can be confirmed by inspection that this enforces either $a_o = 0$ or $a_\perp = 0$, which inevitably results in a reduction to the trivial solution.

These considerations do not necessarily imply that the heat-flux scaling (7.23) can never be realised in systems with finite plasma beta, for which $A_\parallel$ and $\delta B_\parallel$ are inevitably non-zero. Indeed, we argued in Section 7.1.2 that this scaling would still hold in the presence of finite-Larmor-radius effects if the outer scale for the turbulence remained within the drift-kinetic limit, despite scale invariance being broken at the smallest spatial scales. A similar argument is applicable here. If the outer scale lies at scales sufficiently *smaller* than the flux-freezing scale, i.e., at $k_\perp d_e \gg 1$ (or $\sim \chi^{-1}$, in the collisional limit), then the scaling (7.23) will continue to hold as, once again, the assumption behind it is that transport is set by the outer scale located in the electrostatic drift-kinetic limit, and the relevant breaking of scale invariance is done by $L_\parallel$, rather than by the flux-freezing scale. This means that the results of Section 7.1.2 may continue to hold even in simulations with a finite plasma beta. For example, [90] performed nonlinear, electromagnetic simulations of JET-ILW pedestals for $k_\perp \rho_i \gtrsim 1$, and observed the same scaling of the heat flux with L_B/L_T as the first expression in (7.1), suggesting that (7.23) was also satisfied, despite the presence of electromagnetic effects.

What is clear, however, is that if the effective injection scale does lie above the flux-freezing scale, i.e., if the turbulence is truly electromagnetic, as the sTAI-driven turbulence discussed above was, then the constraints imposed by the scale invariance

---

[1] This relationship is actually still present in the electrostatic regime, as (7.8) must always be satisfied. It can, however, simply be regarded as a constitutive relation from which $A_\parallel$ can be determined, given that it plays the role of a spectator field in this regime.

of electrostatic drift kinetics are lifted. It may be that there are classes of transformations different from (7.11)-(7.15) (e.g., those involving two parameters) that will leave (7.5) and (7.6) invariant in the electromagnetic regime; this is the subject of ongoing investigations.

Chapter 9

Summary and discussion

In this thesis, we have considered electromagnetic instabilities and turbulence driven by the electron-temperature gradient in a local slab model of a tokamak-like plasma with constant equilibrium gradients (including magnetic drifts but not magnetic shear, see section 2.1), with the governing equations (section 2.3) derived in a low-beta asymptotic limit of gyrokinetics. The formal ordering of the equilibrium parameters was given by $m_e/m_i \ll \beta_e \ll 1$ and $\nu_* \sim 1$ for the electron-beta and normalised collisionality, respectively, while the perturbations were ordered as in (2.6)-(2.8). Central to our considerations was the electron inertial scale d_e, which divided our system into two distinct physical regimes: electrostatic (perpendicular scales below d_e, $k_\perp \gg d_e^{-1}$, or $d_e^{-1}\chi^{-1}$ in the collisional limit, where $\chi = L_T/\lambda_{ei}\sqrt{\beta_e}$) and electromagnetic (perpendicular scales above d_e, but still smaller than the ion gyroradius, $\rho_i^{-1} \ll k_\perp \ll d_e^{-1}$, or $d_e^{-1}\chi^{-1}$ in the collisional limit), distinguished by whether or not the magnetic field lines were frozen into the electron flow (2.34).

In the electrostatic regime (Chapter 3), magnetic field lines are decoupled from the electron flow, and so electrons are free to flow across field lines without perturbing them. In this regime, we recovered both the familiar electrostatic electron-temperature gradient (sETG, sections 3.1 and 3.2) and curvature-mediated ETG (cETG, Section 3.3) instabilities, noting in particular that the mechanism responsible for the extraction of free energy from the (radial) equilibrium temperature gradient was the fluctuating $\boldsymbol{E} \times \boldsymbol{B}$ flow — the usual electrostatic linear drive — in that it converted the equilibrium temperature variation into perturbations of the electron temperature [see, e.g., the third equation in (3.4)].

In the electromagnetic regime (Chapter 4), the magnetic field lines are frozen into the electron flow (2.34), meaning that perpendicular magnetic-field perturbations $\delta\boldsymbol{B}_\perp$ are created as electrons move across field lines and drag the latter along. Crucially, this means that the equilibrium temperature gradient has a component along the perturbed field line, viz., its projection onto the radial component of the perturbed magnetic field [see, e.g., the second term in (2.21)], which proved to be responsible for the electromagnetic destabilisation associated with the novel thermo-Alfvénic instability (TAI). We showed that the TAI exists in both a slab version (sTAI, destabilising kinetic Alfvén waves, sections 4.3.2 and 4.4.1) and a curvature-mediated version (cTAI, sections 4.1 and 4.4). The transition between these two occurs at the critical parallel wavenumber $k_{\parallel c}$ (4.21): from sTAI at $k_\parallel \gg k_{\parallel c}$ to cTAI at $k_\parallel \lesssim k_{\parallel c}$. Another important scale for the TAI is the perpendicular wavenumber $k_{\perp *}$ (4.26), which controls the transition between the isobaric ($k_{\perp *} \lesssim k_\perp \lesssim d_e^{-1}$, or $d_e^{-1}\chi^{-1}$ in the collisional limit) and isothermal ($\rho_i^{-1} \ll k_\perp \lesssim k_{\perp *}$) limits. In the isobaric limit (section 4.4), we demonstrated that cTAI is subdominant to sTAI, and can be regarded as an electron-scale extension of MHD-like modes, such as kinetic-ballooning modes (KBMs). In contrast, in the isothermal limit (section 4.1), we found that the cTAI is the dominant instability, with a peak growth rate (4.15) greater than that of the cETG (3.15), exciting electromagnetic perturbations with a specific parallel wavenumber (4.24) (unlike the cETG, which is two-dimensional). This isothermal cTAI's physical mechanism hinges on the fact that — in the presence of either dominant parallel streaming $k_\parallel v_{\text{the}}$ (in the collisionless limit) or thermal conduction $\kappa k_\parallel^2 \propto k_\parallel^2 v_{\text{the}}^2/\nu_e$ (in the collisional one) — perturbations of the magnetic field are coupled to those of the electron temperature as the latter must always adjust to cancel the variation of the equilibrium temperature along the perturbed field line [see, e.g., the isothermal condition (4.12)]. Such an instability mechanism can only be present in the electromagnetic regime, when perturbations of the magnetic field's direction are significant.

Informed by this extensive linear analysis (summarised in Chapter 5), we used a critical-balance phenomenology analogous to [12] to construct an *a priori* turbulent-cascade theory for the free energy injected by both the electrostatic and electromagnetic instabilities (Chapter 6). Scalings for the turbulent heat fluxes were derived in both the collisionless and collisional limits, demonstrating that the cTAI dominated the turbulent transport for temperature gradients L_B/L_T larger than $\beta_e^{-1}(L_B/L_\parallel)^2$ (Section 6.4). Moreover, the turbulent electron heat flux carried by the fluctuations at the cTAI injection scale (6.33) turned out to scale more steeply with the temperature gradient than the heat flux due to the electrostatic sETG turbulence in this regime, thus giving rise to stiffer transport [see (6.45) in the collisionless limit and (6.46) in the collisional one].

In Chapter 7, we showed that the dependence of the electrostatic heat flux on parallel system size, as derived in Chapter 6, is in fact a direct consequence of the scale invariance of drift kinetics in the electrostatic limit, with the argument leading to this conclusion relying on only three assumptions: that the system was spatially periodic, that it was able to reach a statistical steady state, and that the heat flux was independent of the system's perpendicular size (as it should be for any valid local model of a plasma). The critically balanced, constant-flux cascade proposed in Chapter 6 provides the dynamical explanation for these scalings, which we demonstrated numerically in simulations of collisional sETG-driven turbulence described in Section 7.2. The effects of dissipation associated with parallel thermal conduction play a key role in determining the saturated state of these simulations, limiting the cascade of free energy in parallel wavenumbers by clamping it to the line of critical balance. This shows that a constant-flux cascade can in fact be compatible with a formal lack of scale separation between injection and dissipation in turbulent plasma systems — a departure from the 'classic' Kolmogorov picture of hydrodynamic turbulence. Analogous simulations of electrostatic cETG-driven turbulence display a lack of saturation reminiscent of previous studies of fluid ITG-driven turbulence (see, e.g., [117]), related to the presence, or otherwise, of zonal activity on electron scales. These simulations were then extended into the electromagnetic regime, were it was shown that electromagnetic, sTAI-driven turbulence fails to saturate similarly to what has been observed more widely within the field (Chapter 8). This demonstrates (numerically) that sTAI is indeed a viable instability capable of driving vigorous turbulence. The nature of this 'blow-up' was then characterised, and some routes towards explanation speculated about (Section 8.2).

The results of this thesis demonstrate two key points: (i) that if finite perturbations of the magnetic-field direction are allowed in the presence of a radial equilibrium electron temperature gradient, then the system is able to extract free energy from the equilibrium temperature gradient via a route that is distinct from the usual $\boldsymbol{E}\times\boldsymbol{B}$

feedback, manifested here in the novel thermo-Alfvénic instability, and that this extraction channel can be dominant — in some sense, infinitely so, as the presence of electromagnetic instabilities such as the TAI can lead to a lack of saturation in local turbulence simulations; and (ii) turbulence in gradient-driven systems, like those encountered in the context of magnetic-confinement fusion, is able to saturate via a constant-flux cascade of energy from some large-scale region of injection to dissipation at small scales. The fact that it should ever do so is not obvious *a priori*; the material of Chapter 7 is one of only two existing demonstrations of this fact, the other being [12], in the context of ITG turbulence. This said, such a saturation mechanism appears to be more fragile than perhaps previously realised: it turns out to be quite easy to find types of ETG-driven turbulence that fail to saturate, one example being the already mentioned blow-up of sTAI-driven turbulence and another the blow up of the cETG-driven one. It may be that in such reduced models of plasma turbulence, saturation is an exception rather than the rule, and each instance of it should be a cause for careful physical investigation.

Given the suitably general nature of these findings, this physics should be of some concern, or at least interest, to those attempting to model the effect of turbulent transport in tokamak-relevant configurations, particularly those in which electromagnetic effects are thought to be dominant.

9.1 Open issues

The results and conclusions of this thesis were derived within the context of a reduced model, as doing so allowed us to focus directly on the fundamental physical processes behind electromagnetic destabilisation on electron scales in the presence of an electron temperature gradient. Such simplifications, however, always come at a cost to general practical applicability, and so we will here devote some space to a discussion of the most pressing questions and lines of investigation left open, or opened up, by this work.

9.1.1 Ion dynamics

With little exception, the results of this thesis have been derived in the limit where the ion density response is Boltzmann, as in (2.22). In terms of perpendicular scales, this is equivalent to the assumption that $k_\perp \gg \rho_i^{-1}$. Simultaneously, the electromagnetic physics — to which we have given much attention — occurs on the scales at which magnetic-field perturbations can be created by electron motions, viz., below the flux-freezing scale, $k_\perp \lesssim d_e^{-1}$ (or $d_e^{-1}\chi^{-1}$, in the collisional limit). Therefore, in order for the adiabatic-ion assumption to remain valid, we need a sufficient separation between ρ_i and the largest perpendicular scale within our system. For the outer scale (6.38) of our putative cTAI turbulence, this implies a restriction on the electron beta of

$$\frac{Z^2 m_e}{\tau m_i} \ll \beta_e \ll \frac{\tau m_i}{Z^2 m_e}\left(\frac{L_T}{L_B}\right)^3 \begin{cases} \left(\dfrac{L_B}{L_\parallel}\right)^4, & \text{collisionless,} \\ \left(\dfrac{L_B}{L_\parallel}\right)^6 \left(\dfrac{\lambda_{ei}}{L_B}\right)^2, & \text{collisional,} \end{cases} \tag{9.1}$$

with the lower bound following from demanding that $\rho_i \gg d_e$. This scale separation is never going to be very large in a realistic plasma, and thus an important question is whether the TAI mechanism — that provides an electromagnetic source of free energy on the largest electron scales — survives at, or indeed across, the ion-Larmor transition, for $k_\perp \rho_i \lesssim 1$. Answering this will require both a careful handling of finite-ion-Larmor-radius (FLR) effects and the introduction of an ion-temperature gradient, in addition to the electron one. Indeed, as we discussed in sections 7.3 and 8.2.1, the inclusion of ion dynamics may be crucial for determining the saturation of electron-scale turbulence. This work is already under way.

9.1.2 Micro-tearing modes

As mentioned in Chapter 1, much of the research into electromagnetic microinstabilities and turbulence in fusion contexts has focused on two microinstability classes: micro-tearing modes (MTMs) and KBMs. While we have already discussed the latter within the context of this work (Section 4.4), we have little to say about MTMs. This is because we did not include in our model any shear of the equilibrium magnetic field — often thought to be a crucial ingredient in MTM dynamics, which encourages the associated tearing of magnetic field lines (see, e.g., [28] and references therein). Note that the effect sometimes viewed as responsible for driving slab MTMs in the absence of magnetic shear, the so-called 'time-dependent thermal force' [26], is negligible within our analysis (see appendix G of [1]). As a result, we conclude that the TAI cannot be classed as a particular branch of the MTM zoo. It is, naturally, an interesting question how the results of this thesis would be modified in the presence of magnetic shear;

given that the TAI mechanism leads to a growth of perturbations of the magnetic field's direction, it is possible that the TAI could drive tearing in a sheared setting. In any case, introducing magnetic shear into our reduced system would perhaps allow for an investigation of MTM dynamics. Another key ingredient required for a complete description of MTM dynamics is the poloidal variation of the magnetic field, since MTMs typically sample an average 'good-curvature' in a tokamak due their extended nature along the field line. Given the alignment of the magnetic-field and electron-temperature gradients in the geometry adopted in Section 2.1, our model is consigned to describe only the 'bad-curvature' region of a tokamak, and so will not capture the (potentially critical) effects of this average 'good-curvature' on MTM dynamics. A model of these modes that includes both the effects of magnetic shear and the poloidal variation of the magnetic field can be found in [109].

9.1.3 Nonlinear saturation of electromagnetic simulations

Lastly, we return to the issue of the saturation failure encountered in simulations of electromagnetic turbulence. The equations that we have been considering are sufficiently simple — in comparison to the full gyrokinetic system employed in more 'complete' simulations — that making theoretical sense of their saturation failure should be a graspable task; we proposed a number of routes towards this in Section 8.2. The issue of the blow-up aside, there is of course the broader question of the structure of the saturated state of electromagnetic turbulence in tokamak plasmas — or even the much simpler tokamak-inspired ones, like ours. The simulations of electrostatic sETG-driven turbulence of Chapter 7 strongly support the assertion that electrostatic gradient-driven plasma turbulence can saturate via a constant-flux, critically balanced cascade of free energy towards small scales; will the same be true in the electromagnetic regime? The numerical studies of Chapter 8 are but a preliminary step toward further investigations that should reveal the answer to this question and many others encountered in the pursuit of a full characterisation of the saturated state of electromagnetic turbulence in tokamak plasmas.

Appendix A

Derivation of electron fluid equations

This appendix details a self-contained derivation of the electron-fluid equations that are used throughout the numerical studies of chapters 7 and Chapter 8. The purposes of its inclusion are two-fold: (i) to demonstrate that (7.25) and (7.26) remain valid even when derived with the correct linearised Landau collision operator, up to the definition of certain coefficients (see the discussion of Section 7.1.3); and (ii) to show that the low-beta equations that we have been considering throughout this thesis are valid for a greater range of parameters and perpendicular scales than those considered in [1]. In what follows, Appendix A.1 describes and physically motivates our electron-scale, collisional ordering, which is then implemented to derive equations describing our ion and electron dynamics in Appendix A.3 and Appendix A.4, respectively. Appendix A.5 introduces useful subsidiary limits of these equations and their reduction to those used throughout the main body of this thesis. Appendix A.6 discusses an instability driven by the ETG in the presence of electron-ion thermal diffusion. All other technical appendices can be found in [1]. We will adopt the same magnetic equilibrium as in Section 2.1.

A.1 Collisional, electron-scale ordering

In our equations, we would like to be able to capture, at a minimum, the physics associated with drift waves, perpendicular advection by both magnetic drifts and $\boldsymbol{E}\times\boldsymbol{B}$ flows, and parallel heat conduction. As such, we postulate an asymptotic ordering in which the frequencies ω of the perturbations in the plasma are comparable to the characteristic frequencies associated with these phenomena, viz.,

$$\nu_{ee} \sim \nu_{ei} \gg \omega \sim \omega_{*s} \sim \omega_{ds} \sim k_\perp v_E \sim \kappa k_\parallel^2, \tag{A.1}$$

where

$$\omega_{*s} = \frac{k_y \rho_s v_{\text{th}s}}{2L_{T_s}}, \quad \omega_{ds} = \frac{k_y \rho_s v_{\text{th}s}}{2L_B} \tag{A.2}$$

are the drift frequency and magnetic-drift frequency, respectively, $\boldsymbol{v}_E = c\boldsymbol{E} \times \boldsymbol{B}/B^2$ is the $\boldsymbol{E} \times \boldsymbol{B}$ drift velocity (c is the speed of light), $\kappa \sim v_{\text{th}e}^2/\nu_{ei}$ is the electron thermal diffusivity, and

$$\nu_{ei} = \frac{4\sqrt{2\pi}}{3} \frac{e^4 n_{0e} \log \Lambda}{m_e^{1/2} T_{0e}^{3/2}}, \quad \nu_{ee} = \frac{\nu_{ei}}{Z} \tag{A.3}$$

are the electron-ion and electron-electron collision frequencies, respectively, with $\log \Lambda$ the Coulomb logarithm [111, 127].

The ordering of the parallel conduction rate with respect to the drift frequencies gives us a constraint relating parallel and perpendicular wavenumbers:

$$\kappa k_\parallel^2 \sim \omega_{*s} \sim \omega_{ds} \sim k_\perp \rho_e \frac{v_{\text{th}e}}{L} \quad \Rightarrow \quad (k_\parallel L)^2 \sim \frac{L}{\lambda_{ei}} k_\perp \rho_e, \tag{A.4}$$

where $\lambda_{ei} = v_{\text{th}e}/\nu_{ei}$ is the electron-ion mean free path and L is some (perpendicular) equilibrium length scale, $L \sim L_{n_s} \sim L_{T_s} \sim L_B \sim R$. The ordering of the parallel conduction rate with respect to the $\boldsymbol{E} \times \boldsymbol{B}$ drifts determines the size of perpendicular flows within our system:

$$\kappa k_\parallel^2 \sim k_\perp v_E \quad \Rightarrow \quad \frac{v_E}{v_{\text{th}e}} \sim \frac{k_\parallel}{k_\perp} k_\parallel \lambda_{ei} \sim \frac{d_e}{L} \sqrt{\beta_e} \equiv \epsilon \sqrt{\beta_e}, \tag{A.5}$$

where $\epsilon = d_e/L$ is the gyrokinetic small parameter (see, e.g., [55]), mandating small-amplitude, anisotropic perturbations. The frequency of these perturbations is small compared to the Larmor frequencies of both the electrons and ions:

$$\frac{\omega}{\Omega_e} \sim \frac{k_\perp v_E}{\Omega_e} \sim k_\perp d_e \epsilon \beta_e, \quad \frac{\omega}{\Omega_i} = \frac{m_i}{Z m_e} \frac{\omega}{\Omega_e} \sim k_\perp d_e \epsilon \beta_e \frac{m_i}{m_e}. \tag{A.6}$$

The ordering of v_E relative to the electron thermal velocity allows us to order the amplitude of the perturbed scalar potential ϕ:

$$\frac{v_E}{v_{\text{th}e}} \sim \frac{c}{B_0} \frac{k_\perp \phi}{v_{\text{th}e}} \sim k_\perp \rho_e \frac{e\phi}{T_{0e}} \quad \Rightarrow \quad \frac{e\phi}{T_{0e}} \sim \frac{\epsilon}{k_\perp d_e}. \tag{A.7}$$

The density perturbations δn_s are ordered anticipating a Boltzmann density response and the temperature perturbations δT_s are assumed comparable to them:

$$\frac{\delta T_e}{T_{0e}} \sim \frac{\delta T_i}{T_{0i}} \sim \frac{\delta n_i}{n_{0i}} = \frac{\delta n_e}{n_{0e}} \sim \frac{e\phi}{T_{0e}} \sim \frac{\epsilon}{k_\perp d_e}. \tag{A.8}$$

For the ordering of perpendicular magnetic field perturbations, we demand that the effects of Lorentz tension (equivalently, of parallel compressions) must always be large enough so as to have an effect on the electron density perturbation, viz., [cf. (A.68)]

$$\frac{\mathrm{d}}{\mathrm{d}t}\frac{\delta n_e}{n_{0e}} \sim \nabla_\parallel u_{\parallel e} \sim \frac{c}{4\pi e n_{0e}} \nabla_\parallel \left[\boldsymbol{b}_0 \cdot (\nabla_\perp \times \delta \boldsymbol{B}_\perp)\right] \quad \Rightarrow \quad \frac{\delta \boldsymbol{B}_\perp}{B_0} \sim \frac{k_\parallel L}{k_\perp d_e \chi}\frac{e\phi}{T_{0e}}, \tag{A.9}$$

whereas the (compressive) parallel magnetic-field perturbations are ordered anticipating pressure balance:

$$\frac{\delta B_\parallel}{B_0} = \frac{4\pi}{B_0^2}\delta\left(\frac{B^2}{8\pi}\right) \sim \frac{4\pi}{B_0^2}\delta(n_s T_s) \sim \beta_e \frac{\delta T_e}{T_{0e}} \sim \frac{\epsilon \beta_e}{k_\perp d_e}. \tag{A.10}$$

In their current form, the orderings (A.4) and (A.5)-(A.10) under-constrain our system, in that they still allow for a choice of ordering for our perpendicular wavenumbers $k_\perp$ with respect to the electron and ion Larmor radii. Here, we choose to append to (A.1) the characteristic frequencies associated with kinetic Aflvén waves, resistivity and thermal diffusivity, viz.,

$$\nu_{ee} \sim \nu_{ei} \gg \omega \sim \omega_{\mathrm{KAW}} \sim \omega_{*s} \sim \omega_{ds} \sim k_\perp v_E \sim \kappa k_\parallel^2 \sim (k_\perp d_e)^2 \nu_{ei} \sim (k_\perp \rho_e)^2 \nu_{ee}, \tag{A.11}$$

where

$$\omega_{\mathrm{KAW}} = \frac{1}{\sqrt{2}} k_\parallel v_{\mathrm{th}e} k_\perp d_e, \tag{A.12}$$

is the kinetic Alfvén wave frequency. Such a choice represents a maximal ordering that allows us to retain all of the relevant electron physics, while making ion dynamics sufficiently simple [see (A.27)]. Then, the ordering of the parallel conduction rate with respect to the KAW implies that

$$\omega_{\mathrm{KAW}} \sim \kappa k_\parallel^2 \quad \Rightarrow \quad k_\perp d_e \sim k_\parallel \lambda_{ei}, \tag{A.13}$$

which, when combined with (A.4), implies that parallel and perpendicular wavenumbers must be ordered as

$$k_\parallel L \sim \sqrt{\beta_e}, \quad k_\perp d_e \sim \sqrt{\beta_e}\frac{\lambda_{ei}}{L} \equiv \chi^{-1}, \tag{A.14}$$

i.e., the perpendicular wavelengths must be ordered comparable to the flux-freezing scale, as anticipated in (2.33). Lastly, the ordering of the resistive and diffusive rates gives

$$(k_\perp d_e)^2 \nu_{ei} \sim (k_\perp \rho_e)^2 \nu_{ee} \quad \Rightarrow \quad d_e \sim \rho_e \quad \Rightarrow \quad \beta_e \sim 1, \tag{A.15}$$

i.e., we must perform our expansion treating β_e as an order-unity parameter (subsidiary orderings with respect to β_e are considered in Appendix A.5).

Together, (A.14) and (A.15) imply the following ordering of frequencies:

$$\frac{\omega}{\Omega_e} \sim \chi^{-1}\epsilon, \quad \frac{\omega}{\Omega_i} \sim \frac{m_i}{Zm_e}\chi^{-1}\epsilon, \tag{A.16}$$

length scales:

$$k_\perp \rho_i \sim \chi^{-1}\sqrt{\frac{m_i}{m_e}}, \quad k_\perp d_e \sim k_\perp \rho_e \sim \chi^{-1}, \quad k_\parallel L \sim 1, \quad \frac{k_\parallel}{k_\perp} \sim \chi\epsilon, \tag{A.17}$$

and fluctuation amplitudes:

$$\frac{e\phi}{T_{0e}} \sim \frac{\delta n_e}{n_{0e}} \sim \frac{\delta n_i}{n_{0i}} \sim \frac{\delta T_e}{T_{0e}} \sim \frac{\delta T_i}{T_{0i}} \sim \frac{\delta \boldsymbol{B}_\perp}{B_0} \sim \frac{\delta B_\parallel}{B_0} \sim \chi\epsilon, \tag{A.18}$$

meaning that all relevant quantities are naturally ordered with respect to some combination of m_e/m_i, χ^{-1}, and the gyrokinetic small parameter $\epsilon = d_e/L$. The above ordering of frequencies, length scales and amplitudes with respect to ϵ is the standard gyrokinetic ordering (see, e.g., [55]). We choose to treat the ordering in χ^{-1} — the fact that this should be formally small following straightforwardly from, e.g., $\nu_{ei} \gg (k_\perp d_e)^2 \nu_{ei}$ — as subsidiary to both the orderings in ϵ and in the mass ratio [see the first expression in (A.17)], meaning that the formal hierarchy of our expansions is

$$\epsilon \ll \sqrt{\frac{m_e}{m_i}} \ll \chi^{-1} \ll 1, \tag{A.19}$$

with all other dimensionless parameters treated as finite. Since $\beta_e \sim 1$, our collisional expansion parameter $\chi^{-1} = \sqrt{\beta_e}\lambda_{ei}/L$ is simply the ratio of the electron-ion mean free path to some (perpendicular) equilibrium length scale, viz., $\chi^{-1} \sim \lambda_{ei}/L \ll 1$, the usual Braginskii ordering [111]. However, we have chosen to use χ^{-1} here to remain consistent with the notation used in [1] for ease of comparison.

A.2 Gyrokinetic equations

Given (A.19), we take as our starting point the gyrokinetic system of equations, in which the gyrokinetic distribution function h_s is described by

$$\frac{\partial}{\partial t}\left(h_s - \frac{q_s \langle\chi\rangle_{\boldsymbol{R}_s}}{T_{0s}} f_{0s}\right) + \left(v_\parallel \boldsymbol{b}_0 + \boldsymbol{v}_{ds}\right)\cdot\nabla h_s + \frac{c}{B_0}\boldsymbol{b}_0 \cdot \left[\nabla\langle\chi\rangle_{\boldsymbol{R}_s} \times \nabla\left(h_s + f_{0s}\right)\right] \\ = \sum_{s'} \left\langle C^{(l)}_{ss'}[h_s]\right\rangle_{\boldsymbol{R}_s}, \tag{A.20}$$

where $\langle\ldots\rangle_{\boldsymbol{R}_s}$ denotes the standard gyroaverage at constant gyrocentre position $\boldsymbol{R}_s$, and

$$\langle\chi\rangle_{\boldsymbol{R}_s} = \sum_{\boldsymbol{k}} e^{i\boldsymbol{k}\cdot\boldsymbol{R}_s}\left[J_0(b_s)\left(\phi_{\boldsymbol{k}} - \frac{v_\parallel A_{\parallel\boldsymbol{k}}}{c}\right) + \frac{2J_1(b_s)}{b_s}\frac{T_{0s}}{q_s}\frac{v_\perp^2}{v_{\mathrm{th}s}^2}\frac{\delta B_{\parallel\boldsymbol{k}}}{B_0}\right] \tag{A.21}$$

is the (gyro-averaged) gyrokinetic potential, with $b_s = k_\perp v_\perp/\Omega_s$. The collision term on the right-hand side of (A.20) involves gyroaverages of the linearised Landau collision operator

$$C^{(l)}_{ss'}[h_s] = \frac{\gamma_{ss'}}{m_s}\nabla_v \cdot \int \mathrm{d}^3\boldsymbol{v}'\, f_{0s}(v) f_{0s'}(v')(\nabla_w\nabla_w w) \\ \cdot\left[\frac{1}{m_s}\nabla_v\left(\frac{h_s(\boldsymbol{v})}{f_{0s}(v)}\right) - \frac{1}{m_{s'}}\nabla_{v'}\left(\frac{h_{s'}(\boldsymbol{v}')}{f_{0s'}(v')}\right)\right], \tag{A.22}$$

where $w = |\boldsymbol{w}|$, $\boldsymbol{w} = \boldsymbol{v} - \boldsymbol{v}'$, and $\gamma_{ss'} = 2\pi q_s^2 q_{s'}^2 \log\Lambda$, and all velocity derivatives are evaluated at constant position $\boldsymbol{r}$. Finally, (A.20) is closed by the three field equations of quasineutrality, the parallel and perpendicular parts of Ampère's law:

$$0 = \sum_s q_s \delta n_s = \sum_s q_s\left[-\frac{q_s\phi}{T_{0s}}n_{0s} + \int \mathrm{d}^3\boldsymbol{v}\,\langle h_s\rangle_{\boldsymbol{r}}\right], \tag{A.23}$$

$$\nabla_\perp^2 A_\parallel = -\frac{4\pi}{c}\sum_s q_s \int \mathrm{d}^3\boldsymbol{v}\, v_\parallel \langle h_s\rangle_{\boldsymbol{r}}, \tag{A.24}$$

$$\nabla_\perp^2 \delta B_\parallel = -\frac{4\pi}{c}\boldsymbol{b}_0\cdot\left[\nabla_\perp \times \sum_s q_s \int \mathrm{d}^3\boldsymbol{v}\,\langle \boldsymbol{v}_\perp h_s\rangle_{\boldsymbol{r}}\right]. \tag{A.25}$$

In Appendix A.3 and Appendix A.4, we systematically expand the gyrokinetic system of equations (A.20)-(A.25) in order to obtain a closed system to leading order in our collisional expansion.

A.3 Ion kinetics

Given that the ordering of perpendicular wavenumbers (A.17) implies that $k_\perp \rho_i \gg 1$ within the expansion in the mass ratio, it is straightforward to show [by, e.g., expanding the Bessel functions in (A.21) for $b_i \gg 1$] that the gyroaveraged terms in (A.20) for $s = i$ are small:

$$\langle \dots \rangle_{\boldsymbol{R}_i} \sim \frac{1}{\sqrt{k_\perp \rho_i}} \ll 1. \tag{A.26}$$

This means that, to leading order in the mass ratio expansion, (A.20) is satisfied by the solution

$$h_i = 0, \tag{A.27}$$

with any contributions to the field equations (A.23)-(A.25) arising from the inhomogeneous solutions to (A.20) being of size

$$\langle h_i \rangle_{\boldsymbol{r}} \sim \left\langle \langle \chi \rangle_{\boldsymbol{R}_i} \right\rangle_{\boldsymbol{r}} \sim \frac{\chi}{k_\perp \rho_i}, \tag{A.28}$$

which can safely be neglected. Thus, the ion dynamics do not enter anywhere into our equations, which is the approximation of 'adiabatic ions'. We will henceforth neglect the ion temperature gradient, and denote the electron temperature gradient $L_{T_e} = L_T$.

A.4 Electron fluid equations

We now proceed with our derivation of the electron fluid equations, expanding our gyrokinetic distribution function h_e in $\chi^{-1} \ll 1$ as

$$h_e = \sum_{n=0}^{\infty} h_e^{(n)}, \quad h_e^{(n)} \sim \chi^{-n} \frac{e\phi}{T_{0e}} f_{0e}. \tag{A.29}$$

The electromagnetic fields will not be expanded in the same way, as it will turn out that they only need to be determined to leading order for a closed system of equations to be obtained.

A.4.1 Zeroth order: perturbed Maxwellian

Given the ordering of timescales (A.11), the collision operator is dominant to leading order:

$$C_{ee}^{(l)}\left[h_e^{(0)}\right]+\mathcal{L}_{ei}\left[h_e^{(0)}\right]=0, \tag{A.30}$$

where $C_{ee}^{(l)}$ is given by (A.22) for $s=s'=e$, and

$$\mathcal{L}_{ei}\left[h_e\right]=\frac{\gamma_{ei}n_{0e}}{m_e^2}\nabla_v\left[f_{0e}\nabla_v\nabla_v v\cdot\nabla_v\left(\frac{h_e}{f_{0e}}\right)\right] \tag{A.31}$$

is the pitch-angle scattering (Lorentz) collision operator, valid to leading order in the mass ratio. We multiply (A.30) throughout by $h_e^{(0)}/f_{0e}$ and integrate over the entire phase space, yielding

$$\int\frac{\mathrm{d}^3\boldsymbol{r}}{V}\int\mathrm{d}^3\boldsymbol{v}\,C_{ee}^{(l)}\left[h_e^{(0)}\right]+\int\frac{\mathrm{d}^3\boldsymbol{r}}{V}\int\mathrm{d}^3\boldsymbol{v}\,\mathcal{L}_{ei}\left[h_e^{(0)}\right]=0. \tag{A.32}$$

Both terms in (A.32) are negative definite and must vanish individually, meaning that the solution is constrained to be a perturbed Maxwellian with no mean flow [127], viz.,

$$h_e^{(0)}=\left[\frac{\delta n_e}{n_{0e}}-\varphi+\frac{\delta T_e}{T_{0e}}\left(\frac{v^2}{v_{\mathrm{ths}}^2}-\frac{3}{2}\right)\right]f_{0e}, \tag{A.33}$$

where φ is as defined in (2.13), and we have imposed the solvability conditions

$$\int\mathrm{d}^3\boldsymbol{v}\,h_e^{(n)}=\int\mathrm{d}^3\boldsymbol{v}\,v^2h_e^{(n)}=0,\quad n\geqslant1, \tag{A.34}$$

in order to determine uniquely the density δn_e and temperature δT_e moments in (A.33). We note that, in general, the Lorentz collision operator constrains the electron distribution function to be isotropic in the frame moving with the parallel ion velocity. However, the parallel ion velocity is zero to all orders within our expansion in χ^{-1} [given the adiabatic ion solution (A.27)], meaning that the electron distribution function will have no parallel velocity moment to leading order.

We now turn our attention to the field equations (A.23)-(A.25). Using the solutions (A.27) and (A.33), as well as the fact that the gyroaverage operators are unity operators at this order in the collisional expansion, quasineutrality and perpendicular Ampère's law straightforwardly become

$$\frac{\delta n_e}{n_{0e}}=-\frac{Z}{\tau}\varphi\equiv-\bar{\tau}^{-1}\varphi,\quad\frac{\delta B_\parallel}{B_0}=-\frac{\beta_e}{2}\left(\frac{\delta n_e}{n_{0e}}-\varphi+\frac{\delta T_e}{T_{0e}}\right). \tag{A.35}$$

The first of these is the first expression in (2.30).

A.4.2 First order: parallel flows

The parallel flows are determined self-consistently from the leading-order perturbations at the next order in our expansion. Given the ordering of wavenumbers (A.17) and field amplitudes (A.18), the terms involving the parallel component of the magnetic vector potential enter at the next order, viz.,

$$\frac{v_\parallel A_\parallel}{c\phi} \sim \frac{1}{k_\perp \rho_e} \sim \chi. \tag{A.36}$$

This means that $h_e^{(1)}$ is determined by the Spitzer-Härm problem [111, 127, 128]:

$$v_\parallel \left[\nabla_\parallel \log p_e + \left(\frac{v^2}{v_{\text{the}}^2} - \frac{5}{2}\right) \nabla_\parallel \log T_e\right] f_{0e} + v_\parallel \frac{eE_\parallel}{T_{0e}} f_{0e} = C_{ee}^{(l)}\left[h_e^{(1)}\right] + \mathcal{L}_{ei}\left[h_e^{(1)}\right]. \tag{A.37}$$

In (A.37), $\nabla_\parallel \log T_e$ and $\nabla_\parallel \log p_e$ are defined in (2.21) and (4.7), respectively, the parallel derivative along the exact field line $\nabla_\parallel$ in (2.11), and the parallel electric field is given by (2.13).

(A.37) can be inverted for $h_e^{(1)}$ by means of standard variational methods. We define the functional:

$$\begin{aligned}\Sigma[h_e] = &- \left\langle h_e, C_{ee}^{(l)}\left[h_e\right]\right\rangle - \left\langle h_e, \mathcal{L}_{ei}\left[h_e\right]\right\rangle \\ &+ 2\left\langle h_e, \left[\nabla_\parallel \log p_e + \frac{eE_\parallel}{T_{0e}} + \left(\frac{v^2}{v_{\text{the}}^2} - \frac{5}{2}\right) \nabla_\parallel \log T_e\right] v_\parallel f_{0e}\right\rangle,\end{aligned} \tag{A.38}$$

where $\langle \ldots, \ldots \rangle$ denotes an inner product in velocity space weighted by the inverse of the electron (Maxwellian) equilibrium f_{0e}. Then, considering small variations $h_e = h_{\min} + \delta h_e$ and using the self-adjointness of the linearised collision operator, it is straightforward to show that the functional $\Sigma[h_e]$ has a minimum at $h_{\min} = h_e^{(1)}$, for any variation δh_e (see, e.g., [127]). Given that the spherical harmonics are eigenfunctions of the linearised collision operator, we choose to expand our distribution function in terms of spherical coordinates in velocity space (x, α, β), with $x = v^2/v_{\text{the}}^2$, as

$$h_e^{(1)} = \sum_{p=0}^{\infty} a_p L_p^{(3/2)}(x) v_\parallel f_{0e}(v) = \sum_{p=0}^{\infty} a_p L_p^{(3/2)}(x) v \cos\alpha f_{0e}(v), \tag{A.39}$$

where $L_p^{(n)}(x)$ are the generalised Laguerre polynomials and a_p coefficients to be determined. Using this in (A.38), one obtains

$$\Sigma\left[h_e^{(1)}\right] = n_{0e}v_{\text{the}}^2\left[\sum_{p=0}^{\infty}\sum_{q=0}^{\infty}\frac{a_p a_q}{2}\left(\nu_{ee}K_{pq}^{ee}+\nu_{ei}K_{pq}^{ei}\right)\right.$$
$$\left. +a_0\left(\nabla_\parallel \log p_e + \frac{eE_\parallel}{T_{0e}}\right) - \frac{5}{2}a_1\nabla_\parallel \log T_e\right], \qquad (A.40)$$

where

$$K_{pq}^{ee} = -\frac{2}{n_e\nu_{ee}}\left\langle x^{1/2}L_p^{(3/2)}(x)f_{0e}(v)\cos\alpha, C_{ee}^{(l)}\left[x^{1/2}L_q^{(3/2)}(x)f_{0e}(v)\cos\alpha\right]\right\rangle, \qquad (A.41)$$
$$K_{pq}^{ei} = -\frac{2}{n_e\nu_{ei}}\left\langle x^{1/2}L_p^{(3/2)}(x)f_{0e}(v)\cos\alpha, \mathcal{L}_{ei}\left[x^{1/2}L_q^{(3/2)}(x)f_{0e}(v)\cos\alpha\right]\right\rangle, \qquad (A.42)$$

are coefficients as calculated in, e.g., [67] (and references therein). Truncating (A.39) at $p = 3$, and demanding that the functional (A.40) be stationary with respect to variations in the coefficients a_p, we find that

$$h_e^{(1)} = \left[a_0 + a_1 L_1^{(3/2)}(x) + a_2 L_2^{(3/2)}(x)\right]v_\parallel f_{0e}, \qquad (A.43)$$

where the coefficients are given by

$$\nu_{ei}a_0 = -\frac{\frac{217}{64}+\frac{151}{8\sqrt{2}Z}+\frac{9}{2Z^2}}{1+\frac{61}{8\sqrt{2}Z}+\frac{9}{2Z^2}}\left(\nabla_\parallel \log p_e + \frac{eE_\parallel}{T_{0e}}\right) - \frac{\frac{5}{2}\left(\frac{33}{16}+\frac{45}{8\sqrt{2}Z}\right)}{1+\frac{61}{8\sqrt{2}Z}+\frac{9}{2Z^2}}\nabla_\parallel \log T_e, \qquad (A.44)$$

$$\nu_{ei}a_1 = \frac{\frac{33}{16}+\frac{45}{8\sqrt{2}Z}}{1+\frac{61}{8\sqrt{2}Z}+\frac{9}{2Z^2}}\left(\nabla_\parallel \log p_e + \frac{eE_\parallel}{T_{0e}}\right) + \frac{\frac{5}{2}\left(\frac{13}{4}+\frac{45}{8\sqrt{2}Z}\right)}{1+\frac{61}{8\sqrt{2}Z}+\frac{9}{2Z^2}}\nabla_\parallel \log T_e, \qquad (A.45)$$

$$\nu_{ei}a_2 = -\frac{\frac{3}{8}-\frac{3}{2\sqrt{2}Z}}{1+\frac{61}{8\sqrt{2}Z}+\frac{9}{2Z^2}}\left(\nabla_\parallel \log p_e + \frac{eE_\parallel}{T_{0e}}\right) - \frac{\frac{5}{2}\left(\frac{3}{2}+\frac{3}{2\sqrt{2}Z}\right)}{1+\frac{61}{8\sqrt{2}Z}+\frac{9}{2Z^2}}\nabla_\parallel \log T_e, \qquad (A.46)$$

which can easily be shown to satisfy the Onsager relations [110]. (A.43) allows us to determine, subject to the solvability condition

$$\int \mathrm{d}^3\boldsymbol{v}\, v_\parallel h_e^{(n)} = 0, \quad n \geqslant 2, \qquad (A.47)$$

the parallel electron flow, and thus the parallel component of the magnetic vector potential via parallel Ampère's law (A.24):

$$u_{\parallel e} = \frac{1}{n_{0e}}\int \mathrm{d}^3\boldsymbol{v}\, v_\parallel h_e^{(1)} = v_{\text{the}}d_e^2\nabla_\perp^2\mathcal{A}. \qquad (A.48)$$

This is the second expression in (2.30). Using the solution (A.43) for $h_e^{(1)}$ in (A.48) and re-arranging the resulting expression for $\partial\mathcal{A}/\partial t$, it becomes the first of our three fluid equations, describing the evolution of the parallel magnetic vector potential perturbations:

$$\frac{\mathrm{d}\mathcal{A}}{\mathrm{d}t} + \frac{v_{\mathrm{th}e}}{2}\frac{\partial\varphi}{\partial z} = \frac{v_{\mathrm{th}e}}{2}\nabla_\parallel \log p_e + \frac{c_2}{c_1}\frac{v_{\mathrm{th}e}}{2}\nabla_\parallel \log T_e + \frac{\nu_{ei}}{c_1} d_e^2 \nabla_\perp^2 \mathcal{A}, \tag{A.49}$$

where we have defined the (ion-charge-dependent) coefficients [cf., for $Z = 1$, (C16) and (C17) in [67]]

$$c_1 = \frac{\frac{217}{64} + \frac{151}{8\sqrt{2}Z} + \frac{9}{2Z^2}}{1 + \frac{61}{8\sqrt{2}Z} + \frac{9}{2Z^2}}, \quad c_2 = \frac{\frac{5}{2}\left(\frac{33}{16} + \frac{45}{8\sqrt{2}Z}\right)}{1 + \frac{61}{8\sqrt{2}Z} + \frac{9}{2Z^2}}, \quad c_3 = \frac{\frac{25}{4}\left(\frac{13}{4} + \frac{45}{8\sqrt{2}Z}\right)}{1 + \frac{61}{8\sqrt{2}Z}} - \frac{c_2^2}{c_1}. \tag{A.50}$$

A.4.3 Second order: electron thermal diffusion

At second order, the electron gyrokinetic equation describes the evolution of the density and temperature perturbations in (A.33), viz.,

$$\begin{aligned} &\frac{\mathrm{d}}{\mathrm{d}t}\left[h_e^{(0)} + \left(\varphi - \frac{v_\perp^2}{v_{\mathrm{th}e}^2}\frac{\delta B_\parallel}{B_0}\right) f_{0e}\right] + \frac{\rho_e v_{\mathrm{th}e}}{2}\left\{h_e^{(0)} + \varphi f_{0e}, \frac{v_\perp^2}{v_{\mathrm{th}e}^2}\frac{\delta B_\parallel}{B_0}\right\} + v_\parallel \nabla_\parallel h_e^{(1)} \\ &\quad + \boldsymbol{v}_{de}\cdot\nabla_\perp h_e^{(0)} + \frac{\rho_e v_{\mathrm{th}e}}{2}\frac{\partial}{\partial y}\left(\varphi - \frac{v_\perp^2}{v_{\mathrm{th}e}^2}\frac{\delta B_\parallel}{B_0}\right)\left[\frac{1}{L_n} + \frac{1}{L_T}\left(\frac{v^2}{v_{\mathrm{th}e}^2} - \frac{3}{2}\right)\right] f_{0e} \\ &= \left\langle C_{ee}^{(l)}[h_e]\right\rangle_{\boldsymbol{R}_e} + \left\langle \mathcal{L}_{ei}[h_e]\right\rangle_{\boldsymbol{R}_e}. \end{aligned} \tag{A.51}$$

Taking the density and temperature moments of (A.51) is straightforward for all terms but the collision operator on the right-hand side, which needs to be evaluated to second order in χ^{-1}, a task on which we shall now focus. In particular, we consider the integral

$$I_{\mathrm{col}} = \frac{1}{n_{0e}}\int \mathrm{d}^3\boldsymbol{v}\, G(v)\left\langle\left\langle C_{ee}^{(l)}[h_e] + \mathcal{L}_{ei}[h_e]\right\rangle_{\boldsymbol{R}_e}\right\rangle_{\boldsymbol{r}}, \tag{A.52}$$

where $G(v) = (1, v^2/v_{\mathrm{th}e}^2 - 3/2)$. Expressing h_e in Fourier components as

$$h_e = \sum_{\boldsymbol{k}} e^{i\boldsymbol{k}\cdot\boldsymbol{R}_e} h_{e\boldsymbol{k}}, \tag{A.53}$$

we can write

$$\langle C[h_e]\rangle_{\boldsymbol{R}_e} = \sum_{\boldsymbol{k}}\left\langle C\left[h_{e\boldsymbol{k}} e^{i\boldsymbol{k}\cdot\boldsymbol{R}_e}\right]\right\rangle_{\boldsymbol{R}_e} = \sum_{\boldsymbol{k}}\left\langle C\left[h_{e\boldsymbol{k}} e^{-i\boldsymbol{k}\cdot\boldsymbol{\rho}_e}\right] e^{i\boldsymbol{k}\cdot\boldsymbol{\rho}_e}\right\rangle e^{i\boldsymbol{k}\cdot\boldsymbol{R}_e}, \tag{A.54}$$

where $\boldsymbol{\rho}_e = \boldsymbol{b}_0 \times \boldsymbol{v}_\perp/\Omega_e$. Then, given the ordering of wavenumbers (A.17), we expand the oscillatory exponential factors in (A.52) to order $(\boldsymbol{k}\cdot\boldsymbol{\rho}_e)^2 \sim \chi^{-2}$:

$$\begin{aligned} I_{\text{col}} = \int \mathrm{d}^3\boldsymbol{v}\, G(v) \sum_{\boldsymbol{k}} e^{i\boldsymbol{k}\cdot\boldsymbol{r}} \Bigg[&\left\langle C_{ee}^{(l)}\left[h_{e\boldsymbol{k}}^{(0)}\right]\right\rangle + \left\langle C_{ee}^{(l)}\left[h_{e\boldsymbol{k}}^{(2)}\right]\right\rangle - \frac{1}{2}\left\langle(\boldsymbol{k}\cdot\boldsymbol{\rho}_e)^2\right\rangle C_{ee}^{(l)}\left[h_{e\boldsymbol{k}}^{(0)}\right] \\ &+ \left\langle C_{ee}^{(l)}\left[-\frac{1}{2}(\boldsymbol{k}\cdot\boldsymbol{\rho}_e)^2 h_{e\boldsymbol{k}}^{(0)}\right]\right\rangle + \left\langle (i\boldsymbol{k}\cdot\boldsymbol{\rho}_e) C_{ee}^{(l)}\left[-(i\boldsymbol{k}\cdot\boldsymbol{\rho}_e)h_{e\boldsymbol{k}}^{(0)}\right]\right\rangle \\ &+ \left\langle \mathcal{L}_{ei}\left[h_{e\boldsymbol{k}}^{(0)}\right]\right\rangle + \left\langle \mathcal{L}_{ei}\left[h_{e\boldsymbol{k}}^{(2)}\right]\right\rangle - \frac{1}{2}\left\langle(\boldsymbol{k}\cdot\boldsymbol{\rho}_e)^2\right\rangle \mathcal{L}_{ei}\left[h_{e\boldsymbol{k}}^{(0)}\right] \\ &+ \left\langle \mathcal{L}_{ei}\left[-\frac{1}{2}(\boldsymbol{k}\cdot\boldsymbol{\rho}_e)^2 h_{e\boldsymbol{k}}^{(0)}\right]\right\rangle + \left\langle (i\boldsymbol{k}\cdot\boldsymbol{\rho}_e)\mathcal{L}_{ei}\left[-(i\boldsymbol{k}\cdot\boldsymbol{\rho}_e)h_{e\boldsymbol{k}}^{(0)}\right]\right\rangle \Bigg], \end{aligned} \tag{A.55}$$

where all terms linear in $\boldsymbol{k}\cdot\boldsymbol{\rho}_e$ have vanished due to the definition of the gyroaverage. Both the electron-electron and electron-ion collision operators conserve both particle number and energy, and so the first, second, fourth, sixth, seventh and ninth terms vanish identically. The third and eighth terms combine to give (A.30), and thus also vanish, leaving

$$I_{\text{col}} = I_{ee} + I_{ei}, \tag{A.56}$$

where

$$I_{ee} = \frac{1}{n_{0e}} \int \mathrm{d}^3\boldsymbol{v}\, G(v) \sum_{\boldsymbol{k}} e^{i\boldsymbol{k}\cdot\boldsymbol{r}} \left\langle (i\boldsymbol{k}\cdot\boldsymbol{\rho}_e) C_{ee}^{(l)}\left[-(i\boldsymbol{k}\cdot\boldsymbol{\rho}_e)h_{e\boldsymbol{k}}^{(0)}\right]\right\rangle, \tag{A.57}$$

$$I_{ei} = \frac{1}{n_{0e}} \int \mathrm{d}^3\boldsymbol{v}\, G(v) \sum_{\boldsymbol{k}} e^{i\boldsymbol{k}\cdot\boldsymbol{r}} \left\langle (i\boldsymbol{k}\cdot\boldsymbol{\rho}_e) \mathcal{L}_{ei}\left[-(i\boldsymbol{k}\cdot\boldsymbol{\rho}_e)h_{e\boldsymbol{k}}^{(0)}\right]\right\rangle. \tag{A.58}$$

These integrals represent the effects of electron thermal diffusion due to electron-electron collisions and electron-ion collisions, respectively. To evaluate the first of them, we follow [64, 67, 129] in writing

$$\boldsymbol{k}\cdot\boldsymbol{\rho}_e = -\boldsymbol{v}\cdot\boldsymbol{\sigma}, \quad \boldsymbol{\sigma} = \frac{\boldsymbol{b}_0 \times \boldsymbol{k}}{\Omega_e}, \tag{A.59}$$

and changing variables inside the integral to $\{\boldsymbol{u},\boldsymbol{w}\} = \{\boldsymbol{v}+\boldsymbol{v}',\boldsymbol{v}-\boldsymbol{v}'\}$. With some judicious integration by parts, we find that (A.57) can be written as

$$\begin{aligned} I_{ee} = -\frac{\gamma_{ee} n_{0e}}{16\pi^3 m_e^2 v_{\text{the}}^6} \sum_{\boldsymbol{k}} e^{i\boldsymbol{k}\cdot\boldsymbol{r}} \frac{\delta T_{e\boldsymbol{k}}}{T_{0e}} \int \mathrm{d}^3\boldsymbol{u} \int \mathrm{d}^3\boldsymbol{w}\, e^{-(u^2+w^2)/2v_{\text{the}}^2} \left(\nabla_w \nabla_w w\right)_{ij} \\ \left[\sigma_i(G(v) - G(v')) + (\boldsymbol{\sigma}\cdot\boldsymbol{v})\frac{\partial G(v)}{\partial v_i} - (\boldsymbol{\sigma}\cdot\boldsymbol{v}')\frac{\partial G(v')}{\partial v_i'}\right]\left[\sigma_j \frac{\boldsymbol{u}\cdot\boldsymbol{w}}{v_{\text{the}}^2} + u_j \frac{\boldsymbol{\sigma}\cdot\boldsymbol{w}}{v_{\text{the}}^2}\right]. \end{aligned} \tag{A.60}$$

This is clearly zero for $G(v) = 1$, reflecting the fact that electron-electron collisions are unable to modify the electron density perturbation. For $G(v) = v^2/v_{\mathrm{the}}^2 - 3/2$, we make use of the properties of the projection operator

$$(\nabla_w \nabla_w w)_{ij} = \frac{w^2\delta_{ij} - w_i w_j}{w^3}, \quad (\nabla_w \nabla_w w)_{ij} w_i = (\nabla_w \nabla_w w)_{ij} w_j = 0, \tag{A.61}$$

where δ_{ij} is the Kronecker delta, as well as the identity

$$(\sigma v_{\mathrm{the}})^2 = (\boldsymbol{b}_0 \times \boldsymbol{k}) \cdot (\boldsymbol{b}_0 \times \boldsymbol{k})\rho_e^2 = \boldsymbol{k} \cdot [\boldsymbol{k} - (\boldsymbol{k} \cdot \boldsymbol{b}_0)\boldsymbol{b}_0]\, \rho_e^2 = (k_\perp \rho_e)^2, \tag{A.62}$$

from which we obtain

$$I_{ee} = \left(0, \frac{1}{\sqrt{2}}\nu_{ee}\rho_e^2 \nabla_\perp^2 \frac{\delta T_e}{T_e}\right). \tag{A.63}$$

Following an entirely analogous procedure for (A.58), we find

$$I_{ei} = \left(\frac{1}{2}\nu_{ei}\rho_e^2\nabla_\perp^2 \left[\frac{\delta n_e}{n_{0e}} - \varphi - \frac{1}{2}\frac{\delta T_e}{T_{0e}}\right], \frac{1}{2}\nu_{ei}\rho_e^2\nabla_\perp^2 \frac{\delta T_e}{T_{0e}} - \frac{1}{4}\nu_{ei}\rho_e^2\nabla_\perp^2 \left[\frac{\delta n_e}{n_{0e}} - \varphi - \frac{1}{2}\frac{\delta T_e}{T_{0e}}\right]\right). \tag{A.64}$$

We see that, unlike in the case of electron-electron collisions (A.63), electron-ion collisions make a contribution to the electron thermal diffusion that appears in the density moment. This arises due to the fact that the Lorentz collision operator (A.31) does not conserve momentum, allowing electron finite-Larmor-radius effects to couple density and temperature perturbations.

With these contributions calculated, we are in a position to take the density and temperature moments of (A.51). Making use of the fact that

$$\boldsymbol{v}_{\mathrm{de}} \cdot \nabla_\perp h_e^{(0)} = \frac{\rho_e v_{\mathrm{the}}}{2}\left(\frac{2}{R}\frac{v_\parallel^2}{v_{\mathrm{the}}^2} + \frac{1}{L_B}\frac{v_\perp^2}{v_{\mathrm{the}}^2}\right)\frac{\partial h_e^{(0)}}{\partial y}, \tag{A.65}$$

and (A.48), the density moment straightforwardly yields (A.68). For the temperature moment, we note that, from (A.43),

$$\frac{1}{n_{0e}}\int \mathrm{d}^3\boldsymbol{v}\, v_\parallel \left(\frac{v^2}{v_{\mathrm{the}}^2} - \frac{3}{2}\right) h_e^{(1)} = \left(1 + \frac{c_2}{c_1}\right) u_{\parallel e} + \frac{\delta q_e}{n_{0e}T_{0e}}, \tag{A.66}$$

where

$$\frac{\delta q_e}{n_{0e}T_{0e}} = -c_3 \frac{v_{\mathrm{the}}^2}{2\nu_{ei}} \nabla_\parallel \log T_e \tag{A.67}$$

is the collisional heat flux arising from the gradient of the total temperature along the perturbed field line ($c_3 = 3.16$ for $Z = 1$, in agreement with [111]). Then, taking the temperature moment yields (A.70).

A.4.4 Summary of equations

The outcome of appendices A.4.1-A.4.3 are the electron fluid equations arising from the moments of the electron gyrokinetic equations corresponding to density

$$\begin{aligned}&\frac{\mathrm{d}}{\mathrm{d}t}\left(\frac{\delta n_e}{n_{0e}}-\frac{\delta B_\parallel}{B_0}\right)+\frac{\rho_e v_{\mathrm{the}}}{2}\left\{\frac{\delta n_e}{n_{0e}}+\frac{\delta T_e}{T_{0e}},\frac{\delta B_\parallel}{B_0}\right\}+\nabla_\parallel u_{\parallel e}+\frac{\rho_e v_{\mathrm{the}}}{2L_n}\frac{\partial\varphi}{\partial y}\\&+\frac{\rho_e v_{\mathrm{the}}}{2}\left(\frac{1}{L_B}+\frac{1}{R}\right)\frac{\partial}{\partial y}\left(\frac{\delta n_e}{n_{0e}}-\varphi+\frac{\delta T_e}{T_{0e}}\right)-\frac{\rho_e v_{\mathrm{the}}}{2}\left(\frac{1}{L_n}+\frac{1}{L_T}\right)\frac{\partial}{\partial y}\frac{\delta B_\parallel}{B_0}\\&=\frac{1}{2}\nu_{ei}\rho_e^2\nabla_\perp^2\left(\frac{\delta n_e}{n_{0e}}-\varphi-\frac{1}{2}\frac{\delta T_e}{T_{0e}}\right),\end{aligned}\tag{A.68}$$

velocity

$$\begin{aligned}\frac{\mathrm{d}\mathcal{A}}{\mathrm{d}t}+\frac{v_{\mathrm{the}}}{2}\frac{\partial\varphi}{\partial z}=&\frac{v_{\mathrm{the}}}{2}\left(\nabla_\parallel\frac{\delta n_e}{n_{0e}}-\frac{\rho_e}{L_n}\frac{\partial\mathcal{A}}{\partial y}\right)+\left(1+\frac{c_2}{c_1}\right)\frac{v_{\mathrm{the}}}{2}\left(\nabla_\parallel\frac{\delta T_e}{T_{0e}}-\frac{\rho_e}{L_T}\frac{\partial\mathcal{A}}{\partial y}\right)\\&+\frac{\nu_{ei}}{c_1}\frac{u_{\parallel e}}{v_{\mathrm{the}}},\end{aligned}\tag{A.69}$$

and temperature

$$\begin{aligned}&\frac{\mathrm{d}}{\mathrm{d}t}\left(\frac{3}{2}\frac{\delta T_e}{T_{0e}}-\frac{\delta B_\parallel}{B_0}\right)+\frac{\rho_e v_{\mathrm{the}}}{2}\left\{\frac{\delta n_e}{n_{0e}}+\frac{7}{2}\frac{\delta T_e}{T_{0e}},\frac{\delta B_\parallel}{B_0}\right\}+\nabla_\parallel\frac{\delta q_e}{n_{0e}T_{0e}}+\left(1+\frac{c_2}{c_1}\right)\nabla_\parallel u_{\parallel e}\\&+\frac{\rho_e v_{\mathrm{the}}}{2}\left(\frac{1}{L_B}+\frac{1}{R}\right)\frac{\partial}{\partial y}\left(\frac{\delta n_e}{n_{0e}}-\varphi+\frac{7}{2}\frac{\delta T_e}{T_{0e}}\right)-\frac{\rho_e v_{\mathrm{the}}}{2}\left(\frac{1}{L_n}+\frac{7}{2L_T}\right)\frac{\partial}{\partial y}\frac{\delta B_\parallel}{B_0}\\&+\frac{3}{2}\frac{\rho_e v_{\mathrm{the}}}{2L_T}\frac{\partial\varphi}{\partial y}=\frac{1}{2}\left(1+\frac{\sqrt{2}}{Z}\right)\nu_{ei}\rho_e^2\nabla_\perp^2\frac{\delta T_e}{T_{0e}}-\frac{1}{4}\nu_{ei}\rho_e^2\nabla_\perp^2\left(\frac{\delta n_e}{n_{0e}}-\varphi-\frac{1}{2}\frac{\delta T_e}{T_{0e}}\right).\end{aligned}\tag{A.70}$$

Given the field equations

$$\frac{\delta n_e}{n_{0e}}=-\bar{\tau}^{-1}\varphi,\quad\frac{u_{\parallel e}}{v_{\mathrm{the}}}=d_e^2\nabla_\perp^2\mathcal{A},\quad\frac{\delta B_\parallel}{B_0}=-\frac{\beta_e}{2}\left(\frac{\delta n_e}{n_{0e}}-\varphi+\frac{\delta T_e}{T_{0e}}\right),\tag{A.71}$$

and the definition of the collisional heat flux (A.67), (A.68)-(A.70) form a closed, three-field system describing the evolution of the electrostatic potential φ, parallel component of the magnetic vector potential $\mathcal{A}$ and electron temperature $\delta T_e/T_{0e}$ perturbations in the presence of an electron temperature gradient, density gradient and magnetic field gradients associated with a magnetic geometry of constant curvature (see Section 2.1).

For the sake of completeness, we note that the usual force balance between the pressures of all plasma species, the equilibrium magnetic pressure, and the magnetic curvature force due to field-line bending gives us a constraint by which the equilibrium length scales of our system are related:

$$\frac{\beta_e}{2}\left(\frac{1}{L_n}+\frac{1}{L_T}\right)+\frac{\bar{\tau}\beta_e}{2L_n}+\frac{1}{L_B}=\frac{1}{R}.\tag{A.72}$$

A.5 Subsidiary limits

We now consider limits of the system (A.68)-(A.70) with respect to subsidiary orderings in the electron plasma beta $\beta_e \ll 1$, which was considered formally order unity for the purposes of the expansion in χ^{-1} [see (A.15)]. Physically, ordering β_e to be anything other than order unity corresponds to introducing a length-scale separation between the electron Larmor radius ρ_e and the electron inertial scale $d_e = \rho_e/\sqrt{\beta_e}$. As we shall shortly discover, this means that, as β_e is made small, one must choose to consider scales comparable to ρ_e (the zero-beta limit, Appendix A.5.1), d_e (the low-beta limit Appendix A.5.2), or somewhere in between (the electrostatic limit, Appendix A.5.3).

We would like any subsidiary ordering that we take to retain the effects of parallel thermal conduction simultaneously with those of the perpendicular drifts, meaning that we demand that

$$\omega \sim \omega_{*s} \sim \omega_{ds} \sim k_\perp v_E \sim \kappa k_\parallel^2, \tag{A.73}$$

as in (A.1). Recalling (A.4), this implies that the ordering of parallel and perpendicular wavenumbers can be written as

$$k_\parallel L_T \sim \sqrt{\sigma}, \quad \text{and} \quad k_\perp \rho_e \sim \sigma \frac{\lambda_{ei}}{L_T} \quad \Leftrightarrow \quad k_\perp d_e \chi \sim \frac{\sigma}{\beta_e}, \tag{A.74}$$

where σ is some constant, yet to be specified, that will be ordered with respect to β_e. Such a choice ensures that these effects will be captured in any subsidiary ordering, regardless of the value of σ. Instead, σ determines the size of the rates of thermal diffusion and resistivity relative to the frequency of the perturbations, viz.,

$$\frac{(k_\perp \rho_e)^2 \nu_{ee}}{\omega} \sim \sigma, \quad \frac{(k_\perp d_e)^2 \nu_{ei}}{\omega} \sim \frac{\sigma}{\beta_e}, \tag{A.75}$$

where we have used the fact that $\omega \sim \kappa k_\parallel^2$, as in (A.73). From (A.8)-(A.10), we then find the ordering of field amplitudes:

$$\varphi \sim \frac{\delta n_e}{n_{0e}} \sim \frac{\delta T_e}{T_{0e}} \sim \frac{\beta_e}{\sigma}\chi\epsilon, \quad \frac{\delta \boldsymbol{B}_\perp}{B_0} \sim \frac{\beta_e}{\sqrt{\sigma}}\varphi, \quad \frac{\delta B_\parallel}{B_0} \sim \frac{\beta_e}{\sigma}\varphi. \tag{A.76}$$

The first and second of these orderings guarantees that we will always retain the effects of $\boldsymbol{E}\times\boldsymbol{B}$ flows [see (A.5)-(A.7)] and parallel compressions [see (A.9)], respectively, while the third follows from the perturbed pressure balance manifest in the last expression in

(A.71). A direct consequence of (A.74) and (A.76) is that the size of the nonlinearities contained in the parallel derivatives $\nabla_\parallel$ [see (2.11)] is also determined by σ, viz.,

$$\frac{\delta \boldsymbol{B}_\perp}{B_0} \cdot \nabla_\perp \sim \frac{\beta_e}{\sigma} \frac{\partial}{\partial z}. \tag{A.77}$$

In light of (A.75) and (A.77), σ can be viewed as an ordering parameter that controls the size of the electromagnetic terms in (A.68)-(A.70) — this is what we will indeed find in the following sections.

A.5.1 Zero-beta limit

Let us first consider the case of $\sigma \sim 1$. From (A.74) and (A.76), we immediately have the ordering of wavenumbers

$$k_\parallel L \sim 1, \quad k_\perp \rho_e \sim \frac{\lambda_{ei}}{L}, \tag{A.78}$$

and amplitudes

$$\varphi \sim \frac{\delta n_e}{n_{0e}} \sim \frac{\delta T_e}{T_{0e}} \sim \beta_e \chi \epsilon, \quad \frac{\delta \boldsymbol{B}_\perp}{B_0} \sim \frac{\delta B_\parallel}{B_0} \sim \beta_e^2 \chi \epsilon. \tag{A.79}$$

(A.75) then implies that the resistive rate is the dominant frequency within the system, viz.,

$$\omega \sim \omega_{*s} \sim \omega_{ds} \sim k_\perp v_E \sim \kappa k_\parallel^2 \sim (k_\perp \rho_e)^2 \nu_{ee} \ll (k_\perp d_e)^2 \nu_{ei}. \tag{A.80}$$

This means that the resistive term on the right-hand side of (A.69) is larger than all other terms containing $\mathcal{A}$ by a factor of β_e — the latter of which can consequently be neglected — while all nonlinearities contained in the parallel derivatives $\nabla_\parallel$ are, from (A.77), small in β_e:

$$\frac{\delta \boldsymbol{B}_\perp}{B_0} \cdot \nabla_\perp \sim \beta_e \frac{\partial}{\partial z} \ll \frac{\partial}{\partial z}. \tag{A.81}$$

This is a consequence of the fact that field lines are not frozen into the electron flow (2.34) on electrostatic scales, and so no finite perturbations to the magnetic field direction can be created. Together, (A.80) and (A.81) imply that (A.69) becomes an equation for the perturbed parallel electron velocity [cf. (7.24)]:

$$u_{\parallel e} = v_{\mathrm{th}e} d_e^2 \nabla_\perp^2 \mathcal{A} = -\frac{c_1 v_{\mathrm{th}e}^2}{2\nu_{ei}} \frac{\partial}{\partial z} \left[\frac{\delta n_e}{n_{0e}} - \varphi + \left(1 + \frac{c_2}{c_1}\right) \frac{\delta T_e}{T_{0e}} \right]. \tag{A.82}$$

$\mathcal{A}$ thus ceases to be a dynamic field, in that it is instantaneously determined from the parallel gradient of the pressure. Substituting (A.82) into (A.68) and (A.70), neglecting any incidences of the parallel magnetic field perturbations according to (A.79), and noting that (A.72) implies that $R = L_B$ for $\beta_e \ll 1$, we find the following two-field system describing the evolution of the perturbations of the electron density

$$\begin{aligned}&\frac{\mathrm{d}}{\mathrm{d}t}\frac{\delta n_e}{n_{0e}} - \frac{c_1 v_{\mathrm{the}}^2}{2\nu_{ei}}\frac{\partial^2}{\partial z^2}\left(\frac{\delta n_e}{n_{0e}} - \varphi\right) - \left(1 + \frac{c_2}{c_1}\right)\frac{c_1 v_{\mathrm{the}}^2}{2\nu_{ei}}\frac{\partial^2}{\partial z^2}\frac{\delta T_e}{T_{0e}} + \frac{\rho_e v_{\mathrm{the}}}{2L_n}\frac{\partial \varphi}{\partial y}\\ &+ \frac{\rho_e v_{\mathrm{the}}}{L_B}\frac{\partial}{\partial y}\left(\frac{\delta n_e}{n_{0e}} - \varphi + \frac{\delta T_e}{T_{0e}}\right) = \frac{1}{2}\nu_{ei}\rho_e^2\nabla_\perp^2\left(\frac{\delta n_e}{n_{0e}} - \varphi - \frac{1}{2}\frac{\delta T_e}{T_{0e}}\right)\end{aligned} \tag{A.83}$$

and temperature

$$\begin{aligned}&\frac{\mathrm{d}}{\mathrm{d}t}\frac{\delta T_e}{T_{0e}} - \frac{2}{3}\left(1 + \frac{c_2}{c_1}\right)\frac{c_1 v_{\mathrm{the}}^2}{2\nu_{ei}}\frac{\partial^2}{\partial z^2}\left(\frac{\delta n_e}{n_{0e}} - \varphi\right) - \frac{2}{3}\left[\left(1 + \frac{c_2}{c_1}\right)^2 + \frac{c_3}{c_1}\right]\frac{c_1 v_{\mathrm{the}}^2}{2\nu_{ei}}\frac{\partial^2}{\partial z^2}\frac{\delta T_e}{T_{0e}}\\ &+ \frac{2}{3}\frac{\rho_e v_{\mathrm{the}}}{L_B}\frac{\partial}{\partial y}\left(\frac{\delta n_e}{n_{0e}} - \varphi + \frac{7}{2}\frac{\delta T_e}{T_{0e}}\right) + \frac{\rho_e v_{\mathrm{the}}}{2L_T}\frac{\partial \varphi}{\partial y}\\ &= \frac{1}{3}\left(1 + \frac{\sqrt{2}}{Z}\right)\nu_{ei}\rho_e^2\nabla_\perp^2\frac{\delta T_e}{T_{0e}} - \frac{1}{6}\nu_{ei}\rho_e^2\nabla_\perp^2\left(\frac{\delta n_e}{n_{0e}} - \varphi - \frac{1}{2}\frac{\delta T_e}{T_{0e}}\right).\end{aligned} \tag{A.84}$$

While we will not make use of these equations in the main body of this thesis, they have been included here for the sake of later comparisons, and to highlight the presence of an instability driven by the ETG in the presence of electron-ion thermal diffusion, which is discussed in Appendix A.6. We have called this the ‘zero-beta’ limit in order to distinguish it from the electrostatic limit of Appendix A.5.3.

A.5.2 Low-beta limit

In the previous section, the primary consequence of the ordering $\sigma \sim 1$ and of the resultant length-scale orderings (A.78) was to eliminate electromagnetic physics entirely from (A.68)-(A.70). Here, however, we wish to be able to resolve simultaneously both electrostatic and electromagnetic physics, the transition between which is controlled by the resistive term on the right-hand side of the parallel momentum equation (A.69) (see discussion in Section 2.4). This means that we must order the parallel conduction and resistive rates to be comparable, which, from (A.75) implies that $\sigma \sim \beta_e$, and so

$$k_\parallel L \sim \sqrt{\beta_e}, \quad k_\perp d_e \sim \chi^{-1} \equiv \sqrt{\beta_e}\frac{\lambda_{ei}}{L}, \tag{A.85}$$

i.e., the perpendicular wavelengths must be ordered comparable to the flux-freezing scale (2.33), as in (A.14), but now for $\beta_e \ll 1$. The ordering of the field amplitudes once again follows directly from (A.76):

$$\varphi \sim \frac{\delta n_e}{n_{0e}} \sim \frac{\delta T_e}{T_{0e}} \sim \chi\epsilon, \quad \frac{\delta \boldsymbol{B}_\perp}{B_0} \sim \chi\epsilon\sqrt{\beta_e}, \quad \frac{\delta B_\parallel}{B_0} \sim \beta_e \chi\epsilon. \tag{A.86}$$

An immediate consequence of this ordering is that, from (A.75), the rate of thermal diffusion is negligible in comparison to the other timescales, viz.,

$$\omega \sim \omega_{\mathrm{KAW}} \sim \omega_{*s} \sim \omega_{ds} \sim k_\perp v_E \sim \kappa k_\parallel^2 \sim (k_\perp d_e)^2 \nu_{ei} \gg (k_\perp \rho_e)^2 \nu_{ee}, \tag{A.87}$$

and so can be neglected everywhere that it appears in (A.68)-(A.70). The ordering of the perpendicular magnetic-field perturbations in (A.86) now allows field variation along the exact (perturbed) field lines to be order-unity different from the variation along the direction of the equilibrium magnetic field, viz., from (A.77),

$$\frac{\delta \boldsymbol{B}_\perp}{B_0} \cdot \nabla_\perp \sim \frac{\partial}{\partial z}, \tag{A.88}$$

meaning that we retain the nonlinear terms inside the parallel derivatives $\nabla_\parallel$ [see (2.11)]. Neglecting the parallel magnetic-field perturbations everywhere according to (A.86), our fluid equations (A.68)-(A.69) become:

$$\frac{\mathrm{d}}{\mathrm{d}t}\frac{\delta n_e}{n_{0e}} + \nabla_\parallel u_{\parallel e} + \frac{\rho_e v_{\mathrm{the}}}{L_B}\frac{\partial}{\partial y}\left(\frac{\delta n_e}{n_{0e}} - \varphi + \frac{\delta T_e}{T_{0e}}\right) = -\frac{\rho_e v_{\mathrm{the}}}{2L_n}\frac{\partial \varphi}{\partial y}, \tag{A.89}$$

$$\begin{aligned}\frac{\mathrm{d}\mathcal{A}}{\mathrm{d}t} + \frac{v_{\mathrm{the}}}{2}\frac{\partial \varphi}{\partial z} = \frac{v_{\mathrm{the}}}{2}\left(\nabla_\parallel \frac{\delta n_e}{n_{0e}} - \frac{\rho_e}{L_n}\frac{\partial \mathcal{A}}{\partial y}\right) + \left(1 + \frac{c_2}{c_1}\right)\frac{v_{\mathrm{the}}}{2}\left(\nabla_\parallel \frac{\delta T_e}{T_{0e}} - \frac{\rho_e}{L_T}\frac{\partial \mathcal{A}}{\partial y}\right) \\ + \frac{\nu_{ei}}{c_1}\frac{u_{\parallel e}}{v_{\mathrm{the}}},\end{aligned} \tag{A.90}$$

$$\begin{aligned}\frac{\mathrm{d}}{\mathrm{d}t}\frac{\delta T_e}{T_{0e}} + \frac{2}{3}\nabla_\parallel \frac{\delta q_e}{n_{0e}T_{0e}} + \frac{2}{3}\left(1 + \frac{c_2}{c_1}\right)\nabla_\parallel u_{\parallel e} + \frac{2}{3}\frac{\rho_e v_{\mathrm{the}}}{L_B}\frac{\partial}{\partial y}\left(\frac{\delta n_e}{n_{0e}} - \varphi + \frac{7}{2}\frac{\delta T_e}{T_{0e}}\right) \\ = -\frac{\rho_e v_{\mathrm{the}}}{2L_T}\frac{\partial \varphi}{\partial y},\end{aligned} \tag{A.91}$$

where we have (once again) used the fact that $R = L_B$ for $\beta_e \ll 1$ [see (A.72)]. Using the expression for the collisional heat flux (A.67), and ignoring all incidences of density and magnetic-field gradients, we obtain exactly (8.1)-(8.3).

Rescaling the collisionality as $\nu_{ei}/c_1 \to \nu_{ei}$ [recalling the definition of the collisional heat flux (A.67)], it becomes clear that the only difference between (A.89)-(A.91) and (2.27)-(2.29) — aside from the presence of some extra magnetic-drift terms, previously neglected — is the presence of the additive c_2/c_1 factors in (A.89) and (A.91). These factors are due to the fact that, in the presence of a temperature gradient, the energy of a particle depends on the direction of its motion, with particles coming from the higher-temperature regions having more energy than particles moving in the opposite direction (coming from the lower-temperature regions). This gives rise to a net frictional force proportional to $\nabla_\| \log T_e$ — manifest on the right-hand side of (A.90) — as the lower-temperature particles will undergo more frequent collisions than their hotter counterparts, and will thus lose more momentum than those coming from the hotter region. These thermal forces (see, e.g., [111, 127]) exist due to the velocity dependence of the collision frequency associated with the Landau collision operator, and hence were not captured by the simplified collision operator used in [1], where the collision frequency was a velocity-independent constant. If one performs the same analysis with (A.89)-(A.91) as was performed with the collisional equations (2.27)-(2.29) used in chapters 2-6, one will find only finite modifications to constant factors entering into all expressions; e.g., the electromagnetic results of Chapter 4 remain valid but with the rescaling $(1 + c_2/c_1)\xi_* \to \xi_*$, where ξ_* is defined in (4.10). This means that our results are robust with respect to the exact choice of collision operator, as we discussed in Section 7.1.3.

Note that (A.89)-(A.91) are identical to the equations (G9)-(G11) in [1]; this is unsurprising, since the ordering (A.87) is similarly identical to theirs [cf. their (A74)]. It may seem that the efforts of this appendix were somewhat futile, given that we have obtained the same set of equations in this low-beta limit. However, there is payoff for these efforts: not only does this appendix provide necessary clarification for the cursory derivation included in [1] [cf. their appendix G.1], but it demonstrates that (A.89)-(A.91) are in fact valid for a greater range of parameters and perpendicular scales than those considered here. Let us explain this point.

In this appendix, we first considered scales comparable to the electron Larmor radius ρ_e [see the first expression in (A.17)], the consequence of which was to make the ions adiabatic, as in (A.27). We then expanded the remaining terms in the electron gyrokinetic equation assuming dominant collisions [see (A.6)], ordering perpendicular wavenumbers to the flux-freezing scale, as in (A.14). Finally, taking the low-beta limit as above, we arrived at (A.89)-(A.91). Formally, such a procedure implies the following relative ordering of dimensionless parameters:

$$\epsilon \ll \sqrt{\frac{m_e}{m_i}} \ll \chi^{-1} \ll \sqrt{\beta_e} \ll 1, \tag{A.92}$$

viz., the expansions χ^{-1} and β_e were successive subsidiary expansions of the expansion in the mass ratio (and indeed also of the gyrokinetic ordering). However, the approach taken in [1] was to first order wavenumbers to be simultaneously comparable to both the ion Larmor radius ρ_i and the electron inertial length d_e, before assuming dominant collisions and imposing the adiabatic-ion limit in an analogous way to above [see their appendix A]. Such a procedure implies the following relative ordering of dimensionless parameters:

$$\epsilon \ll \sqrt{\beta_e} \sim \sqrt{\frac{m_e}{m_i}} \ll \chi^{-1} \ll 1. \tag{A.93}$$

From a comparison of (A.92) and (A.93), it is clear that the expansions in β_e and χ commute, implying that (A.89)-(A.91) are valid for a large range of electron beta:

$$\sqrt{\frac{m_e}{m_i}} \lesssim \sqrt{\beta_e} \ll 1. \tag{A.94}$$

Most importantly, the fact that the same equations can be obtained whether one first considers scales comparable to the electron Larmor radius (as we did here) or the ion Larmor radius (as in [1]) implies that they extend over a much greater range of perpendicular scales than is immediately obvious, viz., they are valid on scales $\rho_i^{-1} \ll k_\perp \ll \rho_e^{-1}$ for the range of beta (A.94). As such, we consider (A.89)-(A.91) to be the inevitable model for describing low-beta, collisional, electron-scale dynamics in the presence of equilibrium density and electron-temperature gradients in a geometry of constant magnetic curvature.

A.5.3 Electrostatic limit

Let us now consider intermediate scales between those corresponding to the zero-beta ($\sigma \sim 1$) and low-beta ($\sigma \sim \beta_e$) limits. Recalling (A.78) and (A.85), this implies that we must order our parallel and perpendicular wavenumbers as

$$\sqrt{\beta_e} \ll k_\parallel L_T \ll 1, \quad (d_e\chi)^{-1} \ll k_\perp \ll \rho_e^{-1}\frac{\lambda_{ei}}{L_T}. \tag{A.95}$$

Comparing (A.95) with (A.74), this means that we must also order $\beta_e \ll \sigma \ll 1$, i.e., σ must have some intermediate value between those corresponding to the zero-beta and low-beta limits; this translates immediately into the ordering (7.30). Then, (A.75) implies that the rates of electron thermal diffusion and resistivity are subdominant and dominant, respectively, viz.,

$$\frac{(k_\perp \rho_e)^2 \nu_{ee}}{\omega} \ll 1, \quad \frac{(k_\perp d_e)^2 \nu_{ei}}{\omega} \gg 1. \tag{A.96}$$

The first of these expressions means that electron thermal diffusion can be neglected everywhere that it appears in (A.68)-(A.70), as was done in Appendix A.5.2. When combined with the fact that the nonlinearities contained in the parallel derivatives $\nabla_\|$ are, from (A.77), once again negligible, viz.,

$$\frac{\delta \boldsymbol{B}_\perp}{B_0} \cdot \nabla_\perp \ll \frac{\partial}{\partial z}, \tag{A.97}$$

the second expression in (A.96) implies that (A.69) once again becomes an equation for the perturbed parallel electron velocity, as in (A.82). Then, in the same way as in Appendix A.5.1, this can be substituted into (A.68) and (A.70), yielding

$$\begin{aligned}
&\frac{\mathrm{d}}{\mathrm{d}t}\frac{\delta n_e}{n_{0e}} - \frac{c_1 v_{\mathrm{the}}^2}{2\nu_{ei}}\frac{\partial^2}{\partial z^2}\left(\frac{\delta n_e}{n_{0e}} - \varphi\right) - \left(1 + \frac{c_2}{c_1}\right)\frac{c_1 v_{\mathrm{the}}^2}{2\nu_{ei}}\frac{\partial^2}{\partial z^2}\frac{\delta T_e}{T_{0e}} + \frac{\rho_e v_{\mathrm{the}}}{2L_n}\frac{\partial \varphi}{\partial y} \\
&+ \frac{\rho_e v_{\mathrm{the}}}{L_B}\frac{\partial}{\partial y}\left(\frac{\delta n_e}{n_{0e}} - \varphi + \frac{\delta T_e}{T_{0e}}\right) = 0,
\end{aligned} \tag{A.98}$$

$$\begin{aligned}
&\frac{\mathrm{d}}{\mathrm{d}t}\frac{\delta T_e}{T_{0e}} - \frac{2}{3}\left(1 + \frac{c_2}{c_1}\right)\frac{c_1 v_{\mathrm{the}}^2}{2\nu_{ei}}\frac{\partial^2}{\partial z^2}\left(\frac{\delta n_e}{n_{0e}} - \varphi\right) - \frac{2}{3}\left[\left(1 + \frac{c_2}{c_1}\right)^2 + \frac{c_3}{c_1}\right]\frac{c_1 v_{\mathrm{the}}^2}{2\nu_{ei}}\frac{\partial^2}{\partial z^2}\frac{\delta T_e}{T_{0e}} \\
&+ \frac{2}{3}\frac{\rho_e v_{\mathrm{the}}}{L_B}\frac{\partial}{\partial y}\left(\frac{\delta n_e}{n_{0e}} - \varphi + \frac{7}{2}\frac{\delta T_e}{T_{0e}}\right) + \frac{\rho_e v_{\mathrm{the}}}{2L_T}\frac{\partial \varphi}{\partial y} = 0,
\end{aligned} \tag{A.99}$$

where we have once again neglected any incidences of the parallel magnetic-field perturbations according to (A.76), and used the fact that that $R = L_B$ for $\beta_e \ll 1$ [see (A.72)]. Making use of the quasineutrality condition (2.22) to express the density perturbations $\delta n_e / n_{0e}$ in terms of φ, defining the constants (7.31), and ignoring the equilibrium density gradient, these become exactly (7.66) and (7.67), respectively. In the absence of magnetic-field gradients, they become (7.25) and (7.26).

The electrostatic equations (A.98) and (A.99) can also be derived directly from either our zero-beta [(A.83) and (A.84)] or low-beta [(A.89)-(A.91)] equations. In the former case, this is done simply by considering the scales $k_\perp \rho_e \ll \lambda_{ei}/L$, as this allows the thermal-diffusion terms to be neglected. In the low-beta case, it is done by considering the scales $k_\perp d_e \chi \gg 1$, and following the same logic as in Section 7.1.3. The viability of both of these routes is unsurprising, given that (A.98) and (A.99) were explicitly derived at the scales intermediate between the two limits. The reason that we have belaboured this point, however, is to stress that σ is allowed to be arbitrary, up to the condition that it must lie within the range $\beta_e \ll \sigma \ll 1$ — the upper bound of this range corresponding to $k_\perp \rho_e \sim \lambda_{ei}/L$, and the lower bound corresponding to $k_\perp d_e \chi \sim 1$. This arbitrary nature of σ is a reflection of the fact that (A.98) and (A.99) are in fact scale-invariant, as we discuss in Section 7.1.3. These electrostatic equations thus represent a smooth connection between the low-beta and zero-beta (asymptotic) limits, and are thus an appropriate set of equations for the purposes of Chapter 7.

A.6 Electron-ion collisional instability

(A.83) and (A.84) contain the usual electrostatic instabilities that were the subject of Chapter 3 — namely, the collisional sETG and curvature-mediated ETG instabilities — a feature that they share with the other systems of equations derived in this appendix. (A.83) and (A.84), however, also contain another instability that relies solely on the presence of electron-ion thermal diffusion and the electron temperature gradient. To demonstrate this explicitly, we specialise to the two-dimensional limit and ignore the equilibrium gradients of both density an the magnetic field. Then, (A.83) and (A.84) become

$$\frac{\mathrm{d}}{\mathrm{d}t}\frac{\delta n_e}{n_{0e}} = \frac{1}{2}\nu_{ei}\rho_e^2\nabla_\perp^2\left(\frac{\delta n_e}{n_{0e}} - \varphi - \frac{1}{2}\frac{\delta T_e}{T_{0e}}\right), \tag{A.100}$$

$$\frac{\mathrm{d}}{\mathrm{d}t}\frac{\delta T_e}{T_{0e}} = -\frac{\rho_e v_{\mathrm{th}e}}{2L_T}\frac{\partial\varphi}{\partial y} + \frac{1}{3}\left(\frac{5}{4} + \frac{\sqrt{2}}{Z}\right)\nu_{ei}\rho_e^2\nabla_\perp^2\frac{\delta T_e}{T_{0e}} - \frac{1}{6}\nu_{ei}\rho_e^2\nabla_\perp^2\left(\frac{\delta n_e}{n_{0e}} - \varphi\right). \tag{A.101}$$

Linearising, Fourier transforming, and making use of the quasineutrality condition (A.35), we find the dispersion relation

$$\begin{aligned}\omega^2 &+ \left[1 + \bar{\tau} + \frac{2}{3}\left(\frac{5}{4} + \frac{\sqrt{2}}{Z}\right)\right]\frac{k_\perp^2\rho_e^2\nu_{ei}}{2}i\omega \\ &- \frac{2}{3}(1+\bar{\tau})\left(1 + \frac{\sqrt{2}}{Z}\right)\left(\frac{k_\perp^2\rho_e^2\nu_{ei}}{2}\right)^2 + \frac{k_\perp^2\rho_e^2\nu_{ei}}{4}i\omega_{*e}\bar{\tau} = 0.\end{aligned} \tag{A.102}$$

If we consider the limit of strong ETG drive, viz.,

$$(k_\perp\rho_e)^2\nu_{ei} \ll \omega \ll \omega_{*e}, \tag{A.103}$$

then the balance of the first and last terms in (A.102) gives us

$$\omega^2 = -i\frac{k_\perp^2\rho_e^2\nu_{ei}\omega_{*e}\bar{\tau}}{4} \quad \Rightarrow \quad \omega = \pm\frac{1-i\,\mathrm{sgn}(k_y)}{\sqrt{2}}\left(\frac{k_\perp^2\rho_e^2\nu_{ei}\,|\omega_{*e}|\,\bar{\tau}}{4}\right)^{1/2}, \tag{A.104}$$

with the unstable root representing the *electron-ion collisional instability.*

Physically, this instability arises due to the fact that the finite gyro-motion of the electrons allows them to sample the inhomogeneity in the equilibrium temperature, providing a feedback mechanism that is somewhat analogous to that provided by the magnetic drifts. The minimal set of equations that describe this process can be obtained from (A.100) and (A.101) under the ordering (A.103):

$$\frac{\mathrm{d}}{\mathrm{d}t}\bar{\tau}^{-1}\varphi = \frac{1}{4}\nu_{ei}\rho_e^2\nabla_\perp^2\frac{\delta T_e}{T_{0e}}, \quad \frac{\mathrm{d}}{\mathrm{d}t}\frac{\delta T_e}{T_{0e}} = -\frac{\rho_e v_{\mathrm{th}e}}{2L_T}\frac{\partial\varphi}{\partial y}. \tag{A.105}$$

Suppose that a small perturbation of the electron temperature is created with $k_y \neq 0$, bringing the plasma from regions with higher T_{0e} to those with lower T_{0e} ($\delta T_e > 0$), and vice-versa ($\delta T_e < 0$). Electrons in the hotter regions, owing to their larger gyro-orbits, will have higher velocities than those in colder regions; the difference between these velocities along the line of unperturbed temperature gives rise to an effective drift of electrons, and thus an electron-density perturbation [first equation in (A.105)]. This mechanism is similar to that which gives rise to the diamagnetic heat flux (see, e.g., [111]). By quasineutrality, the electron density perturbation gives rise to an exactly equal ion density perturbation, and that, via Boltzmann response, creates an electric field that produces an $\boldsymbol{E} \times \boldsymbol{B}$ drift which pushes hotter particles further into the colder region, and vice-versa [second equation in (A.105)], completing the feedback loop required for the instability.

Though (A.104) has been derived considering purely two-dimensional modes, the instability in fact extends to finite parallel wavenumbers, until it is quenched by thermal conduction and immediately replaced by the sETG instability. This is shown in Figure A.1(b). At short enough perpendicular wavelengths, it is eventually quenched by thermal diffusion, which erases both the density and temperature perturbations in

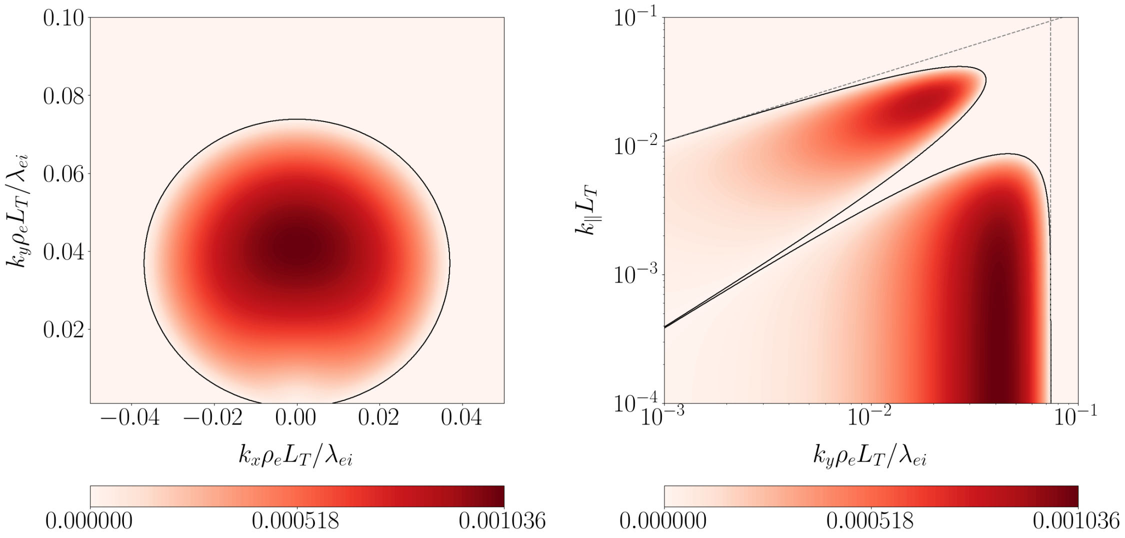

(a) $k_\parallel L_T = 0$

(b) $k_x\rho_e L_T/\lambda_{ei} = 0$

Figure A.1: Contour plots of the positive growth rates ($\gamma > 0$) arising from the linear dispersion relation of (A.83) and (A.84) in the (a) (k_x, k_y) and (b) $(k_y, k_\parallel)$ planes. The growth rates are normalised to $(\lambda_{ei}/L_T)^2\nu_{ei}/2$, and we have set $\bar{\tau} = Z = 1$ and $\omega_{de} = 0$. In both panels, the solid black line is the contour of zero growth rate. In panel (b), the vertical grey dashed line is (A.107), the stability boundary associated with the two-dimensional electron-ion collisional instability (A.104). The slanted grey dashed line is stability boundary of the collisional sETG instability (3.10), as derived from (A.83) and (A.84). The upper and lower regions of positive growth rate correspond to the sETG and electron-ion collisional instabilities, respectively.

(A.100) and (A.101). To see this, we consider the exact stability boundary of (A.102): assuming that ω is purely real, the real and imaginary parts of (A.102) are, respectively,

$$\omega^2 - \frac{2}{3}(1+\bar{\tau})\left(1+\frac{\sqrt{2}}{Z}\right)\left(\frac{k_\perp^2\rho_e^2\nu_{ei}}{2}\right)^2 = 0, \quad \left[1+\bar{\tau}+\frac{2}{3}\left(\frac{5}{4}+\frac{\sqrt{2}}{Z}\right)\right]\omega + \frac{\bar{\tau}}{2}\omega_{*e} = 0. \tag{A.106}$$

These can straightforwardly be combined to yield

$$\left(k_\perp\rho_e\frac{L_T}{\lambda_{ei}}\right)^2 = \frac{3}{8}\frac{\bar{\tau}^2}{(1+\bar{\tau})\left[1+\bar{\tau}+\frac{2}{3}\left(\frac{5}{4}+\frac{\sqrt{2}}{Z}\right)\right]^2}\frac{k_y^2}{k_\perp^2}, \tag{A.107}$$

where the perpendicular wavenumber normalisation has been chosen consistently with the ordering (A.78). This is the vertical grey dashed line in Figure A.1(b); to the right of this line, corresponding to the limit $(k_\perp\rho_e)^2\nu_{ei} \gg \omega_{*e}$, all modes are damped due to rapid thermal diffusion. The maximum growth rate of the instability is, therefore, reached asymptotically at $\omega_{*e} \sim (k_\perp \rho_e)^2 \nu_{ei}$. Indeed, maximising the growth rate from (A.102), we find that

$$\gamma_{\max} = C(\bar{\tau}, Z)\omega_{*e}, \tag{A.108}$$

where $C(\bar{\tau}, Z)$ is some constant formally of order unity, e.g., $C(1,1) \approx 0.025$. This means that the maximum growth rate of the electron-ion collisional instability is always (formally) comparable to that of the sETG [cf. (3.11)] at these scales.

We note that this instability does not appear within the low-beta equations (A.89)-(A.91) — or indeed the electrostatic equations (A.98) and (A.99) — on which we focus in this thesis, owing to the fact that the effects of thermal diffusion are negligible in both limits [see (A.87) or (A.96)]. However, given that we are primarily interested in electrostatic and electromagnetic instabilities on either side of the flux-freezing scale (2.33), we do not see the absence of the electron-ion collisional instability from our equations as particularly problematic for the current study.

References

[1] T. Adkins, A. A. Schekochihin, P. G. Ivanov, and C. M. Roach. Electromagnetic instabilities and plasma turbulence driven by electron-temperature gradient. J. Plasma Phys., 88:905880410, 2022.

[2] D.R. Hatch, M. Kotschenreuther, S.M. Mahajan, M.J. Pueschel, C. Michoski, G. Merlo, E. Hassan, A.R. Field, L. Frassinetti, C. Giroud, J.C. Hillesheim, C.F. Maggi, C. Perez von Thun, C.M. Roach, S. Saarelma, D. Jarema, F. Jenko, and JET Contributors. Microtearing modes as the source of magnetic fluctuations in the JET pedestal. Nucl. Fusion, 61:036015, 2021.

[3] J. C. Adam, W. M. Tang, and P. H. Rutherford. Destabilization of the trapped-electron mode by magnetic curvature drift resonances. Phys. Fluids, 19:561, 1976.

[4] M. A. Beer and G. W. Hammett. Bounce averaged trapped electron fluid equations for plasma turbulence. Phys. Plasmas, 3:4018, 1996.

[5] A. B. Mikhailovskii and L. I. Rudakov. The stability of a spatially inhomogeneous plasma in a magnetic field. Sov. Phys.–JETP, 17:621, 1963.

[6] N. A. Krall and M. N. Rosenbluth. Universal instability in complex field geometries. Phys. Fluids, 8:1488, 1965.

[7] R. E. Waltz. Three-dimensional global numerical simulation of ion temperature gradient mode turbulence. Phys. Fluids, 31:1962, 1988.

[8] S. C. Cowley, R. M. Kulsrud, and R. Sudan. Considerations of ion-temperature-gradient-driven turbulence. Phys. Fluids B, 3:2767, 1991.

[9] M. Kotschenreuther, W. Dorland, M. A. Beer, and G. W. Hammett. Quantitative predictions of tokamak energy confinement from first-principles simulations with kinetic effects. Phys. Plasmas, 2:2381, 1995.

[10] W. Dorland, F. Jenko, M. Kotschenreuther, and B. N. Rogers. Electron temperature gradient turbulence. Phys. Rev. Lett., 85:5579, 2000.

[11] F. Jenko, W. Dorland, M. Kotschenreuther, and B. N. Rogers. Electron temperature gradient driven turbulence. Phys. Plasmas, 7:1904, 2000.

[12] M. Barnes, F. I. Parra, and A. A. Schekochihin. Critically balanced ion temperature gradient turbulence in fusion plasmas. Phys. Rev. Lett., 107:115003, 2011.

[13] A. N. Kolmogorov. Local structure of turbulence in incompressible viscous fluid at very large Reynolds numbers. Dokl. Acad. Nauk SSSR, 30:299, 1941.

[14] R. C. Wolf. Internal transport barriers in tokamak plasmas. Plasma Phys. Control. Fusion, 45:R1, 2003.

[15] C. M. Roach, D. J. Applegate, J. W. Connor, S. C. Cowley, W. D. Dorland, R. J. Hastie, N. Joiner, S. Saarelma, A. A. Schekochihin, R. J. Akers, C. Brickley, A. R. Field, M. Valovic, and MAST Team. Microstability physics as illuminated in the spherical tokamak. Plasma Phys. Control. Fusion, 47:B323, 2005.

[16] C. M. Roach, I. G. Abel, R. J. Akers, W. Arter, M. Barnes, Y. Camenen, F. J. Casson, G. Colyer, J. W. Connor, S. C. Cowley, D. Dickinson, W. Dorland, A. R. Field, W. Guttenfelder, G. W. Hammett, R. J. Hastie, E. Highcock, N. F. Loureiro, A. G. Peeters, M. Reshko, S. Saarelma, A. A. Schekochihin, M. Valovic, and H. R. Wilson. Gyrokinetic simulations of spherical tokamaks. Plasma Phys. Control. Fusion, 51:124020, 2009.

[17] Y. Ren, E. Belova, N. Gorelenkov, W. Guttenfelder, S. M. Kaye, E. Mazzucato, J. L. Peterson, D. R. Smith, D. Stutman, K. Tritz, W. X. Wang, H. Yuh, R. E. Bell, C. W. Domier, and B. P. LeBlanc. Recent progress in understanding electron thermal transport in NSTX. Nucl. Fusion, 57:072002, 2017.

[18] W. Guttenfelder, J. L. Peterson, J. Candy, S. M. Kaye, Y. Ren, R. E. Bell, G. W. Hammett, B. P. LeBlanc, D. R. Mikkelsen, W. M. Nevins, and H. Yuh. Progress in simulating turbulent electron thermal transport in NSTX. Nucl. Fusion, 53: 093022, 2013.

[19] W. Guttenfelder, R. J. Groebner, J. M. Canik, B. A. Grierson, E. A. Belli, and J. Candy. Testing predictions of electron scale turbulent pedestal transport in two DIII-D ELMy H-modes. Nucl. Fusion, 61:056005, 2021.

[20] Y. Shimomura, Y. Murakami, A. R. Polevoi, P. Barabaschi, V. Mukhovatov, and M. Shimada. ITER: opportunity of burning plasma studies. Plasma Phys. Control. Fusion, 43:385, 2001.

[21] A. C. C. Sips. Advanced scenarios for ITER operation. Plasma Phys. Control. Fusion, 47:A19, 2005.

[22] B. S. Patel, D. Dickinson, C. M. Roach, and H. R. Wilson. Linear gyrokinetic stability of a high β non-inductive spherical tokamak. Nucl. Fusion, 62:016009, 2021.

[23] R. D. Hazeltine, D. Dobrott, and T. S. Wang. Kinetic theory of tearing instability. Phys. Fluids, 18:1778, 1975.

[24] J. F. Drake and Y. C. Lee. Kinetic theory of tearing instabilities. Phys. Fluids, 20:1341, 1977.

[25] J. F. Drake, N. T. Gladd, C. S. Liu, and C. L. Chang. Microtearing modes and anomalous transport in tokamaks. Phys. Rev. Lett., 44:994, 1980.

[26] A. B. Hassam. Fluid theory of tearing instabilities. Phys. Fluids, 23:2493, 1980.

[27] A. B. Hassam. Higher-order Chapman-Enskog theory for electrons. Phys. Fluids, 23:38, 1980.

[28] A. Zocco, N. F. Loureiro, D. Dickinson, R. Numata, and C. M. Roach. Kinetic microtearing modes and reconnecting modes in strongly magnetised slab plasmas. Plasma Phys. Control. Fusion, 57:065008, 2015.

[29] J. L. Larakers, R. D. Hazeltine, and S. M. Mahajan. A comprehensive conductivity model for drift and micro-tearing modes. Phys. Plasmas, 27:062503, 2020.

[30] J. L. Larakers, M. Curie, D. R. Hatch, R. D. Hazeltine, and S. M. Mahajan. Global theory of microtearing modes in the tokamak pedestal. Phys. Rev. Lett., 126:225001, 2021.

[31] D. J. Applegate, C. M. Roach, J. W. Connor, S. C. Cowley, W. Dorland, R. J. Hastie, and N. Joiner. Micro-tearing modes in the mega ampere spherical tokamak. Plasma Phys. Control. Fusion, 49:1113, 2007.

[32] W. Guttenfelder, J. Candy, S. M. Kaye, W. M. Nevins, R. E. Bell, G. W. Hammett, B. P. LeBlanc, and H. Yuh. Scaling of linear microtearing stability for a high collisionality National Spherical Torus Experiment discharge. Phys. Plasmas, 19: 022506, 2012.

[33] D. Dickinson, C. M. Roach, S. Saarelma, R. Scannell, A. Kirk, and H. R. Wilson. Microtearing modes at the top of the pedestal. Plasma Phys. Control. Fusion, 55:074006, 2013.

[34] I. Predebon and F. Sattin. On the linear stability of collisionless microtearing modes. Phys. Plasmas, 20:040701, 2013.

[35] S. Moradi, I. Pusztai, W. Guttenfelder, T. Fülöp, and A. Mollén. Microtearing modes in spherical and conventional tokamaks. Nucl. Fusion, 53:063025, 2013.

[36] T. Rafiq, J. Weiland, A. H. Kritz, L. Luo, and A. Y. Pankin. Microtearing modes in tokamak discharges. Phys. Plasmas, 23:062507, 2016.

[37] W. M. Tang, J. W. Connor, and R. J. Hastie. Kinetic-ballooning-mode theory in general geometry. Nucl. Fusion, 20:1439, 1980.

[38] P. B. Snyder. Gyrofluid theory and simulation of electromagnetic turbulence and transport in tokamak plasmas. PhD thesis, Princeton University (URL: `https://w3.pppl.gov/~hammett/gyrofluid/papers/1999/thesis.pdf)`, 1999.

[39] P. B. Snyder and G. W. Hammett. Electromagnetic effects on plasma microturbulence and transport. Phys. Plasmas, 8:744, 2001.

[40] P. B. Snyder and G. W. Hammett. A Landau fluid model for electromagnetic plasma microturbulence. Phys. Plasmas, 8:3199, 2001.

[41] M. J. Pueschel, M. Kammerer, and F. Jenko. Gyrokinetic turbulence simulations at high plasma beta. Phys. Plasmas, 15:102310, 2008.

[42] M. J. Pueschel and F. Jenko. Transport properties of finite-β microturbulence. Phys. Plasmas, 17:062307, 2010.

[43] R. E. Waltz. Nonlinear subcritical magnetohydrodynamic beta limit. Phys. Plasmas, 17:072501, 2010.

[44] W. Wan, S. E. Parker, Y. Chen, Z. Yan, R. J. Groebner, and P. B. Snyder. Global Gyrokinetic Simulation of Tokamak Edge Pedestal Instabilities. Phys. Rev. Lett., 109:185004, 2012.

[45] W Wan, S. E. Parker, Y. Chen, R. J. Groebner, Z. Yan, A. Y. Pankin, and S. E. Kruger. Global gyrokinetic simulations of the h-mode tokamak edge pedestal. Phys. Plasmas, 20:055902, 2013.

[46] A. Ishizawa, S. Maeyama, T. H. Watanabe, H. Sugama, and N. Nakajima. Gyrokinetic turbulence simulations of high-beta tokamak and helical plasmas with full-kinetic and hybrid models. Nucl. Fusion, 53:053007, 2013.

[47] A. Ishizawa, T.-H. Watanabe, H. Sugama, S. Maeyama, and N. Nakajima. Electromagnetic gyrokinetic turbulence in finite-beta helical plasmas. Phys. Plasmas, 21:055905, 2014.

[48] A. Ishizawa, D. Urano, Y. Nakamura, S. Maeyama, and T. H. Watanabe. Persistence of Ion Temperature Gradient Turbulent Transport at Finite Normalized Pressure. Phys. Rev. Lett., 123:025003, 2019.

[49] P. W. Terry, D. Carmody, H. Doerk, W. Guttenfelder, D. R. Hatch, C. C. Hegna, A. Ishizawa, F. Jenko, W. M. Nevins, I. Predebon, M. J. Pueschel, J. S. Sarff, and G. G. Whelan. Overview of gyrokinetic studies of finite-beta microturbulence. Nucl. Fusion, 55:104011, 2015.

[50] K. Aleynikova and A. Zocco. Quantitative study of kinetic ballooning mode theory in simple geometry. Phys. Plasmas, 24:092106, 2017.

[51] G. G. Howes, S. C. Cowley, W. Dorland, G. W. Hammett, E. Quataert, and A. A. Schekochihin. Astrophysical gyrokinetics: basic equations and linear theory. Astrophys. J., 651:590, 2006.

[52] I. G. Abel and A. Hallenbert. Multiscale modelling for tokamak pedestals. J. Plasma Phys., 84:745840202, 2018.

[53] J. F. Parisi, F. I. Parra, C. M. Roach, C. Giroud, W. Dorland, D. R. Hatch, M. Barnes, J. C. Hillesheim, N. Aiba, J. Ball, P. G. Ivanov, and JET contributors. Toroidal and slab ETG instability dominance in the linear spectrum of JET-ILW pedestals. Nucl. Fusion, 60:126045, 2020.

[54] J. F. Parisi, F. I. Parra, C. M. Roach, M. R. Hardman, A. A. Schekochihin, I. G. Abel, N. Aiba, J. Ball, M. Barnes, B. Chapman-Oplopoiou, D. Dickinson, W. Dorland, C. Giroud, D. R. Hatch, J. C. Hillesheim, J. Ruiz Ruiz, S. Saarelma, D. St-Onge, and JET Contributors. Three-dimensional inhomogeneity of electron-temperature-gradient turbulence in the edge of tokamak plasmas. Nucl. Fusion, 62:086045, 2022.

[55] I. G. Abel, G. G. Plunk, E. Wang, M. Barnes, S. C. Cowley, W. Dorland, and A. A. Schekochihin. Multiscale gyrokinetics for rotating tokamak plasmas: fluctuations, transport and energy flows. Rep. Prog. Phys., 76:116201, 2013.

[56] C. S. Liu. Instabilities in a magnetoplasma with skin current. Phys. Rev. Lett., 27:1637, 1971.

[57] Y. C. Lee, J. Q. Dong, P. N. Guzdar, and C. S. Liu. Collisionless electron temperature gradient instability. The Physics of Fluids, 30:1331, 1987.

[58] W. Horton, B. G. Hong, and W. M. Tang. Toroidal electron temperature gradient driven drift modes. Phys. Fluids, 31:2971, 1988.

[59] M. Kotschenreuther, X. Liu, D. R. Hatch, S. Mahajan, L. Zheng, A. Diallo, R. Groebner, the DIII-D TEAM, J. C. Hillesheim, C. F. Maggi, C. Giroud, F. Koechl, V. Parail, S. Saarelma, E. Solano, A. Chankin, and JET Contributors. Gyrokinetic analysis and simulation of pedestals to identify the culprits for energy losses using 'fingerprints'. Nucl. Fusion, 59:096001, 2019.

[60] M. J. Pueschel, P. W. Terry, F. Jenko, D. R. Hatch, W. M. Nevins, T. Görler, and D. Told. Extreme Heat Fluxes in Gyrokinetic Simulations: A New Critical β. Phys. Rev. Lett., 110:155005, 2013.

[61] M. J. Pueschel, D. R. Hatch, T. Görler, W. M. Nevins, F. Jenko, P. W. Terry, and D. Told. Properties of high-β microturbulence and the non-zonal transition. Phys. Plasmas, 20:102301, 2013.

[62] M. J. Pueschel, P. W. Terry, and D. R. Hatch. Aspects of the non-zonal transition. Phys. Plasmas, 21:055901, 2014.

[63] M. J. Pueschel, P. W. Terry, D. Told, and F. Jenko. Enhanced magnetic reconnection in the presence of pressure gradients. Phys. Plasmas, 22:062105, 2015.

[64] P. G. Ivanov, A. A. Schekochihin, W. Dorland, A. R. Field, and F. I. Parra. Zonally dominated dynamics and Dimits threshold in curvature-driven ITG turbulence. J. Plasma Phys., 86:855860502, 2020.

[65] P. Ricci, B. N. Rogers, W. Dorland, and M. Barnes. Gyrokinetic linear theory of the entropy mode in a Z pinch. Physics of Plasmas, 13:062102, June 2006. doi: 10.1063/1.2205830.

[66] P. G. Ivanov, A. A. Schekochihin, and W. Dorland. Dimits transition in three-dimensional ion-temperature-gradient turbulence. J. Plasma Phys., 88: 905880506, 2022.

[67] M. R. Hardman, F. I. Parra, C. Chong, T. Adkins, M. C. Anastopoulos-Tzanis, M. Barnes, D. Dickinson, J. F. Parisi, and H. R. Wilson. Extended electron tails in electrostatic microinstabilities and the nonadiabatic response of passing electrons. Plasma Phys. Control. Fusion, 64:055004, 2022.

[68] J. P. Dougherty. Model Fokker-Planck Equation for a Plasma and Its Solution. Phys. Fluids, 7:1788, 1964.

[69] L. Landau. On the vibration of the electronic plasma. Zh. Eksp. Teor. Fiz., 16: 574, 1946.

[70] J. D. Callen. Drift-wave turbulence effects on magnetic structure and plasma transport in tokamaks. Phys. Rev. Lett., 39:1540, 1977.

[71] W. M. Manheimer and I. Cook. A theory of particle and energy flux from the magnetic flutter of drift waves. US Defense Technical Information Center (URL: `https://apps.dtic.mil/sti/citations/ADA053947`), 1978.

[72] A. A. Schekochihin, S. C. Cowley, W. Dorland, G. W. Hammett, G. G. Howes, E. Quataert, and T. Tatsuno. Astrophysical gyrokinetics: kinetic and fluid turbulent cascades in magnetized weakly collisional plasmas. Astrophys. J. Suppl., 182:310, 2009.

[73] A. A. Schekochihin, Y. Kawazura, and M. A. Barnes. Constraints on ion versus electron heating by plasma turbulence at low beta. J. Plasma Phys., 85: 905850303, 2019.

[74] I. G. Abel and S. C. Cowley. Multiscale gyrokinetics for rotating tokamak plasmas: II. Reduced models for electron dynamics. New J. Phys., 15:023041, 2013.

[75] J. Zielinski, A. I. Smolyakov, P. Beyer, and S. Benkadda. Electromagnetic electron temperature gradient driven instability in toroidal plasmas. Phys. Plasmas, 24:024501, 2017.

[76] S. Boldyrev, K. Horaites, Q. Xia, and J. C. Perez. Toward a Theory of Astrophysical Plasma Turbulence at Subproton Scales. Astrophys. J., 777:41, 2013.

[77] A. Zocco and A. A. Schekochihin. Reduced fluid-kinetic equations for low-frequency dynamics, magnetic reconnection, and electron heating in low-beta plasmas. Phys. Plasmas, 18:102309, 2011.

[78] T. Passot, P. L. Sulem, and E. Tassi. Electron-scale reduced fluid models with gyroviscous effects. J. Plasma Phys., 83:715830402, 2017.

[79] R. Xu and M. W. Kunz. Linear Vlasov theory of a magnetised, thermally stratified atmosphere. J. Plasma Phys., 82:905820507, 2016.

[80] S. Maeyama, S. Kusaka, and T.-H. Watanabe. Effects of ion polarization and finite-β_e on heat transport in slab electron-temperature-gradient driven turbulence. Phys. Plasmas, 28:052512, 2021.

[81] A. A. Schekochihin, S. C. Cowley, W. Dorland, G. W. Hammett, G. G. Howes, G. G. Plunk, E. Quataert, and T. Tatsuno. Gyrokinetic turbulence: a nonlinear route to dissipation through phase space. Plasma Phys. Control. Fusion, 50: 124024, 2008.

[82] G. J. Colyer, A. A. Schekochihin, F. I. Parra, C. M. Roach, M. A. Barnes, Y.-c. Ghim, and W. Dorland. Collisionality scaling of the electron heat flux in ETG turbulence. Plasma Phys. Control. Fusion, 59:055002, 2017.

[83] P. Goldreich and S. Sridhar. Toward a theory of interstellar turbulence. 2: Strong Alfvénic turbulence. Astrophys. J., 438:763, 1995.

[84] P. Goldreich and S. Sridhar. Magnetohydrodynamic turbulence revisited. Astrophys. J., 485:680, 1997.

[85] S. Boldyrev. On the spectrum of magnetohydrodynamic turbulence. Astrophys. J., 626:L37, 2005.

[86] S. V. Nazarenko and A. A. Schekochihin. Critical balance in magnetohydrodynamic, rotating and stratified turbulence: towards a universal scaling conjecture. J. Fluid Mech., 677:134, 2011.

[87] A. A. Schekochihin, J. T. Parker, E. G. Highcock, P. J. Dellar, W. Dorland, and G. W. Hammett. Phase mixing versus nonlinear advection in drift-kinetic plasma turbulence. J. Plasma Phys., 82:905820212, 2016.

[88] T. G. Adkins and A. A. Schekochihin. A solvable model of Vlasov-kinetic plasma turbulence in Fourier-Hermite phase space. J. Plasma Phys., 84:905840107, 2018.

[89] F. I. Parra and M. A. Barnes. private communication, 2012.

[90] B. Chapman-Oplopoiou, D. R. Hatch, A. R. Field, L. Frassinetti, J. Hillesheim, L. Horvath, C. F. Maggi, J. Parisi, C. M. Roach, S. Saarelma, and J. Walker. The role of ETG modes in JET–ILW pedestals with varying levels of power and fuelling. Nucl. Fusion, 62:086028, 2022.

[91] J. Cho and A. Lazarian. The anisotropy of electron magnetohydrodynamic turbulence. Astrophys. J., 615:L41, 2004.

[92] J. Cho and A. Lazarian. Simulations of electron magnetohydrodynamic turbulence. Astrophys. J., 701:236, 2009.

[93] G. G. Howes, J. M. Tenbarge, W. Dorland, E. Quataert, A. A. Schekochihin, R. Numata, and T. Tatsuno. Gyrokinetic simulations of solar wind turbulence from ion to electron scales. Phys. Rev. Lett., 107:035004, 2011.

[94] S. Boldyrev and J. C. Perez. Spectrum of kinetic-Alfvén turbulence. Astrophys. J., 758:L44, 2012.

[95] R. Meyrand and S. Galtier. Anomalous $k_\perp^{-8/3}$ spectrum in electron magnetohydrodynamic turbulence. Phys. Rev. Lett., 111:264501, 2013.

[96] D. Told, F. Jenko, J. M. TenBarge, G. G. Howes, and G. W. Hammett. Multiscale nature of the dissipation range in gyrokinetic simulations of Alfvénic turbulence. Phys. Rev. Lett., 115:025003, 2015.

[97] D. Grošelj, A. Mallet, N. F. Loureiro, and F. Jenko. Fully kinetic simulation of 3D kinetic Alfvén turbulence. Phys. Rev. Lett., 120:105101, 2018.

[98] D. Grošelj, C. H. K. Chen, A. Mallet, R. Samtaney, K. Schneider, and F. Jenko. Kinetic turbulence in astrophysical plasmas: waves and/or structures? Phys. Rev. X, 9:031037, 2019.

[99] L. Franci, S. Landi, A. Verdini, L. Matteini, and P. Hellinger. Solar wind turbulent cascade from MHD to sub-ion scales: large-size 3D hybrid particle-in-cell simulations. Astrophys. J., 853:26, 2018.

[100] O. Alexandrova, J. Saur, C. Lacombe, A. Mangeney, J. Mitchell, S. J. Schwartz, and P. Robert. Universality of solar-wind turbulent spectrum from MHD to electron scales. Phys. Rev. Lett., 103:165003, 2009.

[101] F. Sahraoui, M. L. Goldstein, G. Belmont, P. Canu, and L. Rezeau. Three dimensional anisotropic k spectra of turbulence at subproton scales in the solar wind. Phys. Rev. Lett., 105:131101, 2010.

[102] C. H. K. Chen, S. Boldyrev, Q. Xia, and J. C. Perez. Nature of subproton scale turbulence in the solar wind. Phys. Rev. Lett., 110:225002, 2013.

[103] A. Bañón Navarro, P. Morel, M. Albrecht-Marc, D. Carati, F. Merz, T. Görler, and F. Jenko. Free energy cascade in gyrokinetic turbulence. Phys. Rev. Lett., 106:055001, 2011.

[104] D. R. Hatch, F. Jenko, V. Bratanov, and A. Bañón Navarro. Phase space scales of free energy dissipation in gradient-driven gyrokinetic turbulence. J. Plasma Phys., 80:531, 2014.

[105] J. T. Parker, E. G. Highcock, A. A. Schekochihin, and P. J. Dellar. Suppression of phase mixing in drift-kinetic plasma turbulence. Phys. Plasmas, 23:070703, 2016.

[106] J. W. Connor and J. B. Taylor. Scaling laws for plasma confinement. Nucl. Fusion, 17:1047, 1977.

[107] G. T. Roberg-Clark, G. G. Plunk, and P. Xanthopoulos. Coarse-grained gyrokinetics for the critical ion temperature gradient in stellarators. Phys. Rev. Res., 4:L032028, 2022.

[108] A. M. Dimits, G. Bateman, M. A. Beer, B. I. Cohen, W. Dorland, G. W. Hammett, C. Kim, J. E. Kinsey, M. Kotschenreuther, A. H. Kritz, L. L. Lao, J. Mandrekas, W. M. Nevins, S. E. Parker, A. J. Redd, D. E. Shumaker, R. Sydora, and J. Weiland. Comparisons and physics basis of tokamak transport models and turbulence simulations. Phys. Plasmas, 7:969, 2000.

[109] M. R. Hardman, F. I. Parra, B. S. Patel, C. M. Roach, J. Ruiz Ruiz, M. Barnes, D. Dickinson, W. Dorland, J. F. Parisi, D. St-Onge, and H. Wilson. New stability parameter to describe low-β electromagnetic microinstabilities driven by passing electrons in axisymmetric toroidal geometry. arXiv e-prints, 2208.10615, 2022.

[110] L. Onsager. Reciprocal relations in irreversible processes. I. Phys. Rev., 37:405, 1931.

[111] S. I. Braginskii. Transport Processes in a Plasma. Rev. Plasma Phys., 1:205, 1965.

[112] SA Orszag. On the elimination of aliasing in finite-difference schemes by filtering high-wavenumber components. J. Atmos. Sci., 28:1074, 1971.

[113] M. Kotschenreuther, G. Rewoldt, and W. M. Tang. Comparison of initial value and eigenvalue codes for kinetic toroidal plasma instabilities. Comp. Phys. Comms., 88:128, 1995.

[114] D. N. Hosking and A. A. Schekochihin. Emergence of long-range correlations and thermal spectra in forced turbulence. arXiv e-prints, 2202.00462, 2022.

[115] A. A. Schekochihin. MHD turbulence: a biased review. J. Plasma Phys., 88: 155880501, 2022.

[116] D. R. Hatch, P. W. Terry, F. Jenko, F. Merz, and W. M. Nevins. Saturation of Gyrokinetic Turbulence through Damped Eigenmodes. Phys. Rev. Lett., 106: 115003, 2011.

[117] G. W. Hammett, M. A. Beer, W. Dorland, S. C. Cowley, and S. A. Smith. Developments in the gyrofluid approach to tokamak turbulence simulations. Plasma Phys. Control. Fusion, 35:973, 1993.

[118] B. N. Rogers, W. Dorland, and M. Kotschenreuther. Generation and stability of zonal flows in ion-temperature-gradient mode turbulence. Phys. Rev. Lett., 85: 5336, 2000.

[119] A. Hasegawa and K. Mima. Pseudo-three-dimensional turbulence in magnetized nonuniform plasma. Phys. Fluids, 21:87, 1978.

[120] A. Hasegawa and M Wakatani. Plasma Edge Turbulence. Phys. Rev. Lett., 50: 682, 1983.

[121] P. W. Terry and W. Horton. Drift wave turbulence in a low-order k space. Phys. Fluids, 26:106, 1983.

[122] R. Meyrand, J. Squire, A.A. Schekochihin, and W. Dorland. On the violation of the zeroth law of turbulence in space plasmas. J. Plasma Phys., 87:535870301, 2021.

[123] G. Miloshevich, D. Laveder, T. Passot, and P.-L. Sulem. Inverse cascade and magnetic vortices in kinetic Alfvén-wave turbulence. J. Plasma Phys., 87:905870201, 2021.

[124] F. I. Parra, M. Barnes, and A. G. Peeters. Up-down symmetry of the turbulent transport of toroidal angular momentum in tokamaks. Phys. Plasmas, 18:062501, 2011.

[125] H. Sugama, T. H. Watanabe, M. Nunami, and S. Nishimura. Momentum balance and radial electric fields in axisymmetric and nonaxisymmetric toroidal plasmas. Plasma Phys. Control. Fusion, 53:024004, 2011.

[126] D. N. Hosking and A. A. Schekochihin. Reconnection-controlled decay of magnetohydrodynamic turbulence and the role of invariants. Phys. Rev. X, 11:041005, 2021.

[127] P. Helander and D. J. Sigmar. Collisional Transport in Magnetized Plasmas. Cambridge University Press, Cambridge, 2005.

[128] L. Spitzer and R. Härm. Transport phenomena in a completely ionized gas. Phys. Rev., 89:977, 1953.

[129] S. L. Newton, S. C. Cowley, and N. F. Loureiro. Understanding the effect of sheared flow on microinstabilities. Plasma Phys. Control. Fusion, 52:125001, 2010.